Development and applications of various $BiFeO_3$ structures for fabrication of high-performing devices using industry-ready technologies

by

Paul FOURMONT

MANUSCRIPT-BASED THESIS PRESENTED TO ÉCOLE DE TECHNOLOGIE SUPÉRIEURE IN PARTIAL FULFILLMENT FOR THE DEGREE OF DOCTOR OF PHILOSOPHY
Ph.D.

MONTREAL, DECEMBER 5, 2022

ÉCOLE DE TECHNOLOGIE SUPÉRIEURE
UNIVERSITÉ DU QUÉBEC

BOARD OF EXAMINERS

THIS THESIS HAS BEEN EVALUATED

BY THE FOLLOWING BOARD OF EXAMINERS

Prof. Sylvain G. Cloutier, Thesis supervisor
Department of Mechanical Engineering, École de technologie supérieure

Prof. Éric David, President of the board of examiners
Department of Electrical Engineering, École de technologie supérieure

Prof. Gaixia Zhang, Member of the jury
Department of Electrical Engineering, École de technologie supérieure

Prof. Caroline A. Ross, External independent jury member
Department of Materials Science and Engineering, Massachusetts Institute of Technology

Prof. Martin Bolduc, External examiner
Department of Mechanical Engineering, Université du Québec à Trois-Rivières

THIS THESIS WAS PRESENTED AND DEFENDED

IN THE PRESENCE OF A BOARD OF EXAMINERS AND THE PUBLIC

ON NOVEMBER 18, 2022

AT ÉCOLE DE TECHNOLOGIE SUPÉRIEURE

ACKNOWLEDGEMENTS

I would like to firstly thank my Family for their endless support and understanding throughout all my scolarity and especially since I chose to live abroad to join l'École de Technologie Supérieure. To my girlfriend Charlotte, I am grateful and feeling lucky to have you. Thanks, for your comprehension and your listening during the past four years. Without you, this experience would not have been the same.

I am thankful to my supervisor, Sylvain Cloutier for is financial support during my thesis and his guidance since I joined his group in 2016 as a master student. Thanks for your trust and for giving me the opportunity to develop my skills both as a scientist and human being. Thanks for your lessons, your patience and for the freedom that you gave me. By doing so, I was able to discover my own path and lead my own investigations.

I am also thankful to Riad Nechache for his assistance as a co-supervisor during the first three years of my doctorate. Thanks for introducing me to Sylvain and to the big world of perovskite. Thanks for pushing me forward and for encouraging me to continue my research activity after my master's degree at ÉTS.

I cannot thank Mohammad Saadati enough for his friendship and his precious help. All the microscope images you will find in this thesis come from his great work. Thanks for your patience and for the hundreds of hours we spent together looking at samples. Even though we probably raise more questions than we were able to solve, your help and the great quality of your work had a huge impact on my findings. Thanks for your patience and our time despite your very busy schedule.

I am thankful to all my colleagues: Abhiroop, Ahmed, Aida, Alain, Alexandre, Arjun, Charles, Dawit, Debika, Emile, Fabrice, Felipe, François-Xavier, Ibrahima, Ivy, Jaime, Shayan, Soraya, Xiaohang and Yin. Thanks for your inputs, your help, your presence and your support. I am grateful for knowing each of you and for the great scientific discussions or collaborations.

Thanks for your patience and for helping me with my poor English skills when I first joined the lab.

I am grateful to all the ÉTS technical support team who participate and contribute to my scientific endeavors: Normand Gravel, Michael Dubois, Serge Plamondon, Christian Talbot and Simon Laflamme. Thank you very much for your help and the training.

I am thankful to both PhD students: Mathieu Gratuze and Victor Brial for their assistance and help with some measurements that you will find later in this thesis.

I also want to acknowledge Emmanuel Guilmeau for giving the opportunity to realize two internships in the laboratories of the CNRT Matériaux in Caen (France) during my undergrad degree. Thanks to these two work experiences, I realized how much I enjoy doing research and without any doubt it pushed me toward this thesis.

I am grateful to Shyamashis Das for his precious work and collaboration on one of the published papers in this thesis.

I am thankful to Jean-Phillipe Masse for his assistance and fruitful conversations about transmission electron microscopy. Thanks for your time and your patience.

Development and applications of various $BiFeO_3$ structures for fabrication of high-performing devices using industry-ready technologies

Paul FOURMONT

ABSTRACT

Production of cleaner energy and the treatment of more and more toxic wastewater are probably the two main challenges humanity will face in the decades to come. Even though tremendous efforts are deployed to bring tangible answers to those problems, a lot of investigations are still needed to find optimal solutions. Among those, ceramic materials and more precisely oxide perovskite are of huge interest. Due to its singular crystalline structure, bismuth ferrite or $BiFeO_3$ (BFO) is today one of the most studied oxide perovskites. In fact, BFO is a unique multiferroic material as it possesses both ferroelectric and ferromagnetic ordering within the same phase at room temperature. Some coupling effects between both orders have also been demonstrated and most of them are still under intense theoretical and experimental investigations. Despite such endeavors, commercial devices based on BFO are still scarce.

The framework of this doctoral thesis aims to contribute to the advancement of devices based on bismuth ferrite. In particular, this thesis focuses on the development of BFO nanofibers and powders to fabricate high-performing devices.

Following an extensive review of the literature about BFO, we first identify sun-based technologies such as photoelectrochemical water-splitting for production of cleaner energy and photocatalysis for better treatment of wastewater. Then, we fabricate devices using industry-ready technologies such as electrospinning and screen printing to facilitate the integration of BFO. As a result, we create various photocatalytic cells based on BFO nanofibers and particles involving smaller material quantities than previous literature reports. The fabrication methods also enable the syntheses of colloidal-free catalysts, which allow live and automated tracking of the pollutant concentration. This strategy holds great promises to bypass the need for catalyst collection of the treated leachate.

For the second part of this thesis, we work toward the integration BFO powder as a high-performing thermistor for the printed circuit board technology. Using screen printing as a deposition method, we report highly reproducible and sensitive thermistors. By mixing and adjusting the graphene quantity added to the BFO powder, we enable room-temperature assessment. We also achieve the highest sensitivity reported for graphene-based printed thermistors for such a large range of operating temperatures.

Overall, this thesis yields a favorable way to achieve high-performance devices based on various BFO structures using industry-ready technologies.

Keywords: $BiFeO_3$, photoelectrochemical reactions, colloidal free photocatalyst, nanofibers, heterojunctions, thermistors

Développements et applications de structures de $BiFeO_3$ pour la fabrication de dispositifs hautes performances par l'intermédiaire de technologies compatibles avec l'industrie

Paul FOURMONT

RÉSUMÉ

La production d'énergies plus propres ainsi que le traitement des eaux usées de plus en plus toxiques sont probablement les deux plus grands défis auxquels l'humanité devra faire face dans les prochaines décennies. Bien qu'énormément d'efforts sont déployés pour apporter des réponses concrètes à ces problèmes, de nombreuses recherches sont encore nécessaires pour trouver des solutions optimales. Parmi ces potentielles solutions, les matériaux céramiques et plus particulièrement les oxydes de pérovskite sont d'un grand intérêt. En raison de sa structure cristalline singulière, la ferrite de bismuth ou le $BiFeO_3$ (BFO) fait aujourd'hui partie des oxydes de pérovskite les plus étudiés. En effet, le BFO est un matériau multiferroïque unique, car il possède un ordre ferroélectrique et un ordre ferromagnétique au sein de la même phase à température ambiante. Quelques effets de couplage entre ces deux ordres ont aussi été démontrés et la plupart font encore l'objet de recherches intenses aussi bien fondamentales que théoriques. Malgré ces études, les dispositifs commercialisés à base de BFO sont toujours rares.

Le cadre de travail de cette thèse de doctorat vise à contribuer à l'avancement de dispositifs basés sur la ferrite de bismuth. En particulier, cette thèse se concentre sur le développement de dispositifs de hautes performances fabriqués à partir de nanofibres et de poudres de BFO.

Suite à une revue de littérature approfondie du BFO, nous avons premièrement identifié les technologies basées sur l'énergie solaire telles que les réactions photoélectrochimiques pour le craquage de l'eau afin de produire de l'énergie plus propre et la photocatalyse pour un meilleur traitement des eaux usées. Ensuite, nous avons fabriqué des dispositifs en utilisant des méthodes de fabrication compatibles avec l'industrie telles que l'électrofilage ou la sérigraphie pour faciliter l'intégration du BFO. Par la suite, nous avons créé différentes cellules photocatalytiques basées sur des nanofibres et des poudres de BFO utilisant des quantités de matériaux moindres que précédemment rapportées dans la littérature. Ces méthodes de fabrication rendent également possible la synthèse de catalyseurs non colloïdaux permettant un suivi en temps réel et automatique de la concentration de polluants. Cette stratégie est prometteuse, car elle permet de se passer de l'étape de récupération du catalyseur après traitement du lixiviat.

Dans la seconde partie de cette thèse, nous avons travaillé sur l'intégration de poudres de BFO sur des cartes de circuits imprimés pour fabriquer des capteurs de température performants. Grâce à l'utilisation de la sérigraphie comme méthode de déposition, nous présentons des capteurs de température hautement reproductibles et sensibles. En mélangeant et en ajustant la quantité de graphène ajoutée aux poudres de BFO, nous rendons possible des mesures à température ambiante. Nous obtenons aussi la plus haute sensibilité reportée pour des capteurs de température imprimés à base de graphène pour une aussi large gamme de fonctionnement.

Dans l'ensemble, cette thèse met en avant des techniques prometteuses pour réaliser des dispositifs performants à base de diverses structures de BFO utilisant des technologies compatibles avec l'industrie.

Mots-clés: $BiFeO_3$, réactions photoélectrochimiques, membranes non colloïdales, nanofibres, hétérojonctions, thermistances

TABLE OF CONTENTS

Page

INTRODUCTION 1

CHAPTER 1 LITERATURE REVIEW 7
1.1 Crystalline structure 7
1.2 Properties of $BiFeO_3$ 9
1.2.1 Ferroelectric order 10
1.2.2 Piezoelectricity and pyroelectricity 11
1.2.3 Ferromagnetic order 11
1.2.4 Light absorption properties 12
1.2.5 Coupling phenomena 13
1.3 Synthesis methods 14
1.4 $BiFeO_3$ heterostructures 15
1.4.1 Metallic $BiFeO_3$-based heterojunctions 16
1.4.2 Oxide $BiFeO_3$-based heterojunctions 17
1.4.3 Organic $BiFeO_3$-based heterojunctions 18
1.5 Development of diverse engineered perovskite materials 19
1.6 Technological maturity of $BiFeO_3$ 20
1.6.1 Challenges faced by $BiFeO_3$ 20
1.6.2 Lines of research 21

CHAPTER 2 STATE OF THE ART 23
2.1 Thermoelectricity 23
2.2 Photocatalysis 25
2.3 Water splitting 27
2.4 Thermistor 29
2.5 Ways to improve $BiFeO_3$ properties and its integration 31
2.5.1 Graphene incorporation 31
2.5.2 Flexible hybrid electronics and printing deposition methods 31
2.5.3 Conductive electrodes and their integration to devices 32

CHAPTER 3 HIGHLY EFFICIENT THERMOELECTRIC MICROGENERATORS USING NEARLY ROOM TEMPERATURE PULSED LASER DEPOSITION 35
3.1 Introduction 35
3.2 Results and discussions 38
3.2.1 Annealing-free PLD-grown polycrystalline thermoelectric thin films 38
3.2.2 Low-dimensional thermoelectric n-type and p-type legs 41
3.2.3 Compact TE microgenerators with highly efficient thermal-electrical conversion 46

3.3 Conclusion 48
3.4 Experimental methods 49
3.4.1 Material synthesis 49
3.4.2 Device fabrication 49
3.4.3 Film characterization 49
3.4.4 Thermoelectric measurement 50
3.4.5 Electrical properties measurement 50

CHAPTER 4 HIGH PERFORMANCE $BiFeO_3$ FERROELECTRIC NANOSTRUCTURED PHOTOCATHODES 53
4.1 Introduction 54
4.2 Results and discussions 57
4.3 Conclusion 66
4.4 Experimental methods 66
4.4.1 Electrode preparation 66
4.4.2 Materials characterization 67
4.4.3 Photoelectrochemical measurements 68
4.5 Additionnal studies 69

CHAPTER 5 REUSABLE $BiFeO_3$ NANOFIBER-BASED MEMBRANES FOR PHOTOACTIVATED ORGANIC POLLUTANT REMOVAL WITH NEGLIGIBLE COLLOIDAL RELEASE 71
5.1 Introduction 71
5.2 Results and discussions 75
5.3 Conclusion 85
5.4 Experimental methods 86
5.4.1 Photocatalyst preparation 86
5.4.2 Materials characterization 87
5.4.3 Photocatalytic activity tests 87
5.5 Additionnal studies 88

CHAPTER 6 SCREEN-PRINTED P-N BiOCl/$BiFeO_3$ HETEROJUNCTIONS FOR EFFICIENT PHOTOCATALYTIC DEGRADATION OF RHODAMINE B 91
6.1 Introduction 91
6.2 Results and discussions 94
6.3 Conclusion 104
6.4 Experimental methods 105
6.4.1 Photocatalytic cells preparation 105
6.4.2 Characterization methods 106
6.4.3 Photocatalytic activity tests 106
6.5 Additionnal studies 107

CHAPTER 7 GRAPHENE-ENHANCED SCREEN-PRINTED $BiFeO_3$-BASED THERMISTORS 111
7.1 Introduction 111
7.2 Results and discussion 114
7.2.1 Characterization of the $BiFeO_3$ powders 114
7.2.2 Characterization of the BFO-based screen-printed thermistors 116
7.3 Conclusion 126
7.4 Experimental methods 126
7.4.1 Material synthesis 126
7.4.2 Characterization methods 127
7.4.3 Thermistor configuration 127

CHAPTER 8 ONGOING WORK 129
8.1 Photonic curing of $BiFeO_3$ films 129
8.2 Pyrophotoelectric effect 130
8.3 Devices based on $BiFeO_3$ nanofibers for the detection of rhodamine B 132

CHAPTER 9 CONCLUSION AND PERSPECTIVES 133
9.1 Summary 133
9.2 Statement of original contributions 133
9.3 Academic achievements 134

APPENDIX I 137

APPENDIX II 143

APPENDIX III 147

APPENDIX IV 151

APPENDIX V 155

BIBLIOGRAPHY 159

LIST OF TABLES

Page

Table 3.1 Properties of Bi_2Te_3 and Sb_2Te_3 Films. 39

Table 5.1 ICP-MS measurements 83

Table 7.1 Ink composition of the printed thermistors and their performances 121

Table 7.2 Comparison with the reported thermistors and temperature sensors 125

LIST OF FIGURES

Page

Figure 0.1 Number of published papers with $BiFeO_3$ as the main topic 2

Figure 1.1 Crystal structure of $BiFeO_3$ 7

Figure 1.2 General classification of multiferroic materials 9

Figure 1.3 Hysteresis curve in a ferroelectric materials 10

Figure 1.4 Synthesis methods to fabricate $BiFeO_3$ 15

Figure 2.1 Schematic of a Peltier cell 24

Figure 2.2 Schematics of the photocatalytic process and a photocatalytic cell 26

Figure 2.3 Schematic of a photoelectrochemical cell 28

Figure 2.4 Examples of NTCR components 29

Figure 3.1 Absolute value of the Seebeck voltage measured as a function of the temperature gradient for Bi_2Te_3 and Sb_2Te_3 films 38

Figure 3.2 SEM images and XRD spectra of Bi_2Te_3 and Sb_2Te_3 films 40

Figure 3.3 Seebeck voltages as function of temperature gradient and different number of thermocouple legs 42

Figure 3.4 Raman spectra of Bi_2Te_3 and Sb_2Te_3 legs 45

Figure 3.5 Fabrication steps and SEM/EDX measurements 46

Figure 3.6 Performances of the thermocouples 47

Figure 4.1 XRD and Tauc plot spectra of three different morphologies of $BiFeO_3$ 58

Figure 4.2 SEM micrographs of three different morphologies of $BiFeO_3$ 59

Figure 4.3 AFM and PFM images of the $BiFeO_3$ NFs 60

Figure 4.4 Linear sweep voltammetry plots of three different morphologies of $BiFeO_3$ 62

Figure 4.5 Linear sweep voltammetry plots of the $BiFeO_3$ NFs and their band diagrams 65

Figure 4.6 Linear sweep voltammetry and chronoamperometry plots 69

Figure 4.7 SEM image and UV-Vis measurements of gold decorated $BiFeO_3$ nanofibers 70

Figure 5.1 XRD and Tauc plot spectra of the $BiFeO_3$ nanofibers plus schematic of the fabrication steps 76

Figure 5.2 SEM micrographs and segmented images 77

Figure 5.3 EDS elemental mapping of the $BiFeO_3$ nanofibers 77

Figure 5.4 Thermogravimetric analysis of the $BiFeO_3$ nanofibers 78

Figure 5.5 Effect of $BiFeO_3$ NFs deposition time on the RhB degradation 80

Figure 5.6 Evolution of Rhodamine B spectra absorption 81

Figure 5.7 Consecutive degradation cycles of RhB 83

Figure 5.8 Scavenger experiments and schematic of RhB degradation mechanisms 85

Figure 5.9 Rhodamine B degradation for $BiFeO_3$ and TiO_2 doped $BiFeO_3$ nanofibers 89

Figure 6.1 SEM micrographs of the BiOCl nanosheets 96

Figure 6.2 XRD and Raman spectra of the photocatalyst 97

Figure 6.3 TEM images, EDX spectra and SAED pattern 98

Figure 6.4 Thermogravimetric analysis 101

Figure 6.5 Photocatalytic degradation of Rhodamine B 102

Figure 6.6 Evolution of Rhodamine B spectra absorption 104

Figure 6.7 Resistivity and humidity over time of the screen-printed humidity sensor 108

Figure 6.8 Images of screen-printed electrodes and devices 109

Figure 7.1 Characterization of the $BiFeO_3$ powders 115

Figure 7.2 Characterizations of the optimal thermistors 117

Figure 7.3 Thermistor's electrical resistance against temperature for different loading of graphene 118

Figure 7.4 Comparison of the conductance of all the $BiFeO_3$ thermistor 123

Figure 8.1 XRD spectra of photonic-cured $BiFeO_3$ thin films 130

Figure 8.2 Photopyroelectric measurements 131

Figure 8.3 Cyclic voltammetry measurements 132

LIST OF ABBREVIATIONS

ABPE	Applied-bias-photon-to-current Efficiency
AFM	Atomic Force Microscopy
BFO	Bismuth ferrite / $BiFeO_3$
EDX	Energy-dispersive X-ray spectroscopy
EIS	Electrochemical Impedance Spectroscopy
FR4	Glass-reinforced epoxy flame-retardant four substrate
FTO	Fluorine-doped Tin Oxide
LSV	Linear Sweep Voltammetry
N	Number of legs
NF	Nanofiber
NTCR	Negative Temperature Coefficient of Resistance
NWB	Nanoweb
OCP	Open Circuit Potential
PCB	Printed Circuit Board
PEC	Photoelectrochemical
PF	Power Factor
PFM	Piezoelectric Force Microscopy
PI	Polyimide
PLD	Pulsed Laser Deposition

PTCR	Positive Temperature Coefficient of Resistance
PVP	Polyvinylpyrrolidone
PZT	Lead Zirconate Titanate
RT	Room Temperature
RTD	Resistance Temperature Detector
SEM	Scanning Electron Microscopy
TCR	Temperature Coefficient of Resistance
TE	Thermoelectric
TEM	Transmission Electron Microscopy
UV-Vis	Ultraviolet Visible light
UV-Vis-NIR	Ultraviolet Visible Near Infrared light
XPS	X-ray Photoelectron Spectroscopy
XRD	X-ray powder Diffraction
ZT	Figure of merit

LIST OF SYMBOLS AND UNITS OF MEASUREMENTS

Ag	silver
A_{leg}	leg area
β	thermal index
B	magnetic field
e	elementary charge
cm	centimeter
cm^{-1}	wavenumber
$cm^2\ V^{-1}\ s^{-1}$	square centimeter per volt second
cm^{-3}	cubic centimeter
eV	electronvolt
E_g	bandgap
gr	gram
hr	hour
Hz	hertz
I	electrical current
in	inch
J-V	current density vs voltage
J-t	chronoamperometry
J_{ph}	photocurrent density

$J\ cm^{-2}$	joules per square centimeter
K	kelvin degree
kHz	kiloHertz
kV	kilovolt
$k\Omega$	kiloohm
$k\Omega\ cm^2$	kiloohm per square centimeter
M	mole per liter
$mbar$	millibar
min	minute
meV	millielectronvolt
mL	milliliter
$mL\ h^{-1}$	milliliter per hour
$mL\ min^{-1}$	milliliter per minute
mg	milligram
$mg\ L^{-1}$	milligram per liter
mm	millimeter
mM	millimole
$m^2\ s^{-1}$	square meter per second
mV	millivolt
$mV\ s^{-1}$	millivolt per second

mW	milliwatt
$mW\ cm^{-2}$	milliwatt per square centimeter
$M\Omega$	megaohm
$m\Omega\ cm$	mohm per centimeter
μA	microampere
$\mu A\ cm^{-2}$	microampere per square centimeter
$\mu C\ cm^{-2}$	microcoulomb per square centimeter
μm	micrometer
$\mu V\ K^{-1}$	microvolt per kelvin
$\mu W\ cm^{-2}$	microwatt per square centimeter
n	carrier concentration
nm	nanometer
$nm\ s^{-1}$	nanometer per second
ns	nanosecond
nW	nanowatt
Ω	ohm
$\Omega\ cm$	ohm per centimeter
$\Omega\ cm^2$	ohm per square centimeter
Pt	platinum
rpm	rotation per minute

R_a	surface roughness
R_{CT}	charge transfer resistance
R_L	load resistance
sec	second
t	thickness
T	temperature
T_C	Curie temperature
T_N	Néel temperature
T_S	substrate temperature
ΔT	temperature gradient
$\rho_{\square}$	sheet resistance
V	volt
V_{OP}	onset potential
$W\ m^{-1}\ K^{-2}$	watt per meter square kelvin
$^{\circ}C$	celsius degree
$^{\circ}C\ min^{-1}$	celsius degree per minute

INTRODUCTION

Historical context about perovskite

Ceramics are classified as inorganic and nonmetallic materials. They are essential to our daily lifestyle and can be used in many domains like construction (tile, glass or even brick) or transportation (shuttles, airplanes or automobiles). Ceramics are by far the most widely produced and used materials by humankind. Bhalla, Guo & Roy (2000) Among this wide class of materials, the perovskite structure is known by the scientific community to be the most versatile ceramic host. Bhalla *et al.* (2000) By doping, incorporating or substituting atoms, their chemical composition can be modified, which in turn directly influences the properties of the synthesized perovskite. The first perovskite material ($CaTiO_3$) was discovered in 1839 in the southern Ural Mountains by Gustav Rose and named after the Russian mineralogist Lev Perovski. Hirose, Sinmyo & Hernlund (2017) This discovery remained a mineralogical curiosity for almost 90 years until Victor Moritz Goldschmidt reported the first functionnal perovskite, $BaTiO_3$. Goldschmidt (1927) A functional material is defined by its ability to perform a certain "function" under a determined stimulus. Vilarinho (2005) This "function" usually relates to magnetic, electric and or optical properties. Following this definition, functional materials can be found in all classes of materials like semiconductors, polymers or metals. Nevertheless, ceramics and more precisely perovskite-based materials are known to possess a wide range of remarkable properties.

Among the perovskite family, bismuth ferrite is one of the most extensively studied multiferroic materials. Bismuth ferrite or $BiFeO_3$ is chosen as the central topic of the investigations performed in this doctoral thesis. $BiFeO_3$ (BFO) was discovered in the beginning of the 1960s, but failed to make an impact until the early 2000s. Catalan & Scott (2009) Due to great difficulties associated with the synthesis of pure and single phase BFO crystals, scientific endeavors remained inconclusive. Ghosh, Dasgupta, Sen & Maiti (2005) Nevertheless, in 2003 some researchers demonstrated a 15-time enhancement of polarization in thin film BFO compared to bulk material. Wang, Neaton, Zheng, Nagarajan, Ogale, Liu, Viehland, Vaithyanathan, Schlom,

Waghmare et al. (2003) Since then, many researchers focused their work on understanding the fundamental physics and on building new devices. This surge of publications about BFO is confirmed by Figure 0.1 with approximately two published papers per day in the past 10 years.

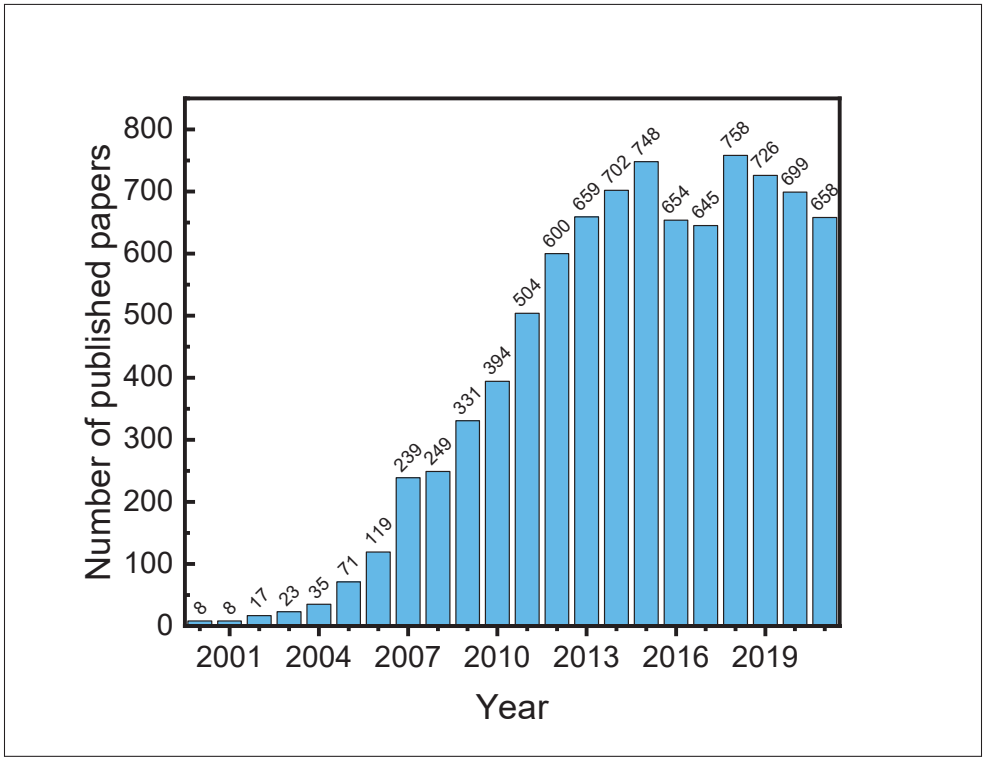

Figure 0.1 Number of published papers with $BiFeO_3$ as the main topic. Data is collected from Web of Science website with the keyword "$BiFeO_3$" from 2000 to 2021

Objectives and motivations

The purpose of this doctoral thesis is to gain a better understanding of the fundamental relationships between the synthesis parameters and the final physical properties of BFO (also called synthesis-structure-property interrelations). Based on this improved understanding, we can reach a better control over those properties. Ultimately, this new knowledge will be exploited for the fabrication of better devices using BFO's unique properties. Motivated to bring practical solutions and to solve critical problems such as climate change, aquatic pollution or production of cleaner energy, we identified BFO as a promising candidate for the following reasons:

- BFO by itself is not composed of rare-earth elements. Bismuth and iron are quite abundant in the Earth's crust. Vesborg & Jaramillo (2012) This point, largely underestimated by the scientific community, remains a requirement for any sustainable energy-based technology to reach viable large-scale manufacturing. Smalley (2005)
- Bismuth is a by-product of the refining of lead, tungsten and copper. Thus, its supply is inelastic. It means that the production stays constant no matter the demand, only the price increases. As a result, its price is relatively low and stable (around US$10 per kilo of 99.99% bismuth ingots in 2018). Miller & Bernechea (2018); Singerling & Callaghan (2018) In addition, iron is the fourth most abundant element in the Earth's crust which makes it a suitable candidate for implementation in mass-produced technologies. Miller & Bernechea (2018)
- BFO is known to be a very stable oxide material, which is also biocompatible. Some studies report that BFO nanoparticles can act as labelling markers to detect cancer cells and also as localized magnetic dose enhancement agents in the context of radiation therapy. Rajaee, Wang, Zhao & Liu (2019); Passemard, Staedler, Sonego, Magouroux, Schneiter, Juillerat-Jeanneret, Bonacina & Gerber-Lemaire (2015)

Since 2009, the framework based on "planet boundaries" has been accepted as a model to describe the safe operating space for humanity with respect to the Earth's systems. Rockstr*ö*m, Steffen, Noone, Persson, Chapin, Lambin, Lenton, Scheffer, Folke, Schellnhuber, Nykvist, de Wit, Hughes, van der Leeuw, Rodhe, S*ö*rlin, Snyder, Costanza, Svedin, Falkenmark, Karlberg, Corell, Fabry, Hansen, Walker, Liverman, Richardson, Crutzen & Foley (2009) Processes that potentially generate unacceptable environmental changes such as climate change, ocean acidification, biodiversity loss or chemical pollution are also interconnected, which means that global solutions must be found. Out of nine identified processes, six are now transgressing their boundaries. Persson, Carney Almroth, Collins, Cornell, de Wit, Diamond, Fantke, Hassellov, MacLeod, Ryberg et al. (2022); Wang-Erlandsson, Tobian, van der Ent, Fetzer, te Wierik, Porkka, Staal, Jaramillo, Dahlmann, Singh et al. (2022) In the beginning of 2022, researchers determined that the green water and the novel entities boundaries are officially exceeding the

planet boundaries. Persson *et al.* (2022); Wang-Erlandsson *et al.* (2022) The novel entities are defined as new compounds from a geological perspective that could have large-scale impacts, even on Earth's integrity. As of today, the pace of production and release in the environment of new chemical components is 50-fold higher than it was in 1950. Persson *et al.* (2022) Hence, no exhaustive assessment or monitoring of these novel entities is currently possible by any government or entity. Consequently, this inaction leads to a poor global evaluation of the risks and regional hazards are often undermined.

To mitigate these problems, tremendous efforts are being deployed to solve major challenges like access to greener energies by avoiding fossil fuels or developing better treatments of domestic and industrial toxic effluents. Following this line of effort, I chose to focus my main research activities on energy-related domains such as photocatalysis, water-splitting and thermoelectricity. In addition, production of high performance and innovative devices like temperature sensors are demonstrated in this doctoral thesis.

The following objectives are the central parameters of this doctoral thesis:

- The proposed methodologies must use straightforward and industry-ready deposition methods. By doing so, an easier technological integration from lab scale to the industry can be achieved.
- The proposed devices should use less material quantity compared to the literature to be economically attractive.
- The proposed devices should provide innovative solutions to the problems that limit large-scale deployment of the technologies mentioned in the previous paragraph.

Contributions and innovations

Following the objectives of the previous section, we chose to switch within the first year of this doctoral thesis from oxide materials used in thermoelectricity to oxide perovskite materials. Despite a low quantity of material needed and the high-quality of the deposited films, the first deposition method used (Pulsed Laser Deposition) does not suit the objectives of this doctoral thesis. In fact, PLD is a complex deposition method that possesses a low deposition

rate and large area depositions still remain challenging. Hence, PLD is mostly used in high-tech fields such as semiconductors or microelectronics and in academia to perform fundamental research and in-depth studies of nanoscale phenomena. Regarding thermoelectric materials, many sizable scientific findings have been reported in the past 20 years but a lot of challenges still lie ahead like energy conversion efficiency, toxicity or repeatability.Wei, Yang, Ma, Song, Zhang, Ma, Yang & Wang (2020) As a result, thermoelectric materials are today only used in niche applications such as satellites to produce energy or in Peltier cells to generate heat flow without producing vibrations. Following the complex deposition method used to fabricate efficient thermoelectric modules, we decided to choose simpler deposition methods which are more suitable toward industry and large-scale applications.

The main contributions of this doctoral thesis can be summed up as follows:

- Two deposition methods, respectively electrospinning and screen printing are used to fabricate low-cost, innovative and efficient devices. We designed and validated a colloidal free setup, which enables automated and live tracking of the pollutant concentration.
- Photocatalytic cells using 100 times less amounts of materials are reported.
- The photocatalytic cells are colloidal free which solve two of the actual limits of photocatalysis: the needs for ultraviolet (UV) sources and for catalyst collection and recovery protocols.
- We prove that the microstructure has a big influence on the photoelectrochemical properties of the BFO-based devices.
- We demonstrate highly sensitive screen-printed temperature sensors based on BFO powder compatible with the printed circuit boards (PCBs) technology. These devices use BFO powders which are synthesized by a straightforward solvothermal solution.

Outline of the thesis chapters

This thesis is divided into 9 chapters. Chapter 1 reports an extensive literature review about BFO. Chapter 2 introduces key concepts that enable the reader to understand the context and technologies used during the research activities. Chapters 3 to 7 are original research articles submitted or published in peer-reviewed scientific journals. Chapter 8 outlines unpublished

work, where promising preliminary results have been found. Finally, chapter 9 reports the statement of original contribution and the perspectives for future works.

CHAPTER 1

LITERATURE REVIEW

This chapter introduces important knowledge about $BiFeO_3$. Its crystalline structure and properties, along with different types of BFO-based heterostructures are reviewed.

1.1 Crystalline structure

BFO crystallizes with a rhombohedral structure described by the group R3c (space group #161) at room temperature. An example of this structure is drawn with black lines in Figure 1.1. There, one can see that BFO displays a perovskite structure (ABO_3) with Bi^{+3} and Fe^{+3} on the A and B sites respectively. The Bi and Fe atoms are located at the corners and at the center of the rhombohedron. The oxygen atoms then envelop the cations to form FeO_6 octahedra and BiO_{12} cuboctahedra as seen in Figure 1.1.

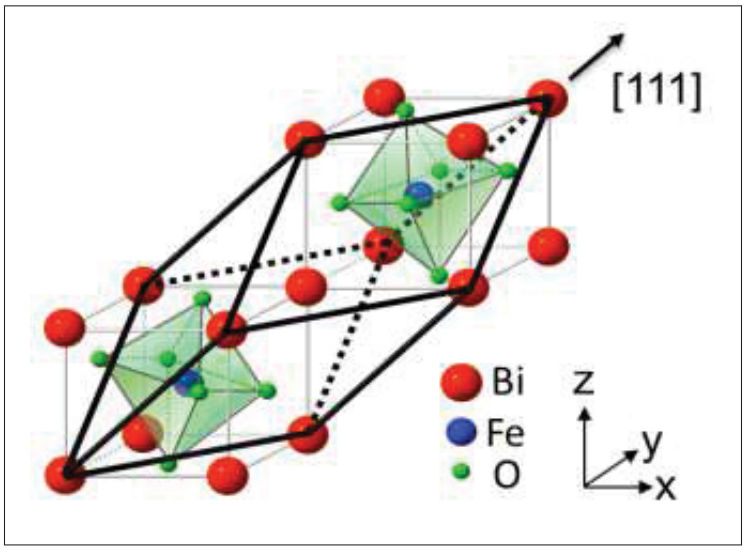

Figure 1.1 Crystal structure of $BiFeO_3$.
Taken from Gómez *et al.* (2016)

In the oxide perovskite structure ABO_3, the A-site is usually an alkaline earth or a rare-earth element with a high atomic number. The B-site is mostly occupied by smaller transition metal elements. These atoms should be small enough to fit in the oxygen octahedrons shown in green

in Figure 1.1. Some relevant review papers report different Bi and Fe doping or substitutions to show how versatile BFO can be. Gebhardt & Rappe (2018); Ishiwara (2012); Arnold (2015); Hussain, Xu, Yuan, Wang, Yang, Yin, Liu & Liu (2014); Zhang, Sando & Nagarajan (2016c); Yakout (2021) This behavior led scientists to examine and characterize a large number of different stoichiometries. This endeavor still attracts a lot of interest as BFO properties are directly influenced by factors such as the synthesis method and processing parameters. Silva, Reyes, Esparza, Camacho & Fuentes (2011)

The first reports of BFO synthesized by sol-gel in 2004 and 2005 did not yield a pure BFO phase. A precise control of the atmosphere during annealing followed by a nitric acid leaching is reported to help reduce the presence of secondary phases. Kim, Kim & Kim (2005); Qi, Dho, Blamire, Jia, Lee, Foltyn & MacManus-Driscoll (2004) Chen et al. managed to obtain pure single phase BFO by coprecipitation method while Mazumder et al. reported 4 to 50 *nm* BFO particles by sonochemical method. Chen & Wu (2007); Mazumder, Ghosh, Mondal, Bhattacharya, Dasgupta, Das, Sen, Tyagi, Sivakumar, Takami et al. (2006) Overall, wet chemical methods are influenced by parameters such as the concentration of the precursors, the amount of solvent, the precursor/solvent ratio, the pH, the presence of surfactants or additives or the duration of synthesis. Esposito (2019)

Nevertheless, contradictory physical behaviors and crystal structures are often reported within the literature. Due to poor understanding and control of fundamental relationships between synthesis parameters and structural properties, more work such as this thesis is still necessary. These differences in the literature are attributed to the complex structural phase diagram of BFO. Arnold (2015) As stated in the previous chapter, pure BFO phase still remains today a challenge to synthesize. The presence of secondary phases such as Bi_2O_3, $Bi_2Fe_4O_9$, or $Bi_{25}FeO_{39}$ is attributed to the phase formation's kinetics during crystallization. Bernardo, Jardiel, Peiteado, Caballero & Villegas (2011)

1.2 Properties of $BiFeO_3$

BFO's properties can be tuned and optimized by modifying its stoichiometry and size. If BFO has drawn a lot of attention in the past two decades, it is mostly because it belongs to the very few existing multiferroic materials at room temperature. BFO is considered a multiferroic material because of its ferroelectric and magnetic orders within the same crystalline phase shown in Figure 1.2. Jangid, Barbar & Roy (2014) This rare behavior is attributed to its crystal structure. Uchino (2018) Other interesting properties will also be discussed in the next subsections. Following the breakthrough report on giant spontaneous polarization in BFO thin films by Ramesh et al. in 2003, most researchers shifted their works from bulk to nanoscale BFO structures. By doing so, enhanced performances were found and it enabled BFO's integration to various devices (solar cells, photodetectors, humidity and gaz sensors). To fit the scope of the thesis, this chapter only focuses on nanomaterials.

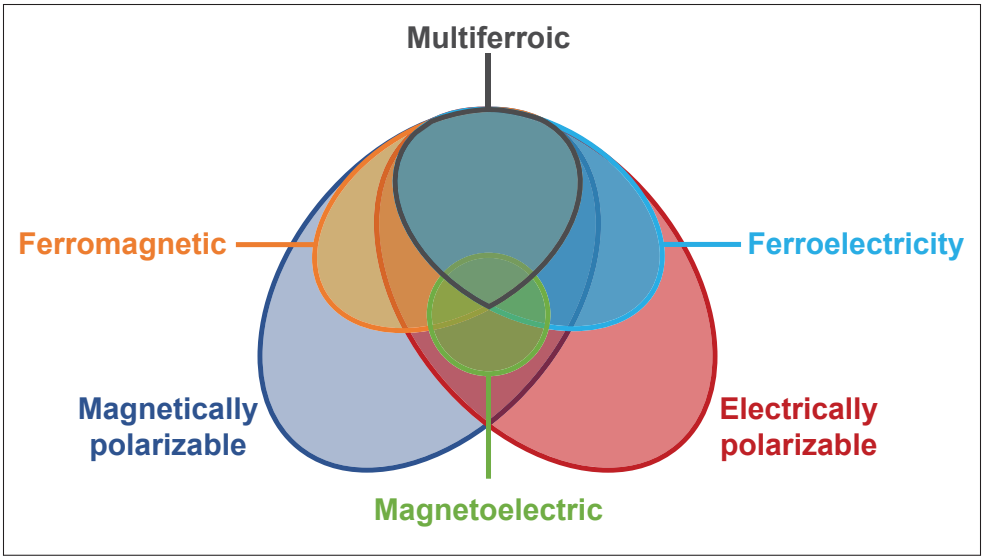

Figure 1.2 General classification of multiferroic materials.
Adapted from Eerenstein *et al.* (2006)

1.2.1 Ferroelectric order

Ferroelectric materials refer to dielectric materials which possess a spontaneous polarization that can be reversed by an electric field. In any ferroelectric material, the crystalline structure is required to be noncentrosymmetric. Thus, ferroelectrics must have their space inversion symmetry broken. With most perovskite, octahedral tilting breaks the centrosymmetry, which in turn affects the ferroelectric properties. Irshad, tul Ain, Zaman, Aslam, Kousar, Asim, Rafique, Siraj, Tabish, Usman et al. (2022) In the case of BFO, ferroelectric order arises from the polar displacements of cations (Bi^{+3}) along the [111] as seen in Figure 1.1.

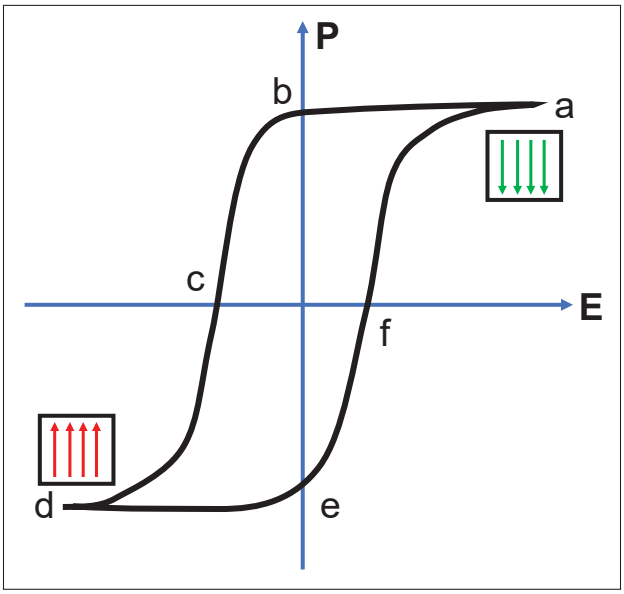

Figure 1.3 Hysteresis curve (polarization vs electrical field) in a ferroelectric materials.[1] Arrows represent the dipole alignments at both saturated polarizations

Ferroelectric materials exhibit a hysteresis loop below the Curie point as seen in Figure 1.3. BFO's Curie temperature is determined to be $T_C \simeq 830$ °C. Selbach, Tybell, Einarsrud & Grande (2008) It implies that below this temperature, BFO shows a ferroelectric behavior and above this

[1] Point (a) is the saturated polarization (P_s), (b) is the remnant polarization (P_r) when there is no the electric field, (c) is the negative coercive electric field (E_c), (d) is the negative saturated polarization (P_s), (e) is the negative remnant polarization (P_r), (f) is the coercive electric field (E_c).

temperature, BFO exhibits a paraelectric behavior. This transition is characterized by abrupt changes in atomic position and by discontinuous volume change. Selbach *et al.* (2008)

1.2.2 Piezoelectricity and pyroelectricity

All ferroelectric materials are both piezoelectric and pyroelectric. Piezoelectricity can be described as the ability of a material to convert mechanical energy into electrical energy. Specifically, this conversion is known as the direct piezoelectric effect. However, the reverse effect known as inverse piezoelectric effect, causes a change in length under externally-applied electrical field. Uchino (2018) This property has attracted a lot of attention and led to a broad variety of industrial products like inkjet printers, ultrasound equipment, speakers or sensors and motors. In the context of energy harvesting, the use of piezoelectric materials has experienced significant growth in the past decades. Anton & Sodano (2007) This need is amplified by new paradigms like internet of things or industry 4.0 which require communication networks between physical objects.

In contrast, pyroelectricity results from the temperature dependence of the spontaneous polarization. A variation of temperature can slightly modify the atoms' positions, resulting in the production of electrical charges on the crystal's surface. Uchino (2018) As sudden changes of temperature are not commonly encountered, pyroelectricity is less popular than piezoelectricity. Nevertheless, some applications based on this property are commercialized like night vision devices or temperature sensors. Zhang, Wu, Bowen & Yang (2021); Bowen, Taylor, LeBoulbar, Zabek, Chauhan & Vaish (2014)

All ferroelectric materials are both piezoelectric and pyroelectric, but it is important to remember that the opposite is not always true.

1.2.3 Ferromagnetic order

Ferromagnetic materials refer to materials which exhibit spontaneous magnetization that can be reversed by an external magnetic field. For any ferromagnetic material, time-reversal symmetry

must be broken. This means that the laws of physics should be the same whether you look at a system going forward or backward in time. For atoms with unpaired spins possessing a net magnetic moment, spin changes sign under time reversal and to invert magnetization. Hence, magnetic order breaks time reversal symmetry. Zaki, Gu, Tsvelik, Wu & Johnson (2021)

Ferromagnetic materials possess a hysteresis loop like ferroelectric materials below the Néel point. BFO's Néel temperature is determined to be $T_N \simeq 370$ °C. Catalan & Scott (2009); Selbach *et al.* (2008) This implies that below this temperature a ferromagnetic behavior is expected. Above T_N, the thermal energy becomes large enough to destroy the magnetic order within the material and ferromagnetic materials show paramagnetic behavior. Spaldin (2010)

For ferromagnets, all the spins are aligned in the same direction, resulting in a net magnetic moment in the absence of an external magnetic field. BFO is a particular case of ferromagnet called antiferromagnet. Each Fe^{+3} spin is surrounded by six antiparallel spins on the nearest Fe neighbors. Catalan & Scott (2009) Antiferromagnets do not have a spontaneous magnetization but in the case of BFO, the spins of Fe atoms are not perfectly antiparallel. This small inclination of the spins about their axis is called the canting effect and is responsible for the weak magnetization of BFO. Catalan & Scott (2009) Consequently, BFO's magnetic order comes from the Fe^{+3} atoms.

1.2.4 Light absorption properties

As a semiconductor with a band gap between 2 and 2.7 eV, BFO is known to absorb some parts of the visible spectrum. Zhang *et al.* (2016c) According to the band structure theory, absorbed photons with energies equal or higher than the bandgap can promote electrons from the valence to the conduction band. Sze, Li & Ng (2006) This creates a vacancy or a hole in the valence band. This phenomenon called photoconductivity has a big impact on the electrical properties of the materials. In the case of BFO, photovoltaic behavior has been reported for different microstructures like nanofibers or thin films. Fei, Hu, Li, Song, Sun, Huang, Gu, Chan & Wang (2015); Xing, Guo, Dong, Hao, Zheng & Zhao (2015) Nevertheless, very low photovoltaic

currents under illumination, mostly in the range of a few nanoampers, severely hampers the integration of BFO as an active absorption layer in photovoltaic solar cells. Hence, BFO-based solar cells show low energy-conversion efficiencies, which are insufficient to compete with hybrid organic–inorganic halide perovskites. The latter achieve power conversion efficiency above 25%. Min, Lee, Kim, Kim, Lee, Kim, Paik, Kim, Kim, Kim et al. (2021); Lee, Bae, Kim & Lee (2020)

As an oxide material, BFO is known to be chemically stable over time, which makes it an interesting candidate for other solar-based technologies like photoelectrochemical reactions. Photochemical reactions are found in photocatalysis or photocatalytic water-splitting and involve light to generate electron-hole pairs using an immersed catalyst. An exhaustive description of these two techniques will be addressed in the next chapter. Catalyst stability during immersion is a prerequisite to ensure good performances over time. Despite having a low power conversion efficiency, which limits its use as photodetector BFO is a promising candidate for other sun-based technologies. In chapter 5, we demonstrate a good photostability of the BFO membranes under solar irradiation, while immersed in water.

1.2.5 Coupling phenomena

Functional materials can be described by the ability of a material to perform a "function" under a determined stimulus. Vilarinho, Rosenwaks & Kingon (2006) In the specific case of multifunctional materials, several properties can be used simultaneously which is of considerable interest. A multiferroic combines at least two of the primary ferroic orderings in the same phase. Spaldin, Cheong & Ramesh (2010) For BFO, ferroelectric and ferromagnetic orders have been determined within the phase because of its unique crystalline structure. Coupling-mechanisms between ferroelectric and magnetic properties, first reported in 2008 are of great importance for data storage, spintronics and high-frequency magnetic devices. Chu, Martin, Holcomb, Gajek, Han, He, Balke, Yang, Lee, Hu et al. (2008) In the last reference, authors were able to control and switch the local magnetism using an external electric field at room temperature. This coupling mechanism is known as the magnetoelectric effect. Some good reviews about

electric-field control of multifunctionalities can be found in the following references. Yang, He, Yu & Chu (2015); Heron, Schlom & Ramesh (2014)

Some other coupling mechanisms can be observed in BFO:

- Photopyroelectricity is a coupling mechanism between the electrical polarization and the absorbed light converted into heat. Mandelis & Zver (1985)
- Photo-generation of terahertz waveforms via ultrafast modulation of the spontaneous ferroelectric polarization using a femtosecond laser. Talbayev, Lee, Cheong & Taylor (2008)
- Magnetostriction is a mechanism that causes materials to change their shape or dimensions under a magnetic field. Kumar, Scott, Martinez, Srinivasan & Katiyar (2012); Lee, Fernandez-Diaz, Kimura, Noda, Adroja, Lee, Park, Kiryukhin, Cheong, Mostovoy et al. (2013)
- The elasto-optic effect consists in the change of the refractive index by any strain applied to the crystalline structure of the material. Sando, Yang, Bousquet, Carrétéro, Garcia, Fusil, Dolfi, Barthélémy, Ghosez, Bellaiche et al. (2016)

1.3 Synthesis methods

As explained in the introduction chapter, one of the most important drawbacks of BFO remains the great difficulties associated with synthesizing pure BFO without secondary phases. In 1967, a study reported that leaching of BFO with nitric acid (HNO_3) can remove small traces of secondary phases like Bi_2O_3 and $Bi_2Fe_4O_9$. Achenbach, James & Gerson (1967) The authors also stated that the "inevitable" secondary phases have caused many investigations to be performed on impure BFO. Thus, contradictory and confusing results have been reported in the literature. To solve this problem, a lot of different methodologies have been investigated to synthesize pure BFO phase. By doing so, researchers have developed and investigated at least a dozen methodologies summarized in Figure 1.4. Two different categories of methods are used targeting 0/1D structures or 2D structures. The former enables to synthesize various 0/1D structures like nanoparticles, nanowires, nanofibers, nanotubes or nanorods. In contrast, the latter allows the creation of thin films. Some good reviews about BFO chemistry and synthesis methods can be

found in the following references. Zhang *et al.* (2016c); Wu, Zhou, Liang, Li & Zhu (2014); Silva *et al.* (2011); Safi & Shokrollahi (2012); Bhalla *et al.* (2000)

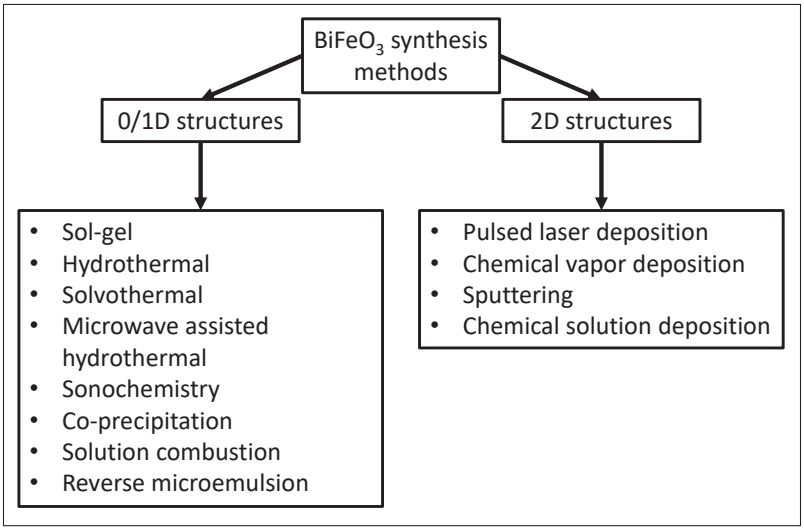

Figure 1.4 Synthesis methods used to fabricate 0, 1 and 2D $BiFeO_3$ structures

All the reported synthesis methods in Figure 1.4 are classified as bottom-up techniques. According to the Britannica encyclopedia, a bottom-up synthesis can be defined as "an approach using chemical or physical forces operating at the nanoscale to assemble basic units into larger structures". Bottom-up approaches are more often used to synthesize BFO as they can allow a finer control over their structural properties through synthesis. This control is of utmost importance to optimize the BFO's properties during atomic substitution or doping.

In this doctoral thesis, a solvothermal recipe is used and optimized for each of the published scientific articles presented in chapters 4 to 7.

1.4 $BiFeO_3$ heterostructures

Creation of BFO heterostructures by coupling different semiconductors is one of the most efficient ways to realize the spatial separation of photo-excited electron-hole pairs. Yang (2021) This phenomenon is of paramount importance to reduce charge carriers' recombination in any semiconductor. By doing so, more charge carriers become available for redox reactions or for

collection at the material's surface. This property is of great interest for photoelectrochemical applications. In most bare semiconductor catalysts, the photo-generated electrons easily recombine with the holes of the valence band resulting in suboptimal performances. In the following subsections, we review different types of BFO heterojunctions. Some of them are investigated and reported in chapters 4, 6 and 7.

1.4.1 Metallic $BiFeO_3$-based heterojunctions

Metallic BFO-based heterojunctions consist of BFO structures decorated with metallic nanoparticles. Noble metal like Pt, Au or Ag have already shown enhanced photoelectrochemical performances compared to pristine BFO. Liu, Zhou, You, Wang, Shen & Fang (2016); Mohan, Subramanian & Sarveswaran (2014); Zhang, Wang, Wang, Xiao, Dai, Wu, Zheng, Ren & Jiang (2015a); Niu, Chen, Qin, Gao, Zhang, Wang, Chen, Wang, Sun & Huang (2015); Jaffari, Lam, Sin & Mohamed (2019a); Li, Li, Chen, Sun, Zhang, Guo & Feng (2019); Li, Zhang, Kibria, Mi, Chaker, Ma, Nechache & Rosei (2013) Among all cited metals, gold nanostructures seem to be the most promising ones as they show more stable behaviors due to their greater anticorrosive properties. Moon, Choi, Hyun & Jang (2021); Eliaz (2019) Beneficial contributions of metallic structures at the semiconductor interfaces can be explained by two phenomena: the surface plasmonic resonance and the Schottky barrier formation. The surface plasmonic resonance can be explained as a coherent oscillation of the electrons resulting in an intense and localized electromagnetic field if the incident light possesses the same frequency. Khan, Chuan, Yousuf, Chowdhury & Cheng (2015) The Schottky-barrier takes place when the deformation of the band structure results in a flow of charge carriers from the BFO structure to the metallic structure due to the alignment of the Fermi energies. Sze *et al.* (2006) Ideally, a synergetic behavior is desirable to maximize both effects. Nevertheless, many factors such as the shape, the size, the distribution of the metallic nanoparticles, the geometry of contact or the presence of ligands should be considered while optimizing both phenomena. Qian, Sweeny, Johnston-Peck, Niu, Graham, DuChene, Qiu, Wang, Engelhard, Su et al. (2014); Moon *et al.* (2021) Consequently,

this narrow field of research is still under a lot of investigations as the number of combinations between all the cited parameters are almost infinite.

In chapters 5 and 6, we show that a thin layer of platinum deposited by sputtering acts as a co-catalyst to enhance the photocatalityc performances of the BFO based membranes. In chapter 4, we demonstrate that the size of gold nanoparticles on BFO nanofibers directly influences the photo-generated current in photoelectrochemical measurements. The smallest gold nanoparticles (5 *nm*) yield the highest photocurrent.

1.4.2 Oxide $BiFeO_3$-based heterojunctions

Oxide BFO-based heterojunctions rely on the intimate contacts between at least two semiconductors. Tremendous amounts of work involving BFO coupled with other semiconductors have been reported on this topic. Semiconductors such as TiO_2, ZnO, $BiVO_4$, Bi_2O_3 or bismuth oxyhalides (BiOX with X = Cl, I or Br) are among the most popular materials used to fabricate heterojunctions. Samran, Tonnonchiang, Chaiwichian et al. (2019); Zhu, Zhao, Li & Shi (2014); Wu, Li, Wang, Jiang, Xi, Du & Ji (2019); Humayun, Zada, Li, Xie, Zhang, Qu, Raziq & Jing (2016); Tiwari, Fermin, Chaudhuri & Ray (2015); Qu & Duan (2013) Even though semiconductors like TiO_2, ZnO or BiOCl are considered as high bandgap material ($E_g > 3\ eV$) and thus do not absorb visible light, they favor electronic band-bending at the heterojunctions interfaces. Yang (2021) A decrease of recombination of the photo-generated charge carriers is often reported and results in better photoelectrochemical properties. Heterojunctions can be fabricated using various methodologies for 0/1D and 2D structures. Some fabrication methods are reported in this reference. Yu, Zhou, Jimmy, Liu & Wei (2014) However, syntheses and formations of such heterojunctions are usually complex, expensive and very challenging, thus limiting their applications to fundamental studies. Some limitation faced by devices based on heterostructures are discussed in the following references. Yang, Zhou, Nan, Gao, Yang, Liu & Sun (2016); Cheng, Wang, Zou & Liao (2019); Liang, Cheng, Cui & Miao (2020) Studies usually report elaborate nanomachining and complex procedures that prevent the integration of heterostructures into mass-produced electronic components. Cheng *et al.* (2019) Large-area depositions and

stability of heterostructures are also important challenges that need to be addressed. Liang *et al.* (2020) Hence, more work like this doctoral thesis is necessary to bridge the gaps between fundamental studies and commercial applications.

To mitigate these challenges, chapter 6 presents a straightforward method involving colloidal free p-n BiOCl/BFO heterojunctions for efficient degradation of rhodamine B and fabricated by screen printing.

1.4.3 Organic $BiFeO_3$-based heterojunctions

Organic BFO-based heterojunctions involve mostly poly(3-hexylthiophene) (P3HT) or carbon sources such as cyanide nitrogen (C_3N_4), graphene, carbon nanofibers/nanotubes or carbon black. Tremel & Ludwigs (2014); Fresno, Portela, Suárez & Coronado (2014); Batool, Nazar, Awan, Tahir, Rahdar, Shalan, Lanceros-Méndez & Zafar (2021); Wang, Bai, Si, Mao, Gao & Liu (2021c); Ruby, Rosaline, Inbanathan, Anand, Kavitha, Srinivasan, Umar, Hegazy & Algarni (2020) The main objectives of all these heterojunctions are summed up in this good review. Yin & Mi (2020) Such heterojunctions are beneficial to prevent charge carriers recombination and boost the photocatalytic or photovoltaic properties. Wang *et al.* (2021c); Liu & Yan (2011) In brief, organic compounds are used to lower the recombination of photo-generated electron-hole pairs, which is beneficial for photoelectrochemical properties. This improvement is possible due to the higher conductivity of the carbon sources compared to the BFO structures. Among the existing BFO/polymer heterojunctions, P3HT has been used extensively in hybrid photovoltaic devices. Liu & Yan (2011, 2012) In fact, P3HT is a well-known semiconductor polymer studied for its unique optoelectronic properties. Some other BFO structures functionalized with carbon fibers are reported for enhanced pollutant detection in water or for humidity sensing. Ramaraj, Mani, Chen, Kokulnathan, Lou, Ali, Hatamleh & Al-Hemaid (2018); Douani, Lamrani, Saidi, Guhel, Chaouchi, Boudart et al. (2020) In addition, BFO nanocomposites mixed with graphene and reduce graphene oxide have demonstrated enhanced electrochemical properties compared to pristine BFO. Moitra, Anand,

Ghosh, Chandel & Ghosh (2018) This last study reports properties comparable to commonly used metal oxide-based electrode materials.

In the framework of this doctoral thesis, chapter 7 reports screen-printed films based on heterojunctions of BFO particles mixed with graphene. The printed films are used as temperature sensors and show high-sensitivity over a wide range of operating temperatures. Some other ongoing work presented in chapter 8 highlight that graphene can be beneficial to reduce the amount of energy necessary to crystallize BFO by photonic curing. This phenomenon is attributed to a more efficient light absorption.

1.5 Development of diverse engineered perovskite materials

As discussed previously, atoms within the perovskite crystalline structure can be replaced, tuned and their concentration optimized to influence the perovskite intrinsinc properties. This phenomenon has motivated scientists to investigate new perovskite structures like double perovskite. This specific structure is ascribed to the following formulas: $AA'B_2O_6$, $A_2BB'O_6$ or $AA'BB'O_6$. Saha-Dasgupta (2020); Afroze, Karim, Cheok, Eriksson & Azad (2019) Half of A and/or B atoms need to be replaced to form a double perovskite, while making sure to respect the Goldschmidt tolerance factor. The Goldschmidt tolerance factor is used to assess the stability and distortion of crystal structures. Sato, Takagi, Deledda, Hauback & Orimo (2016) The ratio of the ionic radii forms a dimensionless number that should be idealy equal to one. Sebastian (2010) Any deviation from this ideal value leads to crystal distortions and the perovskite adopts structures of lower symmetry than the cubic one. Sato *et al.* (2016) This parameter can be used for both perovskite oxides (ABO_3) and double perovskite. Sebastian (2010) Considering the large number of double perovskite structures possible, this is a very active field opening a wide range of possibilities. Yin, Weng, Ge, Sun, Li & Yan (2019) Among these double perovskites, Bi_2FeCrO_3 thin films exhibits a high-power conversion efficiency of 8.1% under irradiation compared to around 1% for BFO thin films. Nechache, Harnagea, Li, Cardenas, Huang, Chakrabartty & Rosei (2015); Nechache, Harnagea, Licoccia, Traversa, Ruediger, Pignolet & Rosei (2011)

1.6 Technological maturity of $BiFeO_3$

1.6.1 Challenges faced by $BiFeO_3$

Despite tremendous amounts of research done on various BFO formulations and structures, its integration into commercial devices still remains challenging. Wang, Luo, Han, Zhang, Zhang, Olin & Yang (2020b) BFO synthesis without secondary phase is difficult to achieve, which in-turn dramatically influences both ferroelectric and magnetic orders. Even if pure BFO phase is obtained using synthesis methods like hydrothermal or pulsed laser deposition, its production is nearly impossible to upscale from the lab to the industry. So far, BFO is mostly studied to show proof of concept and integrated into small devices.

In the context of photovoltaic applications, silicon and hybrid organic-inorganic perovskite based materials dominate the market by their high-power conversion efficiencies. With only a few percent of power conversion efficiency, BFO can only be relevant in a context of a harsh environment as it is chemically inert and stable over time. Li, Li, Shen, Han, Chen, Dong, Chen, Zhou & Wang (2021)

For photoelectrochemical applications and more precisely hydrogen production, low energy efficiencies (due to the coupling of photon absorption plus the chemical separation of water molecules) and the relatively low cost of other sources of energy limit the deployment of this technology. Photocatalytic integration of BFO structures to water treatment plants are mostly limited due to catalyst recovery protocols. In fact, most of the reported catalysts in the literature are colloidal nanoparticles which make them unfit to treat high quantity of pollutants and difficult to recover. This catalyst recovery must be maximal to avoid the contamination of the treated leachate and to ensure a cost-effective treatment. The cost of BFO-based catalysts is also another limitation for its large-scale integration. Compared to commercially available metal oxides like TiO_2 or ZnO, BFO remains a more expensive catalyst due to its more complex synthesis process.

1.6.2 Lines of research

Integration of various BFO structures to fabricate efficient devices requires to first improve its intrinsic properties. Fast carrier recombination, high leakage currents from oxygen and Bi/Fe vacancies or valence fluctuations of Fe atoms should be reduced. Spaldin *et al.* (2010); Ishiwara (2012) In parallel, theoretical work to identify and understand all the coupled phenomena in presence at room temperature should be performed. For example, the mechanisms associated with the photovoltaic effect and catalytic behavior are still elusive. Wang *et al.* (2020b) Development of more efficient devices can be expected if both fundamental and physical aspects of BFO are investigated simultaneously. Unfortunately, fundamental understanding of the properties at the atomic level remains a difficult task to carry out.

Among those technologies of potential interest, the creation of ferroelectric based memory devices received a lot of attention. As this topic is beyond the scope of this doctoral thesis, only a quick mention of this booming research domain is reported. The recent coupling of Ferroelectric Random Access Memory (FeRAM) with Magnetic Random Access Memory (MRAM) opens the opportunity to create innovative memory devices. Yakout (2021) In addition, a significant decrease of power consumption can be expected as electric-field control of magnetic spins does not need generation of magnetic fields like actual computers. Combination of multiferroic materials also unlocks the possibility to use the ferroelectricity to write and the magnetism to read operations, which will potentially enhance the writing speed.

CHAPTER 2

STATE OF THE ART

This chapter introduces key concepts and some technologies needed to understand the framework of this doctoral thesis.

2.1 Thermoelectricity

Even though thermoelectricity is not using BFO, a brief mention of this technology is needed. Thermoelectricity was indeed a part of this initial doctoral project. Some results in chapter 3 were obtained during my master project at ÉTS and the manuscript writing was performed during my first year as a doctoral student.

Thermoelectricity was discovered in Europe at the beginning of the XIXth century by Thomas Seebeck and Jean-Charles Peltier. The first discovered thermoelectric effect is the Seebeck effect. This phenomenon occurs when two different joined metal are at different temperatures. An electrical potential proportional to the temperature difference is created between the two metals. This effect is used for example in thermocouples to determine the temperature or in nuclear batteries for spatial explorations (satellites Voyager 1 and 2). The reverse effect, called the Peltier effect, enables to generation of heat by applying an electrical current to the metallic junction. Due to cost considerations, the Peltier effect is used in niche applications such as coolers or microscopes to mostly cool down small environments without generating vibrations or using refrigerant gas. A schematic of a Peltier cell producing a cooling effect is presented in Figure 2.1. Good reviews discussing basic principles of thermoelectricity and performances of generators can be found in the following references. Mamur, Bhuiyan, Korkmaz & Nil (2018); Haras & Skotnicki (2018)

Thermoelectricity was an intense field of research at the beginning of the 2000s to enhance electrical devices efficiency and electrical consumption. However, despite a lot of research, conversion of heat loss to electrical energy is still around few percents. Nozariasbmarz,

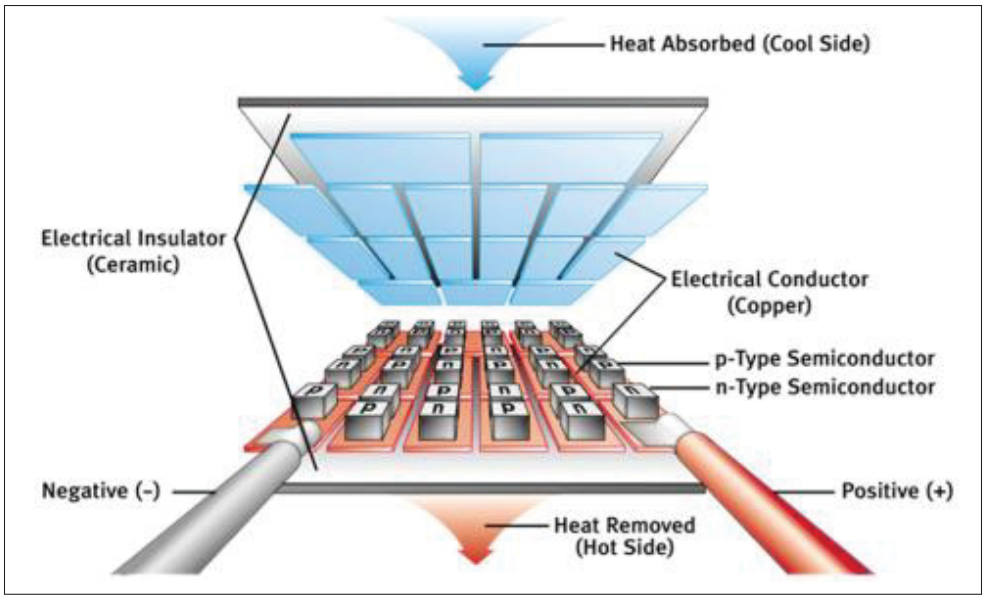

Figure 2.1 Schematic of a Peltier cell used to generate cold surfaces. Taken from Ivanov *et al.* (2019)

Poudel, Li, Kang, Zhu & Priya (2020) As such, integration of thermoelectric modules into combustion engines or electrical devices like computers is not financially attractive. The reasons of this drawback lie probably in the stringent requirements expected from high-performing thermoelectric materials. In fact, an ideal thermoelectric material must possess a high electrical conductivity, coupled with a low thermal conductivity. Pei, LaLonde, Heinz, Shi, Iwanaga, Wang, Chen & Snyder (2011) Both properties intimately depend on the number of charge carriers. Zevalkink, Smiadak, Blackburn, Ferguson, Chabinyc, Delaire, Wang, Kovnir, Martin, Schelhas et al. (2018) A compromise must be found as too many carriers increases the thermal conductivity, while a small density of carriers reduces the electrical conductivity. Snyder & Toberer (2011) Thermal conductivity is also a difficult parameter to characterize, especially at the nanoscale. Toberer, Baranowski & Dames (2012) Therefore, it limits the fundamental understanding of the physical phenomena. Toberer *et al.* (2012) Other problems like toxicity of commonly used thermoelectric materials or the high purity needed to reach optimal performances also prohibit their large-scale integration. Bell (2008)

2.2 Photocatalysis

The first reference to photocatalysis was reported in 1911 by a German chemist called Alexander Eibner. Irshad *et al.* (2022) He studied the decolorization of Prussian blue by irradiating ZnO with light. Eibner (1911) In this study, a metal oxide was used as a catalyst. The catalyst itself does not participate to the reaction but rather accelerates the reaction rate.

Photocatalysis is a light-based technology used for water decontamination and purification. As the global population is expected to grow by 2 billion in the next four decades, industrial and domestic wastewater are expected to increase accordingly. Vollset, Goren, Yuan, Cao, Smith, Hsiao, Bisignano, Azhar, Castro, Chalek et al. (2020) This worldwide issue deals with contaminants such as drugs, pesticides or personal care products. Xie, Zhou, He, Pan, Yao & Lai (2021) Some molecules, especially antibiotics or hormones are released from water treatment plants into wildlife without any proper treatments. In turn, this greatly affects the biodiversity and such contaminants are found at the top of the food chain. Yang, Song & Lim (2020a); Verraes, Van Boxstael, Van Meervenne, Van Coillie, Butaye, Catry, De Schaetzen, Van Huffel, Imberechts, Dierick et al. (2013)

To mitigate these problems, photocatalysis uses semiconductor materials to harvest solar energy and eliminate harmful substances via the formation of free radicals. While absorbing light, semiconductors generate photo-charges which can further participate to oxidation reduction (redox) reactions before they recombine as seen in Figure 2.2(a). To maximize this effect, catalysts must be in the nanoscale range and possess huge surface-to-volume ratios to lessen the short lifetime of the photo-generated carriers. Kabra, Chaudhary & Sawhney (2004) Other strategies involving nano-engineered materials with complex heterojunctions have been proposed. Batool *et al.* (2021); Duan, Ma, Lv, Sheng, Lu, Zhu, Du, Chen & Chen (2021) Such structures allow the photo-generated charges to reach the catalyst surface and enable redox reactions.

Nevertheless, most catalysts like TiO_2 or ZnO possess high band gaps ($> 3\ eV$), limiting their uses. Photocatalytic efficiencies of such semiconductors are hampered as ultraviolet (UV) light represents a small fraction ($\sim 6\%$) of the solar irradiation reaching the surface of Earth. Fresno

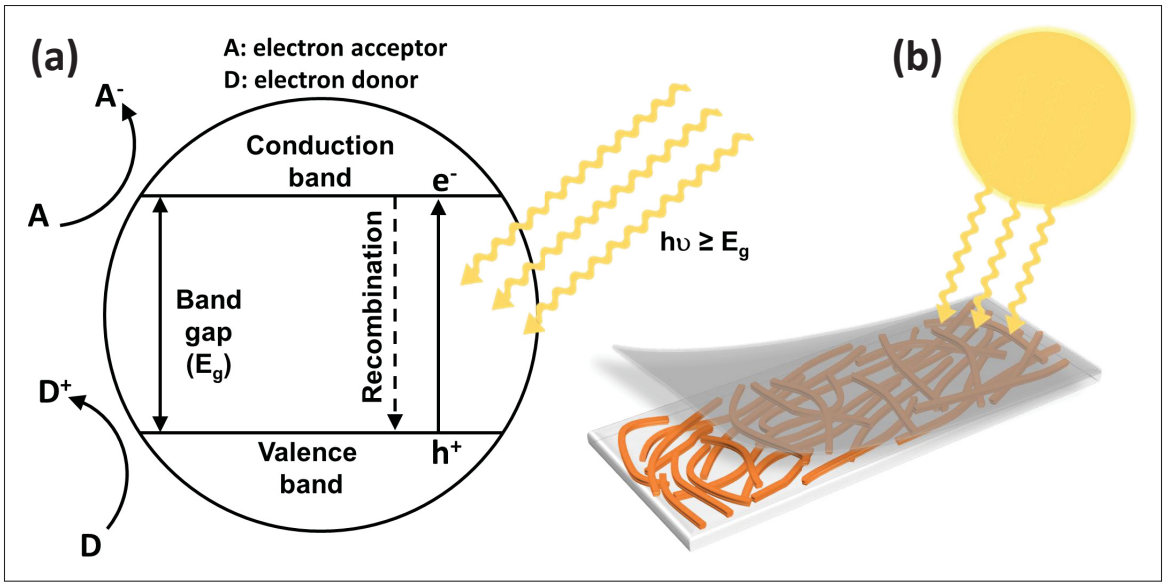

Figure 2.2 (a) Schematic diagram illustrating the principles of photocatalytic process and (b) Schematic of the $BiFeO_3$ nanofibers-based photocatalytic cell used in chapter 5. The top layer represents the thin layer of platinum deposited by sputtering

et al. (2014) Hence, expensive, environmentally harmful and constraining UV sources are generally used in photocatalytic reactors. To simulate and track pollutant degradation over time, dyes such as Rhodamine B, Congo Red, Methyl Orange or Methylene Blue are used. Lam, Sin & Mohamed (2017) These dyes are commonly used as their degradation can be easily estimated. It is known that concentrations in the range of $mg\ L^{-1}$ can be directly measured from the absorbance through the Beer-Lambert equation.

With a low band gap between 2 and 2.7 eV that permits visible light absorption, BFO is a good candidate for photocalytic applications. As mentioned previously, BFO has the advantage of being biocompatible, chemically inert, photostable and its precursors are quite abundant in Earth's crust. Consequently, multiple reports presenting various BFO structures with different synthesis methods can be found in the literature. Lin, Gong, Wang, Wang & Zhang (2022); Xie *et al.* (2021); Lam *et al.* (2017); Gao, Chen, Huang, Niu, Huang, Qin & Huang (2015); Yin *et al.* (2019)

In the literature, most authors report colloidal solutions and use centrifugation to separate the catalyst from the treated leachate. Centrifugation is not compatible with water treatment plant functioning and adequate alternatives must be developed. In chapter 5, we report colloidal free photocatalytic BFO-based membranes for efficient rhodamine B degradation as illustrated in Figure 2.2(b). In chapter 6, a second colloidal-free photocatalytic cell is fabricated and used to degrade rhodamine B.

2.3 Water splitting

The growing demand for energy and concerns about greenhouse gaz effects from fossil fuels have encouraged researchers toward production of cleaner and renewable energies. Available technologies include wind turbines or solar panels. Photocatalytic water splitting appears as a promising solution as it uses two of the most abundant, clean and natural energy sources: sunlight and water. Ahmad, Kamarudin, Minggu & Kassim (2015) This technique is based on the separation of water into hydrogen and oxygen, thanks to interaction of photo-charges generated by semiconductors under light irradiation. By collecting and storing solar energy in chemical energy (in the formed of atomic bonds), this process is mimicking natural photosynthesis. Cox, Pantazis, Neese & Lubitz (2015)

The first hydrogen production was firstly reported by Fujishima in 1972 using TiO_2. Fujishima & Honda (1972) Like photocatalysis, water splitting ideally requires photostable and nano-engineered semiconductors that can absorb visible light. A basic photoelectrochemical cell consists of a cathode where the reduction takes place ($2H^+ + 2e^- = H_2$) and an anode where O_2 is produced ($2H_2O = 4H^+ + O_2 + 4e^-$). Arunachalam & Al Mayouf (2019) A schematic of such a cell is shown in Figure 2.3. In the case of a photoelectrochemical cell producing both hydrogen and oxygen, two different semiconductors respectively p- and n-type are required. Joy, Mathew & George (2018) Only the minority carriers, which are the holes for the photoanode and the electrons for the photocathode are used to drive chemical reactions. N-type semiconductors for oxygen production have been reported extensively in the literature as they tend to be more

easily synthesized. In contrast, p-type semiconductors possess a smaller choice of photocathodes available. Jang & Lee (2019)

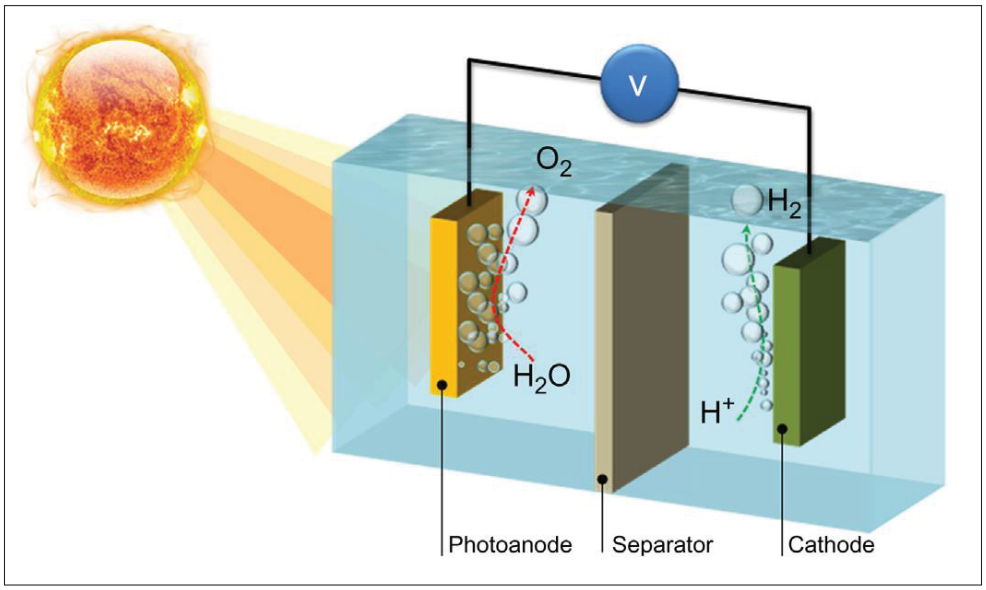

Figure 2.3 Schematic of a photoelectrochemical cell.
Taken from Arunachalam & Al Mayouf (2019)

Some drawbacks inherent to water splitting are reported in these references. Ipek & Uner (2019); Song, Kim, Lee, Cho, Cha, Jeong, An, Kim, Jung, Park et al. (2018) The following problems have been identified:

- Charge recombination of the photo-charges before reaching the catalyst surface.
- Back-oxidation reactions (interactions of H_2 and O_2 to produce H_2O).
- Mass transfer limitations. This phenomenon happens when the rates of the mass transfer of the products from the catalyst surface are slower than the oxidation/reduction rates. Hence, produced O_2 and H_2 would stay longer on the surface and promote back-oxidation reactions.

Depending on synthesis parameters, BFO can be either an n- or p-type material. As a result, BFO is a promising candidate for both photocathode and photoanode. As a ferroelectric material, one can switch BFO's polarization and influences the chemical reaction at the catalyst-electrolyte interface. Song *et al.* (2018) BFO is also photostable under light irradiation, which is an important parameter for water splitting performance. A review discussing in detail the

photocorrosion mechanisms involved in photoelectrochemical water splitting can be found in the following reference. Chen, Huang, Xu, Xue, Lei, Cheng, Wang, Liu & Deng (2020b) In chapter 4, we demonstrate that BFO nanofibers deposited by an electrospinning technique can be used for water-splitting and yield better photocurrent compared to thin films. The deposited microstructure must be carefully controlled to improve the photoelectrode performance and to reduce the amount of material.

2.4 Thermistor

The most common physical quantity acquired and monitored is the temperature. In fact, many physical, chemical, electronic or biological systems perform only within a narrow range of temperatures. To ensure optimal performances, temperature sensors are necessary to provide inputs and command control systems. Yadav, Srivastava, Singh, Kumar & Yadav (2012) The basic mechanism of a temperature sensor lies in the change of its capacitance or resistivity under a variation of temperature. Among these sensors, ceramic-based thermistors are widely produced as they tend to be very sensitive (up to -6%/°C) and accurate compared to metallic thermocouples (+1%/°C for Pt) at room temperature. Feteira & Reichmann (2010) Some ceramic-based thermistors are presented in Figure 2.4. They have different shapes, sizes and geometries depending on their applications.

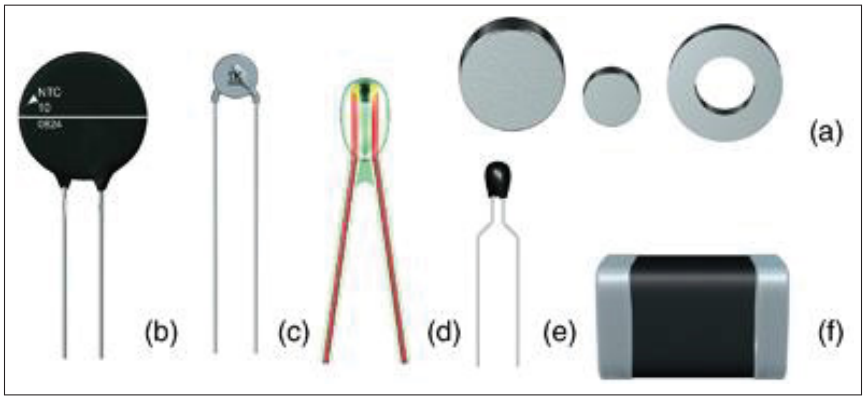

Figure 2.4 Examples of NTCR components: (a) leadless, (b,c) lead space, (d) glass-encapsulated, (e) resin-encapsulated, (f) surface-mounted device. Taken from Feteira (2009)

Ceramic-based thermistors can show two different types of behavior. If their resistivities rise with an increase of temperature, they exhibit a Positive Temperature Coefficient (PTC). Such devices are usually needed for electric current control. In contrast, a decrease of resistivity associated with an increase of temperature results in a Negative Temperature Coefficient (NTC) thermistor and is mostly used for temperature sensing. The first NTC behavior was discovered by Michael Faraday in 1833, while measuring variations using resistance of silver sulphide (Ag_2S). A hundred years later, some commercial thermistors started to be industrially manufactured. Feteira (2009) Industry-driven research and development was imperative to improve the first ceramic-based thermistors suffering from poor reproducibility and stability over time. These problems were attributed to the complex stoichiometry and processing conditions of the spinel-structured ceramics. Jagtap, Rane, Mulik & Amalnerkar (2007); Feteira (2009); Reimann, Töpfer, Barth, Bartsch & Müller (2013)

In the context of the internet of things and more precisely the telemedicine, researchers are developing innovative thermistors to measure and monitor the human body. Yan, Wang & Lee (2015) Good reviews describing and discussing wearable platforms for monitoring personal healthcare and human activity can be found in the following references. Trung & Lee (2016); Khan, Ostfeld, Lochner, Pierre & Arias (2016) As most ceramic-based thermistors tend to be rigid and not compatible with flexible substrates, carbon-based materials embedded in a polymer matrix are being investigated to address this issue. A variation of the electrical resistivity can be measured in such devices, as the thermal expansion of the polymer matrix tends to increase the distance between the carbon nanostructures. Graphene, carbon nanotubes or graphene oxide are among the most widespread carbon sources. In chapter 7, we propose innovative screen-printed BFO-based thermistors directly printed and integrated atop printed circuit boards. By adjusting the loading of the graphene and using a constant amount of BFO, we demonstrate a synergetic effect of both materials resulting in high-sensitivity and large operating temperature range thermistors.

2.5 Ways to improve $BiFeO_3$ properties and its integration

2.5.1 Graphene incorporation

Graphene can be defined as a single layer of carbon atoms densely arranged to form a periodic hexagonal lattice structure. Novoselov, Geim, Morozov, Jiang, Zhang, Dubonos, Grigorieva & Firsov (2004) It is a zero-bandgap semiconductor (also called a semimetal). Graphene can be prepared by mechanical cleavage and liquid exfoliation of graphite (top-down syntheses) or by chemical vapor deposition and molecular beam epitaxy (bottom-up syntheses). Young, Kinloch, Gong & Novoselov (2012)

Graphene was discovered in 2004 by Konstantin Novoselovand and Andre Geim, who received the Nobel Prize in Physics for this in 2010. Since then, graphene has received tremendous attention due to its exceptional properties such as ballistic transport, high thermal conductivity, high current density, chemical inertness or optical transmittance at nanometer scale. A high electron mobility up to 15 000 $cm^2\ V^{-1}\ s^{-1}$ at room temperature and an electrical resistivity of $10^{-6}\ \Omega\ cm$ makes graphene the lowest resistivity material known at room temperature. Choi, Lahiri, Seelaboyina & Kang (2010) As a consequence, tremendous amount of studies using graphene as a transparent conducting electrode, sensor or for components of integrated circuits such as ballistic transistors or field emitters have been reported.

In the context of this doctoral thesis, graphene is mixed with BFO powder and used as a short-range conductive media to fabricate highly sensitive thermistors.

2.5.2 Flexible hybrid electronics and printing deposition methods

Flexible electronics targets the fabrication of innovative devices that cannot be addressed by wafer-based electronics. Sun & Rogers (2007) Various fabrication methods such as spin-coating, spray-coating, roll-to-roll, 3D printing, inkjet printing and screen printing are compatible with flexible electronics fabrication. Compared to photolithography, vacuum deposition and echting

for silicon-based electronics, these methods require less expensive equipment and are more compatible with large-scale environments. Zhou, Zhang, Liu & Huang (2021)

By coupling inkjet printing and screen printing with flexible hybrid electronics, direct interfacing of soft substrates (usually polymer-based) and hard electronics components can be achieved (so-called Flexible Hybrid Electronics). Some applications of flexible electronics devices can be found in biomedical devices, wearable electronics, electronic skin or displays (like foldable phones). The global flexible electronics market already represents several tens of billions USD and its expanding growth is expected to follow a double-digit increase in the next five years. Zhou *et al.* (2021)

In the framework of this doctoral thesis, fabrication methods used in flexible electronics are relevant to create cost-efficient and highly reproducible devices. In chapter 8, we report fully screen-printed and flexible humidity sensors using BFO powder on kapton substrates. Screen printing is a relevant deposition method that fulfills all the objectives set in the introduction chapter. It allows an easy transfer of prototypes made in research laboratories to the industry. Screen printing is used in two published papers in chapters 6 and 7 to create photocatalytic cells and thermistors. In chapter 6, we show a 22% mass reduction of catalysts involved compared to the literature for RhB degradation.

2.5.3 Conductive electrodes and their integration to devices

From a device perspective, two situations can be faced while integrating any BFO structures. The first one is encountered when BFO is not crystallized and a thermal conversion needs to be performed to produce the BFO phase. The second situation occurs when BFO is already crystallized. In this case, BFO can be directly deposited by methods evoked in the previous subsection and may be compatible with printed electronics. In the course of this doctoral thesis, both approaches have been used.

The first approach is used in chapters 4 and 5 when nanofibers are deposited atop substrates like Fluorine-doped Tin Oxide (FTO) coated glass or aluminum oxide. In both chapters, an

electrospinning technique is used to control and to investigate the influence of the microstructures on the photoelectrochemical properties. However, the disadvantage of this approach lies in the annealing temperature (usually over 500 °C) necessary to crystallize BFO. As such, it excludes all polymer-based substrates and requires high-temperature substrates. FTO or Indium Tin Oxide (ITO) are commonly used as transparent conductive electrodes. FTO is usually preferred to ITO as it is more thermally stable and less expensive. Way, Luke, Evans, Li, Kim, Durrant, Hin Lee & Tsoi (2019) Strontium titanate ($SrTiO_3$) is also a popular substrate, especially for thin films depositions under high temperature. This perovskite material can be used to grow epitaxial structure and shows both conductivity regimes (p or n-type conduction) depending on the surrounding environment. Ohly, Hoffmann-Eifert, Guo, Schubert & Waser (2006) Notwithstanding the success of this previous approach we demonstrate that photonic curing can be used as a promising alternative to cure BFO on polymer-based substrates like polyimides. So far, no report of BFO crystallized by photonic curing has been reported in the literature. Using this technique could possibly unlock a wide range of possibilities to create innovative and commercially viable BFO devices.

The second approach based on crystallized BFO structures is used in chapters 6 and 7. We prepare BFO powder-based inks to fabricate devices by screen printing. In these cases, the annealing temperature is used to remove or cure the polymer matrix needed to disperse the BFO powder. We report using this technique in one paper in chapter 7 based on thermistor devices and another one in chapter 6 based on p-n BiOCl/BFO heterojunctions for photocatalytic applications.

CHAPTER 3

HIGHLY EFFICIENT THERMOELECTRIC MICROGENERATORS USING NEARLY ROOM TEMPERATURE PULSED LASER DEPOSITION

Paul Fourmont[1] , Luis Felipe Gerlein[1] , François-Xavier Fortier[1] , Sylvain G. Cloutier[1] , Riad Nechache[1]

[1] Department of Electrical Engineering, École de Technologie Supérieure, 1100 Notre Dame West, Montreal, Quebec, Canada

Abstract: Thermoelectric Bi_2Te_3 and Sb_2Te_3 thin films with high-power factor were successfully obtained by pulsed laser deposition (PLD). Here, we demonstrate a well-controlled deposition of Bi_2Te_3/Sb_2Te_3 structures on glass substrates, through a shadow mask with micrometer-scale features. We establish an optimal growth temperature of 45 $°C$ to attain compounds with suitable stoichiometric composition, as well as structural and electrical properties, to achieve high thermoelectric power factor. These films are produced without additional postannealing treatment or added gases. Indeed, crystalline films with Seebeck coefficients of 624 and -78 μV K^{-1} are obtained for Sb_2Te_3 and Bi_2Te_3, respectively. Microgenerators consisting of four pairs of n-type Bi_2Te_3 and p-type Sb_2Te_3 legs connected in series generate a maximum voltage of 50 mV and a power density of around 120 μW cm^{-2} for a temperature difference of 30 K across the hot and cold ends of the device. This low-temperature and simple PLD-deposited device represents an important step toward practical thermoelectric materials as well as efficient and compact microgenerators for low-temperature energy-harvesting applications.

3.1 Introduction

Recently, multiple research efforts have been focused on thermoelectric (TE) microgenerators to convert heat energy generated by various physical signals and chemical reactions into electrical power. DiSalvo (1999); LeBlanc, Yee, Scullin, Dames & Goodson (2014) Thermoelectric microgenerators have emerged as a promising technology for energy harvesting and refrigeration. This technology can be of interest in fields ranging from wearable energy sources powered by human body heat to exhaust waste heat recovery systems attached to automobile exhaust

pipes or radioisotope thermoelectric generators for space applications. Patel, Park, Bonato, Chan & Rodgers (2012); Chen, Madan, Wright & Evans (2011); Zheng, Liu, Yan & Wang (2014); Liu, Jie, Kim & Ren (2015) In particular, industrial and transportation sectors can greatly benefit from these microgenerators where most of the energy consumed by production plants and vehicles is wasted as heat generation. Laboratory (2013) With the growing need for miniaturized power sources and the advent of microscale devices with wearable systems, the development of advanced, reliable, and cost-effective TE microgenerators becomes a critical challenge. Thermoelectric generation is a dependable source of power with additional advantages such as silent operation due to the absence of moving mechanical parts, being environmentally friendly making it ideal for electrical generation and cooling applications. The performance of TE materials inherently defines the conversion efficiency of the microgenerators, where large Seebeck coefficients (α) are needed to achieve highly sensitive generator devices. Müller, Budde, Gottfried-Gottfried, Hübel, Jähne & Kück (1996) Bi_2Te_3 and Sb_2Te_3 are the leading material systems commonly employed as TE films in microgenerator devices Satterthwaite & Ure Jr (1957); Chen, Dresselhaus, Dresselhaus, Fleurial & Caillat (2003) Such semiconductors have narrow band-gap and superior TE properties at room temperature (RT), with a figure of merit (ZT) around the unit. The figure of merit ZT is defined by $ZT = (\sigma\alpha^2/\lambda) \times T$, where T is the temperature in kelvin, α is the Seebeck coefficient, σ and λ are, respectively, the electrical and thermal conductivities, and the term $\sigma\alpha^2$ represents the power factor (PF). As the parameters α and σ usually vary in an opposite manner, this makes any improvement of the figure of merit (ZT) challenging. Chen, Han, Yang, Cheng & Zou (2012)

Conventional TE systems based on bulk Bi_2Te_3 and Sb_2Te_3 are not suitable for integrated microsystems because of their limited mechanical properties (i.e., adhesion, stress accommodation, design flexibility) during the device microfabrication. Bux, Fleurial & Kaner (2010) Such microsystems usually involve complex and expensive deposition techniques to achieve high-quality TE films. Thus, producing high-quality thermoelectric thin films with good uniformity, adhesion and figures of merit (ZTs) comparable to those of bulk materials is crucial to sustain future progress in fabrication and applications of novel TE microsystems. Most TE film depositions

are achieved at high substrate temperatures (~250 $^{\circ}C$), making patterning using conventional photolithography and etching process complicated. Deposition through shadow masks has been successful to pattern thin films with lateral dimensions as small as 23 μm. Huang, Lawrence, Gross, Hwang, Ghafouri, Lee, Kim, Li, Uher, Najafi et al. (2008) Additional attempts to deposit high-quality TE thin films using techniques such as co-evaporation, Kim, Choi, Bae, Kim & Oh (2013); Zou, Rowe & Min (2001) three-dimensional printing, Madan, Chen, Wright & Evans (2012); Wang, Chen, Winslow, Madan, Juang, Nill, Evans & Wright (2012) co-sputtering, Zeng, Yang & Hu (2013) flash evaporation, Völklein, Baier, Dillner & Kessler (1990) and pulsed laser deposition (PLD) Dauscher, Thomy & Scherrer (1996) have also been reported. It is essential for the stoichiometry of the reaction to be maintained within the solubility limits of the Bi/Sb-Te phase diagrams to achieve high values for ZT. Goncalves, Alpuim, Min, Rowe, Couto & Correia (2008) Among the available techniques for fabrication of TE thin films, PLD is the most straightforward method to reproduce the composition of the ablated target material in the film. Eason (2007); Nechache *et al.* (2015)

In this work, we employ PLD to grow thermoelectric films with the desired stoichiometry for microgenerator device applications. Lateral-lateral-type TE microgenerators based on Bi_2Te_3/Sb_2Te_3 thermocouples are fabricated directly on glass substrates. In contrast to the cross-plane type, this device geometry is more appropriate for TE applications because it produces higher voltages at smaller temperature gradients with relatively short processing time while keeping the fabrication process simple. Feinaeugle, Sones, Koukharenko & Eason (2013) Although previous investigations focused on optimization and characterization of TE materials deposited by PLD, this study demonstrates the first PLD-grown planar TE microgenerator device for low-temperature energy-harvesting applications. Such generators are suitable for applications in microelectronic systems as an auxiliary electrical power source.

3.2 Results and discussions

3.2.1 Annealing-free PLD-grown polycrystalline thermoelectric thin films

Typically, the TE figure of merit of bismuth and antimony telluride materials is related with their composition and crystalline structure, regardless of the deposition method. Goncalves *et al.* (2008); Abdel Aziz, Elsayed, Abu Bakr, El-Rifai, Van der Donck, Celis, Leonov, Fiorini & Sedky (2010) With PLD, the key deposition parameters include substrate temperature (T_S), partial pressure, and laser fluence to affect the chemical composition and the crystalline phase of the deposited films. Nechache, Harnagea, Carignan, Gautreau, Pintilie, Singh, Ménard, Fournier, Alexe & Pignolet (2009) We fabricated films of Bi_2Te_3 and Sb_2Te_3 at four different T_S values, 25, 45, 80, and 150 $°C$, and measured their Seebeck voltage response (cf. Figure 3.1) and resistivity values.

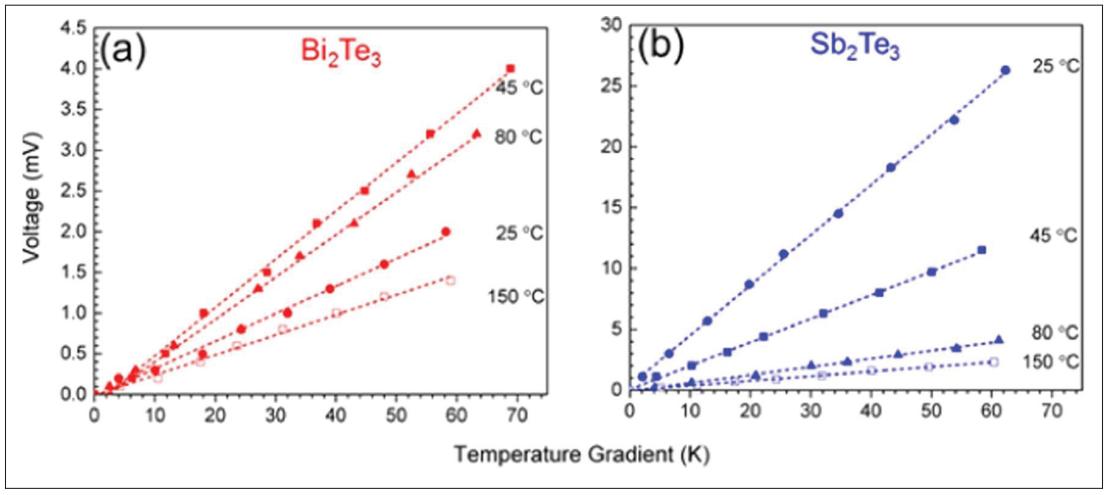

Figure 3.1 Absolute value of the Seebeck voltage measured as a function of the temperature gradient for (a) Bi_2Te_3 and (b) Sb_2Te_3 films

The Seebeck coefficient, α, measured for the Bi_2Te_3 films is negative due to its n-type nature, which was confirmed by Hall effect measurements (cf. Experimental Section). Absolute α values ranged from 24.7 to 52.1 $\mu V\ K^{-1}$ (cf. Figure 3.1a). These coefficients are much lower than 200 $\mu V\ K^{-1}$ reported for bulk Bi_2Te_3, Park, Song, Medvedeva, Kim, Kim & Freeman (2010)

possibly due to higher carrier concentrations, in the range of $1 \times 10^{21} - 7 \times 10^{21} cm^{-3}$, induced by the defects formed in films during the PLD growth. In contrast, the carrier concentration required for optimal TE performance is in the order of $10^{19} - 10^{20} cm^{-3}$. Fang, Zeng, Yan & Hu (2013)

In case of p-type Sb-Te films, the α coefficients are positive and exhibit a maximum value of 412.8 $\mu V\ K^{-1}$ at T_S = 25 $°C$ (cf. Figure 3.1b). Increasing T_S dramatically reduces α to 38.4 $\mu V\ K^{-1}$ at T_S = 150 $°C$. Such substrate temperature dependence on α might relate to the degree of crystallinity and chemical composition of the resulting films. High Seebeck coefficients obtained for Sb_2Te_3 films deposited at T_S = 25 $°C$ can be attributed to the amorphous nature of the Sb_2Te_3 film, as evidenced by X-ray diffraction (XRD) analysis (cf. Figure A I-1). Baily & Emin (2006); Damodara Das, Soundararajan & Pattabi (1987) Indeed, amorphous Sb-Te films exhibit much higher Seebeck coefficients (as high as 750 $\mu V\ K^{-1}$), compared to our crystalline films grown at $T_S \geqslant 45\ °C$.

Using the four-probe technique, we measure the electrical resistivity (ρ) of both TE films. The lowest ρ values of 1.95× 10^{-5} and 0.03× 10^{-5} $\Omega\ m$ are obtained for films grown at 45 $°C$, resulting in maximal power factors of 3.17× 10^{-3} and 8.38× 10^{-3} $W\ m^{-1}\ K^{-2}$ for Sb_2Te_3 and Bi_2Te_3, respectively (cf. Table 3.1). To better understand the fundamental intricacies responsible for the unusual TE properties obtained for films deposited at 45 $°C$, we first investigated their chemical ratio and microstructural properties, including crystal structure and morphology.

T_S (°C)	Sb_2Te_3					Bi_2Te_3				
	ρ ($m\Omega cm$)	α ($\mu V\ K^{-1}$)	PF ($mW\ m^{-1}K^{-2}$)	atom %		ρ ($m\Omega cm$)	α ($\mu V\ K^{-1}$)	PF ($mW\ m^{-1}K^{-2}$)	atom %	
				Sb	Te				Bi	Te
25	926.57	412.8	$1.84 \cdot 10^{-2}$	34.1	65.9	14.08	-33.8	$8.11 \cdot 10^{-3}$	32.7	67.3
45	1.95	249.2	3.17	39.6	60.4	0.03	-52.1	8.38	39.4	60.6
80	15.42	66.3	$2.85 \cdot 10^{-2}$	37.8	63.2	0.22	-39.1	$6.41 \cdot 10^{-1}$	40.9	59.1
150	5.23	38.4	$2.82 \cdot 10^{-2}$	29.1	70.9	2.56	-24.7	$2.44 \cdot 10^{-2}$	38.8	61.2

Table 3.1 Room-temperature properties of Bi_2Te_3 and Sb_2Te_3 films deposited by PLD at different T_S

The surface scanning electron microscopy (SEM) images of the Sb_2Te_3 and Bi_2Te_3 films deposited on glass substrates at 45 $°C$ are shown in Figures 3.2(a,c). Smooth surfaces are

observed for both TE films, where only small crystal grains and blurry boundaries characterize the films. More details about the film morphology are obtained by atomic force microscopy (AFM) measurements (cf. Figure A I-1). Average grain sizes (d) of 9.85 and 29.33 *nm* with surface roughnesses (R_a) of 2.37 and 6.41 *nm* are obtained for Sb_2Te_3 and Bi_2Te_3 films, respectively (cf. Table A 3.1).

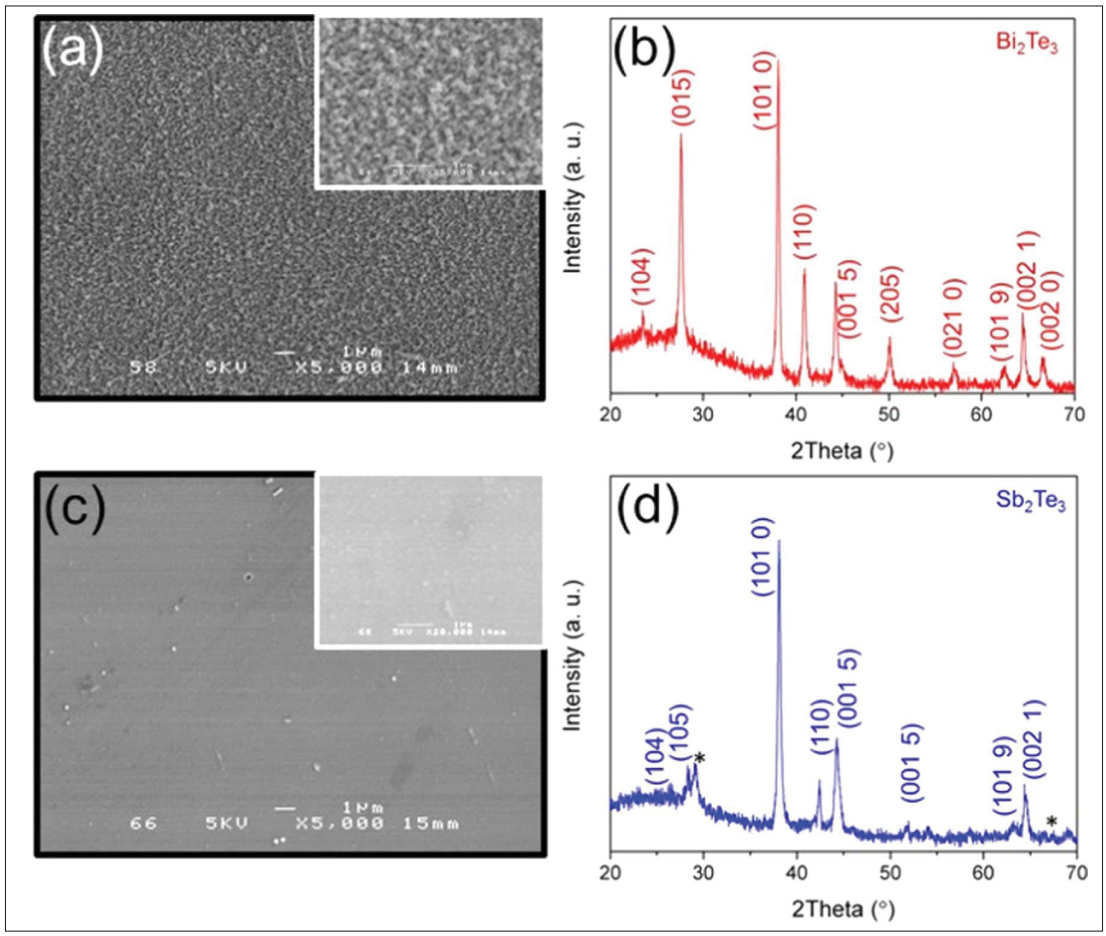

Figure 3.2 Scanning electron microscopy images of (a) Bi_2Te_3 and (c) Sb_2Te_3 film surfaces and (b, d) their corresponding XRD spectra. Both films are grown at a substrate temperature of T_S = 45 °*C*

These results are confirmed by X-ray diffraction (XRD) analysis. Using Scherrer's equation, d is calculated to be ~10.52 *nm* for Sb_2Te_3 film and ~28.76 *nm* for Bi_2Te_3 film. The XRD patterns of TE films prepared by PLD reveal the polycrystalline structure of both the Sb_2Te_3 and Bi_2Te_3 phases, as shown in Figures 3.2(b,d), with no impurities such as Te or Sb elements.

This suggests that the films crystallize in unique phases of Sb_2Te_3 and Bi_2Te_3 with the desired stoichiometric ratio and hexagonal structure (JCPDS files #15-863 and #15-874 for Bi_2Te_3 and Sb_2Te_3, respectively). During growth, the Sb_2Te_3 and Bi_2Te_3 films are under a bombardment of high-energetic particles, which increases the surface diffusion needed for crystallization. Because of the complex lattice structure of stoichiometric TE phases, film crystallization at low deposition temperatures is promoted by the surface diffusion activated from high-energetic atoms and ions ablated from the material target. Eason (2007) These results highlight the ability to crystallize films of Sb_2Te_3 and Bi_2Te_3 bypassing the requirement for high-temperature annealing (or post-treatment annealing), and in exchange, the high-energy particles compensate the lower substrate temperature. Because the films are deposited under high vacuum, we have increased the target-substrate distance to 11.5 cm to hinder the deep penetration of high-energy particles and thus prevent a partial destruction of the lattice structure of TE films.

Energy-dispersive X-ray (EDX) spectroscopy (cf. Figure A II-2(d,e)) confirms near-stoichiometric atomic percentages (atom %) of the TE films grown at $T_S = 45\ °C$: Sb_2Te_3 with 39.6 ± 0.5 atom % of Sb and 60.4 ± 0.5 atom % of Te; and Bi_2Te_3 with 39.4 ± 0.5 atom % of Bi and 60.6 ± 0.5 atom % of Te (cf. Table 3.1). This stoichiometric composition deviates when the substrate temperature changes, resulting in α and ρ variations. This agrees with previous reports Fang *et al.* (2013); Fan, Zheng, Liang, Zhang & Cai (2010) demonstrating that an excess of Te or Sb significantly reduces carrier concentration and therefore resulting in high ρ and low PF.

3.2.2 Low-dimensional thermoelectric n-type and p-type legs

To further investigate the electrical and TE properties of the films, we deposited at $T_S = 45\ °C$ N number of legs of either Bi_2Te_3 or Sb_2Te_3 on glass substrates through patterned masks (cf. Figure A I-3(a)). The length and width of a single leg are about 1 cm and 450 μm (cf. Figure A I-3(b)), respectively. To perform electrical and thermoelectric measurements, the N legs of one material are connected in parallel using Ag paste as electrodes (cf. inset of Figure 3.3(a)).

To measure the in-plane Seebeck coefficients, temperature gradients (ΔT) of up to 80 K are applied across the samples to produce Seebeck voltages, using a homemade Seebeck coefficient measurement system (cf. Figure 3.3(a)). A high Seebeck coefficient of 624 $\mu V\ K^{-1}$ was recorded for Sb_2Te_3 legs at ΔT = 11 K (Figure A I-4).

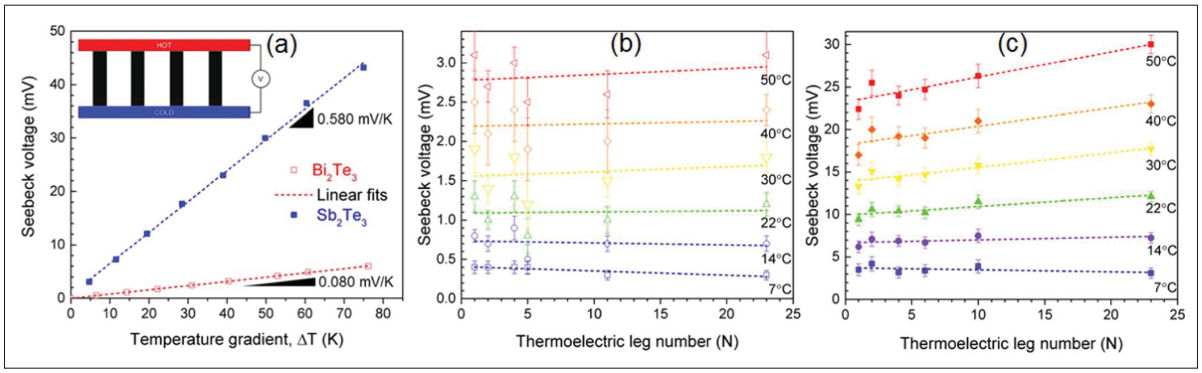

Figure 3.3 Seebeck voltage as a function of temperature gradient measured for (a) Bi_2Te_3 and Sb_2Te_3 legs. (b, c) Seebeck voltages are measured while varying the number of thermocouple legs (N) for Bi_2Te_3 (b) and Sb_2Te_3 (c) films at different temperature gradients

Thermoelectric performance and stability of the film legs were investigated by measuring their Seebeck voltage dependence on the temperature gradient (ΔT) (Figure 3.3(b,c)) for N legs connected in parallel. The generated Seebeck voltage connecting 23 legs, increasing the gradient temperature shows maximum values of 25 and 3 mV at ΔT = 50 K for Sb_2Te_3 and Bi_2Te_3, respectively. The output Seebeck voltages present variations of up to 25% according to the number N of legs involved during the measurement, which originates from PLD growth inhomogeneity of the film properties over the large deposited area (i.e., length and width of 3 and 1 cm, respectively). Bailini, Donati, Zamboni, Russo, Passoni, Casari, Bassi & Bottani (2007) The thermostability of the devices was evidenced by the absence of hysteresis in the TE cycling measurements (Figure A I-5). The Seebeck voltage generated by the devices after cycles of positive/negative temperature gradients (with a temperature in the hot side T_h of up to 100 $°C$) showed a linear dependence with insignificant slope deviance (Figure A I-5(a,b)). This was confirmed by XRD analysis in which a slight change in the microstructure (e.g., grain size) is observed after 15 cycles of TE measurement. The XRD reflections of the hexagonal

phase for both Bi_2Te_3 and Sb_2Te_3 slightly shift to higher θ angles, suggesting the occurrence of a partial strain relaxation induced by a thermal annealing (Figure A I-5(c)). However, a further measurement at temperature exceeding 100 $°C$ results in an enhanced XRD reflection intensity and larger grain sizes of both TE legs. To further evaluate the thermal stability of Bi_2Te_3 and Sb_2Te_3 legs-based devices, samples were kept at 60 and 100 $°C$ and the temporal change of the TE properties was measured for more than 1 hr. As depicted in Figure A I-5(d-f), the devices exhibit a performance variation of less than 3% as well as a long-term stability exceeding a year.

The low electrical resistivity of the Sb_2Te_3 film yields in a moderate power factor of 1.98×10^{-3} $W\ m^{-1}\ K^{-2}$, a TE performance similar to the values reported for SnSe. Zhao, Lo, Zhang, Sun, Tan, Uher, Wolverton, Dravid & Kanatzidis (2014); Sassi, Candolfi, Vaney, Ohorodniichuk, Masschelein, Dauscher & Lenoir (2014) The high α might result from size effects in our Sb_2Te_3 films, which helps to adjust electron and phonon transport, in addition to their electronic structure (including energy band structure and electronic density of states), thus improving the Seebeck coefficient. Dresselhaus, Chen, Tang, Yang, Lee, Wang, Ren, Fleurial & Gogna (2007) Seebeck voltages for both Bi_2Te_3 and Sb_2Te_3 films display a linear dependence on ΔT, with their corresponding slopes of 80 and 580 $\mu V\ K^{-1}$ (cf. Figure 3.3(a)).

As mentioned earlier, both Sb_2Te_3 and Bi_2Te_3 have a layered rhombohedral crystal structure of space group $R3m$. Each rhombohedral unit cell contains five atoms, and consequently, TE materials exhibit 15 normal modes at the Γ point of the Brillouin zone represented by the irreducible representation: $\Gamma = 2(A_{1g} + E_g) + 3(A_{2u} + E_u)$, where g and u represent the active Raman and IR modes. Souza, Trichês, De Lima, Grandi & De Biasi (2010) Sosso et al. reported the main active Raman modes for Sb_2Te_3 at room temperature and ambient pressure to be (1) E_g modes at 46 and 113 cm^{-1} and (2) A_{1g} modes at 62 and 166 cm^{-1}. Sosso, Caravati & Bernasconi (2009)

Confocal Raman microspectroscopy mappings of both TE films (cf. Figure 3.4(d)) show the peak corresponding to the Eg mode at 113 cm^{-1} for our Sb_2Te_3 thin film. This Eg mode peak, however, is shifted to a higher frequency at 118 cm^{-1}. The intensity of this peak is strong and

narrow, confirming the good crystallinity of the films. Three additional modes located at 90, 140, and 189 cm^{-1} are observed, which correspond to the characteristic modes of $E_u^{2a}(LO)$, $2A_{1g}$, and $Eu_u^{2a}(TO)$ of Sb_2Te_3. Sosso *et al.* (2009) This can be explained by symmetry breaking in nanostructured films, allowing the appearance of modes originally prohibited and/or by the anisotropic confinement in the nanograins, thus shifting the Raman modes. These Raman modes may also correspond to those of β-Sb_2Te_3 phase that nucleates when the material is under strain. The β-phase has a monoclinic $C2/m$ structure, which is isostructural to α-As_2Te_3, which has been recently found under ambient conditions as a metastable phase after high-pressure and high-temperature treatment of the rhombohedral α-Sb_2Te_3. Buga, Serebryanaya, Dubitskiy, Semenova, Aksenenkov & Blank (2011) The formation could be the source of the additional XRD peaks observed at $2\theta = 29.3$ and 67.6° (reflections labelled with asterisks in Figure 3.2(d)). Under stress, interatomic distances are modified, thus tuning the material properties. Badding, Meng & Polvani (1998); Ovsyannikov, Shchennikov, Vorontsov, Manakov, Likhacheva & Kulbachinskii (2008) Meanwhile, the Raman spectrum of Bi_2Te_3 is mainly characterized by four modes: Jenkins, Rayne & Ure Jr (1972); Kullmann, Geurts, Richter, Lehner, Rauh, Steigenberger, Eichhorn & Geick (1984) E_{1g} at 36.5 cm^{-1}, A_{1g}^1 at 62 cm^{-1}, E_{2g} at 102 cm^{-1},and A_{1g}^2 at 134 cm^{-1} (cf. Figure 3.4(c)). Raman and XRD spectra present only the characteristic Bi_2Te_3 peaks and reflections (detection of the low-frequency E_{1g} and A_{1g}^1 peaks was difficult). An additional, strongest peak identified as A_{1u} appears in the Raman spectrum at 117 cm^{-1}. The A_{1u} peak (which is the infrared-active mode in bulk crystalline Bi_2Te_3) is likely to become Raman-active due to the symmetry breaking in atomically thin films. Shahil, Hossain, Teweldebrhan & Balandin (2010) The thin Bi_2Te_3 films may have incomplete quintuple layers at the surface. Atoms located on and near the surface that have less neighbors and low electron density possess higher energies and are more likely to move out of the plane and thus break the symmetry along the c axis and make the A_{1u} modes Raman-active. Zhao, Hughes, Su, Zhou & Gregory (2011)

To elucidate the low resistivity measured for PLD-deposited TE films at 45 $°C$, we performed Hall effect measurements on single TE leg connected by Ag electrodes to apply currents and

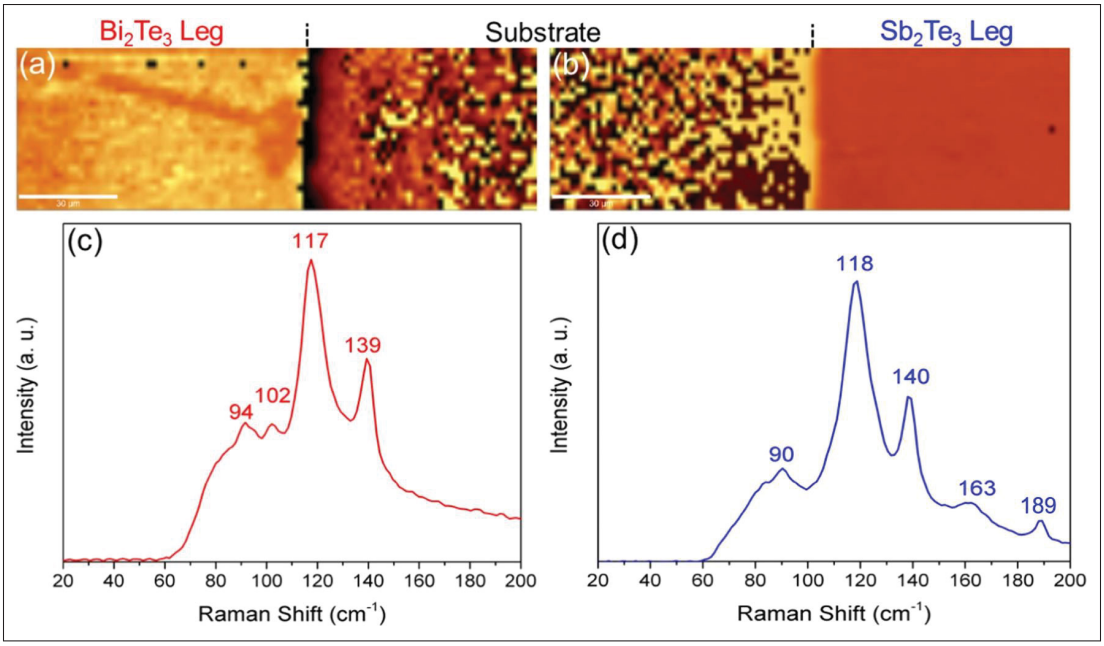

Figure 3.4 (a, b) Micro-Raman mapping and (c, d) the corresponding spectra measured for Bi_2Te_3 and Sb_2Te_3 legs

record voltages (Figure A I-6(a)). By applying simultaneously a current through terminals 1-6 and a magnetic field perpendicular to the sample surface, the Hall voltage across the leg could be measured between terminals 2 and 3 or 4 and 5 (denoted V_{2-3} and V_{4-5}, respectively). We first measured Hall voltages V_{2-3} and/or V_{4-5} at room temperature as a function of the applied magnetic field B for current sourced through terminals 1-6, $I_{1-6} = 100\ \mu A$ (Figure A I-6(b)). From the experimental data, the different regions of the legs exhibit slight difference in Hall characteristics. The Hall voltage V_H can be approximately described by $V_H = \frac{I_{1-6} \cdot B \cdot L}{n \cdot e \cdot A_{leg}}$, where n is the electron concentration, e is the elementary charge, A_{leg} is the TE leg area, and L is the distance between the points where the voltage terminals probe the potential. Using the present geometry, the linear fits shown in Figure A I-6(b) provides the carrier concentration. We find that the carrier concentration is similar along the legs and is calculated to be $n = 1.6 \times 10^{19}$ and $6.7 \times 10^{19} cm^{-3}$ for Sb_2Te_3 and Bi_2Te_3, respectively.

3.2.3 Compact TE microgenerators with highly efficient thermal-electrical conversion

A TE generator is basically designed to convert a thermal gradient into electrical power to supply electronic devices. As such, a minimal output voltage of several millivolts is required for commercial applications. To maximize this voltage, materials (n- and p- types) with opposite signs of α are connected in series (cf. Figure 3.5(a)) to add the individual output voltages of each material. The overall Seebeck coefficient α_{tot} over a p-n combination in such a configuration is $\alpha_{tot} = \alpha_{p\text{-}type} - \alpha_{n\text{-}type}$, where $\alpha_{p\text{-}type} > 0$ and $\alpha_{n\text{-}type} < 0$.

The SEM images in Figures 3.5(b,c) show well-defined device components with n and p legs separated by a gap of around 200 μm. This result is confirmed by EDX mapping, where the main chemical elements are detected (cf. Figure 3.5(d)). More detailed analysis demonstrates a near-stoichiometric composition of both TE materials with a good homogeneity across the whole device area.

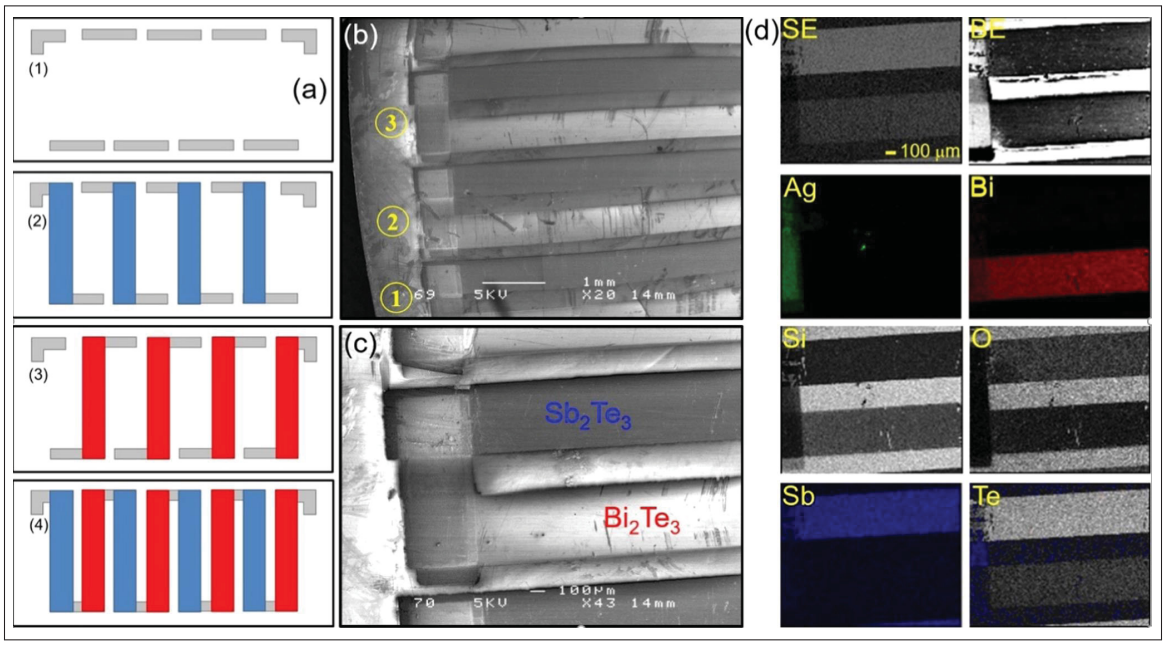

Figure 3.5 (a) Schematic describing the fabrication process of a TE microgenerator. SEM images of (b) multiple pairs of thermocouple legs denoted by the numbers 1-3 and (c) single thermocouple showing the morphology of both legs of Bi_2Te_3 and Sb_2Te_3 and their corresponding separation. (d) Corresponding EDX mappings performed on a single thermocouple

The TE performance of the devices is characterized by measuring the temperature gradient dependence of the Seebeck voltage (cf. Figure 3.6) for N connected thermocouples/ junctions within the patterned generator. As expected, for a given ΔT, the output Seebeck voltage increases linearly with the N number of thermocouples connected in series (cf. Figure 3.6(a)). The maximum α coefficient taken from the slope of these curves was found to be 401 $\mu V\ K^{-1}$ for one single thermocouple leg (i.e., $N = 1$) (cf. Figure 3.6(b)). This value is lower than the expected Seebeck coefficient of 660 $\mu V\ K^{-1}$ that arises from the coefficients measured individually for each material in the thermocouple, for the same number N of legs (cf. Figure 3.3). Indeed, the overall theoretical Seebeck coefficient comes from the contribution of both p- and n-type materials because they are in series and have dissimilar signs. This could be explained by the formation of a Schottky barrier at electrode-TE material interface and/or the shortening of the active area of TE legs overlapped by metal contacts.

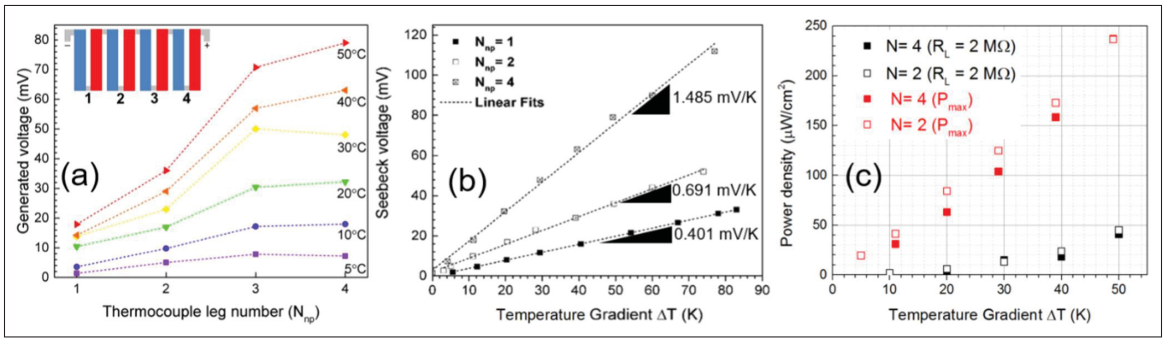

Figure 3.6 (a) Seebeck voltage vs connected thermocouple leg number (N) generated at different temperature gradients. (b) Seebeck voltage as a function of temperature gradient measured for Bi_2Te_3/Sb_2Te_3 thermocouple legs connected in series. (c) Power density generated by TE devices at different temperature gradients

Figure 3.6(c) illustrates the output power curves for the characterized TE microgenerators. All devices exhibit a strong dependence on ΔT. The best devices delivered cross-sectional areal power densities of ~120 and 640 $\mu W\ cm^{-2}$ for ΔT of 30 and 70 K, respectively (Figure A I-7(a)). The calculated maximum output power extractable from the device at $\Delta T = 30\ K$ is ~0.5 nW per leg pair, a value exceeding that reported for other lateral-lateral devices. Feinaeugle *et al.* (2013) The output power density is reduced when a load resistance of 2 $M\Omega$ is used (Figure A I-7(b)). This result indicates that PLD near room temperature via shadow masks is a promising pathway

toward rapid and low-cost fabrication of square centimeter area TE generator devices without the need for complex and expensive lithographic steps. The fabricated devices could be scaled for many low-power technologies, including those related with radiofrequency and wearable sensors. Further optimization of device design, fabrication, and material processing are under work to improve our TE microgenerator performance.

3.3 Conclusion

In this study, the microstructure and the thermoelectric properties of thin films of Bi_2Te_3 and Sb_2Te_3 deposited by PLD at a temperature close to room conditions without additional postannealing treatment results were investigated. We demonstrated crystalline films with Seebeck coefficients of 624 and -78 $\mu V\ K^{-1}$ for Sb_2Te_3 and Bi_2Te_3, respectively. Anisotropic effects have been exploited by depositing thin legs of both TE materials using patterned metallic shadow masks. Microstructural characterizations performed on films indicate that optimal TE performances are possible when the films are near stoichiometric ratio and well crystallized in the hexagonal single phase. SEM and AFM analyses revealed very smooth surfaces with small grains and very low roughness, which directly influences the electrical properties. Microgenerator devices are fabricated by connecting several Bi_2Te_3/Sb_2Te_3 thermocouples in series. Connecting four thermocouples generates a maximum voltage of 50 mV and a power density of around 120 $\mu W\ cm^{-2}$ for a temperature difference of 30 K across the hot and cold ends of the device. Thickening the TE thin-film legs and optimizing their dimensions could further improve the overall performances of the microgenerators. The proposed approach using a low-temperature PLD growth provides a promising alternative to achieve practical TE materials and efficient and compact microgenerators.

3.4 Experimental methods

3.4.1 Material synthesis

A 1 mm thick glass substrate was ultrasonically cleaned in 1% Hellmanex and isopropyl alcohol for 10 min before the deposition and then washed in deionized water to remove organic residuals. For the deposition of n-type and p-type films by PLD, stoichiometric bismuth tellurite (99.999%) and antimony tellurite (99.96%) 1 in. targets were ablated using a 240 nm excimer laser with a pulse duration (τ) of 15.4 ns. Laser fluence, pulse frequency, and target-to-substrate distance were kept at ~2.2 $J\ cm^{-2}$, 10 Hz, and ~11.5 cm, respectively. The film growth was carried out under a vacuum level of $10^{-5}\ mbar$ at substrate temperature (T_S) ranging from RT to 150 $°C$. Under these PLD conditions, the growth rates of Bi_2Te_3 and Sb_2Te_3 films were typically 0.5 and 0.2 $nm\ s^{-1}$, respectively. The film thickness ranged from 200 to 600 nm measured using a Dektak profilometer.

3.4.2 Device fabrication

Gold/silver metal contacts were first deposited at RT on 1 mm thick glass substrates by evaporation via shadow mask. The obtained electrodes are rectangles of 200 $\mu m \times 500\ \mu m$ spaced by a gap of 200 μm. Using a patterned metal mask, we deposited Sb_2Te_3 thin-film legs of 10 mm length and 0.5 mm width at different substrate temperatures by PLD. Then, we formed Bi_2Te_3 thin-film legs using the same procedure. The masks were designed to have an optimized overlapping of the TE legs with the electrodes contacts.

3.4.3 Film characterization

Crystal structure and phase impurity analyses were carried out by X-ray diffraction in grazing incidence mode and micro-Raman (λ = 532 nm) mapping. The film thickness was obtained using a Dektak surface profile measurement system. The stoichiometry and the composition ratio of the deposited films were determined by a scanning electron microscope equipped with an

energy-dispersive X-ray (EDX) spectroscopy microanalysis system. Their surface morphology roughness was characterized by atomic force microscopy (AFM) in tapping mode.

3.4.4 Thermoelectric measurement

TE characterization was performed with a homemade setup composed of two Peltier cells as hot/cold sources to produce a variable temperature gradient. The Peltier cells employed in this setup are commercially available. They were calibrated and validated for our measurement (i.e., temperature vs applied power). The cells are placed on two sinks to improve heat dissipation and increase thermal gradient between hot and cold junctions. With this system, temperature gradients up to 100 K were achieved. The power generation characteristics of TE devices were measured by placing the device between hot/cold sources. The temperature difference ΔT across the device was measured using thin K-type thermocouples hardly fixed between the thin-film device and the hot/cold sources. The samples were fixed on the Peltier cells using a thermal paste to optimize the heat transfer. After reaching a steady-state ΔT, the generated voltage and current were recorded using a multimeter and confirmed with I-V curve measurements using a Keithley 2400 source meter unit. The Seebeck coefficient of the TE material is calculated as follows: $\alpha = V/\Delta T$, where V indicates voltage produced by the Seebeck effect and ΔT is the temperature gradient. As reproducibility and stability of TE performance is an important concern for any nanostructured thermoelectric materials, we measured the voltages of Bi_2Te_3 and Sb_2Te_3 samples from different deposition batches in three consecutive evaluations. The detailed statistical analysis indicated a standard deviation for the device performance of less than 5%. The power factor (PF), which determines the performance of the TE device, was calculated using the following equation: $PF = \sigma\alpha^2$. The output power densities were calculated with total cross-sectional areas of TE legs with and without load resistances (R_L).

3.4.5 Electrical properties measurement

Electrical resistivity was measured using the four-probe technique on thin films. This simple apparatus is composed of four tips, which are at equal distance from each other (1 mm). The

determination of sheet resistance is possible thanks to the injection of current through two outer probes and by measuring the voltage through the inner probes. The sheet resistance is given by the formula $\rho_{\square} = \frac{\pi}{ln(2)}\frac{V}{I}$, where V and I are, respectively, the measured voltage and the injected current. The measurement of bulk resistivity is given as follows: $\rho = \frac{\pi}{ln(2)} t \frac{V}{I}$, where the film thickness t is measured using a profilometer. The Hall effect measurements of TE legs were performed using a homemade setup based on van der Pauw configurations (Figure A I-5(a)) to obtain carrier concentrations (n). The Hall effect measurements were performed at RT and under different currents and magnetic fields.

Acknowledgement

S.G.C. and R.N. acknowledge the NSERC Discovery Program. R.N. is also supported by NSERC Strategic programs. S.G.C. also acknowledges the Canada Research Chair program for support. The authors are grateful to MPB Inc. for their fruitful discussions.

CHAPTER 4

HIGH PERFORMANCE $BiFeO_3$ FERROELECTRIC NANOSTRUCTURED PHOTOCATHODES

Shyamashis Das[1,2,*] , Paul Fourmont[3,*] , Daniele Benetti[2] , Sylvain G. Cloutier[3] , Riad Nechache[2] , Zhiming M. Wang[1] , Federico Rosei[2]

[1] Institute of Fundamental and Frontier Sciences, University of Electronic Science and Technology of China, Chengdu 610054, China
[2] Centre Énergie Matériaux et Télécommuniactions, Institut National de la Recherche Scientifique, 1650 Boul. Lionel Boulet, Varennes, Québec J3X 1S2, Canada
[3] Department of Electrical Engineering, Ecole de Technologie Supérieure, 1100 Notre Dame West, Montreal, Quebec, Canada
[*] *These authors contributed equally to this work.*

Reproduced from Shyamashis Das et al., High performance $BiFeO_3$ ferroelectric nanostructured photocathodes, J. Chem. Phys. 153, 084705 (2020); https://doi.org/10.1063/5.0013192; with the permission of AIP Publishing.

Abstract: Ferroelectric materials may be used as effective photoelectrocatalysts for water splitting due to enhanced charge carrier separation driven by their spontaneous polarization induced internal electric field. Compared to other ferroelectric materials, $BiFeO_3$ (BFO) exhibits a high catalytic efficiency due to its comparatively smaller bandgap which enables light absorption from a large part of the solar spectrum and its higher bulk ferroelectric polarization. Here we compare the photoelectrochemical properties of three different BFO morphologies, namely nanofibers, nanowebs and thin films synthesized via electrospinning, directly on FTO coated glass substrates. A significant photocathodic current in the range from -86.2 to -56.5 $\mu A\ cm^{-2}$ at -0.4 V bias (vs Ag/AgCl) has been recorded for all three morphologies in 0.1 M Na_2SO_4 aqueous solution (pH = 6.8). Among these morphologies, BFO nanofibers exhibit higher efficiency because of their larger surface area and improved charge separation resulting from rapid diffusion of photoinduced charge carriers along the axis of the nanofiber. In the case of BFO nanofibers, we obtained the highest photocurrent density of -86.2 $\mu A\ cm^{-2}$ at -0.4 V bias (vs Ag/AgCl electrode) and an onset potential of 0.22 V. We also observed that the

onset potential of the photocathodic current can be increased by applying a positive polarization voltage, which leads to favorable bending of band edges at the electrode/electrolyte interface resulting in increased charge carrier separation.

4.1 Introduction

Efficient storage of solar energy is a promising and sustainable approach to address the energy challenge, caused by the limited supply of fossil fuels. A photoelectrochemical (PEC) cell permits direct conversion of an inexhaustible and clean solar energy into chemical energy by splitting water on the surface of a semiconductor photoelectrode. The electrochemical photolysis of water was first reported by Fujishima and Honda in 1972, using a semiconducting TiO_2 electrode. Fujishima & Honda (1972) In short, when a semiconductor electrode is placed in contact with an electrolyte, a charge redistribution takes place at the interface to generate a space-charge layer. Gerischer (1966) Illumination of the electrode with sunlight leads to light absorption and separation of photoexcited charge carriers by the electric field which is built-in within this layer. Photo-generated carriers then participate in oxidation and reduction reactions to decompose water into oxygen and hydrogen. Grätzel (2001)

The separation and transport of photoexcited charge carriers are more effective when there is an internal electric field in the semiconducting photocatalyst in addition to the electric field due to the interfacial space-charge layer. Yu & Wang (2018) The internal dipolar electric field of a semiconducting ferroelectric material can help achieve this purpose. Ferroelectric oxides featuring a low band gap are promising for harvesting solar energy. Grinberg, West, Torres, Gou, Stein, Wu, Chen, Gallo, Akbashev, Davies et al. (2013); Nechache *et al.* (2015); Das, Ghara, Mahadevan, Sundaresan, Gopalakrishnan & Sarma (2018) PEC oxidation and reduction have been shown to occur at negatively/positively polarized domains of ferroelectric materials. Nasby & Quinn (1976); Giocondi & Rohrer (2001) Thus, the same electrode can be used either as photoanode or as photocathode depending on the orientation of the internal electric field on the surface of the material. Moreover, by applying an external electric field one can simply switch the direction of ferroelectric polarization on the surface, allowing to achieve

preferential oxidation or reduction by a ferroelectric photoelectrode. Marshall, Malashevich, Disa, Han, Chen, Zhu, Ismail-Beigi, Walker & Ahn (2014) Different ferroelectric materials, for example $BaTiO_3$, Li, Zhang, Han, Cao, Duan & Zeng (2018); Vonrüti & Aschauer (2020) $BiFeO_3$ (BFO), Ji, Yao, Lim, Liang & Suwardi (2013); Li *et al.* (2013); Cao, Wang, Wen, Mi & Lei (2014); Liu *et al.* (2016); Zhang, Huang, Jin, Rosei, Vetrone & Claverie (2017a); Gu, Zhou, Zheng, Fang, Dong & Shen (2017a); Zhang, Li, Chu, Rong, Xiao & Zhang (2016a); Lee, Joo, Yoon, Lee, Lee, Choi, Park & Choi (2017) Bi_2FeCrO_6, Li, AlOtaibi, Huang, Mi, Serpone, Nechache & Rosei (2015); Huang, Harnagea, Tong, Benetti, Sun, Chaker, Rosei & Nechache (2019) $BiMnO_3$, Chakrabartty, Barba, Jin, Benetti, Rosei & Nechache (2017) $KNbO_3$, Li, Zhang, Zhang, Huang, Harnagea, Nechache, Zhu, Zhang, Lin, Ni et al. (2017); Yu, Liu, Zhang, Li, Zhao, Zhu, Liu, Lin, Liu & Zhang (2019) $NaNbO_3$ Singh & Khare (2017) and PZT Wang, Cao, Wen, Xu, Obergfell, Mi, Zhan, Nasori, Demsar & Lei (2016c) either in the form of thin film or as nanostructures have been used to fabricate electrodes for PEC cells. BFO is recognized as a promising material for visible-light driven photoelectrocatalysis of water thanks to its high ferroelectric polarization ($\sim$150 $\mu C\ cm^{-2}$), small band-gap (2.0-2.7 eV), good chemical stability, high resistance to photocorrosion and non-toxicity. Chen, Chen, Pei, Lu, Zhang, Zhang & He (2019)

Thin films and nanostructures of BFO with different morphologies have been found to be efficient for PEC water splitting. Ji *et al.* (2013); Li *et al.* (2013); Cao *et al.* (2014); Liu *et al.* (2016); Zhang *et al.* (2017a); Gu *et al.* (2017a); Zhang *et al.* (2016a); Lee *et al.* (2017) Among these, one-dimensional (1D) nanostructures, such as nanofibers, nanotubes and nanobelts are considered particularly promising. Li *et al.* (2013); Lee *et al.* (2017) The reduced radial dimension and large surface-to-volume ratio of 1D nanostructures promote rapid diffusion of photogenerated charge carriers to surfaces before recombination can occur, thereby increasing charge separation efficiency. Hochbaum & Yang (2010) In addition, ballistic charge transport along the axis of a single crystalline nanofiber is more efficient than diffusive transport in a polycrystalline film. Poncharal, Berger, Yi, Wang & de Heer (2002); De Picciotto, Pfeiffer, Baldwin & West (2004) Many techniques are available to synthesize such structures, such

as pulsed laser ablation, Huang, Chang, Van, Liu, Tsai, Chen, Kuo, Tzeng, Chen, Wu et al. (2016) magnetron sputtering, Ji *et al.* (2013) electrodeposition, Radmilovic, Smart, Ping & Choi (2020) chemical vapour deposition Moniz, Quesada-Cabrera, Blackman, Tang, Southern, Weaver & Carmalt (2014) or electrospinning. Zhang, Shen, Qiu, Liu, Xiong, Shi & Wei (2017b); Queraltó & Mathur (2018) The latter is a very promising deposition method because of its low-cost, reliability, ease of scale-up and precise control over material morphology. Xue, Wu, Dai & Xia (2019) A high level of control is crucial to ensure good material adhesion to the substrate and maintain the integrity of the electrode. This approach also allows to avoid any contamination from the photocatalyst to the electrolyte. Yang, Liu, Wei, Pan, Xiong & Shi (2014)

Here we report the relative photoelectrocatalytic efficiency of three different morphologies of BFO electrospun on FTO coated glass substrates. We developed a reproducible approach to control BFO morphology, from nanofibers to thin films using electrospinning. By carefully setting the ambient relative humidity at 40% during the deposition, we found that 5 minutes deposition yields NFs. As the deposition time increases from 10 to 15 minutes, the morphology first changes to a nanoweb (NWB) and then to a thin film. The BFO nanostructures show photocathodic behavior in PEC water splitting experiments.

While ferroelectric materials have been widely used to fabricate highly efficient photoanodes, Ji *et al.* (2013); Li *et al.* (2017); Radmilovic *et al.* (2020); Rioult, Datta, Stanescu, Stanescu, Belkhou, Maccherozzi, Magnan & Barbier (2015) there are few reports on ferroelectric photocathodes. Gu *et al.* (2017a); Li *et al.* (2015) In a PEC cell a photocathode leads to hydrogen generation because electron transfer is favorable at the electrode/electrolyte interface, due to favorable band bending at the photocathode's conduction band edge. There has recently been a growing interest to identify and investigate cost-effective p-type oxide-based photocathode materials with small band gap suitable for visible light absorption, which exhibit efficient charge transfer to the electrode/electrolyte interface, and are chemically stable under illumination. Kang, Hill, Park & Choi (2016); Wheeler & Choi (2018); Jiang, Reyes-Lillo, Liang, Liu, Liu, Toma, Prendergast, Sharp & Cooper (2019) In that respect, a robust ferroelectric low band gap oxide

like BFO is an ideal photocathodic material. Here, we demonstrate that PEC water splitting can be achieved by employing BFO nanostructures as photocathode near neutral pH. This work provides insights for the future development of efficient photocathodes for PEC water splitting.

4.2 Results and discussions

X-ray diffraction (XRD) patterns of the BFO nanostructures deposited on FTO-coated glass substrates were used to determine the crystal quality and identify the crystallographic phase. Figure 4.1 (a) displays the XRD patterns of BFO nanostructures of all three morphologies. Peaks attributed to the FTO substrate are marked with diamond symbols. Compared with the diffraction pattern of standard bulk BFO we infer that the as prepared samples exist in the rhombohedral crystallographic phase.

Diffracted beams are most intense for the thin film morphology where the thickness of the deposited film is highest. However, even the NF morphology shows clearly distinguishable peaks, suggesting good crystallinity. Moreover, no impurity peak is observed in the XRD patterns, indicating the absence of any secondary phase such as $Bi_2Fe_4O_9$ or Bi_2O_3 in these samples. Figure 4.1(b) shows the UV-Vis absorption spectra for all three BFO nanostructures measured in reflectance mode. The intensity of light absorption increases with surface coverage of the samples on the FTO substrate (from NF to thin film morphology). However, the absorption onset remains the same for all three samples. We determined the optical band-gap of our BFO samples as 2.26 eV from the Kubelka-Munk plot ($(\alpha E)^2$ vs photon energy) of thin film sample (cf. the inset of Figure 4.1b). The extrapolated tangent line in the Kubelka-Munk plot intersects the horizontal line at $\alpha = 0$ at 2.26 eV. This optical band-gap is in agreement with previously reported values of BFO nanostructures. Radmilovic *et al.* (2020)

A qualitative investigation of the different morphologies of BFO nanostructures was performed by SEM imaging. To obtain these morphologies, the ambient relative humidity must be precisely controlled during electrospinning. While the relative humidity is often overlooked, this parameter is particularly important as it greatly influences solvent evaporation. Figures 4.2(a-c) show

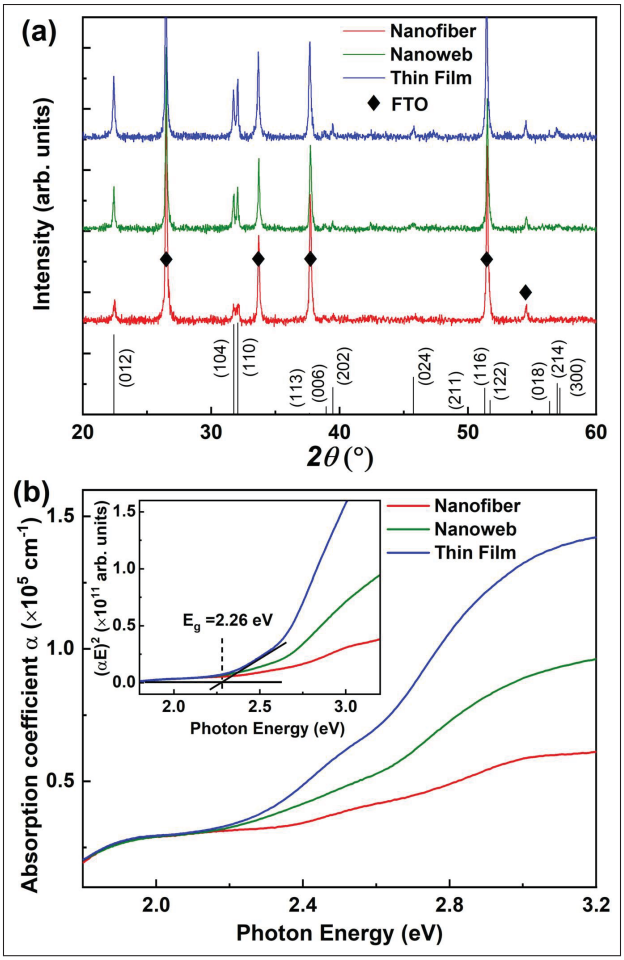

Figure 4.1 (a) X-ray diffraction pattern of three different morphologies of $BiFeO_3$. The standard diffraction pattern of rhombohedral phase of $BiFeO_3$ is also shown for comparison. Peaks obtained due to diffraction from the FTO substrate are labelled with diamonds. (b) Optical absorption spectra of $BiFeO_3$ nanostructures in UV-Vis range. The inset shows the Kubelka-Munk plot for the estimation of optical band-gap

SEM images of the three different morphologies of as-prepared BFO. The corresponding SEM images at higher magnification are shown in figures 4.2(d-f). Figure 4.2(d) shows that the NF morphology appears flattened. This occurrence is due to the presence of residual solvent when

the NF is adsorbed on the substrate. In this case, the wetted NF "collapses" on the FTO surface, leading to such morphology. Using the same electrospinning parameters with a relative humidity of 35%, well defined and distributed NFs are forming as shown in Figure A II-2. NF and NWB morphologies can be distinguished from Figures 4.2(d,e), respectively where the positions of BFO nanostructures and FTO substrates are marked. The synthesis of NWBs is promoted by additional deposition of BFO NFs on the substrate. The thin film sample covers almost the entire substrate and hence FTO is not visible in the image (Figure 4.2(f)). Further electrospinning of BFO NFs, i.e. 15 *min*, thin films are obtained. BFO NFs are several micrometers in length and the radial dimension of BFO NFs is in the 200 – 400 *nm* range. In the case of NWB, several NFs merge and cover a larger portion of the FTO substrate. The thin film morphology is essentially a continuous film of thickness approximately 150 *nm* as seen in the cross-sectional SEM image (Figure A II-3).

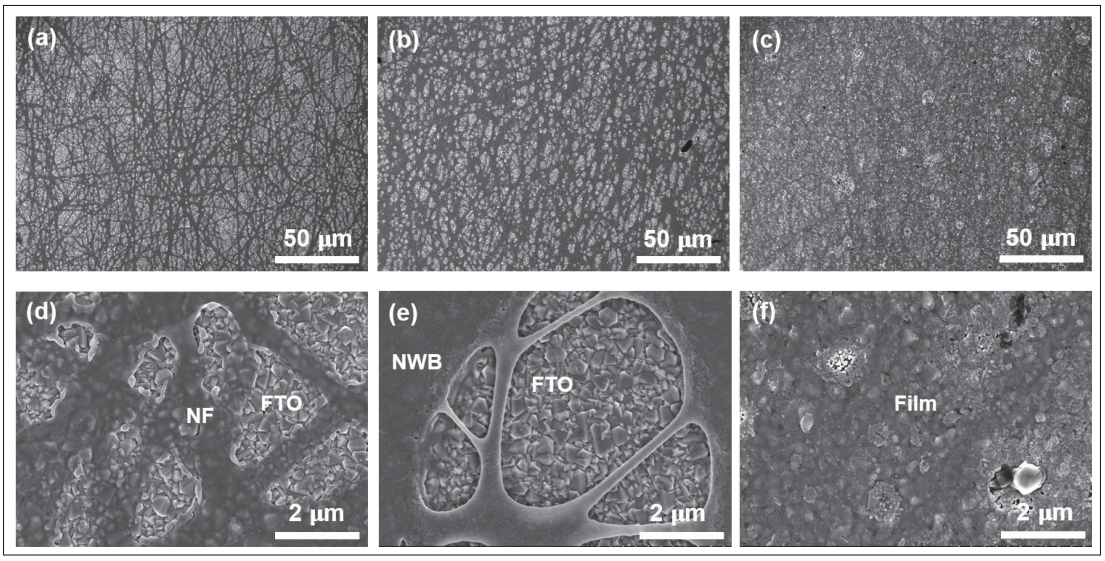

Figure 4.2 SEM images of three different morphologies of $BiFeO_3$ - (a) nanofiber (NF), (b) nanoweb (NWB) and (c) thin film. Higher magnification images corresponding to (a)-(c) are shown in images (d)-(f) where positions of nanostructures on FTO substrates are marked

We further characterized the morphology of BFO NFs by imaging with atomic force microscopy (AFM). Figures 4.3(a,b) show AFM topography images of a $10 \times 10\ \mu m^2$ region and a $2 \times 2\ \mu m^2$ region of BFO NFs, respectively. Interconnected branches of NFs are visible in Figure 4.3(a),

which is consistent with SEM images (Figure 4.2(d)). In higher magnification AFM topography images (Figure 4.3(b)), individual crystallographic grains of the nanofibers are visible. The electrical polarization due to the piezoelectric effect of the BFO NFs was recorded using PFM. Figure 4.3(c) displays a PFM image of the same area of which AFM topography is depicted in Figure 4.3(b). High piezoresponse along with bright and dark contrasts only from the region where the NF is lying suggest a significant piezoelectric polarization randomly oriented on the surface. As illustrated in the AFM and PFM images, the size and shape of individual grains (figures 4.3(b,c), respectively) are quite similar. High bright and dark contrast in the PFM image (Figure 4.3(c)) indicate that the piezoresponse signals measured from different grains are different in magnitude.

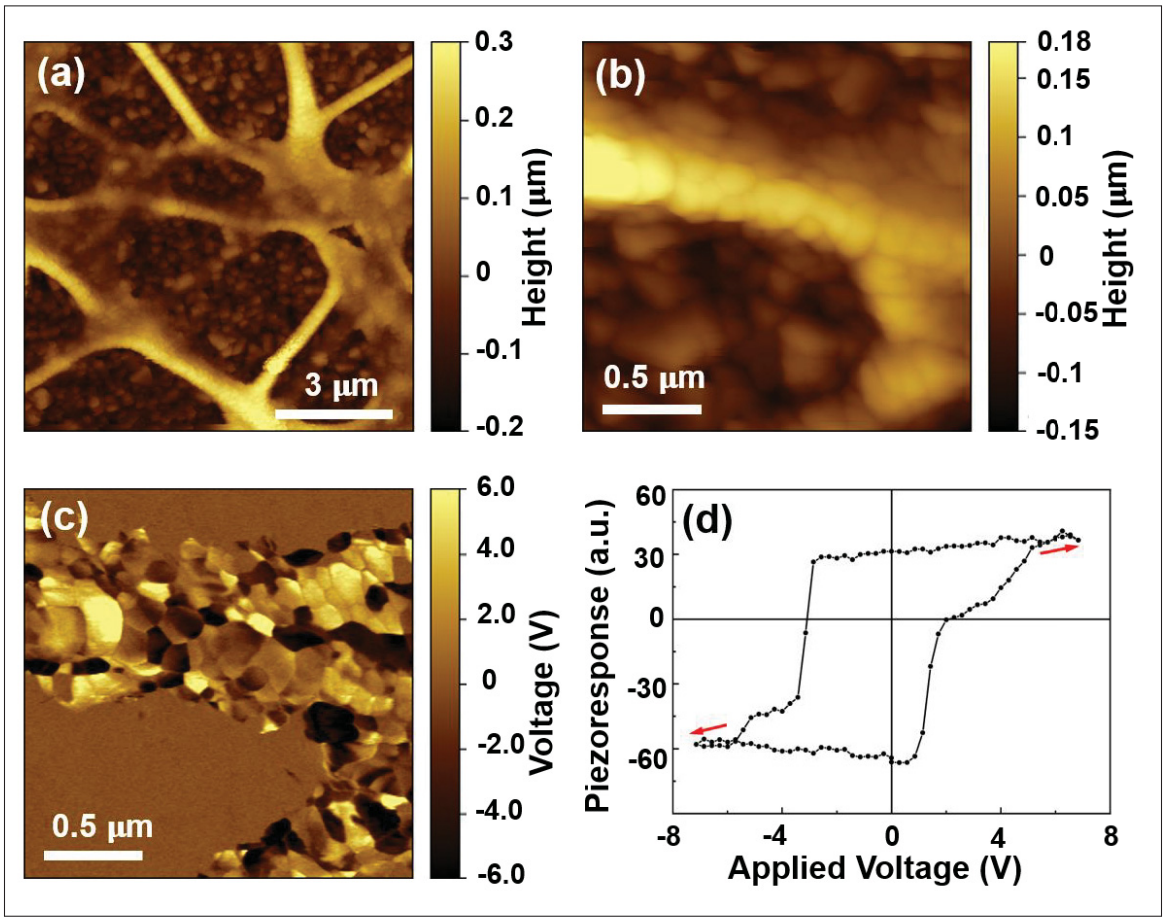

Figure 4.3 AFM topography images of $BiFeO_3$ nanofibers of (a) a $10 \times 10\ \mu m^2$ region and (b) a $2 \times 2\ \mu m^2$ region, (c) PFM image of the same region corresponding to (b), (d) local piezoresponse hysteresis loop of this $BiFeO_3$ nanofibers

The high electrical polarization of these BFO NFs is expected to efficiently separate photoexcited charge carriers, rendering it a suitable photoelectrode material. The ferroelectric behavior of the BFO NFs yields the infield hysteresis loop (Figure 4.3(d)), which was recorded from regions of high contrast difference in the PFM image. Such a clear hysteresis loop recorded by placing the AFM tip on a high-contrast region of the PFM image confirms the presence of local ferroelectric behavior of the NFs. We also measured the piezoresponse and characterized the local ferroelectric properties of NWB and thin film morphologies. The corresponding results are shown in Figure A II-4. Both morphologies show significant piezoresponse and exhibit local hysteresis loops, confirming the ferroelectric behavior in such BFO morphologies.

We performed PEC experiments using all three BFO nanostructures deposited on FTO as photoelectrodes. A schematic of the experimental setup for PEC measurements is shown in Figure A II-1. Figures 4.4(a-c) show linear sweep voltammetry (LSV) curves (J–V) for BFO NFs, NWBs and thin film photoelectrodes, respectively in dark, in continuous and in chopped simulated solar illumination. Chopped illumination was used to compare the dark current and photocurrent in a single scan. The results clearly indicate the presence of a transient photocurrent immediately after photoexcitation. We find a negative photocurrent for all three electrodes, which is consistent with photocathodic properties. Li *et al.* (2015) However, this behavior is strongly dependent on the morphology of the BFO nanostructures. At -0.4 V (vs Ag/AgCl electrode) the recorded photocurrent densities (J_{ph}) for NFs, NWBs and thin film photocathodes are -86.2, -64.9 and -56.5 $\mu A\ cm^{-2}$, respectively. The higher photocurrent density for the BFO NFs photocathode compared to the NWBs and thin film photocathode is a consequence of the larger surface area, better charge extraction and transport in the case of NF morphology. Additionally, as the density of BFO nanostructures increases and their morphology changes from NFs to NWBs and then to thin film, the extent of recombination of charge carriers becomes higher and consequently reduces the PEC activity of the corresponding nanostructures. The onset potential (V_{OP}) of the photocathodic current is also higher for NFs than NWB and thin film photocathode. V_{OP} has been found to be 0.22 V for the BFO NFs, while the value is 0.19 V and 0.15 V for NWB and thin film, respectively. Both the photocurrent density and the onset potential of our

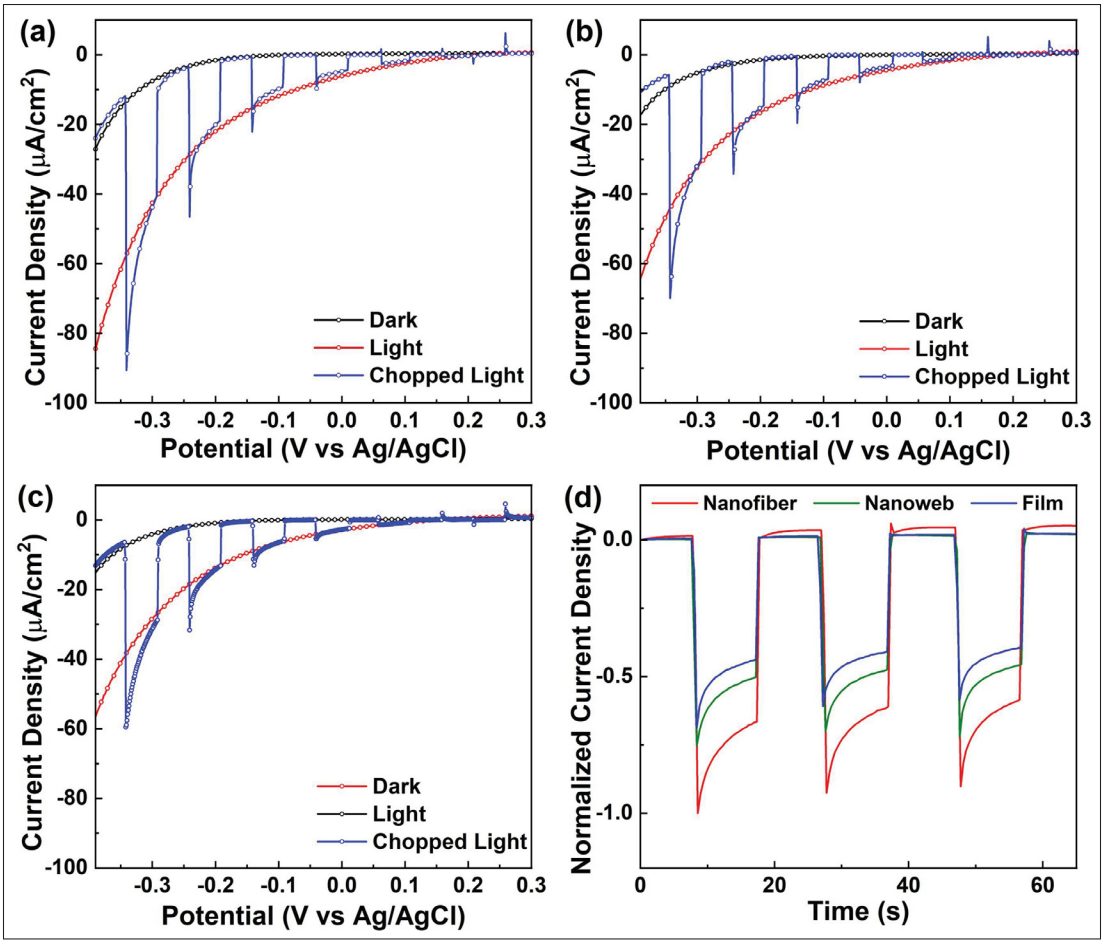

Figure 4.4 Linear sweep voltammetry plots recorded in the photoelectrocatalysis experiment in dark (black), upon illumination with continuous (red) and chopped (blue) simulated sunlight with three different morphologies of $BiFeO_3$ nanostructures - (a) $BiFeO_3$ nanofibers, (b) $BiFeO_3$ nanoweb and (c) $BiFeO_3$ thin film as photoelectrode. (d) Normalized chronoamperometry (*J-t*) plots of $BiFeO_3$ nanostructure of three different morphologies at 0.4 *V* (vs Ag/AgCl electrode)

BFO photocathodes are comparable to previous reports of photocathodes made of BFO thin films. Liu *et al.* (2016); Gu *et al.* (2017a) Figure 4.4(d) displays normalized chronoamperometric (*J-t*) curves recorded at -0.4 *V* (vs Ag/AgCl electrode) for the three different BFO nanostructures used as photocathode. All three curves are normalized with respect to the maximum recorded current density of BFO NFs to compare the relative magnitude of the photocurrent density obtained from different nanostructures. The photocurrent appears instantly after switching on the light, then decreases to reach a steady equilibrium state. Like LSV curves, we also find that

the photocurrent is decreasing when going from NFs to NWBs to thin film morphology. Based on this analysis we infer that NFs are a more suitable morphology than NWB and thin films to carry out PEC hydrogen generation, thanks to its larger surface area and better charge extraction. The NF morphology is also a cost-effective alternative for large-scale applications, due to the small precursor quantity needed to achieve the desired functional nanostructures. To prepare NFs only a few hundreds of micrograms of BFO need to be deposited on each substrate, thereby limiting waste. These nanostructured photoelectrodes are suitable for PEC water splitting even for longer durations. Chronoamperometric data (Figure A II-5) indicates that after an initial decrease, the photocurrent tends to stabilize, retaining 50-60% of the initial photocurrent density after 1 hr of PEC water splitting.

To understand the improved performance of the BFO nanofibers compared to the other morphologies, the charge transfer resistance (R_{CT}) was extrapolated from electrochemical impedance spectroscopy (EIS) measurements. Nyquist plots of the three photocathodes are shown in Figure A II-6 along with their fit. The equivalent circuit used to model these data is shown in the inset of Figure A II-6. Analogous models have been already used for similar materials. Hernández, Hidalgo, Sacco, Chiodoni, Lamberti, Cauda, Tresso & Saracco (2015); Qi, Wolfe, Fichou & Chen (2016); Shi, Benetti, Li, Wei & Rosei (2020) A low R_{CT} value indicates an improved charge transfer for the photoelectrode. By fitting the data, we find that the normalized RCT value for NF is 170 $\Omega\ cm^2$, while for the NWB and thin film morphologies values of 241 $\Omega\ cm^2$ and 9.2 $k\Omega\ cm^2$ are obtained respectively. These values support the hypothesis of an improved charge transfer mechanism in the NF morphology, allowing the generation of higher photocurrents when used as a photocathode.

To calculate the applied-bias-photon-to-current efficiency (ABPE) we recorded J-V curves of BFO NFs (Figure A II-7(a)) in a two-electrode configuration. The ABPE was calculated using the following equation: Chen *et al.* (2011); Cho, Chen, Forman, Kim, Rao, Jaramillo & Zheng (2011)

$$ABPE = \frac{J_{ph}\left[mA \cdot cm^{-2}\right] \times (1.23 - V_b)\,[V]}{P_{Total}\left[mW \cdot cm^{-2}\right]} \tag{4.1}$$

where J_{ph} is the photocurrent density obtained under an applied bias V_b between the working electrode (BFO NFs deposited on FTO) and the counter electrode (Pt). P_{Total} is the intensity of the incident solar light. Figure A II-7(b) shows the calculated ABPE as a function of external potential (V vs Pt). Because of the photocathodic behavior the magnitude of ABPE decreases with the increase of the external potential. We recorded an ABPE of 0.014% for BFO NFs at 0 V. Though the magnitude of ABPE is not high. However, compared with the dark current we found a significant photoconversion by the BFO nanofiber photocathode.

To study the effect of the ferroelectric polarization on the PEC activity of our BFO NFs, we first poled the sample macroscopically and then performed PEC measurements with the polarized sample. A positive and negative external potential applied on the BFO photocathode is defined as positive and negative poling, respectively. For poling, 10 pulses of +4 V or -4 V with an alternating 0.1 sec on time and 1 sec off time were applied between the FTO and Ag/AgCl reference electrode immersed in the electrolyte. Figure 4.5(a) shows $J - V$ curves of the BFO NFs before poling whereas figures 4.5(b,c) show $J - V$ curves after +4 V and -4 V poling, respectively. The onset potential (V_{OP}), defined as the intersection of the dark current and the photocurrent, is found to be dependent on the polarization direction. Before applying any polarizing potential, we find V_{OP}= 0.22 V which increases to 0.25 V when positive poling is applied and decreases to 0.18 V when the poling direction is reversed. A large external poling voltage can induce a significant change in the band structure at the BFO/electrolyte interface. To illustrate this aspect, qualitative diagrams of the band structure before and after poling (in the presence of positive and negative potentials) are shown in figures 4.5(d-f). A poling potential, particularly when it is larger than the coercive field of BFO will reorient the distribution of ferroelectric domains and change the magnitude of the internal polarization field. Choi, Lee, Choi, Kiryukhin & Cheong (2009); Yi, Choi, Choi, Oh & Cheong (2011) A positive poling strengthens the depolarization field in BFO pointing from the direction of the electrolyte to

FTO (Figure 4.5(e)). As a result, downward band-bending at the BFO/electrolyte interface is further enhanced (Figure 4.5(e)) compared to band-bending before applying any poling potential (Figure 4.5(d)).

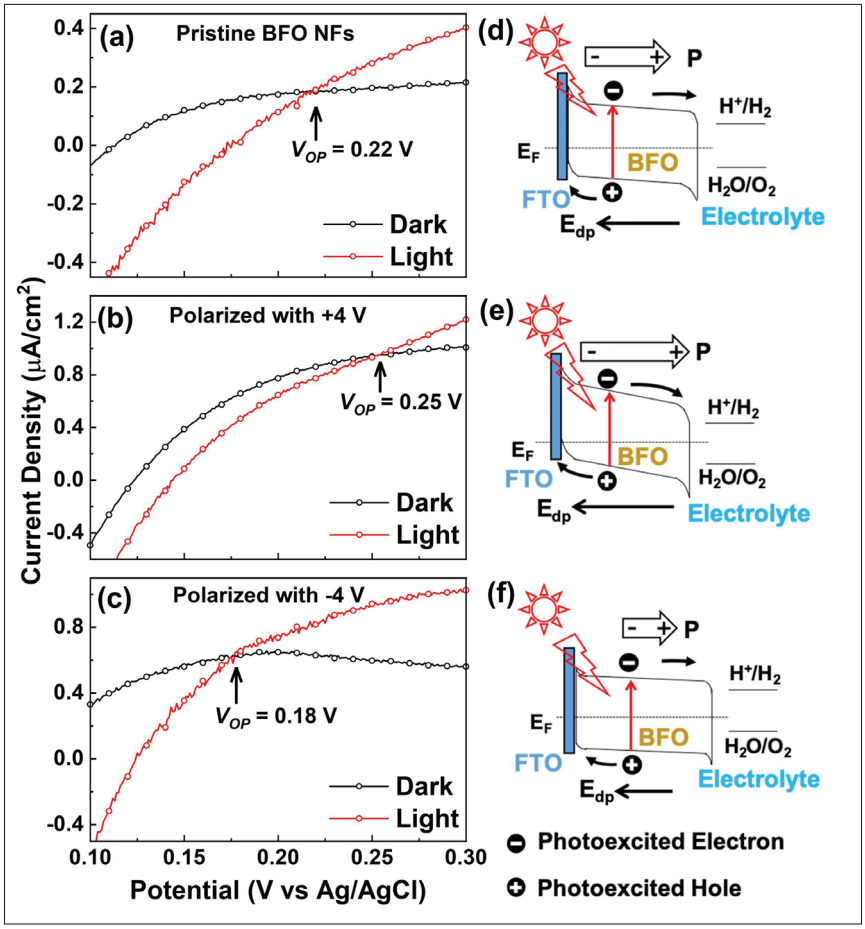

Figure 4.5 Linear sweep voltammetry (a) before poling and after (b) positively and (c) negatively poling $BiFeO_3$ nanofibers. Schematic of energy band diagrams corresponding to the cases (a)-(c) are shown in (d)-(f)

Such an enhanced downward band-bending facilitates transport of the photogenerated electrons to the surface of BFO. On the other hand, upward band-bending at the FTO/BFO interface drives the photo-generated holes toward the FTO and reduces the possibility of electron-hole recombination. Thus, a positive poling increases the onset potential of the photocathodic current and improves the PEC activity of BFO. In contrast, a negative poling weakens the depolarization

field and reduces downward band bending at the BFO/electrolyte interface (Figure 4.5(f)). This results in a decrease in the extent of electron-hole separation and a reduced onset potential of the photocathodic current in the PEC water splitting experiment.

4.3 Conclusion

In summary, we report a systematic study of the PEC properties of three different morphologies of BFO nanostructures produced using electrospinnng. The ferroelectric polarization of BFO and larger surface area of the nanoscale morphologies enable efficient PEC hydrogen generation at almost neutral condition (pH = 6.8). In our experiments we recorded a negative photocurrent which indicates cathodic behavior of our BFO nanostructures. We found magnitude of photocurrent is strongly dependent on morphology of nanostructures. In comparison to the other morphologies, BFO NFs exhibit higher photocurrents when implemented as photocathode for water splitting measurement. This is explained by an improved charge transfer mechanism in the BFO NFs as confirmed by EIS analysis. The ferroelectric properties of BFO allow to tune the material's polarization direction by applying an external electric field which in turn leads to a tunable onset potential of cathodic photocurrent. This facile all solution-based deposition technique will pave the way toward fabrication of better photocathodes for hydrogen generation.

4.4 Experimental methods

4.4.1 Electrode preparation

All chemicals were used as received, without further purification. The precursor solution was prepared by weighing and dissolving 1.9095 *gr* of bismuth nitrate ($Bi(NO_3)_3{\cdot}5H_2O$) and 1.5904 *gr* iron nitrate ($Fe(NO_3)_3{\cdot}9H_2O$) into 4.5 *gr* of DMF (N,N- Dimethylformamide). The ratio was kept equimolar between iron and bismuth nitrates. Then, 10 wt% of PVP (Polyvinylpyrrolidone) with an approximate molecular weight of 1,300,000 was added to increase the viscosity of the solution. Magnetic stirring was performed for 24 *hr* to obtain a homogenous mix. This solution was loaded into a 6 *ml* plastic syringe, then placed in an infusion pump at a constant flow rate

of 0.18 $ml\ h^{-1}$. A 12 kV electric field was applied between the needle and the collector while keeping a distance of 10 cm between the two. FTO substrates were placed in a rotative collector, with the rotation speed set at 1000 rpm. To control the morphology of BFO nanostructures, the relative humidity was kept at 40%. Changing this parameter affects solvent evaporation and leads to thin film morphology after few minutes of deposition. The collected material was finally heated at 250 $°C$ for 15 min to allow solvent evaporation and then at 520 $°C$ for 2 hr in ambient conditions to achieve crystallization.

4.4.2 Materials characterization

Crystalline quality and phase purity of the prepared BFO electrodes were characterized using X-ray diffraction (XRD; D8 Advance, Bruker, Ni-filtered Cu Kα radiation). Optical absorption spectra were recorded in reflectance mode using an integrating sphere to collect all reflected light in a UV-VIS-NIR spectrophotometer (Perkin Elmer, Lambda 750). The surface morphology of BFO nanostructures deposited on FTO was recorded using scanning electron microscopy (SEM; Hitachi, SU8230). The corresponding topography of the electrode's surface was characterized by atomic force microscopy (AFM, Veeco Enviroscope). An atomically sharp titanium nitride tip from Bruker was used to record AFM images. Piezoresponse force microscopy (PFM) implemented in the same AFM instrument was used to study the ferroelectric properties of the films. Nechache *et al.* (2011); Nechache, Huang, Li & Rosei (2016); Huang, Harnagea, Benetti, Chaker, Rosei & Nechache (2017); Chakrabartty, Harnagea, Celikin, Rosei & Nechache (2018) BFO nanostructure induced piezoelectric vibrations were detected using a lock-in amplifier from Signal Recovery (model 7265). Estimations of surface coverage of each of the electrodes were obtained by analyzing scanning electron microscopy (SEM) images. Image segmentation was performed using the Dragonfly software (ORS, Montreal, Canada). For each BFO morphology, several micrographs were acquired and analyzed to obtain an average estimation of the surface coverage.

4.4.3 Photoelectrochemical measurements

All photoelectrochemical measurements were conducted using an electrochemical workstation (Gamry Interface 1000 E Potentiostat) in a three-electrode system using BFO nanostructures deposited on FTO as working electrode, a Pt plate as counter electrode, and standard Ag/AgCl as reference electrode. BFO nanostructures on FTO were partly covered by an insulating coating to expose only a small area to the electrolyte for electrochemical reaction. The typical exposed area of the BFO electrode was $\sim 1\ cm^{-2}$. The electrochemical reaction was carried out in a glass cell fitted with a quartz window through which the sample was illuminated (see Figure A II-1 in Supplementary Material). To this end, the working electrode was illuminated by filtering light from a xenon lamp through an AM 1.5 G filter. The light intensity was calibrated to 100 $mW\ cm^{-2}$ (1 sun) using a radiometer. 0.1 M Na_2SO_4 aqueous solution was employed as electrolyte (pH = 6.8). Linear sweep voltammograms were recorded at a scan rate of 20 $mW\ s^{-1}$. Photocurrent density measurements of the photoelectrode as a function of time ($J - t$) with on and off cycles were carried out at a fixed bias of -0.4 V vs. Ag/AgCl. Electrochemical impedance spectroscopy (EIS) was carried out under light (1 Sun) by using a Gamry 1000E station at open circuit potential (OCP) and a sweep in frequency from 300 kHz to 0.3 kHz. All impedance measurements were fitted with an appropriate equivalent circuit using Z-View software (v3.5, Scribner Associate, Inc.).

Acknowledgement

S.D. acknowledges funding from the China Postdoctoral Science Foundation. S.D. also acknowledges Institut National de la Recherche Scientifique for partial salary support. Z.M.W. acknowledges the National Key Research and Development Program of China (2019YFB2203400), the “111 Project” (B20030) and the UESTC Shared Research Facilities of Electromagnetic Wave and Matter Interaction (Y0301901290100201). Z.M.W. is also grateful to the University Kebangsaan Malaysia for a distinguished international Professor appointment. F.R. is grateful to the Canada Research Chairs program for funding and partial salary support. The authors thank Dr. Catalin Harnagea for useful discussions related to PFM measurements.

4.5 Additionnal studies

Further work is currently being done to improve the photoelectrochemical properties of the BFO nanofibers. Preliminary results show an improvement of the photocurrent by decorating the nanofibers with gold nanoparticles in figures 4.6(a-b).

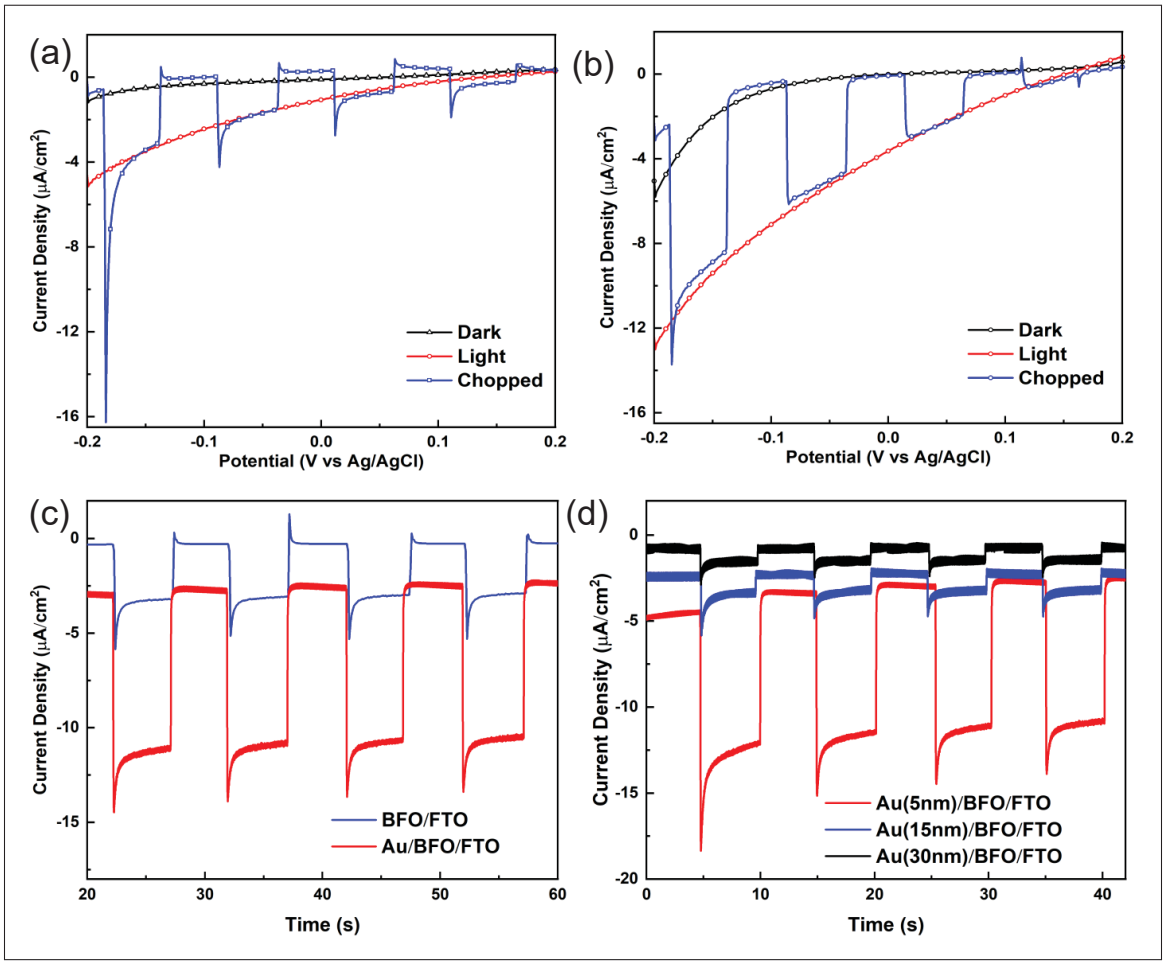

Figure 4.6 Linear sweep voltammetry plots recorded in the photoelectrocatalysis experiment in dark (black), upon illumination with continuous (red) and chopped (blue) simulated sunlight with (a) pure $BiFeO_3$ NFs electrode and (b) Au (5 *nm*)/$BiFeO_3$ NFs composite electrode. (c) Chronoamperometry (*J-t*) plots of $BiFeO_3$ nanostructure of pure $BiFeO_3$ (blue) and Au NPs (5 *nm*) deposited $BiFeO_3$ electrodes at -0.2 *V* (vs Ag/AgCl electrode).(d) Chronoamperometry plots recorded at -0.2 *V* (vs Ag/AgCl) bias showing comparison of photocurrents from 5 *nm*, 15 *nm* and 30 *nm* gold nanoparticles decorated $BiFeO_3$ photocathodes

Choronoamperometry plots in Figure 4.6(c) show that gold nanoparticles can enhance the photocurrent from -6 $\mu A\ cm^{-2}$ for pristine BFO nanofibers to -14 $\mu A\ cm^{-2}$ for 5 *nm* gold decorated BFO nanofibers at -0.2 *V* (vs Ag/AgCl). We also check the influence of different sizes of gold nanoparticles (5 *nm*, 15 *nm*, 30 *nm*). In Figure 4.6(d), we demonstrate that the smallest gold nanoparticles give the highest photocurrent.

Overall, the same methodology presented in this article is used to deposit and crystallize the nanofibers. Functionalization of the BFO nanofibers is achieved via the immersion of the samples in an acetone solution containing 1% of 3-aminopropyltrimethoxysilane (APTMS). A high magnification SEM micrograph of the BFO nanofibers decorated with 5 *nm* gold nanoparticles is shown in Figure 4.7(a). All the gold nanoparticles are well distributed and not agglomerated. From Figure 4.7(b), a clear plasmonic effect from the gold nanoparticles is visible as more light is absorbed compared to the pristine BFO nanofibers. As mentioned in chapter 1, this effect increases light absorption and improve photoelectrochemical properties thanks to the creations of heterojunctions.

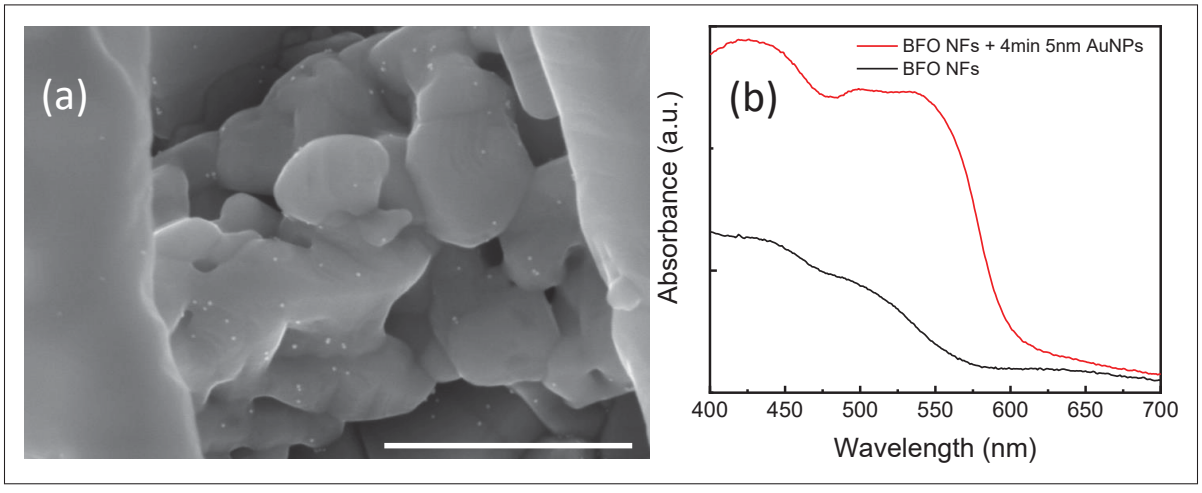

Figure 4.7 (a) SEM micrograph of the 5 *nm* gold nanoparticles decorated $BiFeO_3$ nanofibers. The scale bar is 500 *nm*. (b) UV-Vis measurements of bare and decorated $BiFeO_3$ nanofibers with a dipping time of 4 *min* in the 5 *nm* gold nanoparticles solution

CHAPTER 5

REUSABLE $BiFeO_3$ NANOFIBER-BASED MEMBRANES FOR PHOTOACTIVATED ORGANIC POLLUTANT REMOVAL WITH NEGLIGIBLE COLLOIDAL RELEASE

Paul Fourmont[1] , Riad Nechache[1] , Sylvain G. Cloutier[1]

[1] Department of Electrical Engineering, Ecole de Technologie Supérieure,
1100 Notre Dame West, Montreal, Quebec, Canada

Abstract: We report on electrospinning-assisted fabrication of highly efficient and reusable $BiFeO_3$ nanofiber-based membranes for photo-activated organic pollutant removal with negligible colloidal release. For validation purposes, we exploit a fluorescent Rhodamine B (RhB)-doped solution photo-degraded using the visible and infrared illumination ($\lambda \geqslant 400\ nm$) from a solar simulator. As such, pollutant degradation can be directly monitored in real-time. Fabrication yields an outstanding control of the fibers' morphology and metal-enhanced photocatalytic properties are achieved by coating the nanofiber membranes with few nanometers of platinum using sputtering technique. This chemical-free functionalization of the nanofibers allows a rapid and efficient RhB degradation. After optimization, 2.4 micrograms of photocatalyst achieve 93% removal after 150 *min* under solar illumination, which is impressively more efficient compared with previous reports. Most importantly, the colloidal release-free photocatalysis activity coupled to a manufacturing-ready fabrication process makes it ideal for large-scale deployment using industrial grade equipment.

5.1 Introduction

Ever since the earliest forms of life, photosynthesis plays the essential role of turning carbon dioxide into oxygen by interacting with sunlight. Such photochemical processes have been crucial for the development of more complex life forms. Falkowski, Fenchel & Delong (2008) Today, these Nature-inspired light-induced processes can also offer appealing solutions in the momentous global efforts to fight man-made pollution and climate changes. Skubi & Yoon (2014); Osterloh (2017) Indeed, the industrial effluents contribute to increasingly toxic environments

around the world. Photocatalysis appears an especially promising mitigation strategy, harvesting solar energy to destroy harmful substances via the formation of free radicals. Bhattacherjee, Sneha, Lewis-Borrell, Tau, Clark & Orr-Ewing (2019); Bi, Li, Zhang, Jin, Zhang, Zhang, Luo, Wu & Xie (2015); Wang, Shi, Xu, Qiu, Zhang, Shen, Zhao, Yu & Zhang (2020c); Johar, Afzal, Alazba & Manzoor (2015) In semiconductor-based photocatalytic cells, charge carriers are generated under illumination. These photo-generated carriers then contribute to redox reactions occurring at the surface of the cell. Due to a very short photo-generated exciton lifetime, the semiconducting photocatalysts must be in the nanometers range to minimize the exciton recombination and maximize the photocatalytic reaction. Kabra *et al.* (2004) Bandgap engineering is also of paramount importance and should be optimized to take full advantage of the broadband light absorption. Johar *et al.* (2015) However, a delicate tuning between both absorption and nanoscale feature dimensions is critical, as the latest tends to increase the bandgap through quantum confinement. Das, Khan, Varma, Mukherjee & Mandal (2013) As an important consequence of using such semiconductor nanostructures, significant cell degradation through colloidal release usually occurs during the photocatalytic reaction. Qu & Duan (2013) This can require significant additional processing to prevent water contamination by the photocatalytic material itself. Fernández-Ibáñez, Blanco, Malato & De Las Nieves (2003) Most photocatalysis cell technologies currently rely on porous nanostructured TiO_2 and ZnO films. Their relatively large bandgaps (> 3.0 eV) severely limit their efficiency by wasting the most significant part (over 90%) of the solar irradiation spectrum, which needs to be replaced with constraining, harmful and expensive UV irradiation sources. Fresno *et al.* (2014) While migrating to lower bandgap materials could rapidly yield significant gains, their photostability, biocompatibility, material and processing costs are also extremely important parameters to consider for large-scale manufacturing. Within the last two decades, some bismuth-based perovskites emerged as promising photocatalyst materials. Zhou, Xu, Chen, Kuang & Su (2018a); Kim, Hwang & Lee (2004); Yao, Xu, Wang, Zhou, Yang, Zhang, Shang & Huang (2004); Gao, Chen, Yin, Dong, Ren, Yuan, Yu, Zou & Liu (2007)

$BiFeO_3$ (or BFO) offers the advantage of being a multiferroic material, which can exhibit both ferroelectric and magnetic ordering at room temperature. Jangid *et al.* (2014) Spontaneous polarization can occur below 830 $°C$ (its Curie Temperature), and spontaneous magnetization below 370 $°C$. These relatively high temperatures make BFO a promising material candi-date for new applications in spintronics, Lee, Fina, Marti, Kim, Hesse & Alexe (2014) sensors, Yu, Wang, Hu, Cao & Chan (2009) actuators, Zeches, Rossell, Zhang, Hatt, He, Yang, Kumar, Wang, Melville, Adamo et al. (2009) water splitting Das, Fourmont, Benetti, Cloutier, Nechache, Wang & Rosei (2020); Li *et al.* (2013) or terahertz microscopy. Takahashi, Kida & Tonouchi (2006) These properties make BFO potentially interesting for photocatalytic applications, due to a lower bandgap (i.e. 2.1 to 2.7 eV), good photostability, non-toxicity and spontaneous electric field for charge-carrier separation. Morris, Pendlebury, Hong, Dunn & Durrant (2016); Haruna, Abdulkadir & Idris (2020) Since 2007, BFO nanoparticles are used as photocatalysts and show degradation efficiencies better than bulk powders. Gao *et al.* (2007); Li, Wang, Zhang, Li, Wang & Wang (2020) Even though these results can be partially explained through an increase in surface-to-volume ratio from using nanoparticles, alternate studies also suggest that this requirement is not necessarily a decisive factor for photocatalytic activity. Bai, Wei, Tian, Liu, Reiss, Guiblin, Gemeiner, Dkhil & C. Infante (2016); He, Guo, Fang, Dong, Zheng & Shen (2013); Huo, Jin & Zhang (2010) It is also recognized that a smaller bandgap should lead to more light absorption and a more efficient photocatalyst, but this causality relationship has not yet been clearly established for BFO structures. Li, Lin, Zhang, Nan & Wang (2009); Gao, Chen, Zhu, Niu, Huang, Qin, Sun & Huang (2014) In contrast, surface-state defects like oxygen vacancies found on BFO nanoparticles seem to contribute more significantly to Rhodamine B (RhB) degradation, as they tend to introduce defects inside the bandgap and achieve a better charge separation. Di, Yang, Xian & Chen (2017) They can also simultaneously reduce the BFO nanoparticles bandgap from 2.20 to 2.01 eV by increasing the oxygen vacancies surface densities. Wang, Chen, Niu, Zhang, Qin & Huang (2016a) This earlier study also confirms that the bandgap is not necessarily a critical parameter, as the particles with the lowest bandgap do not always yield the best photocatalytic properties. Meanwhile, most papers tend to conclude that smaller structures are more efficient because of the lower band gap

without investigating the surface defects. Xian, Yang, Dai, Wei, Ma & Feng (2011); Cadenbach, Lascano, Vera, Vizuete & Debut (2019); Pattnaik, Behera, Martha, Acharya & Parida (2018); Hao, Xiang, Hou, Lv, Lv, Hu, Liu et al. (2014) However, varying the dimensions of the BFO nanostructures also tend to produce significant morphology fluctuations, which can in turn affect their properties. Mocherla, Karthik, Ubic, Ramachandra Rao & Sudakar (2013) Overall, it appears a compromise should be found between the size, bandgap and surface-state defect density for the BFO nanoparticles to achieve optimal photocatalytic efficiency. Recombination of charge carriers resulting in low photocurrent is still the main limitation in BFO, limiting its suitability for many applications. You, Zheng, Fang, Zhou, Tan, Zhang, Ma, Schmidt, Rusydi, Wang et al. (2018) Compared to bulk photocatalyst materials, better performances are usually achieved using one-dimensional (1D) geometries as they can offer a higher surface to volume ratio and a shorter direct pathway to the redox surface reducing these recombination losses. Hochbaum & Yang (2010) Substitution of either Bi or Fe atoms or doping with rare or alkaline earth atoms elements constitutes another potentially interesting mitigation strategy. Jangid *et al.* (2014); You *et al.* (2018); Gebhardt & Rappe (2018); Silva *et al.* (2011) Another successful approach involves depositing a noble metal like Pt, Au or Ag nanoparticles on various BFO structures to achieve significant enhancement through Schottky-barrier and/or surface plasmon resonance-induced absorption enhancement. Li *et al.* (2013); Niu *et al.* (2015); Zhang, Cai & Ma (2015b); Jaffari, Lam, Sin & Zeng (2019b); Di, Yang, Hu, Xian, Ma, Jiang, Li & Wei (2014); Sze *et al.* (2006) In this work, we explore electrospinning deposition of a precursor solution on glass substrate to form high-quality crystalline BFO nanofibers for colloidal release-free photo-catalysis applications. This BFO morphology promotes both a higher surface-to-volume ratio and enhanced diffusion of the photo-generated charge carriers for photocatalysis. The significantly lower bandgap of BFO also constitutes a major advantage to maximize absorption and achieve an efficient photocatalytic solar membrane. Following the BFO nanofiber synthesis, we deposit a thin Pt layer using conventional magnetron sputtering technique to further enhance the photocatalytic membrane's performances. We use the RhB organic dye as a test pollutant, to directly monitor the photocatalytic activity in real-time without additional processing steps. Di *et al.* (2017) With these photocatalytic membranes, we perform multiple degradation cycles without using extra

chemicals for catalyst recovery. Indeed, we show that very minute amounts of photocatalyst material are released in each degradation cycle. This report is the first to demonstrate a reusable colloidal release-free BFO nanofiber-based photocatalytic membrane. Most importantly, this manufacturing-ready approach yields a spectacular 93% removal of the RhB after only 150 *min* under solar light irradiation over multiple cycles with very little BFO nanofibers degradation.

5.2 Results and discussions

Following electrospinning deposition and thermal conversion of the precursor solution to BFO nanofibers on glass, X-ray diffraction (XRD) analysis is performed to assess their structural properties as shown in Figure 5.1(a). The sharp and narrow diffraction peaks confirm a good crystallization into the desired rhombohedral crystallographic phase that belongs to group R3c. For reference, standard XRD pattern of BFO in red (ICDD card #086-1518) is added to Figure 5.1(a). Ponraj, Vinitha & Daniel (2020) While Figure A III-1 shows the amplitudes increase as a result of longer material deposition, no visible impurity phase can be detected from the XRD results. The presence of secondary phases like Bi_2O_3, $Bi_{25}FeO_{39}$ and $Bi_2Fe_4O_9$ is typical during crystallization of BFO because of the phase formation's kinetics. Bernardo *et al.* (2011) While the literature suggests that such secondary phases can also possess interesting photocatalytic properties, Wang, Cheng, He, Hu, Deng, Mao & Wang (2019a); Zhang, Gong, Wang, Ning, Wang, Zhao, Ren & Zhang (2011) our results indicate only the presence of the pure BFO phase. As discussed in the introduction, the bandgap energy (E_g) can play an important role for photocatalytic membrane performances. Here, the bandgap energy value is extracted from the absorption spectra using the linear extrapolation of the band-edge in the Tauc plot shown in the inset of figure 5.1(a). Viezbicke, Patel, Davis & Birnie III (2015) The value for the bandgap energy is 2.15 eV, which is in consistent with previous reports. He *et al.* (2013); Huo *et al.* (2010); Wang *et al.* (2016a); Niu *et al.* (2015)

Scanning electron microscopy (SEM) imaging is also per-formed to explore the nanofiber morphologies after their deposition and thermal conversion. Figure 5.2 shows typical BFO nanofibers resulting from 30- to 300-second (5 *min*.) depositions. The low magnification

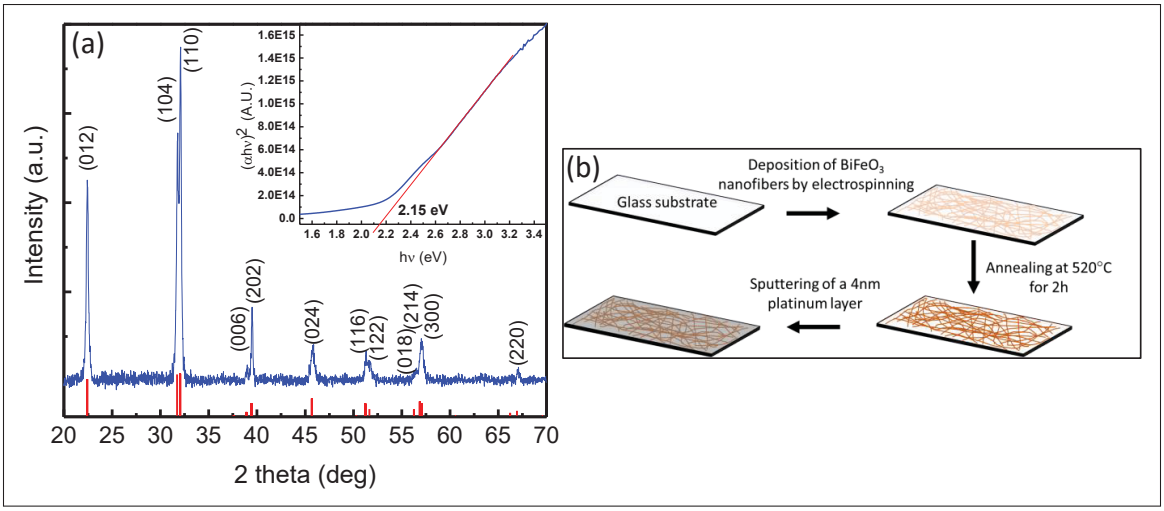

Figure 5.1 (a) XRD patterns of $BiFeO_3$ nanofibers for 5 *min* deposition. The inset shows a Tauc plot representation with the line-ar fitting of the band-edge. (b) Schematic illustration of the fabrication steps of the $BiFeO_3$ membranes

images in Figures 5.2(a-e) highlight the good uniformity of the BFO nanofibers, while the higher magnification images (cf. Figures 5.2(f-j)) point out their morphologies. Shorter deposition times (30 *sec*. and 1 *min*.) yield straight and well-defined nanofibers. After 2 minutes of electrospinning, multiple layers of nanofibers start to overlap each-other as the film gets denser and some fibers begin to break. We can tentatively explain this phenomenon by the evaporation of the residual solvent from the underlayers of nanofibers during crystallization of BFO, which damages the upper layers. For longer depositions (3 *min* and 5 *min*), nanofibers continue to aggregate and collapse to form flake- and film-like structures. A similar transition from nanofibers to thin films was also observed in our previous work on electrospuned BFO. Das *et al.* (2020) There, we establish how this transition can be carefully controlled by adjusting the humidity and solvent evaporation together with varying the deposition time. This morphology evolution becomes more obvious using more advanced image segmentation analysis as shown in Figures 5.2(k-o). This advanced image analysis from the SEM images is generated using the commercially available Dragonfly software. Badran, Marshall, Legault, Makovetsky, Provencher, Piché & Marsh (2020) Figure 5.3 displays energy-dispersive X-ray spectroscopy (EDX) elemental mappings suggesting uniform distributions of the bismuth and iron within the fibers. The EDX

mapping of oxygen is not presented here, as both the glass substrate and the nanofibers also have strong oxygen content.

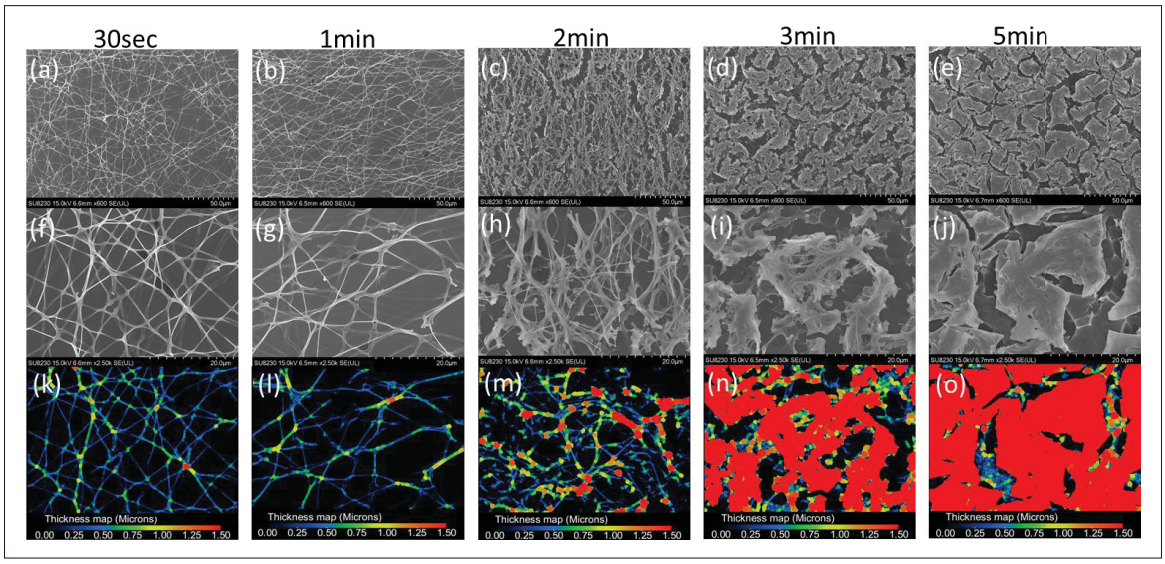

Figure 5.2 SEM images of $BiFeO_3$ nanofibers at two magnifications for different deposition times. (a-e) Micrographs at low (600×) magnifi-cation (scale bar: 50 μm). (f-j) Micrographs at higher (2,500×) magnification (scale bar: 10 μm). (k-o) Thickness maps generated by image segmentation using the high-resolution micrographs (f-j)

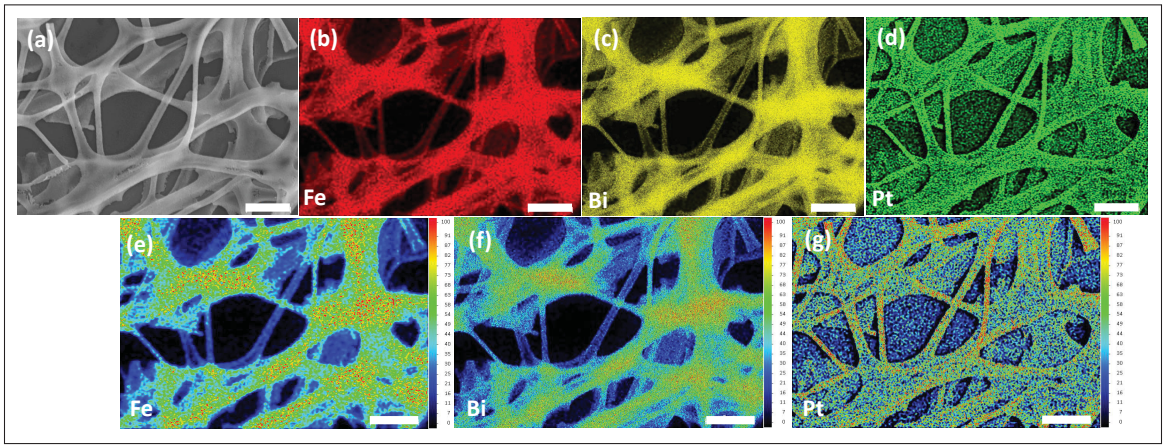

Figure 5.3 Energy Dispersive Spectroscopy (EDS) elemental mapping of the $BiFeO_3$ nanofibers resulting from a 2-minute deposi-tion. (a) SEM micrograph. (b) Iron distribution mapping. (c) Bismuth distribution mapping. (d) Platinum distribution mapping. (e), (f) and (g) show the intensity mappings of iron, bismuth and platinum respectively. The scale bar for all the images is 2 μm

To estimate the weight of the photocatalyst material depos-ited, thermogravimetric (TGA) measurements are carried out for pristine nanofibers after precursor deposition (cf. Figure 5.4). From 50 to 150 $°C$, the 5.4% loss weight is directly attributed to the evaporation of residual water. The N,N-Dimethylformamide solvent evaporation subsequently takes place at 153 $°C$, causing an additional 59.9% loss. As illustrated in Figure 5.4, this residual solvent in the nano-fibers can explain why they start to break during the an-nealing for longer deposition times. Between 160 $°C$ and 500 $°C$, PVP and nitrates degradation leads to another 8.7% reduction. Only 26% (weight) of BFO nanofibers remains after annealing, which is consistent with previous reports using similar synthesis protocols. Bharathkumar, Sakar, Balakumar et al. (2015); Melo, Santos, Gualdi, Tsai, Sigmund & Bretas (2017) Based on this measurement, we can provide a fair estimate of the BFO nanofibers weight of 0.6, 1.2, 2.4, 3.6 and 6.0 mg for samples obtained after 0.5, 1, 2, 3 and 5-minutes, respectively.

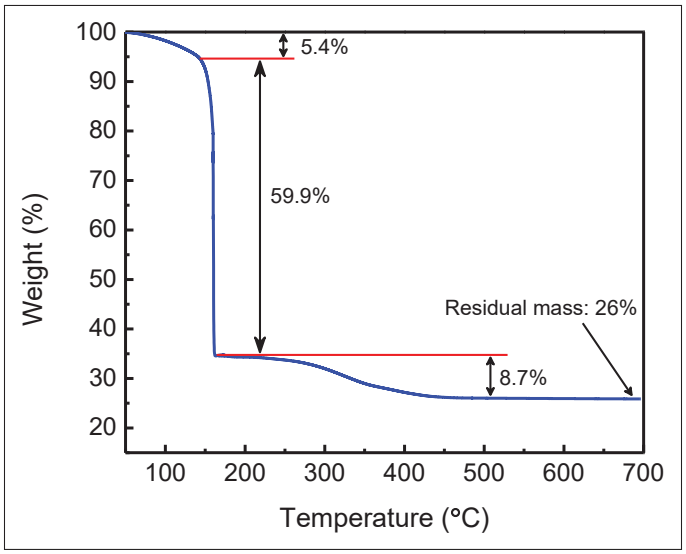

Figure 5.4 Thermogravimetric analysis of the $BiFeO_3$ nanofibers

The fabrication steps of the BFO membranes used to degrade RhB are illustrated in Figure 5.1(b). To maximize the photocatalytic degradation using synthesized BFO nanofibers, a 4 nm platinum coating is deposited using magnetron sputtering. This simple, cost-effective, and chemical-free platinum deposition creates an efficient Schottky barrier to act as a better electron sink. Sze

et al. (2006); Yang (2021) In turn, this better extraction of the photo-generated charge carriers promotes a more efficient pollutant degradation. The smooth and uniform coatings achieved by sputtering is also an advantage over metallic nanoparticles that tend to agglomerate into clusters, which is detrimental for the photocatalytic degradation. Niu *et al.* (2015) This use of metallic nanoparticles is not straightforward and can often involve complex processing steps. Meanwhile, a thin platinum film also provides more photocatalytic sites for the reaction compared with metallic nanoparticles. However, the thickness of the deposited film is carefully selected to achieve the maximum effect, while allowing enough light to reach the BFO photocatalyst. Previous reports show that 13 nm-thick platinum films deposited by sputtering yields around 50% transmission from 400 to 800 nm. Tompkins, Tasic, Baker & Convey (2000) As such, we chose a 4 nm-thick platinum deposition to achieve the best possible photocatalytic effect, while preserving a good transparency. Compared to state-of-the-art reporting BFO nanoparticles coated with platinum, similar photocatalytic performances are obtained by reducing the photocatalyst weigh by two orders of magnitude using our approach. Niu *et al.* (2015); Jaffari *et al.* (2019a)

To evaluate the photocatalytic membranes performances, we irradiate the samples using a solar simulator (AM 1.5G). A longpass filter ($\lambda \geqslant 400\ nm$) is added to remove UV light from the irradiation spectrum, since this latter can yield some photodegradation of the Rhodamine B (RhB) dye. Wang, Li, Chi, Li, Yan, Li & Shao (2013) Figure 5.5 compares the organic content removal (from the RhB degradation) corresponding to BFO nanofibers synthesized at different electrospinning times. In dark conditions, no absorption-desorption reaction is detected when the membranes are immersed in RhB. To initiate the reaction, light is switched on and H_2O_2 (at 7.5 mM) is added to the RhB solution to initiate the photocatalytic degradation. After 150 min under illumination, the membranes with the 2-minutes and 3-minutes BFO deposition times yield the highest degradations with 93% and 91% removal, respectively. This is significantly better than the 3.5%, 54% and 81% degradations observed with the 30-seconds, 1-minute and 5-minutes depositions. These results can be directly correlated with the morphology of the deposited BFO nanofibers shown previously in Figure 5.2. From 30-seconds to 2-minutes depositions, the nanofiber density increases and the photocatalytic activity of the cell improves. Then, their

efficiency starts to waver due to the loss of active surface when the morphology evolves from a dense nanofiber network to flake- and film-like architectures for longer depositions. The low photocatalytic degradation rates from membranes with shortest deposition times confirm that (i) photolysis is negligible and the RhB dye remains stable under visible light and (ii) H_2O_2 and platinum alone are not responsible for the RhB degradation. As an additional control experiment, measurements using only a 4 *nm*-thick platinum layer deposited directly on glass is shown in Figure A III-2. No noticeable RhB degradation can be observed. Another important baseline experiment shown in Figure A III-2 consists in looking at the degradation of the RhB using our best cell configuration (2-minutes BFO deposition), with no light irradiation whatsoever. There, only 5% RhB degradation can be observed after 150 minutes. These results confirm that a very limited adsorption-desorption reaction occurs and that photo-generated charge carriers are mainly responsible for the RhB degradation reaction. For comparison, other studies report dye degradation up to 15% in only 30 *min* due to adsorption-desorption equilibrium prior to any illumination. Gao *et al.* (2014); Di *et al.* (2017); Niu *et al.* (2015); Jaffari *et al.* (2019b); Wang *et al.* (2013); Zhang, Chen, Niu, Wang, Qin & Huang (2016b) For comparison, the same experiment is reported without the platinum layer in Figure A III-2. No RhB degradation is detected using our setup.

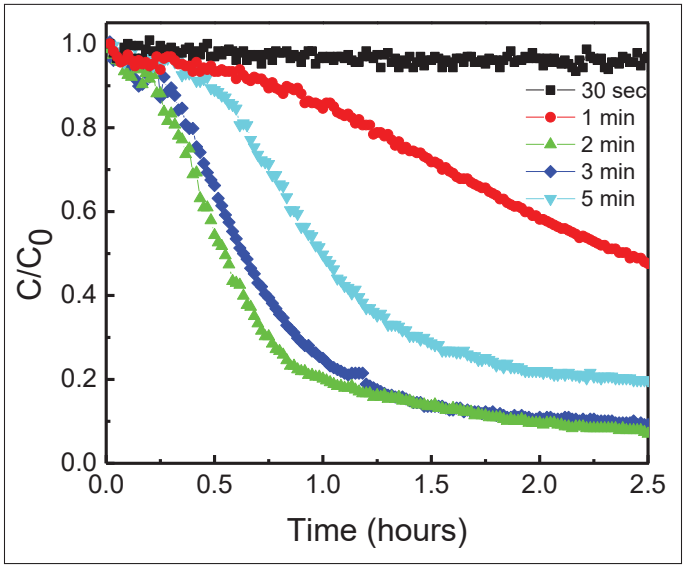

Figure 5.5 Effect of $BiFeO_3$ NFs deposition time on the RhB degradation

As an indicator, Figure 5.6(a) shows the spectral evolution of the RhB absorption spectra taken at each 20 minutes during the photocatalytic degradation reaction using the optimized cell configuration. Figure 5.6(b) shows the main absorption peak's position evolution during the RhB degradation. During the first hour of the reaction where around 80% of the RhB degradation occurs, the absorption peak's blue-shift is negligible. This is because the degradation is primarily achieved by the cleavage of the whole chromophore structure (cyclo-reversion) in the photocatalytic process. Wu, Liu, Zhao, Hidaka & Serpone (1998) After one hour, the absorption peak begins to blue-shift from 552 *nm* down to 542 *nm*. Indeed, the peak absorption of the N,N,N'-Triethyl-rhodamine byproduct of the cleavage is located at 539 *nm*. Watanabe, Takizawa & Honda (1977) This result suggests that the de-ethylation begins to dominate the photocatalytic degradation after one hour. Watanabe *et al.* (1977)

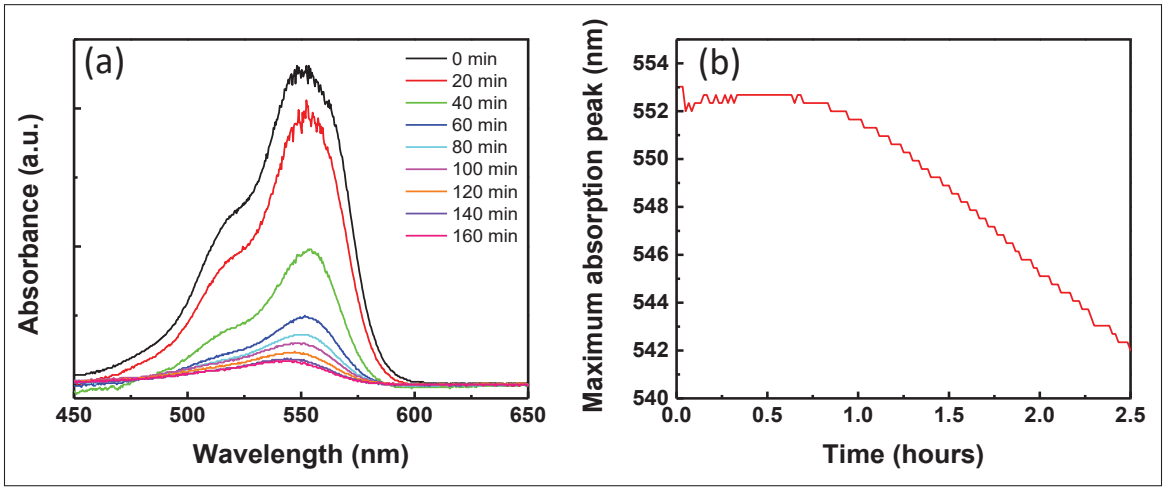

Figure 5.6 RhB absorption change during the photocatalytic degradation cycle for the $BiFeO_3$ nanofibers resulting from a 2 *min* deposition. (a) Spectral evolution under illumination. (b) Maximum absorption peak position and its evolution over time.

Among many criteria, stability and recyclability of the photocatalysts are especially important in order to develop a viable photocatalytic device technology. As an inorganic oxide material, BFO is already known to be chemically stable and robust for photocatalytic reactions. Huo *et al.* (2010) To verify that our BFO nanofibers' structural properties are preserved during the photocatalytic reaction, absorption measurements and crystalline structure (cf Figure A III-3) are performed and confirm that both properties remain intact after three full RhB degradation

cycles. Figure 5.7 records the optimal device performances over five (5) consecutives RhB degradation cycles. More than 80% of the RhB solution is still degraded after 5 cycles and only a 12% reduction compared to a pristine device which in agreement with previous reports. Di *et al.* (2017); Wang *et al.* (2016a); Ponraj *et al.* (2020) We can tentatively attribute this phenomenon to the colloidal release or to the progressive saturation and destruction of the photocatalytic sites. Qu & Duan (2013); Herrmann (2000); Seliem, Komarneni & Khadra (2016) To better understand the mechanism underlaying this degradation, the leachates are analyzed after each cycle of degradation using Inductively Coupled Plasma Mass Spectrometry (ICP-MS). This technique allows to track the photocatalyst colloidal release over time looking for metallic traces of bismuth and iron from the BFO photocatalyst and the platinum. Results summarized in Table 5.1 confirm that the concentration of bismuth and iron found in the leachate represents approximately 0.03% of the initial mass of the photocatalyst confirming the previously reported values. Luo, Zhu, Wang, Tang, Cao & She (2010) This validates that BFO nanofibers strongly adhere to the glass substrate and negligible contamination by the photocatalyst occurs during RhB removal. The same observation can be made for Pt layer, as only 0.1% of the initial mass is released after each cycle. Hence, colloidal release of the photocatalyst appears to be negligible. We postulate that saturation or destruction of photocatalytic sites will progressively reduce the active surface area which results in slight reduction of degradation over these 5 cycles. Qu & Duan (2013) Despite a lack of precise studies on platinum carcinogenicity and data availability to determine the exact risks, it has been reported that Pt nanoparticles can induce DNA damage, increased mortality and decreased growth of the offspring among mice. Czubacka & Czerczak (2019) Nevertheless, the Pt concentration after each cycle remains in the $\mu g\ L^{-1}$ range. This is at least one order of magnitude lower than threshold values used for platinum toxicity on wildlife. Zimmermann, Wolff & Sures (2017)

To further evidence the beneficial role of the platinum in the photocatalytic degradation enhancement, trapping experiments can be conducted to determine the main reactive species. Chemical-free radicals like $\bullet OH$, O_2^- or photogenerated charges are known to dominate the photocatalyst reactions. Niu *et al.* (2015); Jaffari *et al.* (2019a); Zhang *et al.* (2016b); Wang,

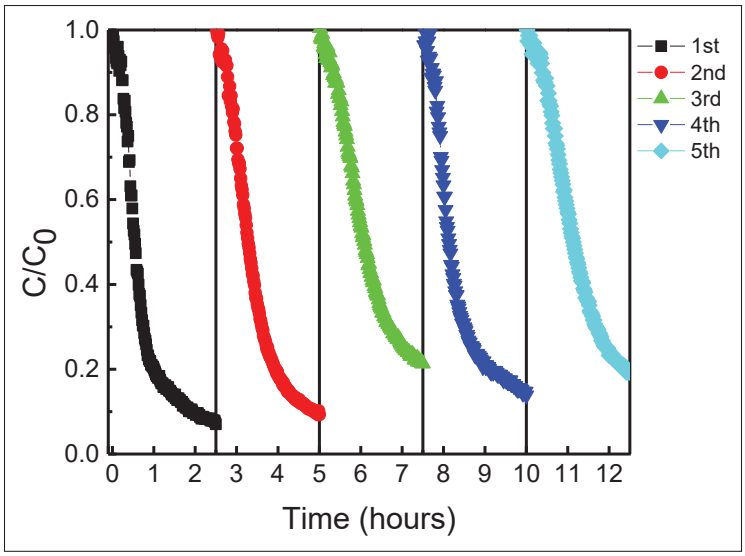

Figure 5.7 Degradation efficiency using $BiFeO_3$ nanofibers resulting from a 2-minute deposition over five (5) consecutive degradation cycles

Cycle number	Bi ($\mu g\ L^{-1}$)	Fe ($\mu g\ L^{-1}$)	Pt ($\mu g\ L^{-1}$)
1	36.6 ± 0.2	15.9 ± 0.5	4.2 ± 0.1
2	41.5 ± 0.2	14.5 ± 0.2	1.44 ± 0.02
3	57.3 ± 0.3	15.9 ± 0.4	3.9 ± 0.2
4	28.8 ± 0.3	11.4 ± 0.2	1.17 ± 0.03
5	34.0 ± 0.2	12.3 ± 0.2	1.26 ± 0.05

Table 5.1 ICP-MS measurements to measure the Bi, Fe and Pt weight release after each degradation cycle

Chen, Niu, Zhang, Qin & Huang (2016b) As such, additional scavengers can be used together with our optimized cell configuration. The consequences of using 2 mM scavengers such as benzoquinone (BQ, a superoxide radicals' scavenger), tert-butanol (TBA, a hydroxyl radicals' scavenger), triethanolamine (EDTA, a hole scavenger) and silver nitrate (AgNO3, an electron scavenger) are summarized in Figure 5.8(a). All these scavengers hamper the RhB photocatalytic degradation. These results stem from the fact that the added H_2O_2 used to initiate the degradation reaction can act either as a reducing or oxidizing agent. Depending on the Pt surface state, H_2O_2 interacts with reduced Pt surface sites to from hydroxyl groups or H_2O_2 can be oxidized

by reducing an oxidized surface site forming O_2 molecules. Katsounaros, Schneider, Meier, Benedikt, Biedermann, Auer & Mayrhofer (2012) In both cases, the H_2O_2 degradation generates highly reactive species with a short lifetime, which are known to actively react with a cationic dye like RhB. Niu *et al.* (2015); Luo *et al.* (2010) Figure 5.8(b) illustrates the photocatalytic synergistic mechanisms between Pt, H_2O_2 and BFO. The trapping experiment reveals that RhB degradation is slightly delayed, from 93% to 65%, in presence of a hole scavenger compared to the other type of scavengers. In fact, photo-generated electrons along with superoxide and hydroxyl radicals are the predominant species involved in the degradation reaction. Di *et al.* (2017); Zhang *et al.* (2016b); Luo *et al.* (2010) The degradation rate is respectively 12%, 28% and 33% after 150 *min* under illumination compared to 93% in the absence of any scavenger. As a cationic dye, RhB is effectively reduced in this study. BFO is known to be either a n- or p-type material depending on the ambient conditions during crystallization. Indeed, studies have already established that an oxygen-poor or ambient atmosphere leads to n-type BFO, while an oxygen-rich atmosphere results in p-type BFO. Rojac, Bencan, Malic, Tutuncu, Jones, Daniels & Damjanovic (2014a) In our case, BFO NFs are annealed in air, so an n-type behavior should be expected. The positive slope of the Mott-Schottky measurement shows in Figure A III-4 confirms the n-type characteristic of the BFO fibers. Therefore, a negatively charged BFO coated with a Pt layer can act as an efficient electron sink and successfully react with a cationic dye like RhB.

With this proposed methodology, absorption measurements can be tracked automatically and in real-time. As no magnetic stirring is needed, this approach is more straightforward to use and easily scalable. In the case of nanoparticle-based cells, turbidity and colloidal releases are usually the main drawbacks. The former degrades the cell performances by preventing the light to reach the active surface while the latter implies photocatalyst losses and deterioration. In contrast, a colloidal release-free cell does not require additional collection and centrifugation steps to separate the photocatalyst from the leachate. Even though magnetic ordering is an advantage of BFO which simplifies postreaction processing and catalyst can be recycled relatively easily using magnets. Nevertheless, this process is not always trivial as the suspended

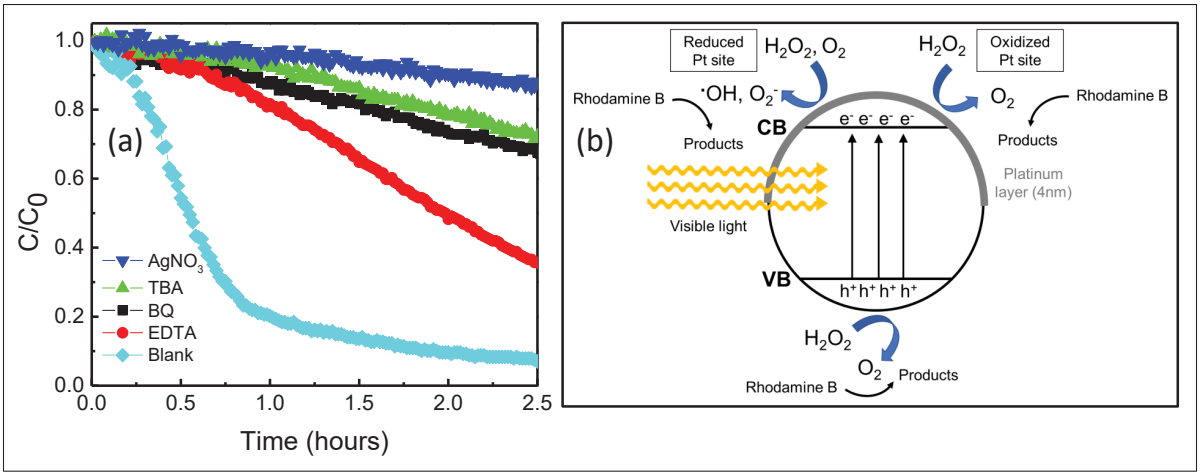

Figure 5.8 (a) Influence of different scavengers on the RhB degradation (b) Illustration of the photocatalytic RhB degradation mechanisms under visible light irradiation

particulates can be easily wasted during this process and pollute again the treated environment. As such, any catalyst should remain unimpaired and easily recovered, both for environmental and economic reasons. Compared with previous colloidal-based technologies where recovery can be challenging, Rueda-Marquez, Levchuk, Ibanez & Sillanpää (2020) the proposed methodology emerges as an environmentally-friendly approach to treat polluted water. By taking advantage of manufacturing-ready technologies like electrospinning and sputtering technics, deployment of colloidal release-free photocatalysts appears promising as it possesses the potential to be scalable for industrial applications.

5.3 Conclusion

This study reports a cost-effective method to synthesize and produce a highly efficient, reusable, and colloidal release-free BFO nanofiber-based photocatalyst technology. Live tracking of the Rhodamine B degradation using absorption measurement is used for concept validation. We demonstrated that a carefully control the nanofibers' morphology using electrospinning is critical to achieve a highly efficient pollutant degradation. Using irradiation from a solar simulator, photo-generated electrons, superoxide and hydroxyl radicals actively contribute to the photocatalytic degradation reaction, leading to achieve up to 93% degradation of RhB. These

performances are explained by (i) the larger active surface involved in the RhB degradation promoted by an optimized nanofiber morphology and (ii) the effective Schottky barrier induced using a 4 nm-thick platinum coating of the nanofibers. In this unique configuration, we achieve an unprecedented material-cost efficiency for RhB degradation using only few milligrams of photocatalyst. Compared to the state-of-the-art involving BFO and platinum as co-catalysts, this represents a reduction of the material weight of two orders of magnitude without compromising photocatalytic performances. From ICP-MS measurements, adhesion of the BFO nanofibers on the substrate is optimal and no significant photo-degradation is detected over multiple cycles. Overall, we believe that such results provide a commercially- and environmentally-attractive approach to treat contaminated water using sunlight and make photocatalysis more accessible for large-scale deployment around the world.

5.4 Experimental methods

5.4.1 Photocatalyst preparation

Electrospun BFO solution is synthesized by mixing an equimolar ratio of bismuth(III) nitrate pentahydrate $[Bi(NO_3)_3 5H_2O]$ and iron(III) nitrate nonahydrate $[Fe(NO_3)_3 9H_2O]$ in N,N-Dimethylformamide (DMF). Then, polyvinylpyrrolidone (PVP) with an average molecular weight about 1,300,000 is added to adjust the viscosity of the prepared solution. These chemicals are purchased from Sigma-Aldrich and use as received, without further purification. Both nitrate precursors are ACS reagent grade with a purity $\geqslant$ 98.0% (catalog numbers are 383074 and 216828 for bismuth and iron nitrates, respectively). After an appropriate mixing, the solution is loaded into a 3 mL syringe. The flow rate is kept constant at 0.15 $mL\ h^{-1}$ during electrospinning to avoid any dripping. The distance between the needle and the planar collector is fixed at 9.5 cm and a tension of 9.5 kV is applied to the needle. The BFO nanofibers are collected on a 25 $mm \times 25\ mm$ glass substrate for different deposition times. By doing so, most of the nanofibers created from the Taylor cone were collected on the substrate for further photocatalytic degradation reported in this paper. Relative humidity is controlled and kept at 25 ± 5% during

the NFs deposition. Crystallization of the nanofibers is carried out in a tube furnace at 520 $°C$ for 2 hr in ambient atmosphere. The final step for sample preparation is the deposition of a 4 nm-thick platinum layer by magnetron sputtering (using a Quorum, Q150T system).

5.4.2 Materials characterization

XRD patterns obtained on a Brucker D8 Advance with a Cu Kα X-ray source to characterize crystallinity and phase purity of the BFO nanofibers. Optical absorption measurements are recorded using an integrating sphere to collect all the diffuse light in a UV-VIS-NIR spectrophotometer (PerkinElmer, Lambda750). Characterization of BFO nanofibers morphology deposited on glass is recorded by scanning electron microscopy (SEM, Hitachi, SU8230). To determine the size of the deposited structures by image segmentation, the commercial Dragonfly software (from ORS, Montreal, Canada) is used. Energy Dispersive X-ray (EDX) detector is used to perform elemental mapping (Bruker, QUANTAX FlatQUAD). Thermogravimetric measurements are accomplished with a flow rate of dry air of 50 $mL\ min^{-1}$ and a temperature ramp of 5 $°C\ min^{-1}$ (PerkinElmer, STA8000). Detection of residual bismuth, iron and platinum in the leachate is conducted by ICP-MS measurements (PerkinElmer, NexION 300x).

5.4.3 Photocatalytic activity tests

To ensure that no UV-light irradiates the RhB solution and the photocatalyst, a cut off filter ($\lambda \geqslant 400\ nm$) is inserted inside the solar simulator right after the AM 1.5G filter. The solar simulator (Newport, 91160-1000) is equipped with a 300 W Xenon lamp. The light intensity is calibrated at 100 $mW\ cm^{-2}$ (1 sun). The light beam from the solar simulator is vertical and the reactant solution is maintained at room temperature to avoid any thermal effect during the reaction. A 50 mL beaker is used in each experiment and a horizontal beam of a tungsten halogen light source (Ocean optic, HL-2000-HP, output power 8.8 mW) allows a live tracking of the RhB signal. This setup is illustrated in Figure A III-5. Absorbance spectrum is recorded every minute to ensure a precise tracking within a wavelength range interval from 400 to 800 nm. All the spectra are analyzed using Matlab to extract the maximum intensity of absorbance

and the position of this peak. Before starting all the experiments, a mother solution mixing RhB powder with distilled water was prepared (pH=6.1) was prepared. 20 mL of this mother solution with a concentration of RhB set to 5 $mg\ L^{-1}$ is taken and degraded in each reaction. The dye concentrations of RhB is known to be proportional to the absorbance at concentration in the range of $mg\ L^{-1}$. Then, determination of the RhB removal is estimated by dividing the maximum absorbance at the beginning of the reaction by the live measured absorbance. After each degradation reaction BFO NFs are rinsed with distilled water to remove residual RhB and dried before another photocatalytic reaction.

Acknowledgement

The authors thank Mr. Alain Picard for his help with the absorbance acquisition set up and Dr Shyamashis Das for his expertise in the Mott-Schottky measurements. The authors also thank Mr. Michael Dubois for his assistance with the thermogravimetric measurements.

5.5 Additionnal studies

Following this paper, the fabrication of BFO/TiO_2 nanofibers by electrospinning is realized to study the degradation performance of RhB. In this work, we follow the objectives set in the introduction chapter and proposed other colloidal-free photocatalytic cells using manufacturing-ready technologies. To create efficient BFO/TiO_2 heterojunctions without complicating the synthesis method, we choose to put ultra-fine uncrystallized TiO_2 powder (7 to 10 nm) directly inside the electrospuned BFO precursor solution. Such fine tuning of the TiO_2 powder is achieved by sol-gel synthesis. In Figure 5.9, we demonstrate enhanced photocatalytic degradation of BFO nanofibers resulting in 94% degradation in only 1 hr of RhB compared to 93% degradation in 150 min in this chapter. We attribute this result to the smaller diameters of the deposited nanofibers and because of their homogeneous depositions. In addition, we report BFO/TiO_2 nanofibers and highlight that better photocatalytic performances can be obtained via these heterojunctions. Indeed, 99% of the initial RhB concentration is degraded after 45 min. For both photocatalytic cells, we kept the deposition time and flux rate the same to study the effect of

the heterojunctions on the photocatalytic properties. The only adjusted parameter is the voltage as the addition of TiO_2 particles tend to reduce the electrical conductivity of the electrospun solution.

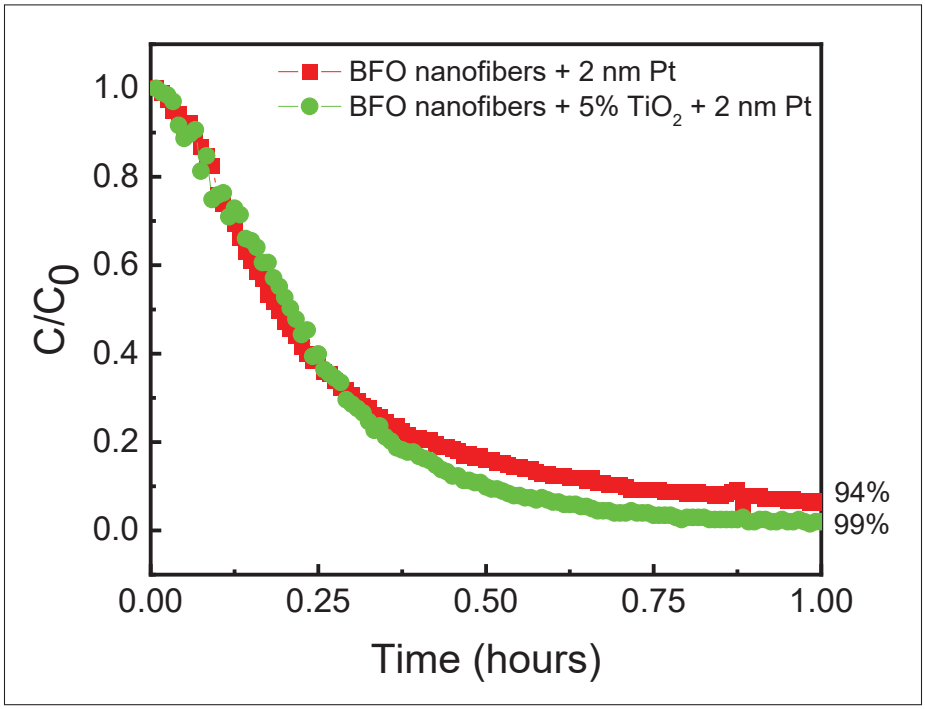

Figure 5.9 RhB degradation of pure $BiFeO_3$ nanofibers and $BiFeO_3$ nanofibers doped with 5% TiO_2 particles. Both photocatalytic cells are coated with 2 *nm* platinum

CHAPTER 6

SCREEN-PRINTED P-N BiOCl/$BiFeO_3$ HETEROJUNCTIONS FOR EFFICIENT PHOTOCATALYTIC DEGRADATION OF RHODAMINE B

Paul Fourmont[1] , Sylvain G. Cloutier[1]

[1] Department of Electrical Engineering, Ecole de Technologie Supérieure,
1100 Notre Dame West, Montreal, Quebec, Canada

Abstract: Colloidal-free screen-printed p-n BiOCl/$BiFeO_3$ heterojunctions are successfully synthesized to achieve photocatalytic degradation of Rhodamine B (RhB) using visible light ($\lambda \geqslant 400\ nm$). The crystalline structure of dense BiOCl nanosheets self-assembled with impressive aspect ratio atop BFO powders is confirmed by XRD, Raman and TEM measurements. Iron impurities inside these $10 \pm 2\ nm$-thick BiOCl nanosheets increase visible light absorption. Fluorescent Rhodamine B (RhB) dye degradation is used to evaluate the photocatalytic performance of this unique heterojunction material. For optimal metal-enhanced RhB degradation, a few nanometers of platinum are deposited using sputtering technique to act as cocatalyst. This unique architecture yields an impressive 92% RhB degradation in only 150 *min* under visible light. Operating at near-neutral pH, the proposed approach also addresses the key issue of catalysis recovery, which remains one of the main drawbacks of current photocatalysis technologies.

6.1 Introduction

The research community is making tremendous efforts to develop more efficient solar-based technologies including photovoltaic, water splitting or photocatalysis cells. As a renewable and an inexhaustible source of energy, solar radiation appears as a promising solution to alleviate some of the most complex climate change issues. Rockström *et al.* (2009); Persson *et al.* (2022) Many semiconducting materials are efficient at absorbing light and generating photo-charges. In contrast, photocatalysis also requires that photogenerated carriers reach the surface of the material and participate in the oxidation-reduction (redox) reaction before recombination. To maximize the photocatalytic performances, the use of nano-engineered materials with large available

surfaces generally helps mitigate the relatively short lifetime of photo-generated excitons. Kabra *et al.* (2004) Ideally, semiconductors with smaller energy band separations ($< 3\ eV$) should be used to favor visible light absorption. As of today, most photocatalytic technologies rely on biocompatible materials with higher bandgaps such as TiO_2 and ZnO. Fresno *et al.* (2014) In these materials, exciton binding energies equal or higher than 60 meV are reported which is far above the value of thermal energy at room temperature (~25.7 meV). Zhou, Umezawa, Ma, Sakai, Ebina, Sano, Liu, Ishida, Aida & Sasaki (2018b); Bouzouraa, Battie, Dalmasso, Zaibi, Oueslati & Naciri (2017); Sze *et al.* (2006) As a result, stable and long-lived excitons can provide an additional contribution to the photocatalytic reaction expected from photo-generated free carriers only. Yang, Chu, Sun, Zhang, Li, Liu, Bai, Qu & Jing (2020b); Wang, Liu, He, Zhang, Zhang & Xie (2020a) Since ultraviolet (UV) light represents only a small fraction (~6%) of the solar radiation reaching the surface of earth, expensive and environmentally harmful UV sources are generally used for photocatalysis. To overcome this problem, nano-engineered photocatalysts should ideally possess adequate energy bandgaps to operate using mostly visible light exposure. Other important factors such as photostability, material and processing costs or biocompatibility should also be carefully considered for future large-scale deployment. Rueda-Marquez *et al.* (2020)

Over the last 20 years, bismuth-based inorganic perovskites or bismuth oxyhalides have drawn a lot of attention due to their unique optoelectronic properties and good photocatalytic behaviors. Wei, Akbar, Raza & Li (2021); Haruna *et al.* (2020) According to the literature, ceramics like $BiFeO_3$ (BFO) and BiOCl possess a good photostability in water, which can allow multiple degradation cycles with minimal efficiency losses. Fourmont, Nechache & Cloutier (2021); Dandapat, Gnayem & Sasson (2016) Indeed, colloidal-free methods can potentially avoid complex collection and separation steps at the end of the photocatalytic degradation reaction. Fourmont *et al.* (2021); Dandapat *et al.* (2016) Rhodamine B (RhB) is commonly used as an organic dye to model, monitor and evaluate the photocatalytic activity. Fourmont *et al.* (2021); Xiong, Cheng, Li, Qin & Chen (2011). Other studies report that BFO and BiOCl are both biocompatible and can be used in the medical field for cancer treatments or to sense disease

biomarkers. Rajaee *et al.* (2019); Ijaz, Zia, Taj, Jameel, Butt, Asim, Jameel, Abbas, Iqbal, Bajwa et al. (2020) Undoped BFO and BiOCl also have direct and indirect energy bandgap energies ranging between 2.1-2.5 *eV* (BFO) and 3.0-3.4 *eV* (BiOCl). Fourmont *et al.* (2021); Dandapat *et al.* (2016); Wu, Yuan, Li, Zhang, Liu & Li (2015); Huang, Hu, Cong, Zhao & Qiu (2015); Shahid, Mehmood, Athar, Hussain, Wei & Khaliq (2020); Das *et al.* (2020) To further increase BiOCl's visible light absorption, many strategies have been explored including elemental doping, incorporation of oxygen vacancies, addition of co-catalysts, morphology control or creation of heterostructures. Wei *et al.* (2021) Good heterostructures require a direct epitaxial contact between two different crystalline structures. He, Shi, Gao, Wen, Chen & Song (2014) Moreover, having two materials with different bandgap energies result in discontinuities at the conduction and valence bands at the interface. Nelson (2003) For a light-harvesting device, the built-in electric field pointing from the n- to the p-type semiconductor contributes to reducing the recombination of photogenerated charge carriers. Long, Cai, Cai, Zhou, Chai & Wu (2006) Despite many studies about BFO and BiOCl as single and independent photocatalysts, superior photocatalytic performances are usually found in composite photocatalysts. Yang (2021); Yan, Yang, Yi & Xian (2019) Only a few papers have reported BiOCl/BFO heterojunctions acting as a photocatalyst material. Shang, Chen, Chen, Wang, Feng, Zhu, Yang & Jia (2019) This last study reported the creation of BiOCl/BFO heterojunctions by acid etching to facilitate photocatalytic degradation of RhB and phenol. Shang *et al.* (2019) Most of BiOCl-based composite nanostructures are synthesized by hydrothermal, solvothermal or precipitation techniques. Yang, Sun, Cui, Yang, Luo & Liang (2021) However, such synthesis methods remain challenging and unfit for large-scale production. Jamkhande, Ghule, Bamer & Kalaskar (2019)

In this work, we propose a facile and straightforward fabrication method of producing p-n BiOCl/BFO heterojunctions with high aspect ratio for highly efficient photocatalytic dye degradation under visible light. Indeed, we demonstrate that this unique synthesis approach can be deployed directly using screen printing for large-area photocatalytic cell fabrication. This process involves the transfer of a stencil design on a substrate using a squeegee and a mesh screen. The ink goes through the mesh as the squeegee is pulled. Some other deposition methods

such as spray coating or dip coating cannot create patterns needed to print photocatalytic cells. For spray coating, it is often difficult to precisely evaluate the effectiveness of the deposited particles. In contrary, dip coating covers all the immersed surfaces of the substrate and multiple dipping is usually needed to achieve a thick layer which makes this process slow. Screen printing tends to be a faster deposition technique as only one pass of the squeegee is needed to print all the stencil design. By carefully controlling the evaporation of the printed ink vehicle mixed with BFO powders, ultra-thin BiOCl nanosheets are synthesized. Thanks to the presence of chlorine in the ink vehicle, a fine control of the BiOCl nanosheets morphology can be achieved. Most importantly, the creation of this intimate BiOCl/BFO heterojunction produced with a high surface-to-volume ratio enables a very efficient RhB photocatalytic degradation compared with similar studies. Shang *et al.* (2019) We reveal that the BFO particles serve as nucleation sites and that diffusion of iron atoms occurs from the BFO to the BiOCl nanosheets. This phenomenon is also beneficial for the photocatalytic degradation process as it significantly increases the BiOCl's visible light absorption. Wei *et al.* (2021); Huang *et al.* (2015); Shahid *et al.* (2020); Xia, Xu, Zhang, Yin, Li, Xu & Di (2013) As we previously reported, a thin platinum layer of several nanometers is deposited directly atop the printed photocatalytic cells to enhance the photocatalytic performances. Fourmont *et al.* (2021) Live monitoring of the photocatalytic degradation is realized by measuring the absorbance of the RhB solution. Most importantly, this can be achieved without the need for any catalyst separation step. Combination of both colloidal-free and screen-printed approaches for photocatalytic degradation of RhB yields a remarkable 92% degradation after only 150 min using a solar simulator without the UV component ($\lambda \geqslant 400\ nm$) to activate the degradation process.

6.2 Results and discussions

To better understand the BiOCl growth, Scanning Electron Microscopy (SEM) images in Figures 6.1(a-c) show the progressive formation of well-defined nanosheets atop the BFO particles after annealing at 150, 225 and 300 $°C$ for 1 hr. After a 150 $°C$ annealing, only some partial nucleation with a few 400 nm-long sheets begins to randomly appears in Figure 6.1(a).

The inset presented in this micrograph also confirms the presence of an intimate junctions between both structures. This parameter is crucial as it affects the charge carriers' extractions and recombination. Dong, Xiong, Sun, Zhang & Zhou (2015) After annealing at 225 $°C$, Figure 6.1(b) shows denser nanosheets reaching up to 1 μm in length. After a 300 $°C$ annealing, these nanosheets form an intricate network across the surface of the BFO particle film as seen in Figure 6.1(c). To assess the increase of surface area of the nano-catalyst, Figures A IV-1(a-b) show micrographs before and after annealing at 300 $°C$. This interconnected sheet-like morphology with impressive aspect ratio promotes a significant increase of the active surface available together with good charge transport properties. As a result, it will have a significant positive impact on photocatalytic properties of the printed photocatalytic cells. In fact, one can see that some nanosheets are transparent to the electron beam, implying a thickness of only few nanometers, while reaching up to 4 to 5 μm in length. The high-resolution micrograph in Figure 6.1(d) suggests a thickness of 10 ± 2 nm. To avoid charging effects, a 4 nm Pt layer is sputtered on all the samples for SEM imaging and traces can be seen in Figure 6.1(d). The effect of this metallic layer acting as a cocatalyst on the photocatalytic performances will be discussed later in Figure 6.5. We tentatively explain that the biggest and densest nanosheets are found when the printed photocatalytic cells are annealed at the highest temperatures because it relates to the ink vehicle's chlorine evaporation after screen printing. As shown in supplementary Figure A IV-2(b), Energy Dispersive X-Ray (EDX) spectroscopy of the printed photocatalytic cells before annealing confirms the presence of chlorine due to the ink vehicle used to disperse the BFO particles. For comparison, the same measurement of the BFO particles without ink vehicle is reported in Figure A IV-2(d) and no chlorine is detected. Thus, it validates that the chlorine contribution comes from the ink vehicle.

To fully assess the crystalline structure of the nanosheets, X-ray diffraction (XRD) and Raman micro-spectroscopy measurements of the screen-printed photocatalytic cell after annealing at 300 $°C$ are presented in Figure 6.2. XRD results in Figure 6.2(a) clearly show the presence of sharp and intense peaks originating from three different crystalline structures. The most intense phase belongs to the tetragonal group P4/nmm and matches the BiOCl crystalline

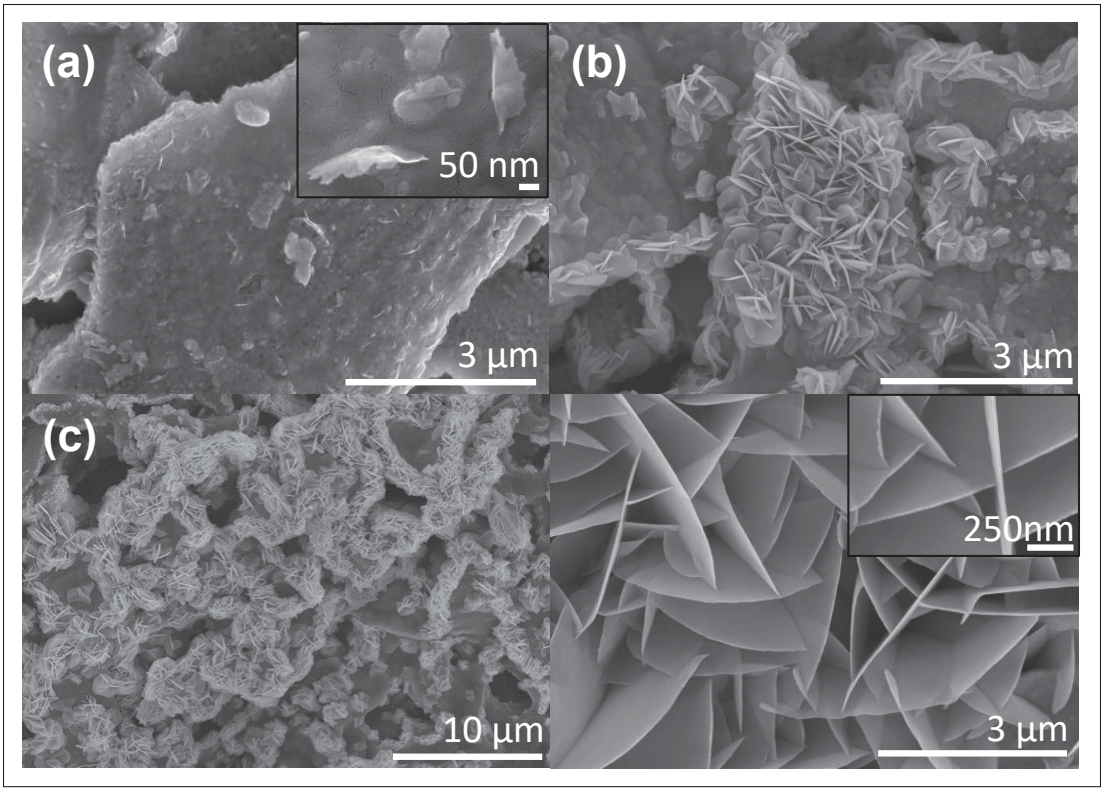

Figure 6.1 SEM micrographs. (a) BiOCl nanosheets outbreaks and heterojunction formation after 150 °*C* annealing. The inset shows an intimate contact between both structures. (b) BiOCl nanosheets formation initiated after 225 °*C* annealing. (c) Fully-grown BiOCl nanosheets after 300 °*C* annealing. (d) Micrograph of the dense networks of BiOCl nanosheets annealed at 300 °*C*. The inset is a high-resolution micrograph used for thickness determination

structure (ICDD card 01-083-7690). Keramidas, Voutsas & Rentzeperis (1993); Biswas, Das, Dey, Banerjee & Poddar (2014); Xu, Xu, Wang, Zhang & Li (2014) This spectrum also confirms that the nanosheets do not grow following a preferential facet and thus BiOCl nanosheets are randomly oriented all-over the surface of the film. The two other crystalline phases belong to BFO and Bi_2O_3. The BFO appears in a rhombohedral phase with a space group R3c (ICDD card 01-086-1518), while the Bi_2O_3 is an impurity state assigned to tetragonal group P-421c (ICDD card 00-027-0050). Ponzoni, Rosa, Cannio, Buscaglia, Finocchio, Nanni & Leonelli (2013); Ponraj *et al.* (2020) This Bi_2O_3 is a common secondary phase that appears during BFO synthesis due to the phase formation's kinetics and is also known to possess photocatalytic

properties. Weidong, Wei, Xiaohong, Xianbo, Long & Zhaohua (2007); Bernardo *et al.* (2011) In Figure 6.2(b) Raman micro-spectroscopy of the screen-printed cells after annealing confirms the presence of both BFO and BiOCl crystalline structures. From BFO spectrum, three main characteristic peaks can be seen at 73, 142 and 167 cm^{-1} and correspond to E_g, E_g and A_1 modes respectively. Wang, Luo, Han, Yun, Tang, Zhu, Nie, Zhao & Feng (2019b) All these modes are attributed to the displacement of Bi atoms cause by their lone pairs of $6s^2$ electrons along the z direction. Chauhan, Kumar, Chhoker & Katyal (2016) The other peaks at 56, 140 and 197 cm^{-1} are indicative of BiOCl crystallization. Xu *et al.* (2014) The first peak corresponds to A_1 external Bi-Cl stretching mode, while the second and third peaks are respectively A_1 and E_g internal Bi-Cl stretching mode. Shahid *et al.* (2020); Yan *et al.* (2019) In the BiOCl spectrum, some residual contribution from the BFO powders underneath can still be observed at 73 and 167 cm^{-1}. The low-concentration Bi_2O_3 phase is not detected in the Raman signal.

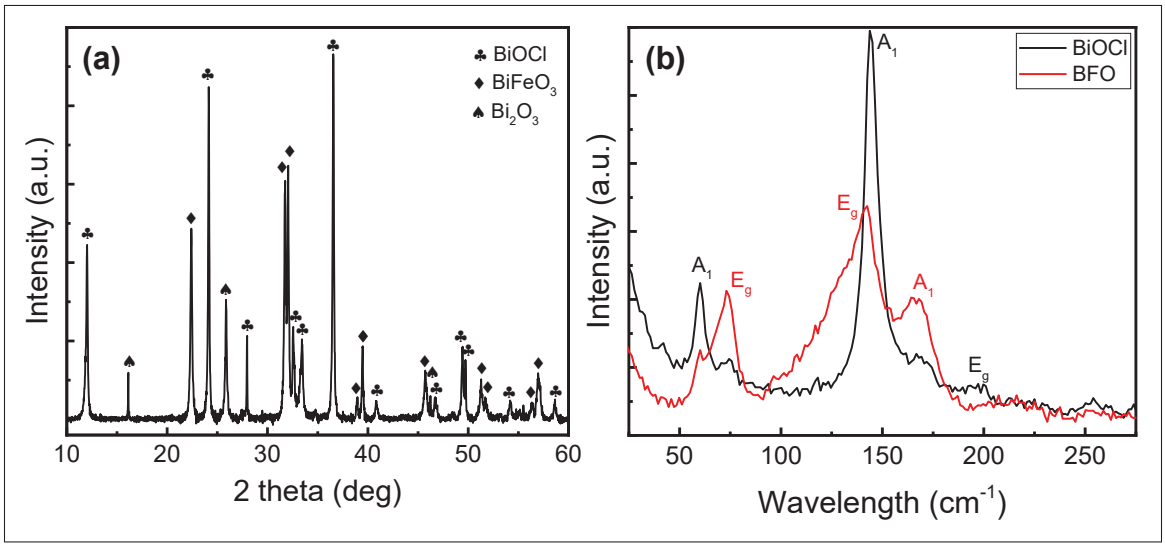

Figure 6.2 (a) XRD and (b) Raman spectra of the photocatalytic material after thermal annealing

In addition, Transmission Electronic Microscopy (TEM) can also be useful to appraise the crystalline structure of the nanosheets. In Figure 6.3(a), the high-resolution TEM micrograph shows nanosheets with multiple sets of lattice fringes depending on their orientation. The left and right fringes indicated by green lines possess a d-spacing of 0.728 *nm* corresponding to the

(001) atomic planes of BiOCl. The other fringes close to the center have a smaller d-spacing of 0.343 *nm* corresponding to (101) atomic planes. TEM micrograph of a typical individual BiOCl nanosheet and the selected area electron diffraction (SAED) pattern are presented in Figures 6.3(d-e), respectively. The calculated interplanar d-spacing is equal to 0.365 *nm* and can be attributed to the (002) atomic plane. These results are consistent with the previous XRD measurements. This layered development is typical from BiOCl structures. Zhang, Xu, Xing, Wang, Fu, Lin & Wang (2015c) Figures 6.3(b-c) show EDX measurements of the areas highlighted in Figure 6.3(a) to survey their elemental compositions. Both spectra suggest the presence of chlorine, bismuth, oxygen and validate the crystalline structure of the nanosheets. Copper and carbon signals stem respectively from the grid and mesh used for observation of the sample. Presence of iron is also detected in both spectra. It suggests that iron inclusion takes place while chlorine evaporates and reacts with BFO particles to create BiOCl nanosheets. Uniform distribution of these iron atoms is validated in Figure A IV-3 by EDX elemental mapping using TEM.

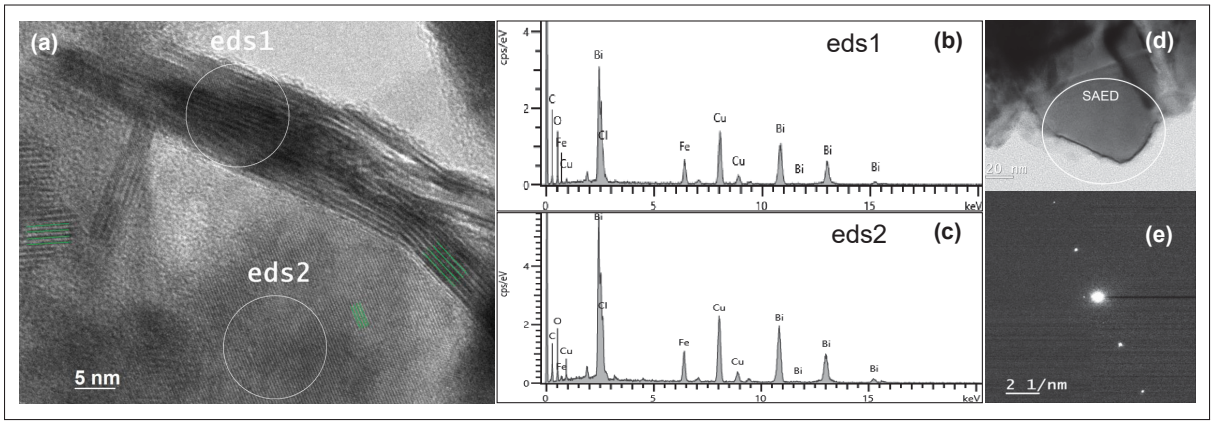

Figure 6.3 (a) High-resolution TEM image of BiOCl nanosheets atop of the $BiFeO_3$ powder. Green lines indicate lattice fringes, (b-c) Energy-dispersive X-ray spectroscopy (EDX) spectra of respective areas marked in (a). (d) TEM image of a single BiOCl nanosheet and (e) selected area electron diffraction (SAED) pattern of the area marked in (d)

Element mapping of the bismuth, oxygen and chlorine are also reported in Figure A IV-3 and confirm a uniform distribution. Transition metal doping and more precisely iron doping of BiOCl nanostructures have been previously reported in the literature for BiOCl. Wei *et al.*

(2021) Besides trapping and releasing electron-hole pairs, Fe atoms act as impurities. Indeed, impressive band-to-band transition enhancement in BiOCl structures have been measured at sub-bandgap energies. Huang *et al.* (2015); Shahid *et al.* (2020); Xia *et al.* (2013); Tian, Li, Zhao, Chen, Li, Liu & Chen (2019); Shen, Li, Lu, Wang, Li, Zhang, Zhang, Wang, Wang, Lv et al. (2021) Thus enhancement of photocatalytic properties can be achieved using Fe-doping compared to pristine BiOCl. Shahid *et al.* (2020); Xia *et al.* (2013); Tian *et al.* (2019); Shen *et al.* (2021) To assess the impact of iron atoms on the screen-printed photocatalytic cells, Ultraviolet-Visible-Near Infrared spectroscopy (UV-Vis-NIR) absorption spectroscopy measurement is shown in Figure A IV-4(a). As explained in the Experimental section, a thin layer of ink is deposited to enable this measurement. It indicates a strong light absorption under 400 *nm* in the UV region which is attributed to BiOCl. A contribution from iron impurities is also apparent as significant visible light is absorbed between 400 and 800 *nm* due to defect-mediated band-to-band transition. For comparison, the same measurement is performed on a printed photocatalytic cell before annealing and is shown in Figure A IV-4(b). The absorbance promptly decreases below 350 *nm* which validates that UV absorption is ascribed to BiOCl. Above 350 *nm*, the BFO absorption spectrum matches with previous reported results. Fourmont *et al.* (2021) Measurements reported in Figures 6.2 and 6.3 confirm that the crystalline structure of the nanosheets on top of the BFO powders matches with BiOCl. Depending on the atmosphere during crystallization, BFO can be either a p or n-type material, while BiOCl is known as a p-type material. Wu *et al.* (2015); He *et al.* (2014); Rojac *et al.* (2014a) In this study, BFO powders are considered as n-type since they are annealed in ambient atmosphere. Therefore, each junction between a BiOCl nanosheet and a BFO particle in Figure 6.1 acts as a local p-n heterojunction.

As shown in Figure 6.4, thermogravimetric analysis (TGA) measurements can be used to quantify the ink vehicle evaporation during annealing and to determine the residual photocatalyst weight involved during the RhB degradation reactions. In Figure 6.4(a), TGA measurement of the ink vehicle shows that most of the weight loss happens under 250 $°C$. In fact, an impressive 85% mass loss is observed between room temperature and 250 $°C$. After 250 $°C$, the mass loss

stabilizes and only 10.6% of the initial mass remains at 400 $°C$. This measurement is consistent with our hypothesis that the formation, size and density of the BiOCl nanosheets depend on the ink vehicle annealing, providing the Cl source for the growth process. Indeed, Figure 6.1 shows that the biggest nanosheets are achieved at 300 $°C$. In supplementary Figure A IV-2, EDX measurements of the printed cell before annealing confirm the presence of chlorine. In contrast, supplementary Figure A IV-5 shows a reference EDX measurement of the same ink vehicle deposited on silicon and annealed at 300 $°C$ for 1h. The EDX spectrum in Figure A IV-5(b) reveals the presence of chlorine, oxygen, carbon, silicon and platinum. The latest is added on purpose to avoid any charging effects during SEM imaging. All other elements come from the ink vehicle residues left after annealing. The main residual elements are carbon and chlorine, according to the intensity of the characteristic peaks of each element. In Figure 6.4(b), TGA measurement of the screen-printed ink is presented. It shows that 43.0% of the initial mass remains at 400 $°C$. This includes roughly the 33% loading used for the BFO powder in the ink vehicle, combined with the 10.6% leftovers from the ink vehicle measured in Figure 6.4(a). Thanks to both TGA measurements, a precise estimation of the amount of photocatalytic material can be obtained. To do so, the weight of the substrate is carefully measured before and after printing. Out of 10 printed photocatalytic cells, the weight of a single printed cell is estimated around 118 mg. As the BFO loading is confirmed to be 33%, some 39 mg of photocatalyst is present on each photocatalytic cell. Compared to similar studies reporting BiOCl/BFO heterojunctions for photocatalytic degradation of RhB, the amount of BiOCl/BFO photocatalyst is reduced by 22%. Shang *et al.* (2019) In this work, the authors reported the fabrication of BiOCl/BFO heterojunctions following a chemical acid etching of BFO powders. A 43% degradation of the RhB solution was performed in 75 min under visible light using a colloidal method.

To assess the performances of these screen-printed photocatalytic cells, we illuminate them using a solar simulator (AM 1.5G). A longpass filter ($\lambda \geqslant 400\ nm$) is implemented to remove any contribution from UV light as it can yield some photodegradation of the RhB. Wang *et al.* (2013) As we previously established, Fourmont *et al.* (2021) a thin layer of platinum is deposited

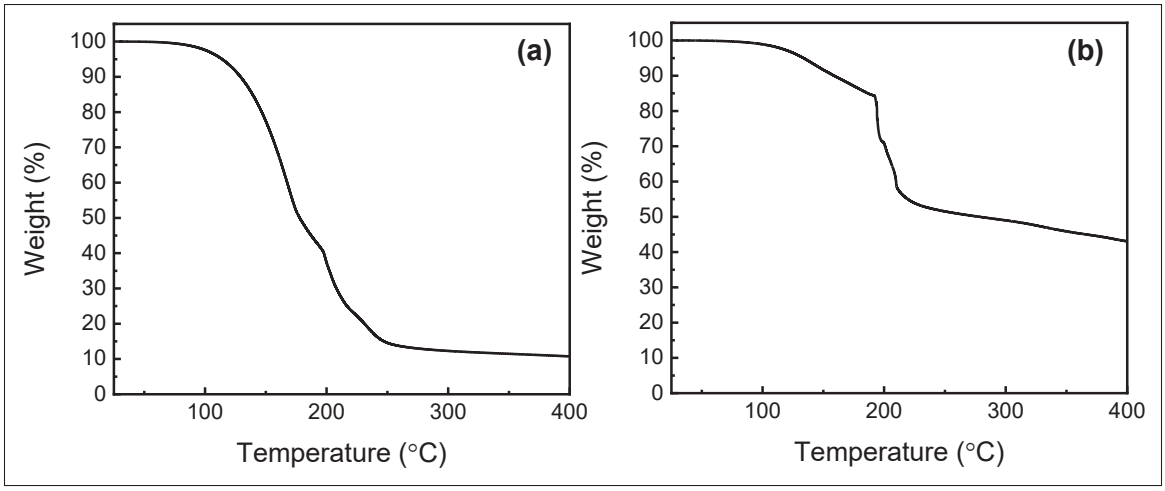

Figure 6.4 Thermogravimetric analysis of (a) the ink vehicle degradation over temperature (b) the ink vehicle and $BiFeO_3$ powder

atop of the annealed screen-printed cells by sputtering to enhance their photocatalytic properties. Adding this thin metallic layer is known to serve as an electron sink by acting as an efficient Schottky barrier. Sze *et al.* (2006); Yang (2021) Post-printing sputtering deposition of this thin layer has the advantage of being straightforward compared to more conventional photocatalyst materials decorated with metallic nanoparticles, which often requires complex processing steps and additional chemicals. Zhang, Liu, Shi & Ye (2018) Compared with sputtered films, nanoparticles tend to agglomerate into clusters to disrupt the photocatalytic reaction. Niu *et al.* (2015) Nevertheless, the thickness of the platinum film must be carefully optimized to avoid light absorption and decrease of photocatalytic properties. In fact, previous studies established that a 13 *nm* thick platinum coating deposited by sputtering yields only 50% transmission from 400 to 800 *nm*. Tompkins *et al.* (2000) In Figure 6.5(a), 2 to 12 *nm* thick platinum layers are sputtered atop of the screen-printed photocatalytic cells. A remarkable degradation of 92% is achieved for the 2 *nm* platinum-coated cell after 150 *min* under illumination at near neutral pH (pH = 6.1). For thicker platinum layers, the degradation steadily decreases from 92% RhB degradation to 90%, 83% and 73% for cells with 4, 8 and 12 *nm* platinum respectively. This phenomenon can be explained through the increased light absorption by the platinum layer. Hence, less light reaches the surface of the p-n BiOCl/BFO heterojunctions and the photocatalytic reaction is

hindered. In comparison, screen-printed photocatalytic cells without any platinum layer achieve only a 66% RhB degradation. This result proves that a thin film of platinum is an effective way to significantly enhance the photocatalytic reaction's efficiency.

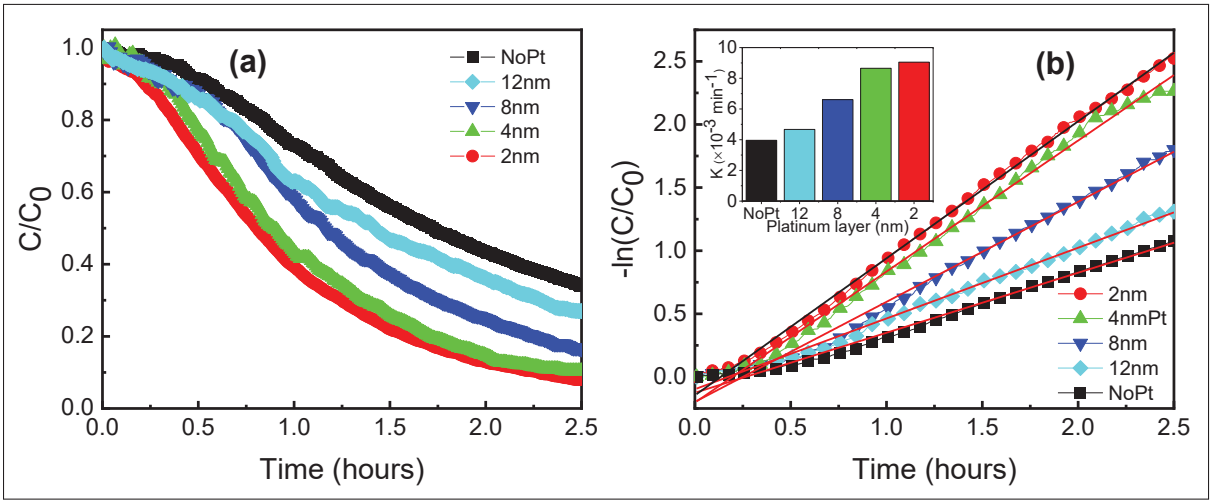

Figure 6.5 (a) Photocatalytic degradation of RhB for different thicknesses of platinum layers. (b) Linear curves used to determine the first-order kinetics of RhB degradation over time. The inset shows the values of the fitted curves' slopes (degradation rate)

As a control experiment, no measurable absorption-desorption reaction is recorded under dark conditions for all our photocatalytic experiments. Also, only 14% degradation can be achieved with over 150 *min* in Figure A IV-6(b), despite the presence of both platinum layer and H_2O_2. Compared with previous papers exhibiting up to 93% of RhB degradation under dark in 30 *min*, we conclude that the degradation in Figure A IV-6(b) can be considered negligible. Xiong *et al.* (2011); Yan *et al.* (2019); Sun, Cai, Xu, Zou, Hu, Jin, Sun, Li & Xia (2018); Gu, Zhao, Yang, Xiong, Wu, Zhou & Yan (2017b) Two conclusions can be drawn from this experiment. First, the photocatalytic degradation reactions are partially triggered by the light beam used to continuously measure absorption from the solution. Secondly, the degradation reactions of RhB necessitate light from the solar simulator to take place and the RhB degradation is not only triggered by combination of both platinum and H_2O_2. Therefore, RhB degradation takes place because of the photo-generated charge carriers in the catalyst, which in-turn triggers the chemical reactions between both H_2O_2 and platinum. Fourmont *et al.* (2021) Degradation curves of RhB

are fitted in Figure 6.5(b) and display a typical Langmuir-Hinshelwood behavior. Yan *et al.* (2019); Sun *et al.* (2018) R-square values higher than 0.99% are obtained for all degradation curves using the pseudo-first-order kinetic equation: $-ln(C/Co) = k_{app}t$, where C and C_o are live and initial concentrations of RhB, k_{app} is the apparent first-order kinetics model (min^{-1}) and t is the time. Gu *et al.* (2017b) The k_{app} values thus obtained are summarized in the inset of Figure 6.5(b). A maximum of 0.00905 min^{-1} is reached for the 2 nm platinum coated cells, while a minimum of 0.00396 min^{-1} is calculated for the reference cell without platinum. The photocatalytic cells with 4, 8 and 12 nm platinum layers display respectively k_{app} values of 0.00865, 0.00661 and 0.00467 min^{-1}. The k_{app} calculated values confirms that 2 nm platinum coated cell possesses a superior photodegradation reaction compared to the others screen-printed photocatalytic cells.

To account for the RhB degradation over time, absorption spectra taken each 20 min are shown in Figure 6.6(a). At $t = 0$, the maximum peak intensity of RhB is found at 553 nm and decreases promptly when the light is turned on. Low RhB concentration of a solution in the $mg\ L^{-1}$ range is known to be proportional to the absorbance. Kim, Hayashi, Nakatani, Kitamura, Sasaki, Hotta & Masuhara (1996) Therefore, the decrease in absorbance observed in Figure 6.6(a) indicates that photocatalytic reactions take place. Thanks to our colloidal free methodology, live monitoring of RhB degradation is achieved and allows a precise tracking of the degradation processes. Two different degradation mechanisms either the cycloreversion and the de-ethylation are involved. Pica, Calzuola, Donnadio, Gentili, Nocchetti & Casciola (2018) The former involves the cleavage of the whole chromophore structure and takes place in the bulk solution, while the latest leads to ethyl groups removal in a stepwise manner. Pica *et al.* (2018) De-ethylation happens when the RhB molecules are adsorbed on the catalyst surface. Pica *et al.* (2018) In that case, degradation reactions create byproducts like N,N,N'-triethyl-rhodamine or N,N'-diethyl-rhodamine with absorption peaks respectively located at 539 and 522 nm. Watanabe *et al.* (1977) In Figure 6.6(b), all the screen-printed cells exhibit a significant blue shift. For all the platinum-coated cells, a clear blue shift from 553 to 535-531 nm is observed after 30 min under illumination. This blue shift indicates that de-ethylation is the main degradation process

and can be explained by the action of active oxygen species on the N-ethyl group. Hu, Li, Wang, Zeng, Li & Shao (2015) In contrast, screen-printed photocatalytic cells without platinum exhibits a much smaller blue shift starting only after 60 *min* under irradiation. Maximum peak position moves from 553 to 546 *nm*. For all the screen-printed cells, this suggests that chromophore cleavage tends to be the dominant degradation mechanism at first, then de-ethylation becomes the most influent degradation mechanism.

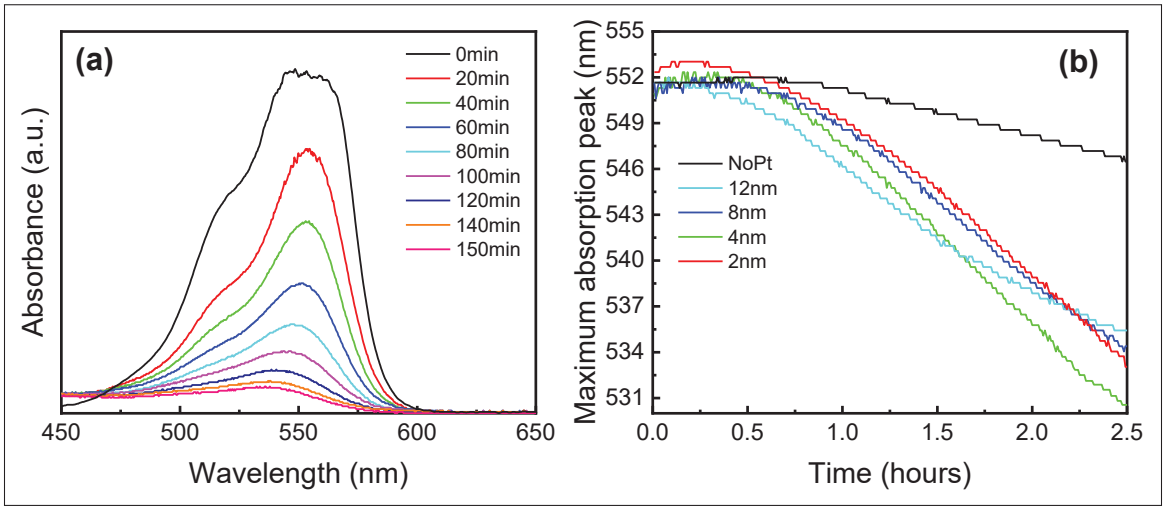

Figure 6.6 Evolution of the RhB spectra absorption during the photocatalytic degradation by the screen-printed photocatalytic cell coated with 2 *nm* of platinum. (a) Spectral evolution under illumination. (b) Maximum absorption peak position and its evolution over time

6.3 Conclusion

In this study, we report a colloidal-free synthesis using screen printing as a simple and effective deposition method to produce highly-efficient photocatalysis cells. Thanks to chemical reaction between the ink vehicle and the BFO powders during annealing, a dense network of interconnected BiOCl nanosheets is forming atop the BFO particle slurry to create local p-n BiOCl/BFO heterojunctions. Moreover, TEM measurements confirm the presence of iron impurities inside the BiOCl lattice. This phenomenon favours visible light absorption using impurities to trap and release photo-generated charges. These BiOCl sheet-like structures boast impressive aspect ratios with a thickness of 10 ± 2 *nm* and several microns in length. These

photocatalytic cells yield an impressive RhB degradation of 92% in 150 *min* under visible light, using a thin platinum layer of 2 *nm* is sputtered on the screen-printed cells to serve as an electron sink. This colloidal free configuration also enables an automated and live tracking of the RhB degradation by recording absorption spectra every 30 *sec*. Compared to BiOCl nano-catalysts usually made by hydrothermal methods, our acid-free approach drastically reduces the synthesis time and can be easily transferred to industry for large scale manufacturing. We hope this methodology will attract more attention as it solves two of the actual limits of photocatalysis which are the needs for UV sources and for catalyst collection and recovery protocols.

6.4 Experimental methods

6.4.1 Photocatalytic cells preparation

BFO powders are synthesized by a solvothermal method. At first, bismuth(III) nitrate pentahydrate [$Bi(NO_3)_3.5H_2O$] and iron(III) nitrate nonahydrate [$Fe(NO_3)_3.9H_2O$] are weight to form an equimolar ratio and dissolved in N,N-dymethylformamide. Polyvinylpyrrolidone is then added as a chelating agent. All the precursors are bought from Sigma-Aldrich and used as it without further purification. The obtained solution is mixed by using a planetary centrifugal mixer to ensure a good dispersion of all the chemical and then annealed for 2 *hr* at 520 $°C$ in ambient atmosphere. The screen-printed ink is then produced by mixing the BFO powders with an ink vehicle from Henkel named SOL 725. The loading of BFO powders is kept constant at 33%. A 325-mesh size is used to screen print the cells with dimensions of 17 by 12 *mm*. Anodized aluminum is used as a substrate. Compared to glass, the roughness of the oxide layer assures a good adhesion of the cells to the substrate. The BiOCl nanosheets on top of the BFO powders are then obtained by annealing the cells up to 300 $°C$ using a reflow oven (Mancorp, MC301N) in an ambient atmosphere. The last step is the deposition of a platinum layer by magnetron sputtering (using a Quorum, Q150T system).

6.4.2 Characterization methods

Micrographs of the cells are obtained by scanning electron microscopy (Hitachi, SU8230) to follow the growth of the BiOCl nanosheets. An EDX detector inside the SEM is used to perform elemental mapping (Bruker, QUANTAX FlatQUAD). Diffraction patterns of the screen-printed photocatalytic cells and phase identification are performed on a Bruker D8 Advance with a Cu Kα X-ray source. A confocal Raman microscope equipped with a 200 mW fiber-coupled continuous-wave laser at 532 nm is used to assess the crystalline structure of the BiOCl nanosheets (Witec, Alpha300). A working voltage of 200 kV is used for all the transmission electron microscopy (Jeol, JEM-2100F) measurements. This microscope is equipped with an EDX detector (Oxford, TEM Xplore) that permits a precise detection and elemental mapping of the chemical elements of both the BiOCl nanosheets and the BFO powder. Ultraviolet-Visible-Near Infrared spectroscopy is performed on a screen-printed cell before annealing to assess the contribution of BFO and on a 30 μm thick layer of the same ink deposited by drawdown bar method on a glass slide substrate. By using drawdown bar deposition method, it enables the light beam to go through the sample and allows a collection of the diffuse light by an integrated sphere (PerkinElmer, LAMBDA 750). Thermogravimetric measurements are performed with a flow rate of dry air of 50 $mL\ min^{-1}$ and a temperature ramp of 5 $°C\ min^{-1}$ (PerkinElmer, STA8000).

6.4.3 Photocatalytic activity tests

A 300 W xenon lamp assembled with a cutoff filter ($\lambda \geqslant 400\ nm$) inserted inside a solar simulator right after the AM 1.5G filter is used to avoid any UV light irradiation. The light intensity of the solar simulator (Newport, 91160-1000) is calibrated at 100 $mW\ cm^{-2}$ (1 sun). Thanks to our colloidal free methodology, a previously reported homemade setup allows an automated and live absorbance measurement. Fourmont *et al.* (2021) Each 30 sec, an absorbance spectrum within a wavelength range interval from 400 to 800 nm is recorded. All spectra are then analyzed using Matlab to extract the position of the maximum peak and its intensity. In each photocatalytic experiment, a 50 mL beaker is used to degrade 20 mL of a RhB solution set at a 5 $mg\ L^{-1}$ concentration. In the $mg\ L^{-1}$ concentration range, it is known that absorbance is proportional

to the dye concentration. Thus, RhB concentration can be calculated by dividing the initial absorbance by the live measured absorbance. All the photocatalytic degradations are performed at near neutral pH (pH= 6.1) and the reactant solution is maintained at room temperature to prevent any thermal effect. 7.5 mM of H_2O_2 from a 30% concentrated bottle is introduced to initiate the photocatalytic degradation. This concentration is found to be optimal as a lower H_2O_2 quantity results in less RhB degradation while higher quantity does not allow an effective recording of the reactions because of the bubbles formation. Fourmont *et al.* (2021) A control experiment without H_2O_2 is performed in Figure A IV-6(c). Negligible RhB degradation is detected despite the presence of the optimal photocatalytic cell. Thus, H_2O_2 is necessary to start the photocatalytic reactions.

Acknowledgement

The authors would like to thank both Victor Brial and Michael Dubois for their expertise with thermogravimetric measurements and Alain Picard for his help with the absorbance acquisition setup. The authors also thank Jean-Phillipe Masse for his fruitful discussions regarding the TEM measurements and Mohammad Saadati for his expertise in SEM/EDX measurements. The authors are grateful for the support of Henkel company by providing the ink vehicle used for this study. S.G.C acknowledges the NSERC-Discovery and Canada Research Chair programs for their financial support.

6.5 Additionnal studies

Following the photocatalytic characterizations of the BFO/BiOCl heterostructures, we investigate their ability to sense humidity. Indeed, both BFO and BiOCl have been recenlty reported in the literature for humidity monitoring. Chen, Feng, Huang, Yao, Jin, Pan & Liu (2020a); Douani *et al.* (2020) Thanks to the high surface-to-volume ratios of the BiOCl nanosheets in Figure 6.1, we took advantage of the impressive surface available for sensing and performed humidity measurements. Some preliminary results are shown in Figure 6.7. As the humidity increases from 15% to 85%, the resistivity of the device decreases and the opposite behavior is visible

when humidity decreases again to 5%. Further characterizations will determine the response time, the potential hysteresis and the stability over time. Different loadings of BFO powder in the ink vehicle are also of interest to obtain the biggest sensitivity.

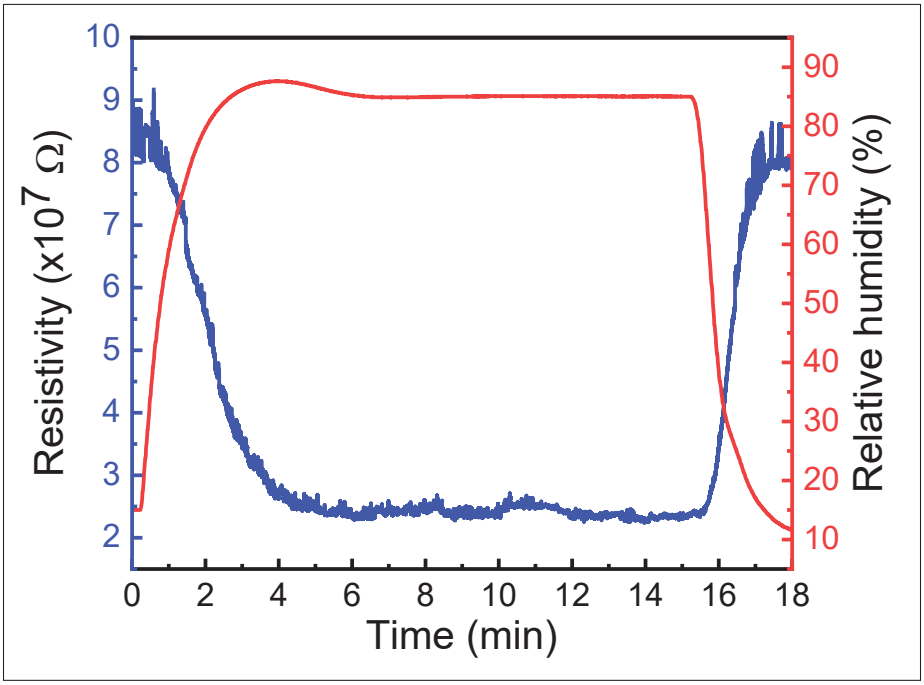

Figure 6.7 Resistivity and humidity over time of the screen-printed humidity sensor

To follow the objectives set in the introduction chapter, we used screen printing to fabricate all-printed humidity sensors. In Figures 6.8(a-b), we show screen-printed interdigitated electrodes made from nickel and silver inks respectively. All the electrodes are printed on kapton which is a flexible polymer-based substrate that can withstand 300 $°C$. In Figure 6.8(c), we present the humidity sensors made of an active layer printed atop the silver interdigitated electrodes. A humidity chamber was acquired in the first semester of 2022 by the electrical department of ÉTS and enables a precise control of the humidity and the temperature.

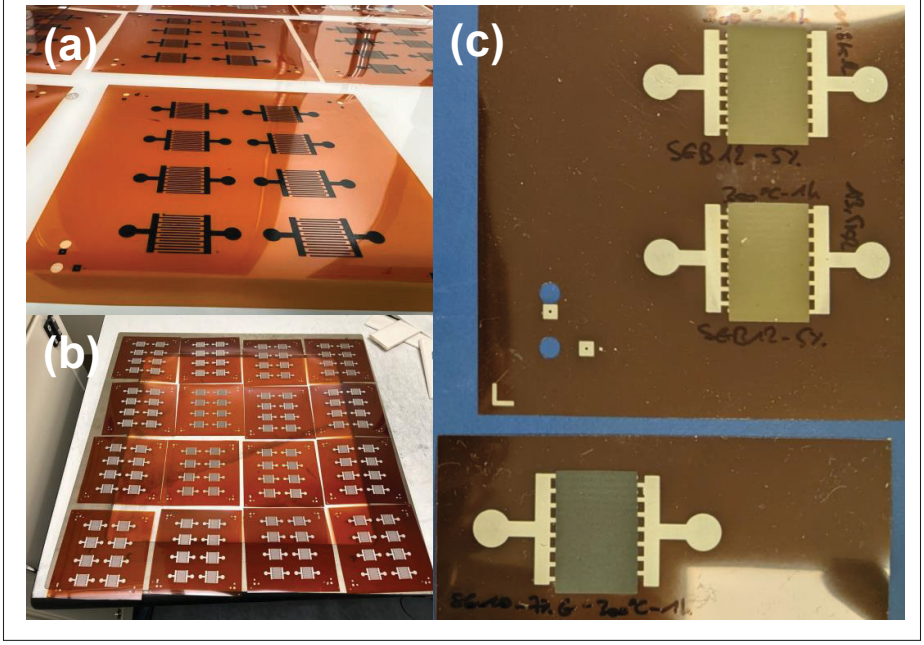

Figure 6.8 Images of screen-printed (a) nickel interdigitated electrodes, (b) silver interdigitated electrodes and (c) devices used to measure humidity

CHAPTER 7

GRAPHENE-ENHANCED SCREEN-PRINTED $BiFeO_3$-BASED THERMISTORS

Paul Fourmont[1] , Yin Bai[1] , François-Xavier Fortier[1] , Sylvain G. Cloutier[1]

[1] Department of Electrical Engineering, Ecole de Technologie Supérieure,
1100 Notre Dame West, Montreal, Quebec, Canada

Abstract:

In this study, serigraphic-grade $BiFeO_3$-based ink formulations are produced and then mixed with graphene to enhance the performances of screen-printed thermistor devices. The devices are printed atop a standard thermally-boosted glass-reinforced epoxy (FR-4) substrate coated with interdigitated gold electrodes. The broader operating temperature range of these thermistors makes them compatible with standard printed circuit boards (PCBs) manufacturing and operating conditions. Thus, we achieve highly-sensitive devices with a temperature coefficient of resistance (TCR) of -0.96 %/°C, which is the highest sensitivity reported yet for any graphene-based thermistor operating from 25 to 170 °C. The best performing devices are loaded with 3.5 wt.% graphene. These low-hysteresis and stable thermistors boast a thermal index (β-coefficient) of 864 K. This optimal graphene loading occurs just above the percolation threshold.

7.1 Introduction

Temperature sensors play a central role in many key applications ranging from wearables & health-monitoring to aircraft & structure-monitoring. Different kinds of sensor architectures can be used depending on the application. Among all commercial temperature sensing devices, the thermistors' high sensitivity (typically between -2%/°C and -6%/°C, at 25°C) allows detection of subtle temperature changes across a wide range of temperatures. Feteira (2009) Thermistors can be used for high-temperature sensing, where a typical thermal index (β) value of 3000 K to 5000 K is needed. However, they can also be used for special circuits and static random access memories, for which a much lower β-value (between 14 K to 170

K) is sufficient. Kumar, Bhatt, Kumar, Sharma, Kumar & Tripathi (2019); Michel, Biswas, Tiwary, Saenz, Hossain, Ajayan & Kaul (2017) Thermistors can be fabricated using different techniques including microfabrication Al-Mumen, Rao, Dong & Li (2013), pressing Zeng, Lu, Wang, Du, Ying & Liu (2014), tape casting Muralidharan, Sunny, Dayas, Seema & Resmi (2011) etc. Among these techniques, additive techniques can combine easy prototyping with cost-effectiveness Wong & Hernandez (2012).

To enable an additive manufacturing process compatible with the PCB industry's requirements, researchers investigated metal- and carbon-based materials. Printed silver Dankoco, Tesfay, Bènevent & Bendahan (2016) and nickel Turkani, Maddipatla, Narakathu, Altay, Fleming, Bazuin & Atashbar (2020) thermistors with TCRs at 0.22 %/°C and 0.3 %/°C respectively have been reported. For most carbon-based thermistors and RTDs, a maximum operating temperature below 100 °C is reported. Bendi, Bhavanasi, Parida, Nguyen, Sumboja, Tsukagoshi & Lee (2016); Yan *et al.* (2015); Tan, Nokhodchi & Münzenrieder (2021); Franco, Alves, Perinka, Tubio, Costa & Lanceros-Mendez (2020) Although some PDMS-based devices with low operating temperatures are relevant for medical applications, they are not compatible with PCB technology. Yan *et al.* (2015) For most PCBs, the operating temperatures can reach 110 to 130 °C. Therefore, we sought to investigate new materials for thermistor fabrication compatible with PCB operating temperatures.

Different ceramic materials are currently used to fabricate negative temperature coefficient resistors. Researchers modify the composition of ceramics according to the cation configuration model and Arrhenius relation for better performances. Macklen (1986) Transfer metal oxides with spinel crystal structure are widely used to fabricate negative temperature coefficient thermistors. Feteira & Reichmann (2010) However, the lack of interchangeability represents a great barrier for industrial manufacturing of ceramic-based devices. Feteira (2009); Kozhukh (2008); Lan, Yang, Chen & Yang (2020) Indeed, the fabrication of ceramic thermistors usually requires careful control of the annealing conditions, combining high temperatures (800-900 °C) and low-oxygen environments. Reimann *et al.* (2013)

Graphene also exhibits unique semi-metal behaviors due to its zero bandgap. Peres & Ribeiro (2009) As a result, its resistivity changes according to variation of temperature. Kuzubasoglu & Bahadir (2020) In turn, researchers have used graphene to fabricate flexible thermistors Bendi *et al.* (2016); Yan *et al.* (2015) and resistance temperature detectors (RTDs). Tan *et al.* (2021); Franco *et al.* (2020) Moreover, graphene's potential use for thermal conductivity enhancement Bilisik & Akter (2021) and mechanical property improvement Porwal, Grasso & Reece (2013); Nieto, Bisht, Lahiri, Zhang & Agarwal (2017) can also offer interesting possibilities.

$BiFeO_3$(BFO) was extensively studied as a promising material candidate with excellent electrochemical properties for energy and storage applications. Wang *et al.* (2020b), Ma, Li & Song (2020) The thermodynamic properties of BFO were previously investigated both theoretically and experimentally. However, its potential use as a Negative Temperature Coefficient of Resistivity (NTCR) material remains to be fully-understood. Wang *et al.* (2020b) NTCR materials show a decreasing resistivity with an increase of temperature. Feteira & Reichmann (2010) The dielectric constant of BFO was already shown to increase with temperature, Lu, Günther, Schrettle, Mayr, Krohns, Lunkenheimer, Pimenov, Travkin, Mukhin & Loidl (2010); Bhadala, Suthar & Roy (2019) and perovskite ceramics display better performances than spinel ceramics at high temperatures. Macher, Reichmann, Fruhwirth, Gatterer & Herzog (1996) Previous researchers have also tried adding Bi_2O_3 into transition-metal oxides as a sintering agent to repair the broken grids in recrystallization in order to fabricate thermistor devices. Torok (1955)

In this report, we first perform the synthesis of the BFO powder to be dispersed in order to obtain a segrigraphic-grade ink formulation. Then, we investigate the thermal properties of BFO ceramics with Bi_2O_3 impurities. In order to improve the performance of this NTCR material at low temperatures, we mix the BFO powder with graphene to enhance our ink formulation. This formulation is then optimized in order to achieve superior thermistor devices. Indeed, we combine the advantages of both materials (BFO and graphene) in order to fabricate thermistors devices operating at temperatures compatible with the PCB industry's requirements.

7.2 Results and discussion

7.2.1 Characterization of the $BiFeO_3$ powders

After thermal conversion of the $BiFeO_3$ (BFO) precursor solution into powder, X-Ray Diffraction (XRD) measurements are performed to evaluate the crystallinity and confirm the BFO phase. Sharp diffraction peaks in Figure 7.1(a) confirm the crystallization into a rhombohedral crystallographic phase, which is associated to group R3c (ICDD card 01-086-1518). Ponraj *et al.* (2020); Michel, Moreau, Achenbach, Gerson & James (1969) Impurity phase from bismuth oxide phase (Bi_2O_3) is also detected and identified by diamond shapes. This phase can be assigned to tetragonal group P-421c (ICDD card 00-027-0050). Ponzoni *et al.* (2013) Contributions from the secondary phases during crystallization of BFO have been extensively reported in the literature and attributed to the phase formation's kinetics. Bernardo *et al.* (2011); Rojac, Bencan, Malic, Tutuncu, Jones, Daniels & Damjanovic (2014b) To further assess the BFO's crystalline phase, Raman micro-spectroscopy measurement performed using a 532 *nm* laser for excitation is shown in Figure 7.1(b). According to group theory, BFO possesses 13 Raman-actives modes that can be classified as $4A_1$ and 9E modes. Wang *et al.* (2019b); He *et al.* (2013) In Figure 7.1(b), $3A_1$ modes at 139, 171 and 217 cm^{-1} are attributed to longitudinal-optical (LO) phonons [A_1(LO)]. Yang, Sun, Zhu, Liu & Wan (2008) The other peaks located at 74, 265, 311, 368, 465, 528 cm^{-1} are associated with transverse-optical E(TO) modes. Yang *et al.* (2008) Compared to XRD measurements, all the Raman peaks are ascribed to BFO phase and no trace of the low-concentration Bi_2O_3 crystalline structure can be detected.

Ultraviolet-Visible-Near Infrared (UV-Vis-NIR) absorption spectroscopy is performed on the BFO powder and shown in Figure 7.1(c). Significant absorption occurs at wavelengths below the band-edge (around 600 *nm*) due to electronic inter-band transitions. Such behavior is confirmed by a linear fitting of the Tauc plot in the inset of Figure 7.1(c). It suggests a bandgap energy of 2.15 *eV* for the BFO powder. Viezbicke *et al.* (2015), which is consistent with previous reports. He *et al.* (2013); Fourmont *et al.* (2021) To further investigate the morphology of the BFO powder, a Scanning Electron Microscopy (SEM) micrograph is presented in Figure 7.1(d).

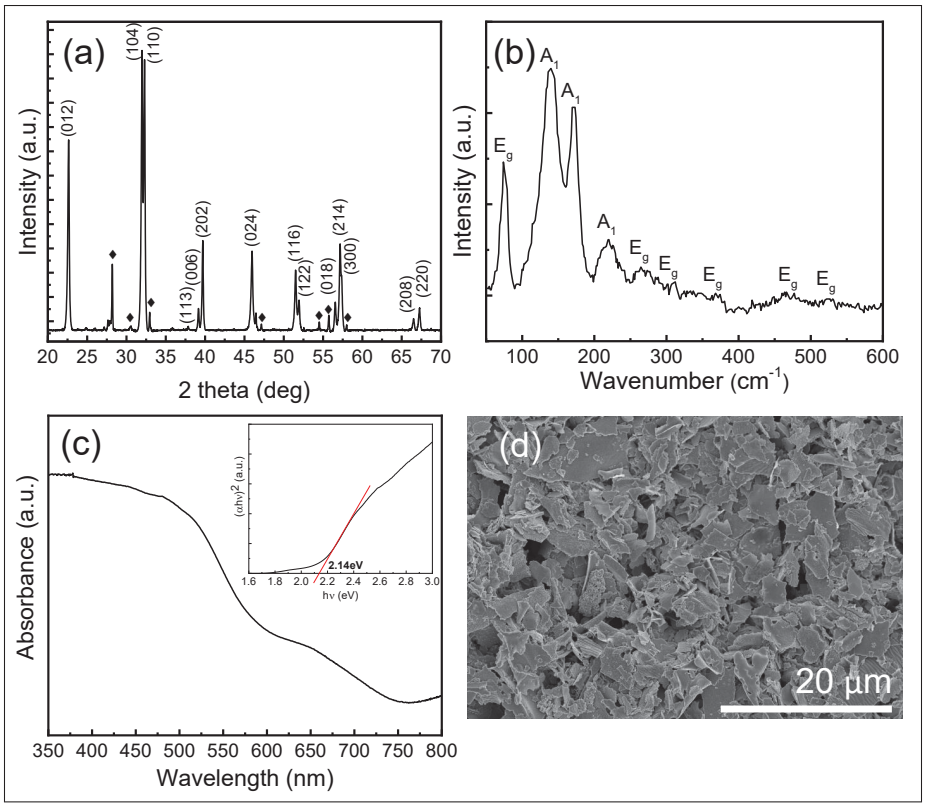

Figure 7.1 Characterization of the $BiFeO_3$ powders. (a) XRD spectra, diamond shapes indicate the Bi_2O_3 phase (bismuth oxide). (b) Raman spectra. (c) UV-Vis spectra with Tauc plot as an inset for bandgap determination. (d) SEM micrograph of the $BiFeO_3$ powders

The straightforward solvothermal synthesis yields micron-scale BFO sheets with a thickness around 200 *nm*. The size distribution of the particles is not homogeneous and varies from 1 to 15 μm. Figure A V-4(a-c) shows TEM micrographs of the BFO powder. In Figure A V-4(a), we observe a single monocrystalline layer of BFO powder. Each grain grows in a preferential direction and the visible fringes in Figure A V-4(b) allow us to measure the interplanar distance between the atoms. A d-spacing value of 0.281 *nm* is determined which can be assign to the (012) atomic plan. Figure A V-4(d-g) shows elemental mapping of Iron, Bismuth, Oxygen and Carbon respectively. No Bi or Fe rich phases are detected which imply a homogeneous distribution of each element. No carbon is also detected at the surface of the BFO particle.

7.2.2 Characterization of the BFO-based screen-printed thermistors

After a thorough characterization of the BFO powders, screen-printed thermistors are prepared by mixing BFO and Poly(pyromellitic dianhydride-co-4,4'-oxydianiline) amic acid solution in a 1:1 weight ratio. As explained in the Experimental section, this polymer is going through a polycondensation during thermal annealing to form polyimide (PI). The thermistors are directly printed atop custom gold interdigitated electrodes on a thermally boosted glass-reinforced epoxy laminate (FR-4) substrate presented in Figure A V-1. FR-4 is a common and reliable substrate used for printed circuit boards (PCBs). Heinig & Papaioannou (2017) For each screen-printed ink, a minimum of 5 devices are fabricated to calculate and extract all the properties of the thermistors. By doing so, a good reproducibility can be demonstrated. Both the substrate and the design of the interdigitated electrodes are chosen to ensure a good compatibility and an easy integration of the printed thermistors to the PCBs. To characterize the thermistor behavior, the electrical resistance over temperature of the BFO thermistors mixed with PI is presented in the inset of Figure 7.2(a). It shows that no electrical resistance can be measured below 161 $°C$. From 161 to 177 $°C$, the electrical resistance drastically decreases from 120 $M\Omega$ to 30 $M\Omega$. Like many metal-oxide materials, a negative temperature coefficient of resistance (NTCR) is observed for the BFO based-thermistors as the electrical resistance decreases while the temperature increases. Aleksic & Nikolić (2017) Thermistors based on BFO and PI are inadequate in the context of the PCB industry as they possess incompatible properties such as high operating temperature and high electrical resistance. Indeed, cost-effective PCBs usually possess operating temperatures around 110 to 130 $°C$. Nevertheless, high-temperature PCBs are required in some sectors like oil & gas or for automotives, where electronic systems need to operate from room temperature up to 200 $°C$. Aviño-Salvado, Sabbah, Buttay, Morel & Bevilacqua (2017)

To increase the operating temperature range of the screen-printed BFO based thermistors, we mixed graphene within the BFO ink formulation. By reducing PI quantity and introducing 3.5 wt.% of graphene, a higher operating temperature range is achieved as shown in Figure 7.2(a). The printed thermistors can operate from 25 $°C$ to 170 $°C$, while their electrical resistance decreases from 578 $k\Omega$ to 223 $k\Omega$. Hence, the thermistors show a clear NTC behavior. In

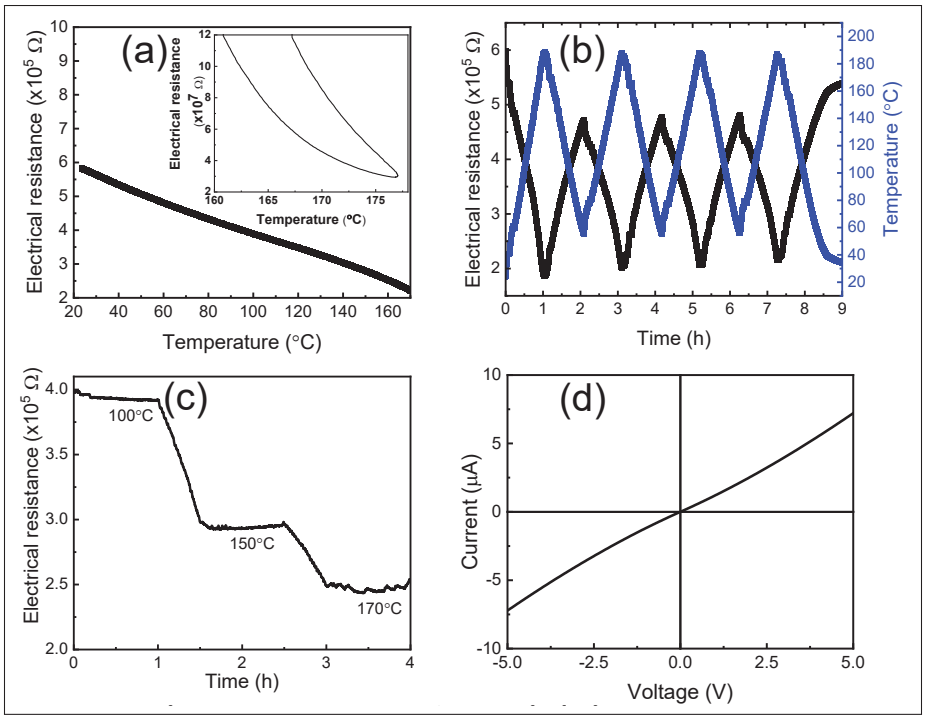

Figure 7.2 Thermistor's electrical resistance (3.5 wt.% graphene) (a) against temperature from 25 to 170 °*C* (the inset shows the electrical resistance of the $BiFeO_3$ thermistors without graphene), (b) for four cycles, (c) stability test, (d) IV curve at room temperature

Figure A V-2(a), we report all the data from the five printed thermistors with a 3.5 wt.% loading of graphene. In the context of a high-performance thermistor, key parameters include stability, reliability and durability. Feteira (2009) In Figure 7.2(b), the resistance of the thermistor is tested during four (4) heating and cooling cycles over a span of 9 *hr*. Both heating and cooling rates are set to one hour and show very little hysteresis (less than 3%). Figure 7.2(b) also shows operation slightly above 170 °*C* for short periods of time (under 20 *min*), while maintaining good device performances. In Figure 7.2(a), we chose to follow the PCB manufacturer's recommendations for the thermally-boosted FR-4 substrates by setting a maximum operating temperature of 170 °*C*. Nevertheless, previous studies about PCB aging and thermal endurance of FR-4 suggest that detrimental thermo-oxidative reactions are insignificant for such small periods of time such as used in Figure 7.2(b). Lahokallio, Hoikkanen, Vuorinen & Frisk (2015); Polanskỳ,

Prosr & Čermák (2014) Thus, alternative substrates such as ceramics or polyimides could be used to investigate the performance of these thermistor devices at higher temperatures. Lahokallio *et al.* (2015) In Figure 7.2(c), the 3.5% wt graphene thermistor is kept for 1 *hr* at 100, 150 and 170 $°C$. These stability tests suggest a constant resistance at a fixed temperature, except at 170 $°C$, where small variations of electrical resistance can be observed. We attribute these changes to the intermittent heater activation of the reflow oven to maintain the sample at the desired temperature. In Figure A V-3 we report the variation of temperature and electrical resistance for 1 *hr* at 100, 150 and 170 $°C$. Variations of temperature of 1 $°C$ are detected by the thermistor in Figure A V-3(b). This feature is of peculiar interest as it demonstrates a high sensitivity for this thermistor. Figure 7.2(d) shows the I-V characteristics of the device at room-temperature. A linear Ohmic behavior is clearly visible from -5 to 5 V. It indicates that the device acts as an ideal resistor and that the current is directly proportional to the voltage.

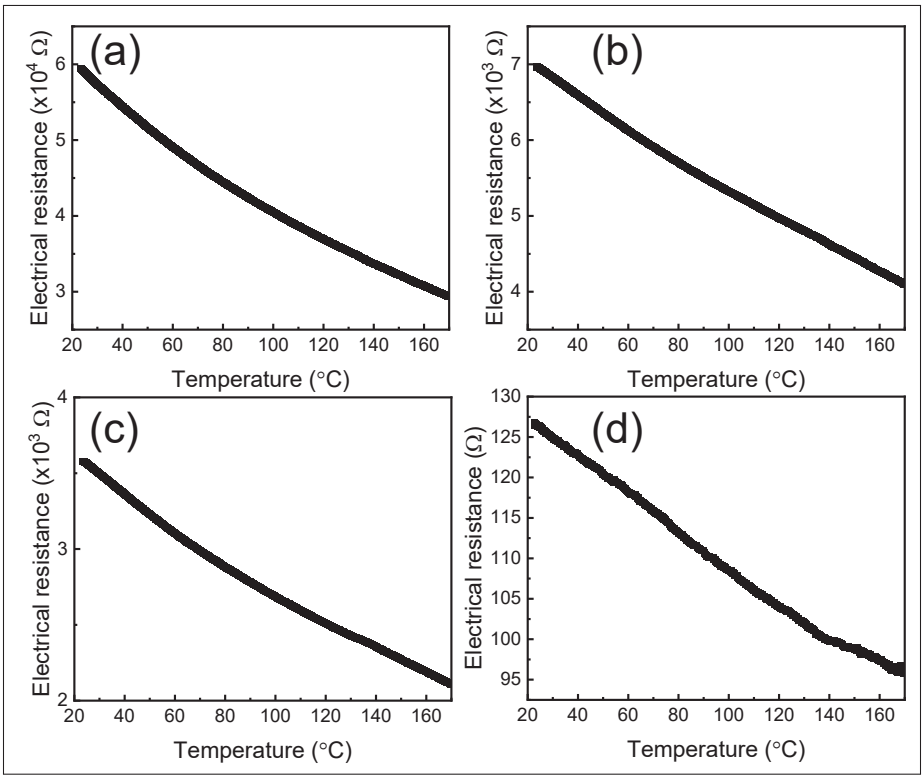

Figure 7.3 Thermistor's electrical resistance against temperature for different loading of graphene. (a) 4 wt.% (b) 4.5 wt.%, (c) 5 wt.% and (d) 20 wt.% graphene, without $BiFeO_3$ powder for reference

From Figure 7.2(a) and Figure 7.3, electrical parameters such as the thermal index (β), temperature coefficient of resistance (TCR) and activation energy (E_a) can be determined. All the printed thermistors in this study possess a dependence electrical resistance given by $R = R_0\ exp(\beta/T)$ with R_0 the electrical resistance at infinite temperatures, $\beta = E_a/2k$ with E_a the activation energy, k the Boltzman constant and T is the absolute temperature. Thus, thermal index and the activation energy can be described using the following equations Sarrión & Morales (1995):

$$\beta = \frac{lnR_1 - lnR_2}{(1/T_1) - (1/T_2)} \tag{7.1}$$

$$E_a = 2k\beta \tag{7.2}$$

where T_1 = 298 K, T_2 = 443 K, R_1 and R_2 the electrical resistance at 25 and 170 $°C$, respectively. The TCR (calculated at 300 K by convention) is estimated by the following formula Prudenziati (1994):

$$TCR = -\frac{\beta}{T^2} \tag{7.3}$$

All the main device characteristics of the best printed thermistor (with 3.5% graphene) are summarized in Table 7.1. From equations (7.1) and (7.3), a thermal index of 864 K and an impressive TCR value of -0.96 %/$°C$ are measured. Using equation (7.2), the activation energy is found to be 149 eV. Compared to other metallic or graphene-based printed thermistors reported in the literature, the thermistors loaded with 3.5% graphene exhibit the highest TCR coefficient for such large range of operating temperatures from 25 to 170 $°C$.

To further study the effect of graphene incorporation on the thermistor properties, different inks are synthesized and their device characteristics are compared in Table 7.1. Thermistors with BFO powder and graphene loading up to 5 wt.% are printed. The electrical resistances against

temperature of the thermistors are compared in Figure 7.3. In Figure A V-2(b-d), we show the data of the electrical resistances of the 5 printed thermistors for different graphene loading from 4 to 5 wt.%. As expected, the electrical resistance decreases as graphene is added. A difference of electrical resistance up to two (2) orders of magnitude is observed between the 3.5 wt.% and the 5 wt.% graphene-loaded thermistors at room temperature. This phenomenon can be attributed to the formation of denser conductive networks of graphene. Zeng *et al.* (2014) Figure A V-5 shows TEM micrographs of the graphene nanopowders. In Figures A V-5(a-c), high-resolution TEM micrographs show many-layer graphene and Figure A V-5(d) shows agglomerated graphene nanopowder As shown in Table 7.1, the thermal index (β) decreases from 864 to 502 K and the TCR also decreases from -0.96 to -0.56 $\%/°C$ when the graphene loading increases from 3.5 wt.% to 5 wt.%. We tentatively explain this behavior because of the poor graphene dispersion which can cause heat retention at the interfaces between the flakes and within the flakes. Sehrawat, Islam & Mishra (2018) Figure A V-6 shows a SEM micrograph of the printed ink with a 5 wt.% loading of graphene. In Figure A V-6(b,c), we show the carbon distribution mapping and its intensity mapping. The carbon is well dispersed on all the surface of the BFO powder but some agglomerations of the graphene nanopowder of 1 μm are visible. Interestingly, the 4.5 wt.% and 5 wt.% graphene thermistors show very similar performances. This behavior can be explained by the entanglement of dense conductive networks above percolation. Moreover, compared to other polymers-based thermistors, polyimide is chosen in this study because of its low thermal expansion coefficient. Numata, Kinjo & Makino (1988) This parameter is beneficial to avoid breakdown of interconnected graphene and BFO powder networks. Zeng *et al.* (2014) Figure A V-7(a-b) shows XPS analyses of N 1s and Fe 2p that can be attributed to polyimide and BFO powder respectively. Giraldo, Almodóvar, López, Rodríguez-Aguado, Rodríguez-Castellón, Galdámez & Álvarez-Serrano (2021); Woo, Park, Jung, Jeon & Seol (2011) For all the printed ink no obvious difference can be seen implying that no degradation can be observed for polyimide and BFO powder. These results are expected as polyimide is known to for its good thermal stability under 200 $°C$. Numata *et al.* (1988) In Figure A V-7(c), XPS spectra of C 1s show a decrease of intensity at 285.5 and 288 eV when the total weight of graphene increases. Woo *et al.* (2011) These changes can be attributed to the variations of the ratio polyimide/graphene.

In previous works on reduced graphene oxide-based thermistors, similar TCR coefficients for 4 wt.% and 5 wt.% loaded devices have been reported. Sehrawat *et al.* (2018)

Ink composition			Thermistor performance		
$BiFeO_3$ (%)	Polyimide (%)	Graphene (%)	Thermal index (K)	TCR (%/°C)	Activation energy (meV)
50	46.5	3.5	864 ± 64	-0.961 ± 0.07	149 ± 11
50	46	4	642 ± 13	-0.693 ± 0.014	108 ± 2
50	45.5	4.5	501 ± 34	-0.557 ± 0.037	86 ± 6
50	45	5	502 ± 13	-0.558 ± 0.015	86 ± 2
0	80	20	250	-0.278	43

Table 7.1 Ink composition of the printed thermistors and their performances

To assess the contribution of graphene, a thermistor without BFO powder is presented in Figure 7.3(d). Up to 20 wt.% of graphene can be added to the polyimide precursor solution to maintain a viscosity suitable for screen printing. This pure graphene thermistor exhibits a NTCR behavior and the electrical resistance at room temperature is one order of magnitude lower than the thermistor with 5 wt.% graphene. Without BFO powder, the thermistor also exhibits significantly inferior performances. A thermal index of 250 K and a TCR of -0.278 %/°C are determined using equations (7.1) and (7.3) respectively. In addition, 3 wt.% graphene thermistors are printed and tested between 25 °C and 170 °C. Even though the upper limit for resistivity measurements of the data logger is set to 120 $M\Omega$, no electrical resistance can be measured for this range of temperature. This result implies that a fine tuning of the graphene amount during the ink preparation is crucial to maximize the device performances. The quality of dispersion of a carbon source within a polymer matrix directly correlates with its effectiveness for improving electrical, mechanical, or thermal properties. Stankovich, Dikin, Dommett, Kohlhaas, Zimney, Stach, Piner, Nguyen & Ruoff (2006) In this last study, the authors report that polystyrene composites prepared with graphite oxide consisting of several-nanometer-thick multilayer stacks possesses higher electrical percolation thresholds compared to individual graphene sheets. Some studies show that the conductivity of the composite mixed with graphene oxide first increases until a loading of 0.1 wt% then the conductivity decrease while the loading reach

0.3 wt%. Yu, Huang, Rhodes, Fang & An (2017) The authors attribute this behavior to the stacking of graphene-oxide sheets that can lead to both carbon-rich and carbon-poor phases within the composite. Decrease of the positive temperature coefficient intensity is also reported at high carbon-nanotubes loading. Zeng *et al.* (2014) These findings demonstrate that the optimal performances of the devices are highly sensitive to the amount of graphene. Zeng *et al.* (2014); Yu *et al.* (2017) The drastic change of electrical resistance between the 3 wt.% and 3.5 wt.% graphene indicates the percolation threshold. Zeng *et al.* (2014); Yu *et al.* (2017) Similar experiments involving carbon nanotubes or graphene oxide-based thermistors demonstrate that small loading variations can change the electrical resistance by several orders of magnitude. Zeng *et al.* (2014); Yu *et al.* (2017)

In Figure 7.4, the conductance of all the printed thermistors is shown as a function of temperature. As expected, the devices loaded with 5 wt.% graphene show the highest conductance. The NTCR behavior of all the thermistor is also clearly visible as the conductance increases with the temperature. The best devices are loaded with 3.5 wt.% graphene, the conductance varies from 0.017 to 0.045 $\times 10^{-4}\ \Omega^{-1}$ at 25 and 170 $^{\circ}C$ respectively. This loading is consistent with previous studies using reduced graphene oxide. Sehrawat *et al.* (2018) Compared with the state-of-the-art, Table 7.2 shows that our 3.5 wt.% graphene-loaded devices exhibit the highest TCR value for all graphene-based printed thermistors reported so-far for such a large operating temperature range.

Among many parameters, the particle size is an important characteristic known to influence the conductivity of the thermistors. Wang, Ouyang, Huang, Huang, Yang, Guo, Wu, Zhang & Wen (2021a); Ikegami, Arima, Tosaki, Matsuoka, Ai, Minorikawa & Asahino (1980) An optimized mix of long- and short-range conductive networks is necessary to reduce the percolation threshold of particles, which in turn enhances both electrical conduction and stability. Wang *et al.* (2021a) Here, the graphene provides short-range conductive channels, while the micron-size BFO powder provides a long-range conductive network. For pristine graphene, the conductance is expected to be minimum as the Fermi energy is situated at the charge neutrality point (Dirac point). Sehrawat *et al.* (2018) Nevertheless, in the context of a temperature sensor the presence of heat or a temperature gradient will act as an external stimulus. Sehrawat *et al.* (2018) Consequently, the

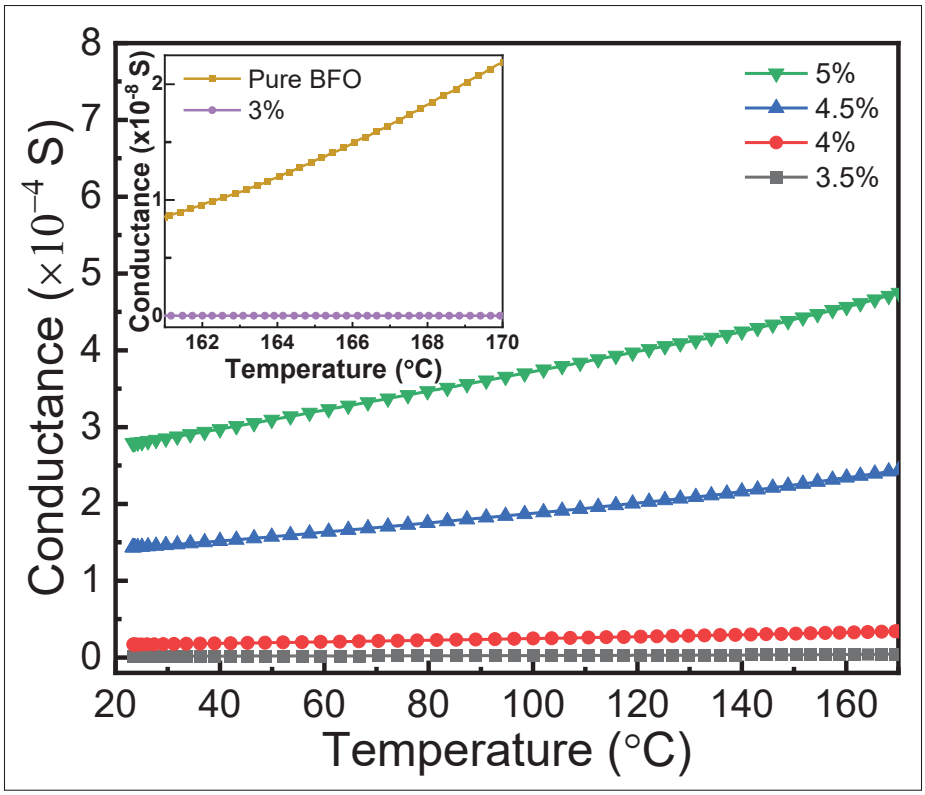

Figure 7.4 Comparison of the conductance of all the $BiFeO_3$ thermistors for different loading of graphene. The inset shows the conductance for the thermistors without graphene and with 3 wt.% graphene

entire band structure can be shifted and the density of states near the Fermi energy will be affected. Sehrawat *et al.* (2018) For graphene-based thermistors, the electrical resistance relies on a competition between both semiconducting and metallic behaviors. Yan *et al.* (2015) The former exhibits a negative TCR (NTCR) behavior dominated by thermally-activated charge carriers, while the later exhibits a positive TCR (PTCR) behavior dominated by charge carrier scattering. Yan *et al.* (2015) These behaviors depend on many parameters such as crystallinity, carrier density, number of layers and defects. Skákalová, Kaiser, Yoo, Obergfell & Roth (2009) From the results shown in Figure 7.3(d), the thermistor device without BFO powder exhibits a clear NTC behavior. Consequently, a semiconductor behavior providing thermally activated charges is expected to be the main mechanism responsible for the change of resistance for this thermistor. We believe the BFO powder morphology shown in Figure 7.1(d) is beneficial for the

thermistors' properties as each particle can act as a capacitor when graphene is introduced. Wang, Lu, Li, Li, Ji, Feteira, Zhou, Wang, Zhang & Reaney (2021b) In fact, the simplest capacitor architecture can be represented as two conductive plates separated by a dielectric medium. Wang *et al.* (2021b)

Depending on the processing parameters, BFO is known to act as either a p-type or n-type material. Maso & West (2012); Rojac *et al.* (2014b) Some studies also report that atomic substitution or doping can create oxygen- or cation-vacancies, which will drastically impact the conductivity. Maso & West (2012); Gebhardt & Rappe (2018) In that case, the stoichiometry will directly influence the grain shape and size, which are key parameters. Despite various methods developed to synthesize BFO particles, the activation energy can be used to estimate the type of charge carrier involved in the conduction mechanism. Makhdoom, Akhtar, Khan, Rafiq, Hasan, Sher & Fitch (2013) Ionic conduction usually dominates for $E_a > 900\ meV$, which is not the case in this study. Makhdoom *et al.* (2013) Otherwise, p-type polaronic hopping should dominate for $E_a > 200\ meV$, while n-type hopping usually dominates for $E_a < 200\ meV$. Makhdoom *et al.* (2013) In this work, all the printed thermistors display an activation energy E_a smaller than 200 meV as shown in Table 7.1. Thus, the main conduction mechanism can be attributed to n-type polaron hopping. This hopping conduction mechanism is well established and confirmed by previous reports. Wu, Wang, Xiao & Zhu (2011); Saravana Kumar, Aswini & Venkateswaran (2014); Arya, Kotnala & Negi (2014) These E_a values are consistent with the energy needed for polarons to hop between Fe^{2+} to Fe^{3+}. Ke, Lou, Wang & Wang (2010) As such, the behavior of polarons at the heterojunctions between the BFO powder and the graphene are beneficial for the thermistors' performances. We assume that the improvement of our thermistor device is due to synergetic effect of BFO and graphene. Zhu, Yang, Liu, Liu, Zhang, Chu, Wang, Yan, Li & Zou (2020)

Material	Temperature Range	Slope (TCR)	Thermal Index (B)	Fabrication Method	Reference
Graphene + cellulose	40 - 100 $°C$	-0.6 %/$°C$	-	Screen printing	Franco et al. (2020)
Graphene + PDMS	25 - 75 $°C$	0.008 /$°C$	-	3D Printing	Wang et al. (2018)
Graphene oxide	25 - 85 $°C$	-	1077	Inkjet printing	Kong et al. (2012)
Reduced graphene oxide	25 - 45 $°C$	0.0013 /$°C$	-	Spray printing	Ozek et al. (2021)
Graphene polylactic acid filaments	15 - 80 $°C$	-0.49 %/$°C$	-	3D Printing	Tan et al. (2021)
Mono-layer of graphene	25 – 80 $°C$	-0.003 /$°C$	-	Microfabrication	Al-Mumen et al. (2013)
Bi-layer of graphene		-0.007 /$°C$	-		
Few-layer of graphene		-0.0015 /$°C$	-		
Graphene in PDMS (0% strain)	30 - 100 $°C$	-1.05±0.28 %/$°C$	847	Lithographic filtration	Yan et al. (2015)
Graphene-coated polypropylene fibers	30 - 45 $°C$	-0.0017 /$°C$	-	Dip coating	Rajan et al. (2020)
$BiFeO_3$ + 3.5 wt.% graphene	25 - 170 $°C$	-0.961 %/$°C$	864	Screen Printing	This work

Table 7.2 Comparison with the reported thermistors and temperature sensors

7.3 Conclusion

In this study, we report high-performance thermistor devices fabricated using straightforward screen printing methods compatible with PCB manufacturing and operating temperatures. By mixing BFO powders and carefully-controlled quantities of graphene, a percolation threshold slightly above 3 wt.% graphene is determined. The best thermistor devices are obtained with a loading of 3.5 wt.% of graphene and exhibit a TCR of -0.96%/°C, along with a high thermal index of 864 K. This TCR is the highest value reported for graphene-based printed thermistors for such a large operating temperature range. At these concentrations, the graphene enables a wide operating temperature range from 25 to 170 °C. Increasing the graphene concentration beyond 3.5% leads to denser networks of graphene and a poorer distribution, which appears to be detrimental for the device performances. Compared to metal oxide-based thermistors requiring very complex and precise stoichiometry along with sintering temperatures above 1000 °C, we propose a facile solvothermal methodology that uses a temperature synthesis of only 520 °C. These findings are valuable as these temperatures are compatible with standard PCB manufacturing and operation conditions.

7.4 Experimental methods

7.4.1 Material synthesis

The $BiFeO_3$ powders are synthesized by a simple solvothermal method. Fourmont *et al.* (2021); Das *et al.* (2020); Fourmont & Cloutier (2022) First, equimolar ratio of bismuth(III) nitrate pentahydrate [$Bi(NO_3)_3{\cdot}5H_2O$] and iron(III) nitrate nonahydrate [$Fe(NO)_3{\cdot}9H_2O$] are weighted and dissolved in N,N-dymethylformamide. Then, polyvinylpyrrolidone is added as a chelating agent. The precursors are bought from Sigma-Aldrich and used as received without further purification steps. This solution is thoroughly mixed using a planetary centrifugal mixer and annealed for 2 hr at 520 °C in air. The screen-printable inks are obtained by mixing the resulting BFO powders along with Poly(pyromellitic dianhydride-co-4,4'-oxydianiline) amic acid solution and graphene. To ensure a good dispersion of both the BFO powder and the commercial

graphene (bought from SSnano), a two-step process is developed. At first, a planetary centrifugal mixer (Thinky, model ARE-310) is used during six cycles of 1 min at 2000 rpm. Then an ultrasonication homogenizer probe (RUPTOR 400 by OMNI INTERNATIONAL) is utilized overnight at low power to prevent solvent evaporation. After screen printing, the printed thermistors are annealed at 200 $°C$ for 15 min in an oven to ensure a complete polymerization. At this temperature, a polycondensation happens between a diamine and a dianhydride which forms polyimide (PI). PI is used as a binder as it can withstand high temperatures (over 300 $°C$) and possesses good bonding properties with metal oxides. Wilson, Stenzenberger & Hergenrother (1990) All the prepared inks are loaded with 50% of BFO powders while the amounts of PI and graphene are adjusted. Appropriate amounts of graphene are varied between 3.5 and 5% of the total solution weight, while the PI varies from 45 to 46.5%.

7.4.2 Characterization methods

Diffraction patterns of the BFO powders and phase identification are performed on a Bruker D8 Advance with a Cu Kα X-ray source to assess crystallinity. The micrographs of the screen-printed thin films are done using scanning electron microscopy (Hitachi, SU8230). This microscope is equipped with an EDX detector that allows a precise mapping of carbon (Bruker, QUANTAX FlatQUAD). Transmission electron microscopy is used to study the BFO powder and the commercial graphene (Jeol, JEM-2100F). Elemental mapping of a BFO particle is carried out with an EDX detector (Oxford, TEM Xplore). The chemical status of the printed films is determined by X-ray photoelectron spectroscopy (Thermo Fisher, VG ESCALAB 250Xi). All the cycling and stability measurements are performed using a reflow oven (Mancorp, MC301N). Electrical resistance and IV curves of the thermistors are obtained using a data acquisition unit (Keithley, DAQ6510) and a source-measure unit (Keithley, 2400).

7.4.3 Thermistor configuration

All the devices are screen-printed using a screen with a 325-mesh size. Dimensions of the printed devices are 16 mm by 11 mm. They are deposited atop a standard thermally-boosted

glass-reinforced epoxy flame-retardant four (FR-4) substrate coated with interdigitated gold electrodes. This printed circuit board was designed by our team and purchased commercially (PCBway). The devices are then cured for 1 h at 200 $°C$ to ensure the polymerization of polyimide. The distance of all the interdigitated gold electrodes is kept constant at 500 μm for this study. The fingers are 22 mm long by 500 μm width with a thickness of 35 μm. Electrical resistance measurements are performed using polyimide-coated wire with a 28 gauge.

Acknowledgement

The authors thank Arjun Wadhwa, François-Xavier Fortier and Alexandre Perrotton for the design of the PCB substrate. Sylvain G. Cloutier acknowledges the NSERC-Discovery program, the Canadian Department of National Defence (DND) and the Canada Research Chair program for their financial support.

CHAPTER 8

ONGOING WORK

In this chapter, we introduce BFO related research projects that have demonstrated significant promise as evidenced by preliminary results.

8.1 Photonic curing of $BiFeO_3$ films

Photonic curing is a thermal process that enables the crystallization of thin films using a pulsed light from a flashlamp. This method fits perfectly with our objectives set in the introduction chapter, as it represents an industry-ready process. More importantly, this process allows the crystallization of BFO thin films on polymer-based substrates, which is not reported yet in the literature. As the pulse duration is fast (usually in the micro to millisecond range), the substrate integrity is preserved and only the conductive film atop is cured. Without any doubt, this technology can unlock the fabrication of low-cost, innovative and performing BFO-based devices especially for sensing and energy-harvesting applications.

We chose to crystallize BFO thin films by photonic curing on both glass and kapton substrates. In Figure 8.1, we report crystallized BFO on glass substrate. The parameters giving the highest crystallinity and the lowest secondary phases are found at an energy density of 8.6 $J\ cm^{-2}$ for 20 pulses in Figure 8.1(a). Below 20 pulses, the BFO phase is less crystalline and two peaks around 27.5° are attributed to secondary phases. To obtain such results, we used a PulseForge Invent (from Novacentrix) platform equipped with a 150 mm length xenon flash lamp and three lamp drivers (950 V 1.5 kW). The lamp drivers enable customizable and intermittent light pulse from 30 microseconds to hundreds of milliseconds.

Despite good preliminary results, we chose to put on hold this project to develop our own sol-gel recipe to solve some drawbacks inherent to the solvothermal solution. In fact, the use of this solvothermal recipe lead to inconsistent results and partial conversion of the films. In addition,

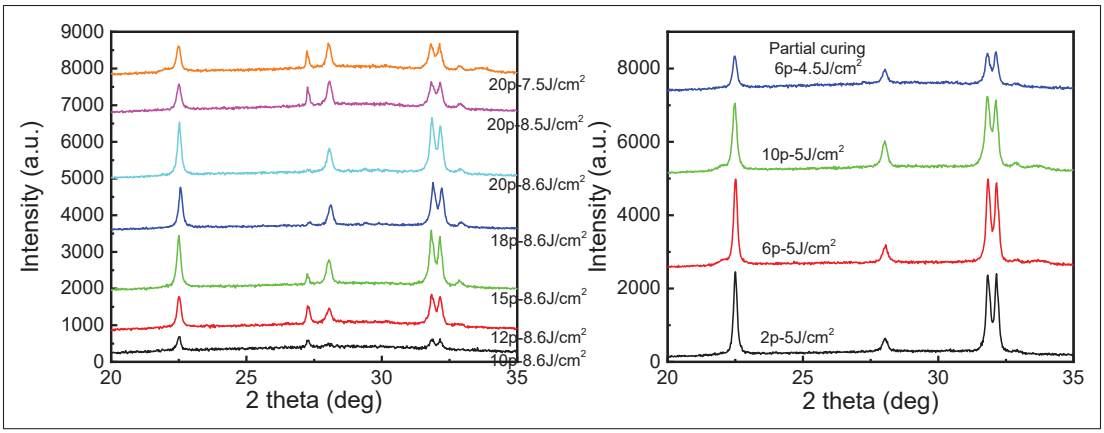

Figure 8.1 XRD spectra of photonic-cured $BiFeO_3$ thin films on glass substrate. Graph (a) shows the influence of the number of pulses on the $BiFeO_3$ crystallization and (b) demonstrates a reduction of the density energy needed to crystallize $BiFeO_3$ when 0.1 wt.% of graphene is added

the solvothermal solution appears to be highly sensitive to humidity which is problematic during the summer season in Montreal.

Moreover, addition of very small graphene quantities (0.1 wt.%) to the BFO solution before flashing was investigated. We demonstrate in Figure 8.1(b) a 40% reduction of the energy density needed to crystallize BFO. We ascribe the reduction of energy density to a better light absorption. In addition, the number of pulses is reduced from 20 to 2 if we compare Figure 8.1(a) and Figure 8.1(b) when mixed with graphene. The XRD measurements in Figure 8.1(b) reveal a good conversion of the film with only one peak of secondary phase at 28° that can be attributed to Bi_2O_3.

8.2 Pyrophotoelectric effect

This project aims to determine the thermal properties of BFO such as the thermal diffusivity and the thermal effusivity. The results stem from a collaboration with Dr Dorin Dadarlat from the National Institute of Isotopic and Molecular Technology in Romania. Very scarce measurements are reported yet in the literature regarding photopyroelectric characterizations of BFO and it motivated us to explore this topic.

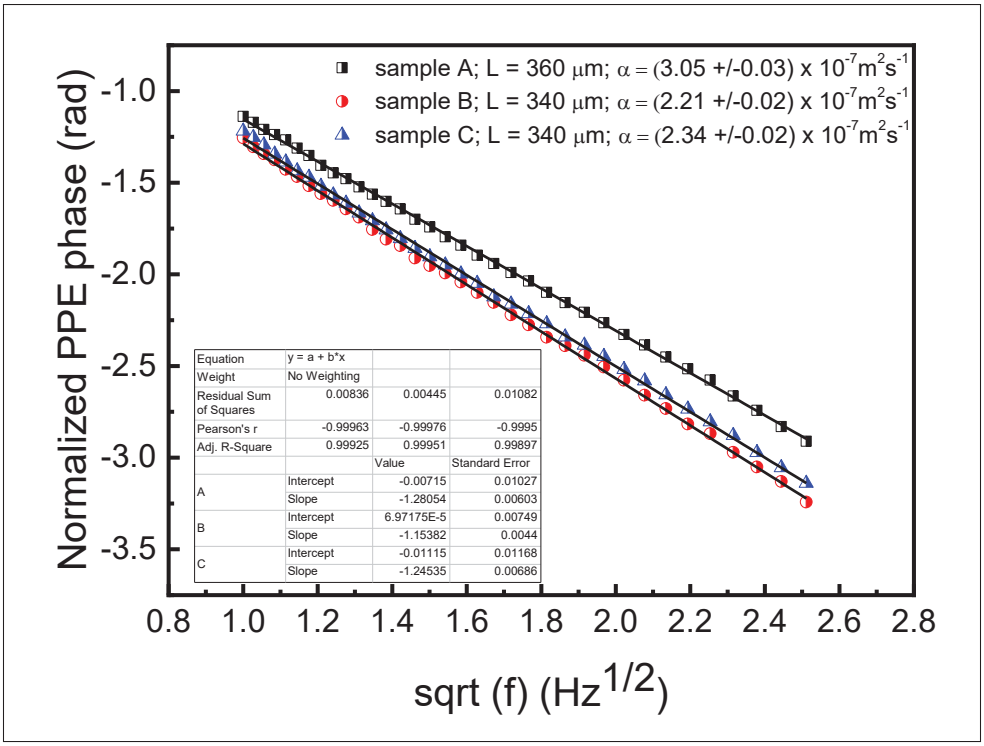

Figure 8.2 Determination of thermal diffusivity by photopyroelectric measurements

To perform these characterizations, BFO powder should be pressed to form a pellet with a thickness smaller than 50 μm. Then a pyroelectric sensor is glued to the pellet with thermal paste. During characterizations, a variation of the pellet's temperature is induced by a modulated light which gives rise to an electrical signal from the pyroelectric sensor. Mandelis & Zver (1985); Sahraoui, Longuemart, Dadarlat, Delenclos, Kolinsky & Buisine (2002) The thermal properties are then determined by a frequency scan of the amplitude and the phase of the pyroelectric signal. Dadarlat, Gibkes, Bicanic & Pasca (1996) In Figure 8.2, we report the thermal diffusivity of some BFO pellets. As the linear regression provides an accurate fit of the data (see inset of Figure 8.2), the measurements' quality is expected to be good. The thermal diffusivity of samples A and B are respectively $3.05 \times 10^{-7}\ m^2\ s^{-1}$ and $2.34 \times 10^{-7}\ m^2\ s^{-1}$. Such a difference can be explained by the variation of the porosity from the pressed pellets. In the case of sample C, the porosity is similar to sample B. However, XRD measurement of this pellet reveals the

presence of the Bi_2O_3 phase. As the value of the thermal diffusivity of sample C is similar to sample B, we can assume that this phase is present in low concentrations.

The next step of this project is the determination of the thermal effusivity.

8.3 Devices based on $BiFeO_3$ nanofibers for the detection of rhodamine B

In chapters 5 and 6, we demonstrate photocatalytic degradations of RhB using BFO under visible light irradiation. Here we deposit BFO atop of FTO substrate by electrospinning to detect and quantify RhB concentration. In Figure 8.3, we report cyclic voltammetry measurements for both bare FTO and FTO coated with BFO. Shifts from the redox peaks are visible as more BFO is deposited. This implies that the surfaces of the electrodes are modified and BFO is less conductive than FTO. In this additional project, we investigate the influence of UV light to enhance the detection of RhB.

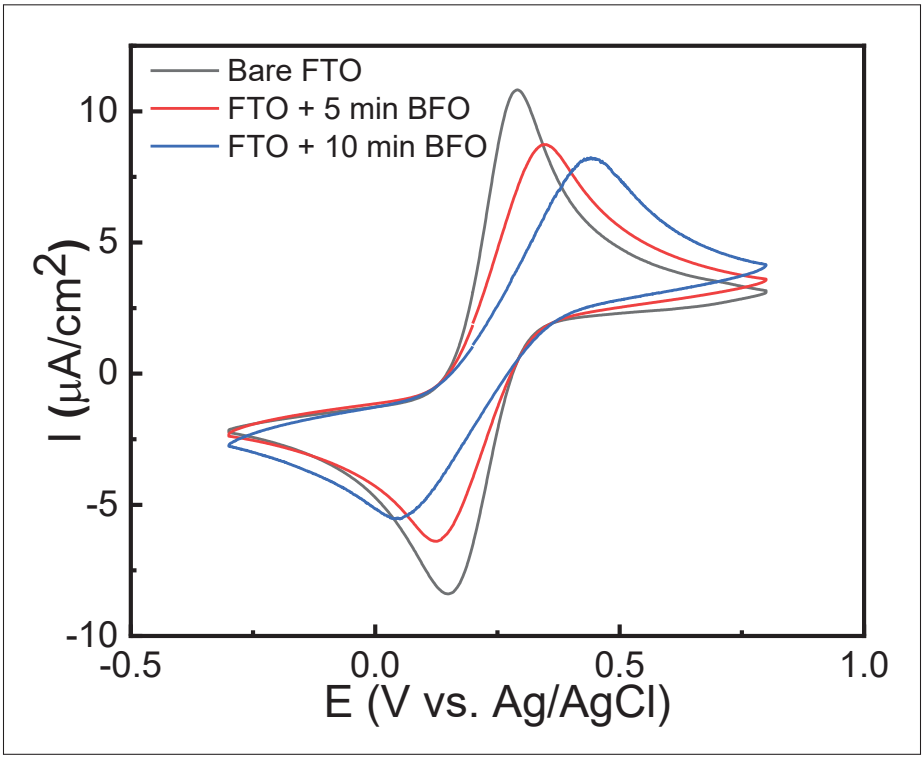

Figure 8.3 Cyclic voltammetry measurements of FTO and FTO covered with $BiFeO_3$ in 0.1 *M* KCl electrolyte

CHAPTER 9

CONCLUSION AND PERSPECTIVES

9.1 Summary

This doctoral thesis at first reported on the fabrication and characterizations of a thermoelectric module in chapter 4. To follow the objectives set in the introduction chapter we then chose to focus on BFO instead. We chose BFO as the main topic of our research because of its chemical stability, its biocompatibility and the abundance of its precursors in the Earth's crust. These advantages are key parameters to allow wide deployment of viable low-cost BFO-based devices and to help address global problems such as production of cleaner energies and better treatment of waste-waters. A special focus on the fabrication methods is taken into account to ensure a possible transfer of the developed devices to the industry. Hence, electrospinning and screen printing are chosen as the two deposition methods used in this thesis to create highly-reproducible devices.

The research activities describe the synthesis and the integration of BFO to fabricate high-performing devices using industry-ready technologies. Mainly, two types of devices are presented: nanofibers-based devices (chapters 4 and 5) and powder-based devices (chapters 6 and 7).

In the first part, devices based on BFO nanofibers demonstrate the influence of the BFO microstructures on the photoelectrochemical properties for water-splitting and photocatalysis applications. In the second part, devices based on BFO powders highlight engineered heterostrutures to create efficient catalysts and temperature sensing materials.

9.2 Statement of original contributions

Different contributions can are highlighted in this doctoral thesis for each type of fabricated devices:

- Thermoelectricity: we fabricate highly-efficient and compact thermoelectric modules by PLD.
- Photoelectrochemical water splitting: we demonstrate the influence of the BFO microstructures on the photocathodic current.
- Photocatalysis: we propose two colloidal-free photocatalytic cells for efficient degradation of RhB. This technique enables an automated and live tracking of the RhB concentration. We prove that a layer of a few nanometers of platinum deposited by sputtering is beneficial for the photocatalytic reactions. We also demonstrate a reduction of the photocatalyst weight compared to the literature.
- Heterostructures syntheses: we report the synthesis of BFO/BiOCl heterojunctions with high aspect ratios by a straightforward methodology without the need of any acid.
- Thermistor: we fabricate and print highly-sensitive thermistors by mixing BFO and graphene. We show the highest sensitivity reported yet for graphene-based thermistors for such a large range of operating temperatures from 25 to 170 $°C$.

9.3 Academic achievements

During this doctoral thesis, the following journal articles with peer reviews have been published:

1. **Fourmont, P.**, Gerlein, L. F., Fortier, F.-X., Cloutier, S. G. & Nechache, R. (2018). Highly efficient thermoelectric microgenerators using nearly room temperature pulsed laser deposition. ACS Applied Materials & Interfaces, 10(12), 10194–10201.
2. **Fourmont, P.**, Nechache, R. & Cloutier, S. G. (2021). Reusable $BiFeO_3$ Nanofiber-Based Membranes for Photo-activated Organic Pollutant Removal with Negligible Colloidal Release. ACS Applied Nano Materials, 4(11), 12261–12269.
3. **Fourmont, P.** & Cloutier, S. G. (2022). Screen-printed p-n BiOCl/$BiFeO_3$ heterojunctions for efficient photocatalytic degradation of Rhodamine B. RSC Advances, 12, 24868-24875.
4. **Fourmont, P.**, Bae, Y., Fortier, F-X., & Cloutier, S. G. Graphene-enhanced screen-printed $BiFeO_3$-based thermistors. *Published on November 28, 2022 in ACS Applied Electronic Materials.* https://doi.org/10.1021/acsaelm.2c01093

5. **Fourmont, P.** & Cloutier, S. G. All printed highly-sensitive humidity sensor based on $BiFeO_3$/BiOCl heterojunctions. *To be submitted.*
6. Asuo, I. M., **Fourmont, P.**, Ka, I., Gedamu, D., Bouzidi, S., Pignolet, A., Nechache, R. & Cloutier, S. G. (2019). Highly efficient and ultrasensitive large-area flexible photodetector based on perovskite nanowires. Small, 15(1), 1804150.
7. Das, S., **Fourmont, P.**, Benetti, D., Cloutier, S. G., Nechache, R., Wang, Z. M. & Rosei, F. (2020). High performance $BiFeO_3$ ferroelectric nanostructured photocathodes. The Journal of Chemical Physics, 153(8), 084705.
8. Benavides-Guerrero, J., **Fourmont, P.**, Gerlein, L. F., Machuca-Martinez, F. & Cloutier, S. G. Black anatase electrodes for visible light photocatalytic remotion of organic contaminants. *To be submitted.*
9. Bae, Y., **Fourmont, P.**, & Cloutier, S. G. UV-assisted photoelectrochemical sensor based on $BiFeO_3$ nanofibers for Rhodamine B detection. *To be submitted.*
10. Ka, I., Asuo, I. M., Basu, S., **Fourmont, P.**, Gedamu, D. M., Pignolet, A., Cloutier, S. G. & Nechache, R. (2018). Hysteresis-Free 1D Network Mixed Halide-Perovskite Semitransparent Solar Cells. Small, 14(38), 1802319.
11. Liu, M., Zhang, H., Gedamu, D., **Fourmont, P.**, Rekola, H., Hiltunen, A., Cloutier, S. G., Nechache, R., Priimagi, A. & Vivo, P. (2019). Halide Perovskite Nanocrystals for Next-Generation Optoelectronics. Small, 15(28), 1900801.

APPENDIX I

SUPPORTING INFORMATION
HIGHLY EFFICIENT THERMOELECTRIC MICROGENERATORS USING NEARLY ROOM TEMPERATURE PULSED LASER DEPOSITION

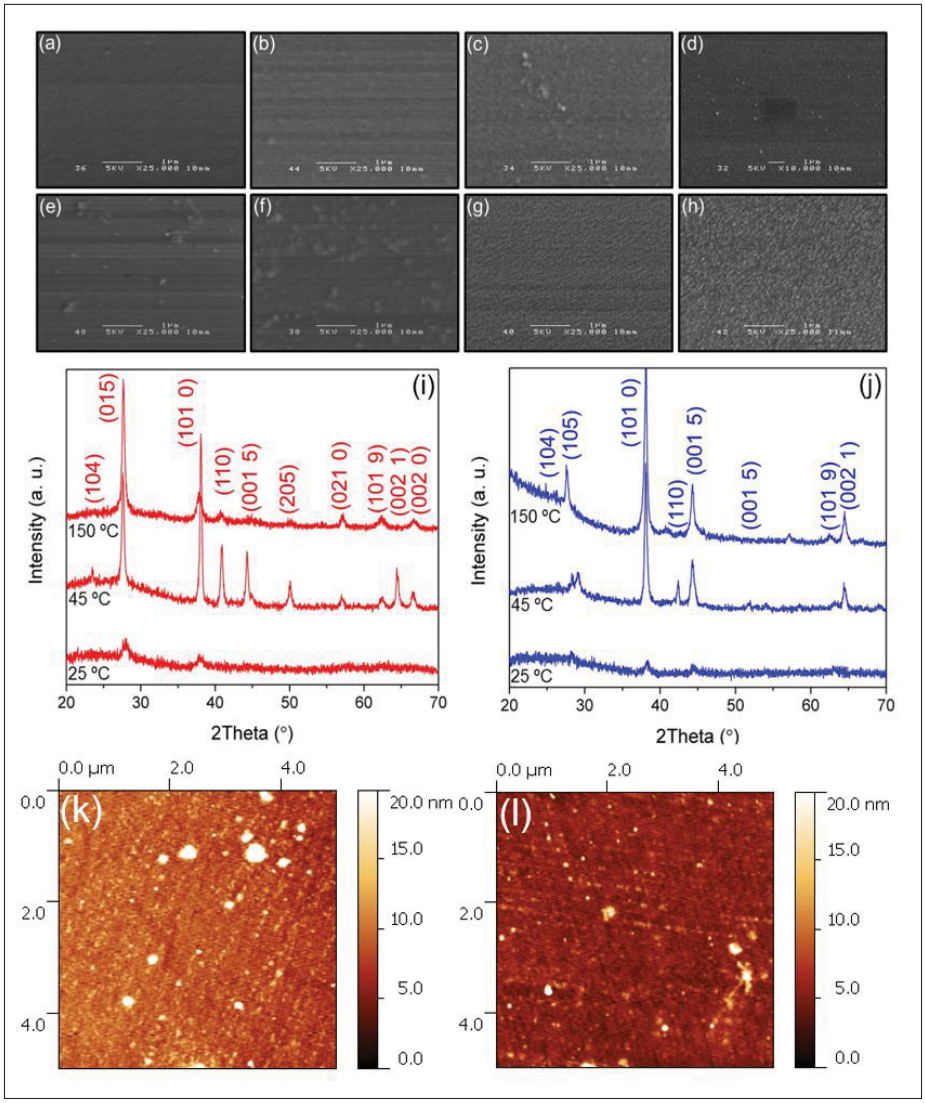

Figure-A I-1 SEM images of (a-d) Sb_2Te_3 and (e-h) Bi_2Te_3 films grown at different substrate temperature (a,e) RT, (b,f) 45 °*C*, (c-g) 80 °*C* , (d,h) 150 °*C* and corresponding XRD patterns for (i) Bi_2Te_3, (j) Sb_2Te_3 films, respectively. AFM images of (k) Bi_2Te_3 and (l) Sb_2Te_3 film surfaces

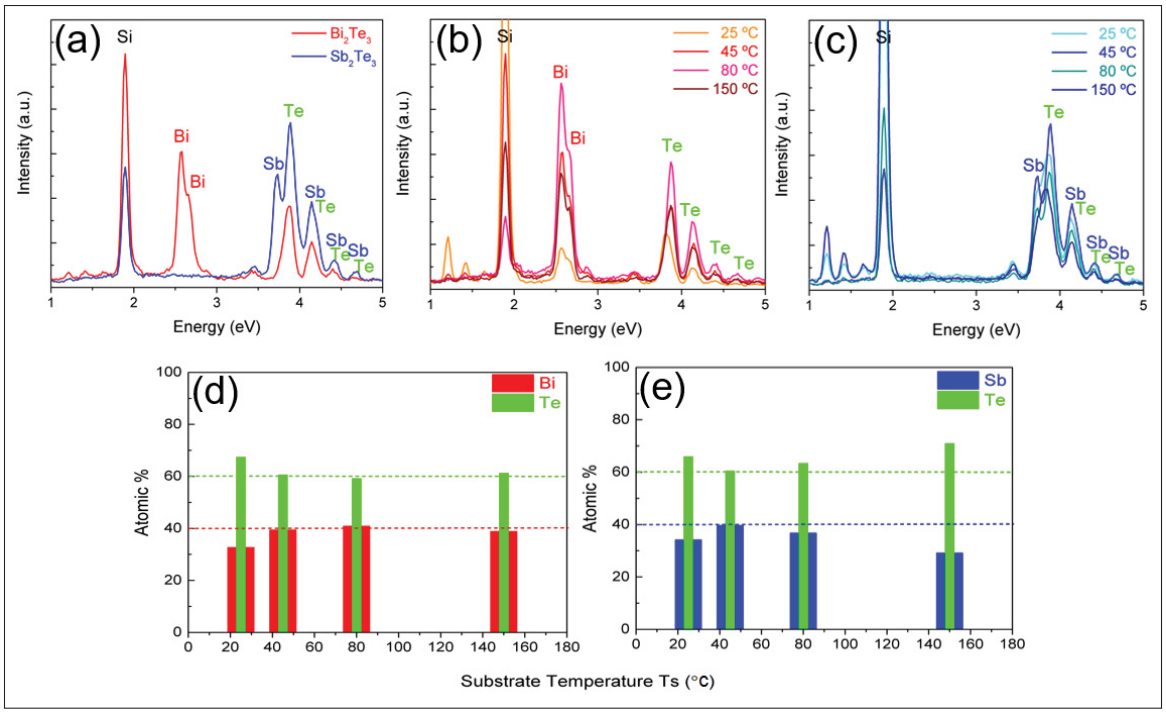

Figure-A I-2 EDX spectra of the stochiometric Sb_2Te_3 and Bi_2Te_3 films deposited (a) at 45 °*C* and (b,c) at different substrate temperature. (d-e) Corresponding chemical compositions

Film	at% Te	at% Bi or Sb	Grain size d (nm)	R_a (nm)
Sb_2Te_3	60.39	39.61	9.85	2.37
Bi_2Te_3	60.57	39.43	29.33	6.41

Table-A I-1 Absolute values of Seebeck coefficients of TE film legs and their corresponding device

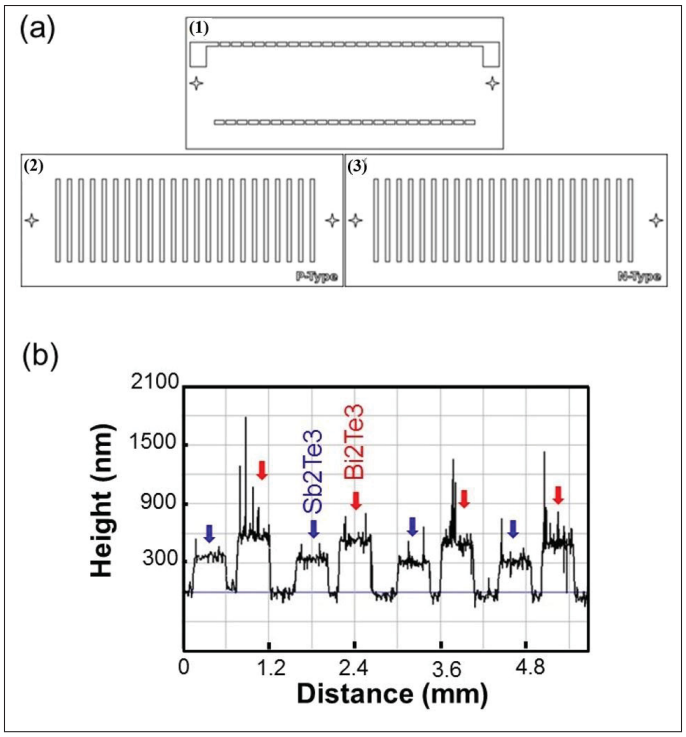

Figure-A I-3 (a) Masks used for (1) the deposition of electrodes by evaporation and (2-3) the deposition of Sb_2Te_3 and Bi_2Te_3 by PLD respectively. (b) Thickness profile of the device with four pairs

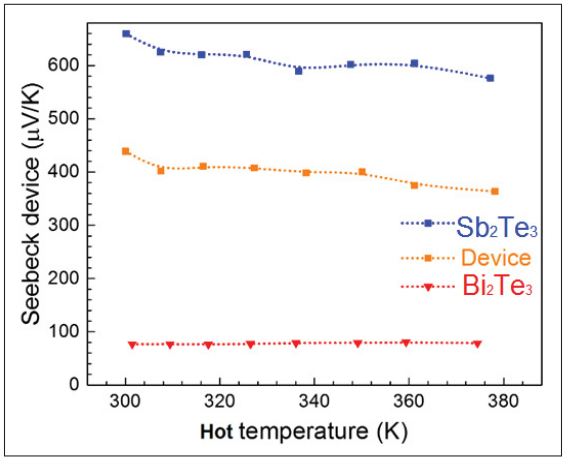

Figure-A I-4 Absolute values of Seebeck coefficients of TE film legs and their corresponding device

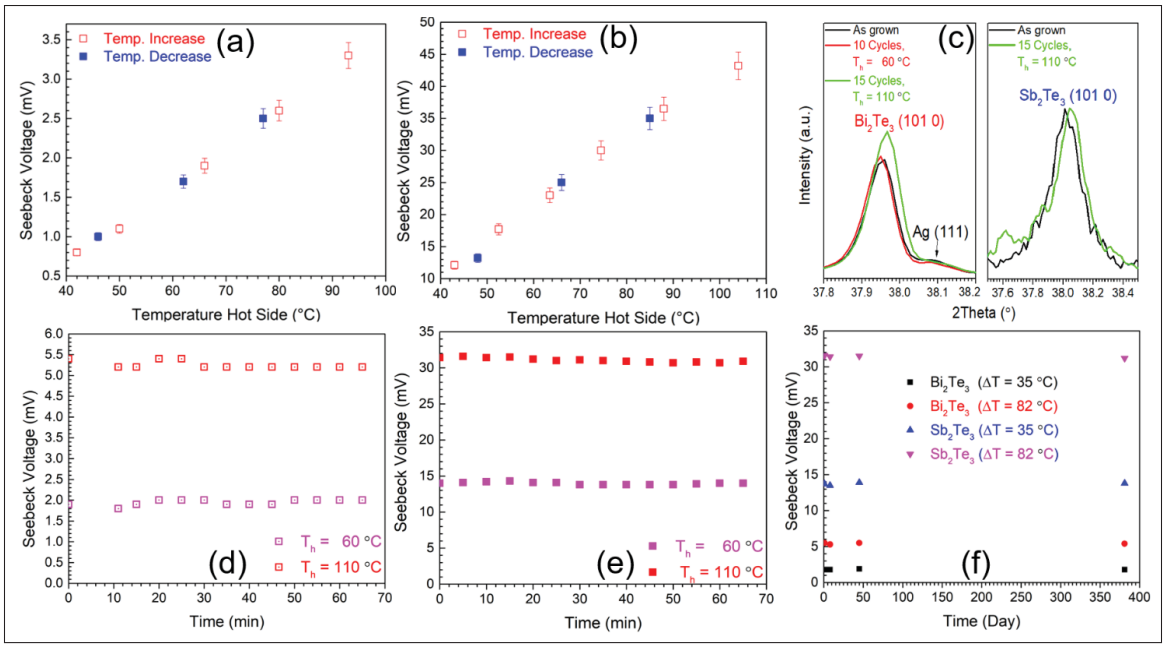

Figure-A I-5 Thermostability of Sb_2Te_3 and Bi_2Te_3 legs deposited at 45°C. Seebeck voltage measured as a function of the temperature T_h (hot side of the device) for (a) Bi_2Te_3 and (b) Sb_2Te_3. (c) (1010) XRD peak intensity upon different thermoelectric measurement cycles at T_h = 60 and 110 °C. Durability of generated Seebeck voltage for (d) Bi_2Te_3 and (e) Sb_2Te_3. (f) Time stability of the thermoelectric performance of the devices at different temperature gradients

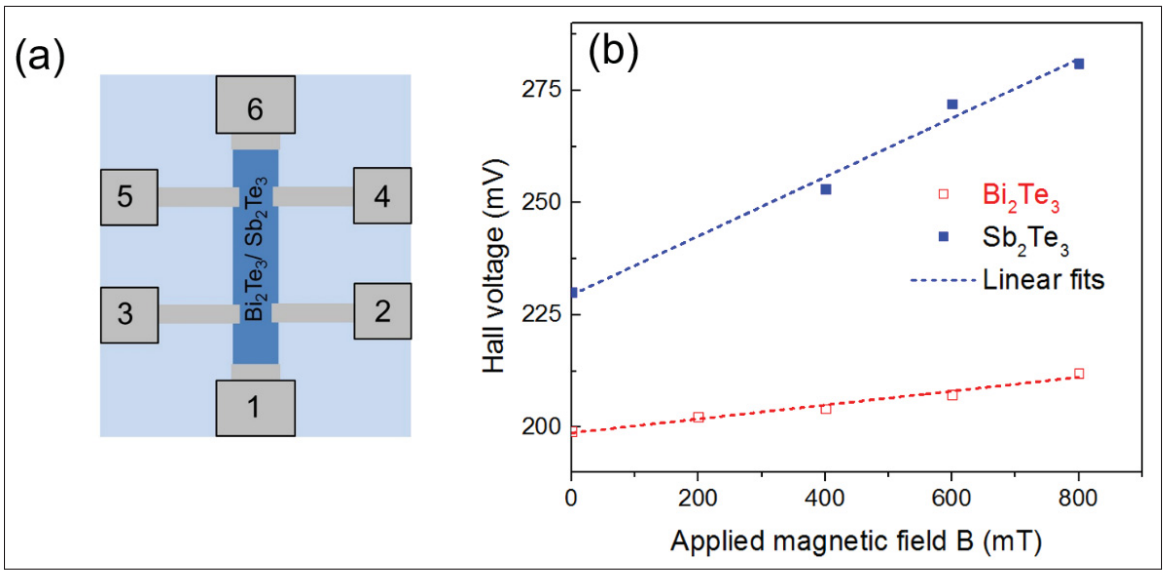

Figure-A I-6 (a) Device geometry used for hall effect measurement of the TE film legs. (b) Corresponding variation of absolute Hall voltage with applied magnetic field under 100 μA

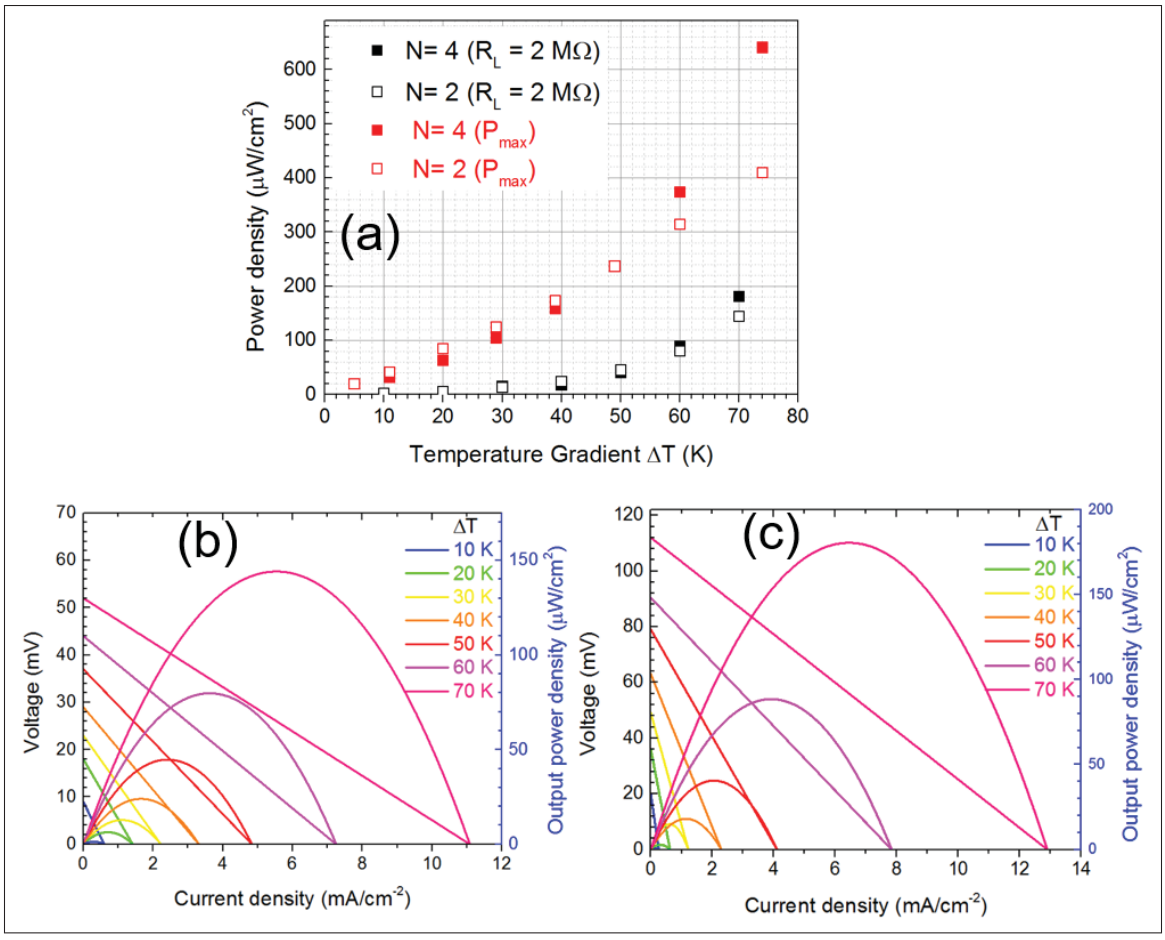

Figure-A I-7 (a) Power density generated by TE devices at higher temperature gradients. Current density dependence of output voltages and power densities of devices with (b) two and (c) four legs pairs

APPENDIX II

SUPPORTING INFORMATION
HIGH PERFORMANCE $BiFeO_3$ FERROELECTRIC NANOSTRUCTURED PHOTOCATHODES

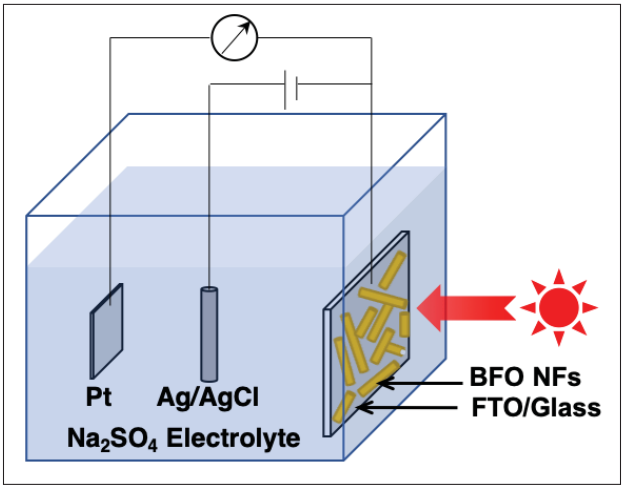

Figure-A II-1 Schematic diagram of experimental setup used for photoelectrocatalysis

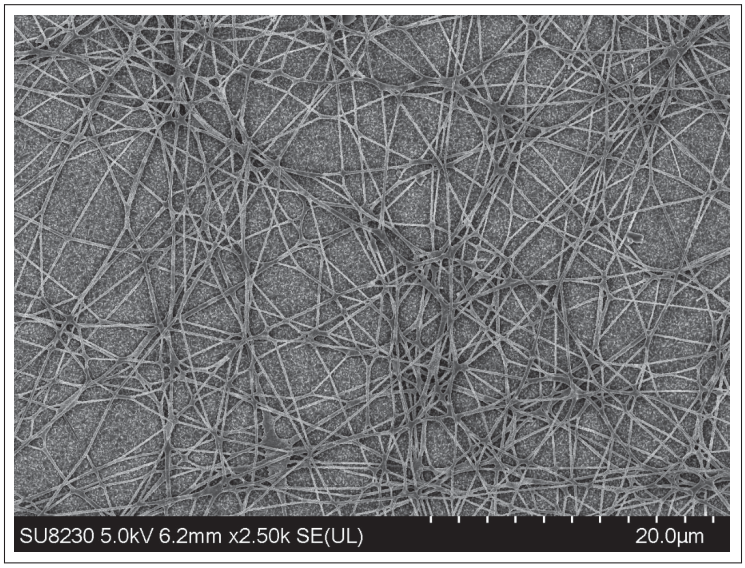

Figure-A II-2 SEM image of $BiFeO_3$ nanofibers deposited during 10 minutes at 35% humidity

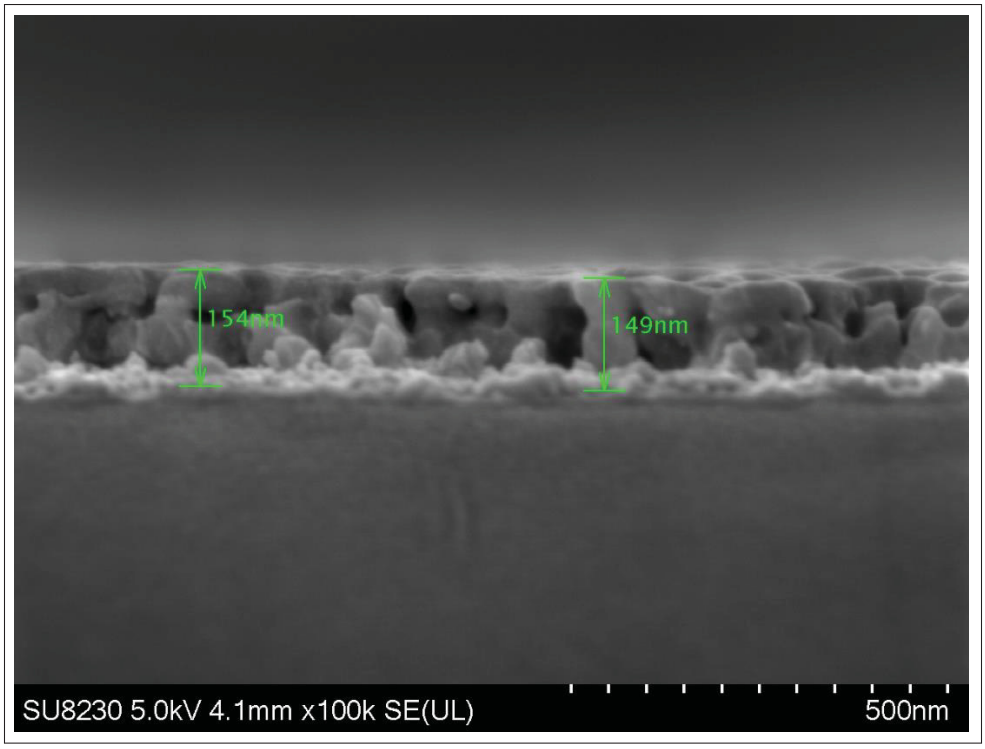

Figure-A II-3 High magnification SEM image of the cross section of a $BiFeO_3$ thin film. Thickness deposition is estimated to be ~150 *nm*

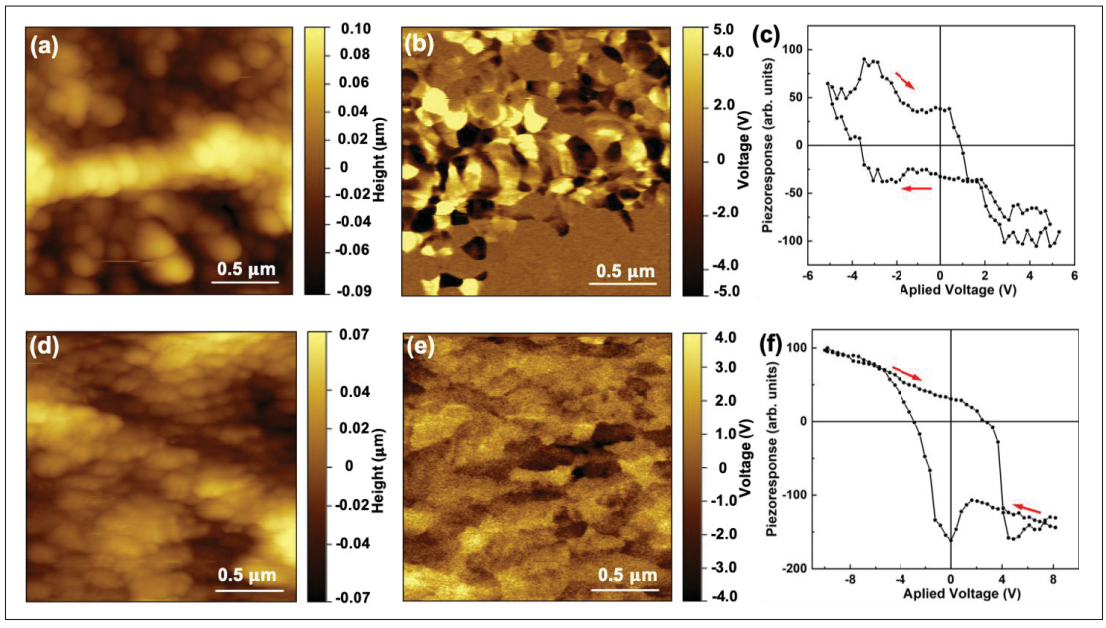

Figure-A II-4 AFM topography images, PFM images of the same area and local piezoresponse hysteresis loops for $BiFeO_3$ nanoweb (a-c) and for $BiFeO_3$ thin film (d-f), respectively

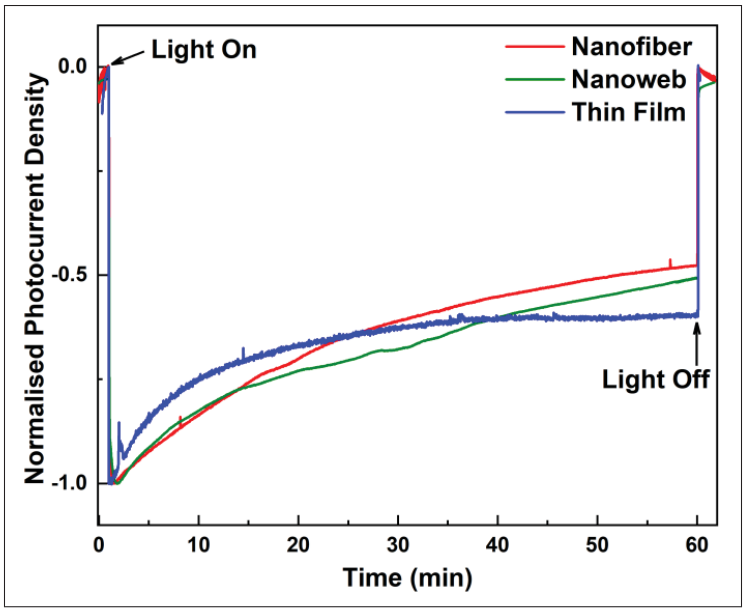

Figure-A II-5 Normalized photocurrent density as a function of time for all three photoelectrodes under continuous light illumination for 1 *hr*

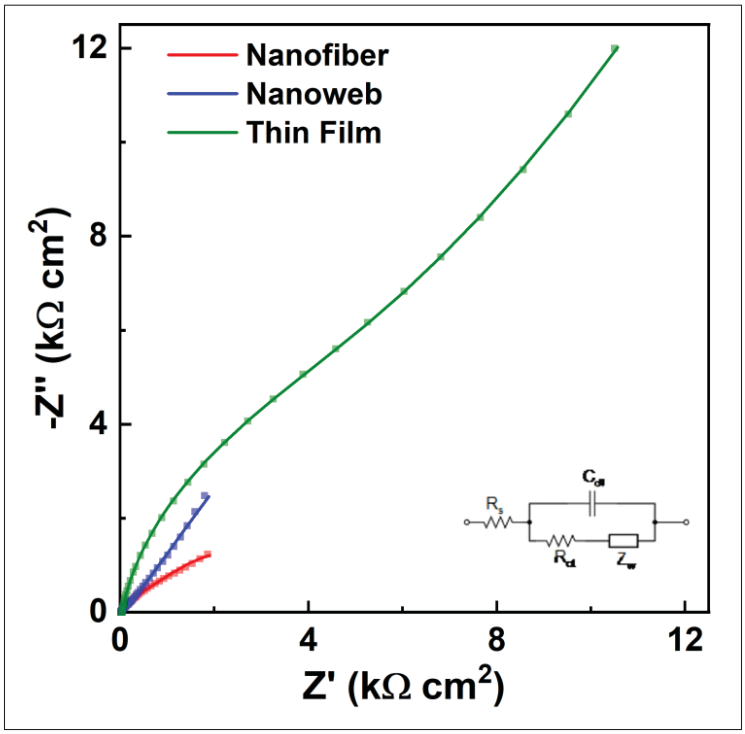

Figure-A II-6 Nyquist plots of three different $BiFeO_3$ photocathodes. The equivalent circuit is shown at the inset of the plot

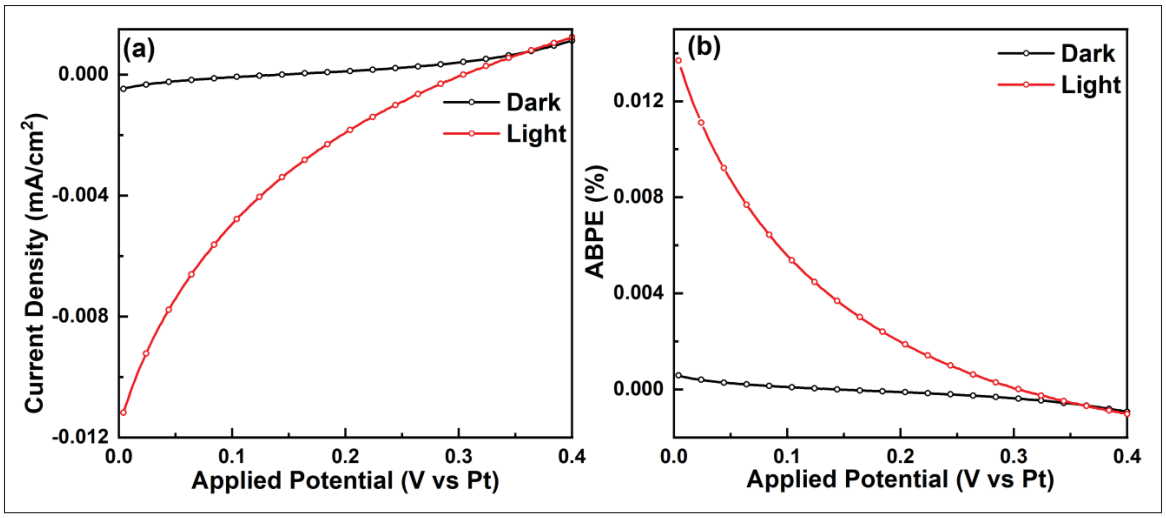

Figure-A II-7 (a) Current density as a function of applied potential in dark and in continuous solar illumination of $BiFeO_3$ nanofiber photocathode recorded in two-electrode configuration. (b) Calculated applied-bias-photon-to-current efficiency (ABPE) of $BiFeO_3$ nanofiber photocathode

APPENDIX III

SUPPORTING INFORMATION
REUSABLE $BiFeO_3$ NANOFIBER-BASED MEMBRANES FOR PHOTO-ACTIVATED ORGANIC POLLUTANT REMOVAL WITH NEGLIGIBLE COLLOIDAL RELEASE

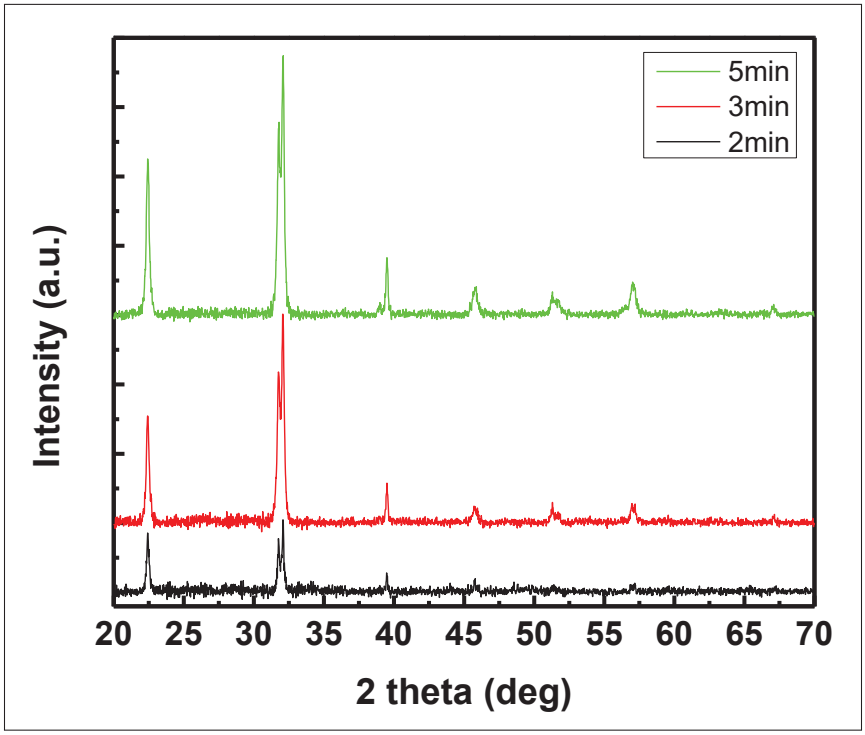

Figure-A III-1 XRD graphs of $BiFeO_3$ nanofibers for different deposition times

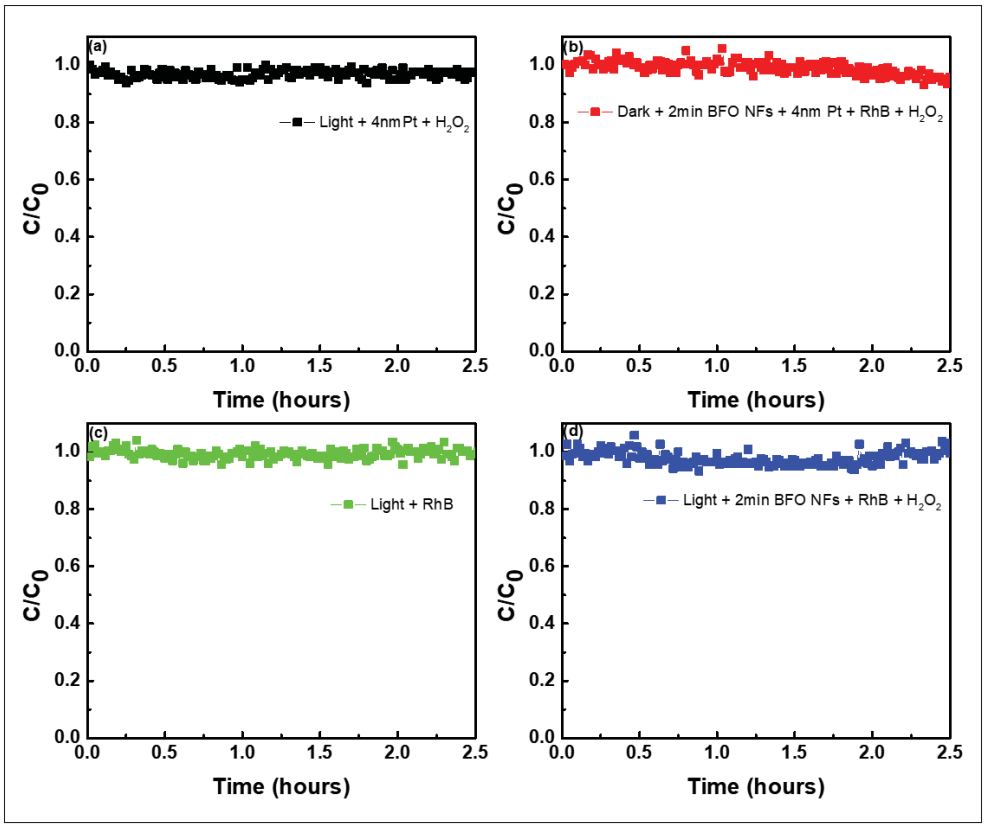

Figure-A III-2 Evolution of RhB degradation (a) without photocatalyst, (b) under dark condition, (c) with light only and (d) without platinum layer

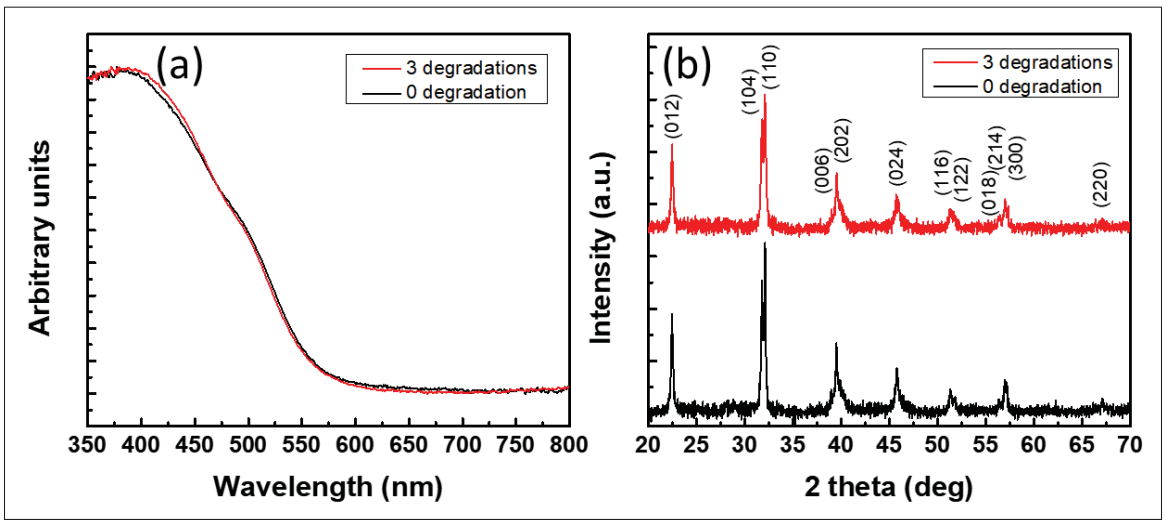

Figure-A III-3 (a) Absorbance measurements and (b) XRD graphs of the $BiFeO_3$ nanofibers before and after 3 cycles of degradation of RhB

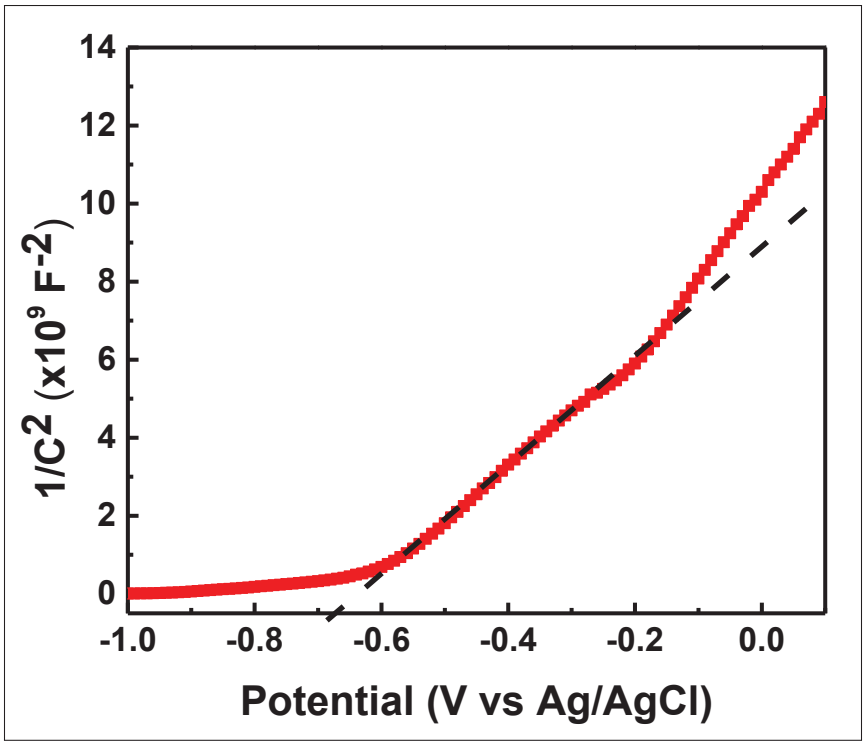

Figure-A III-4 Mott-Schottky plot of the $BiFeO_3$ nanofibers

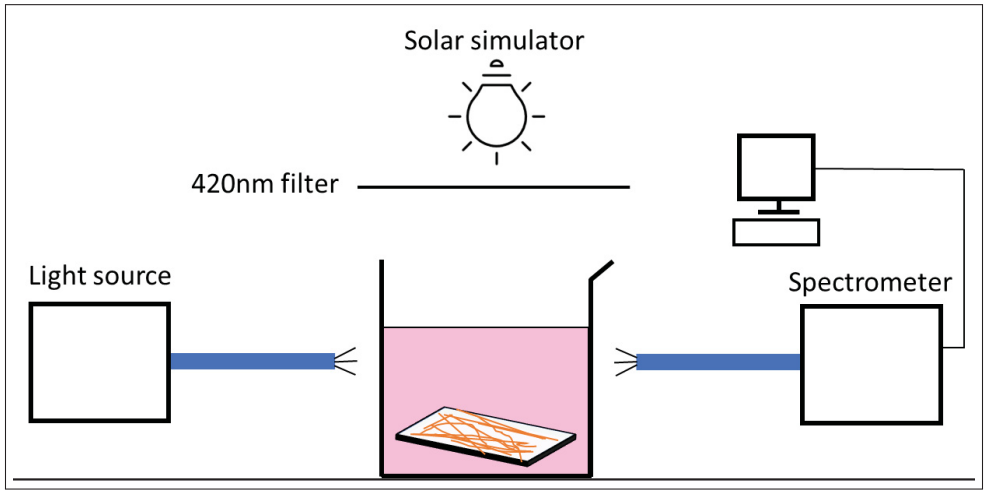

Figure-A III-5 Schematic of the experimental setup for RhB degradation

APPENDIX IV

SUPPORTING INFORMATION
SCREEN-PRINTED P-N BiOCl/$BiFeO_3$ HETEROJUNCTIONS FOR EFFICIENT PHOTOCATALYTIC DEGRADATION OF RHODAMINE B

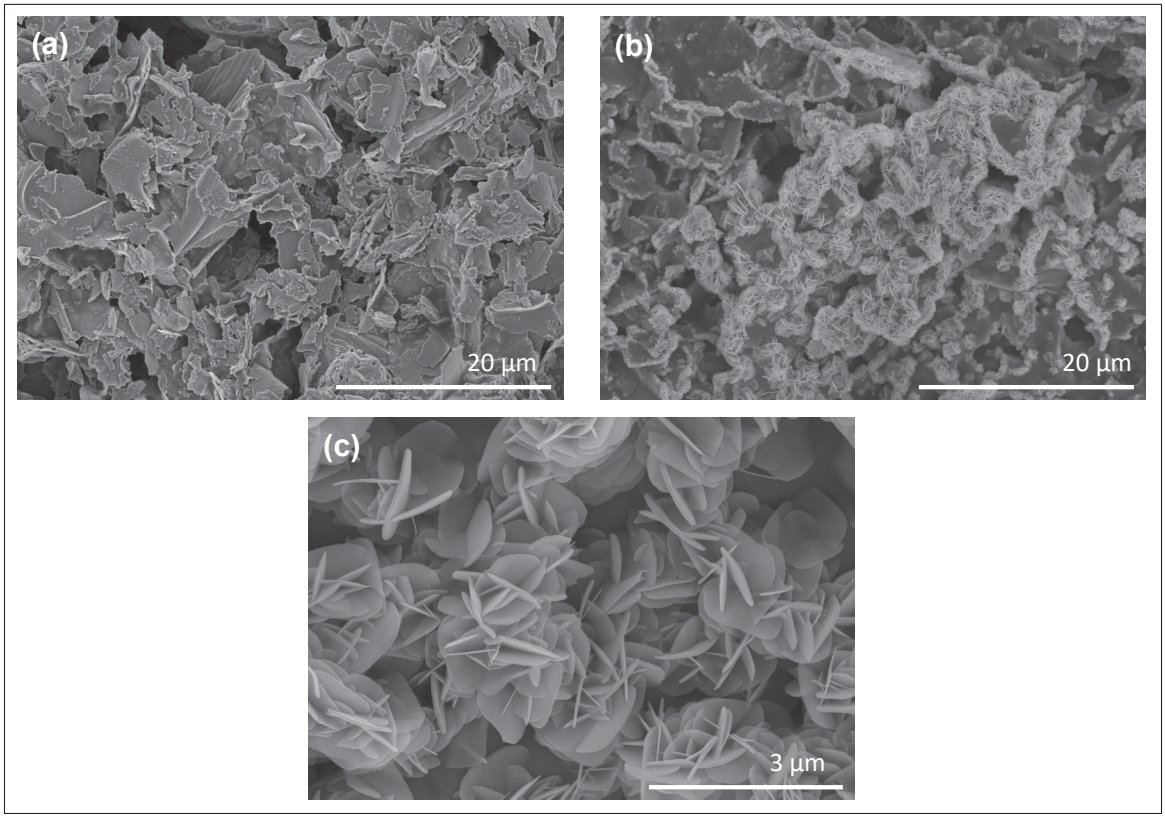

Figure-A IV-1 SEM micrographs of the screen-printed photocatalytic cells (a) before annealing and (b-c) after annealing at 300 °*C*

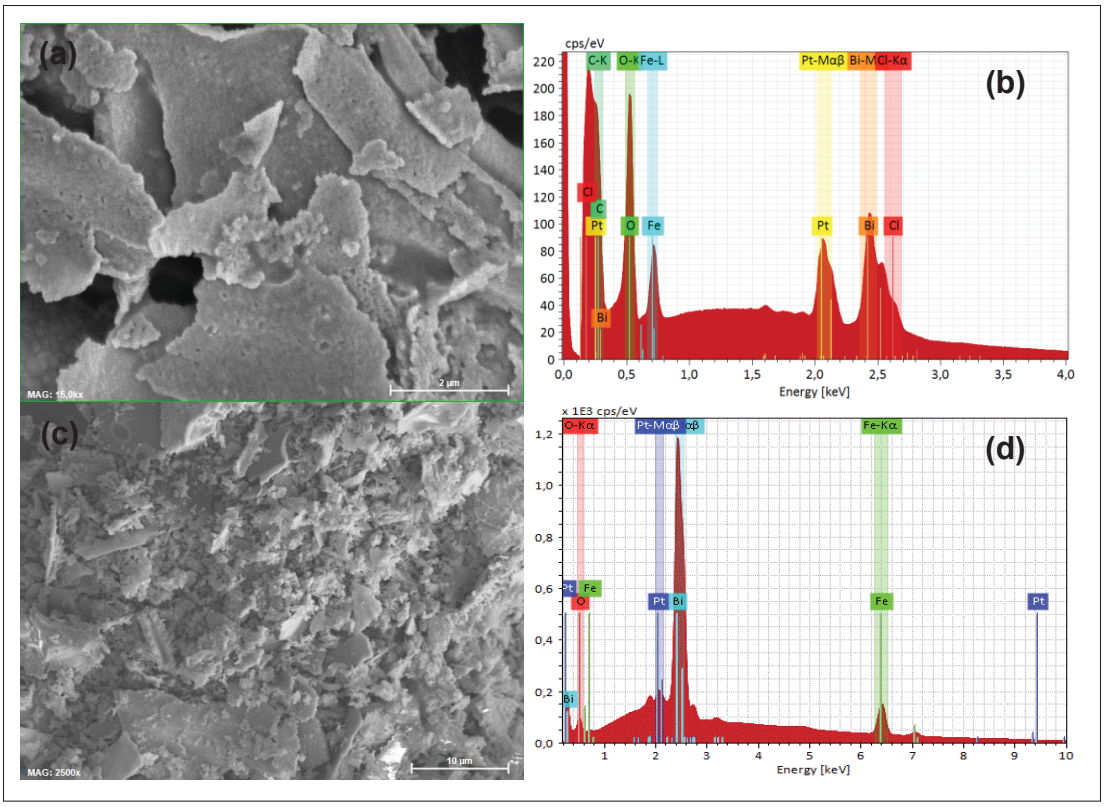

Figure-A IV-2 (a) SEM micrograph of the screen-printed photocatalytic cell. (b) EDX spectra of the micrograph shown in (a). (c) SEM micrograph of the $BiFeO_3$ particles. (d) EDX spectra of the micrograph shown in (c)

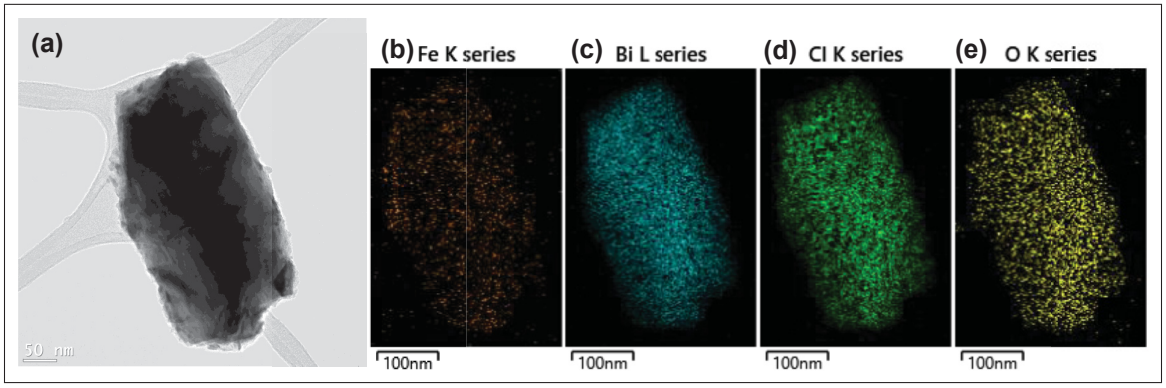

Figure-A IV-3 (a) TEM image of the screen-printed photocatalytic cell. Images (b-d) show elemental maps of iron, bismuth, chlorine and oxygen respectively

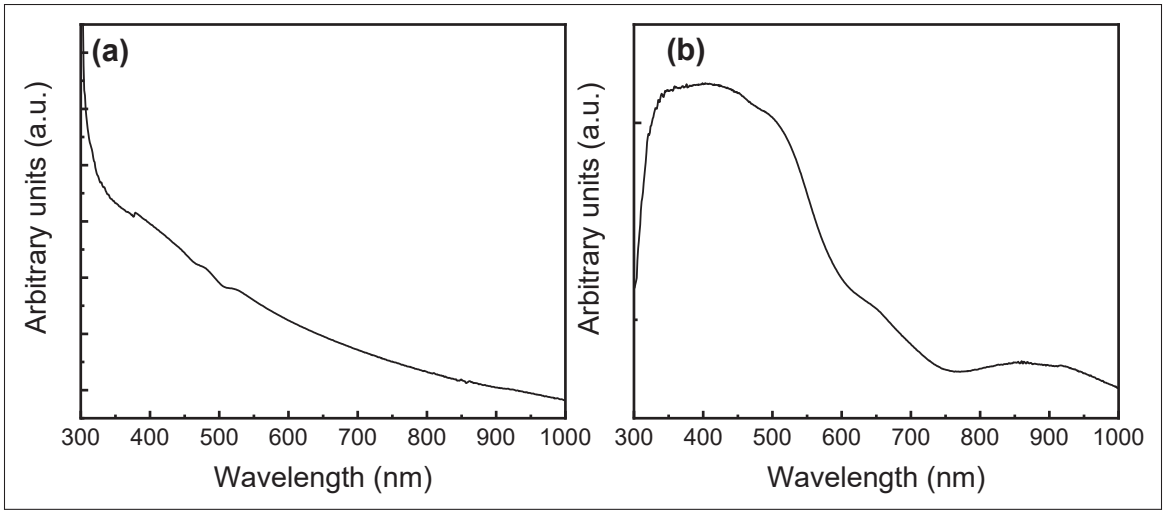

Figure-A IV-4 UV-Vis-NIR measurements of (a) BiOCl nanosheets with iron atoms inclusions and (b) screen-printed photocatalytic cell before annealing

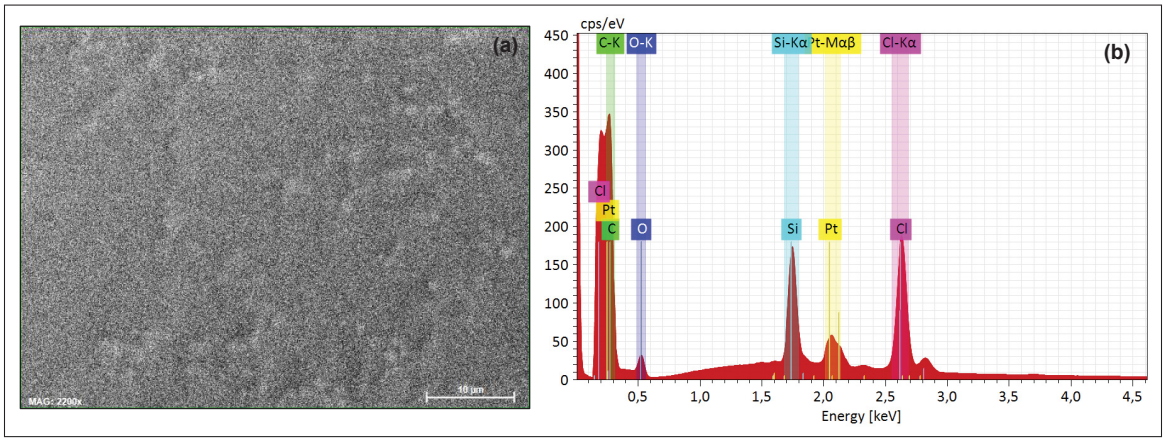

Figure-A IV-5 (a) SEM micrograph of the ink vehicle on silicon wafer after annealing at 300 °*C* for 1 *hr* (b) EDX spectrum of micrograph shown in (a)

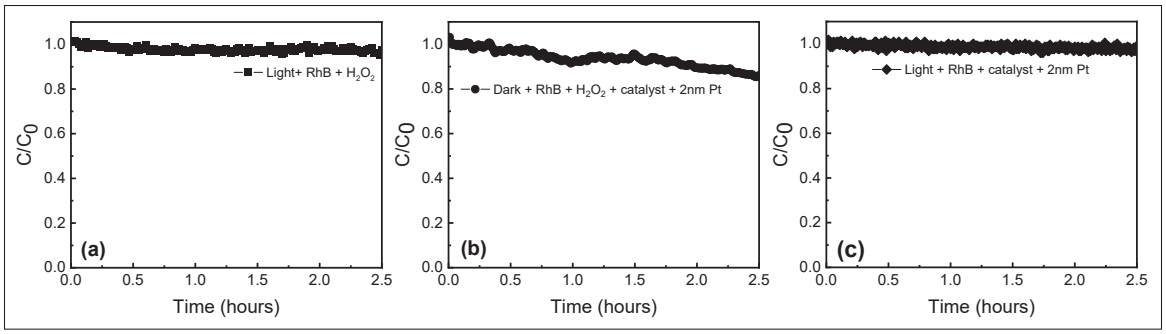

Figure-A IV-6 (a) Evaluation of photolysis proving that light and H_2O_2 are not degrading RhB (b) RhB degradation under dark conditions (c) RhB degradation without H_2O_2

APPENDIX V

SUPPORTING INFORMATION
HIGHLY SENSITIVE AND LARGE OPERATING TEMPERATURE SCREEN-PRINTED $BiFeO_3$-BASED THERMISTORS

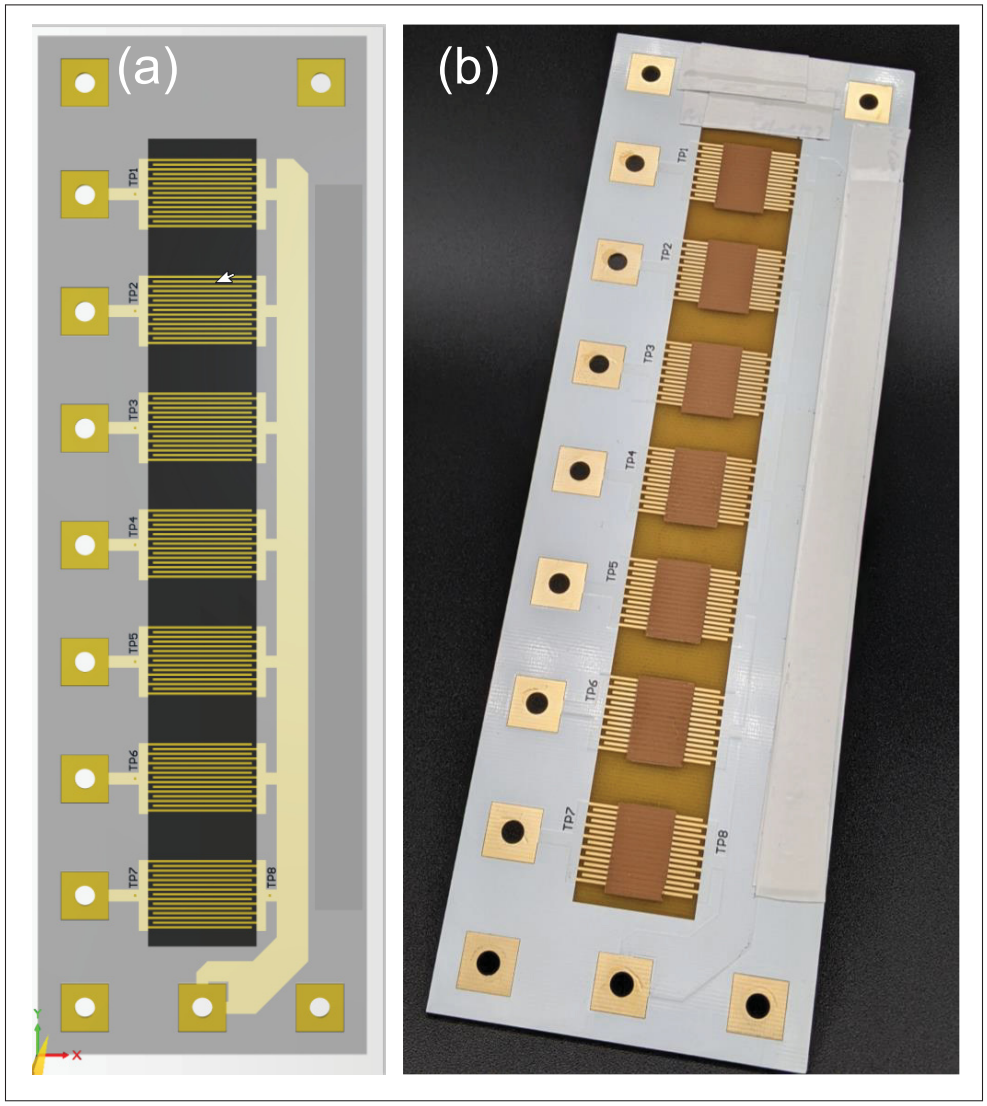

Figure-A V-1 (a) Schematic of the FR4 substrate and (b) pure $BiFeO_3$ screen-printed thermistors

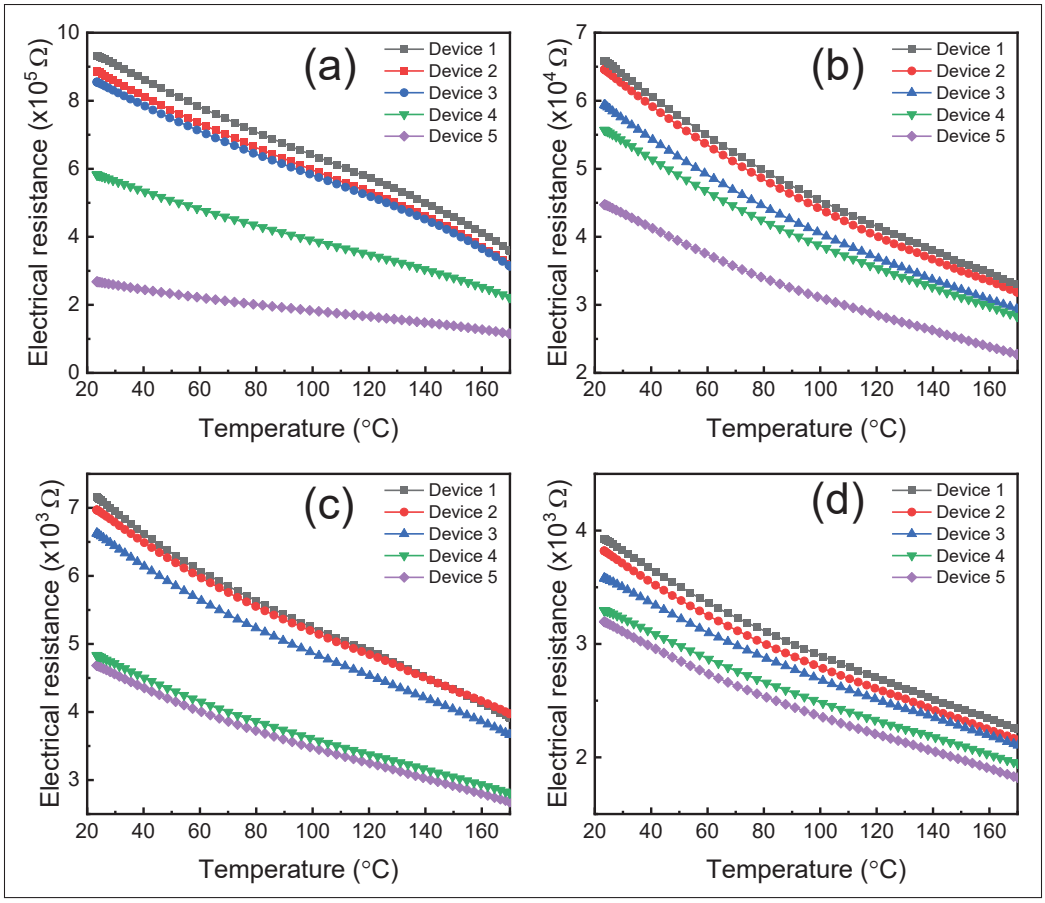

Figure-A V-2 Thermistor's electrical resistance against the temperature for the five printed thermistors with a loading of graphene of (a) 3.5 wt.%, (b) 4 wt.%, (c) 4.5 wt.% and (d) 5 wt.%

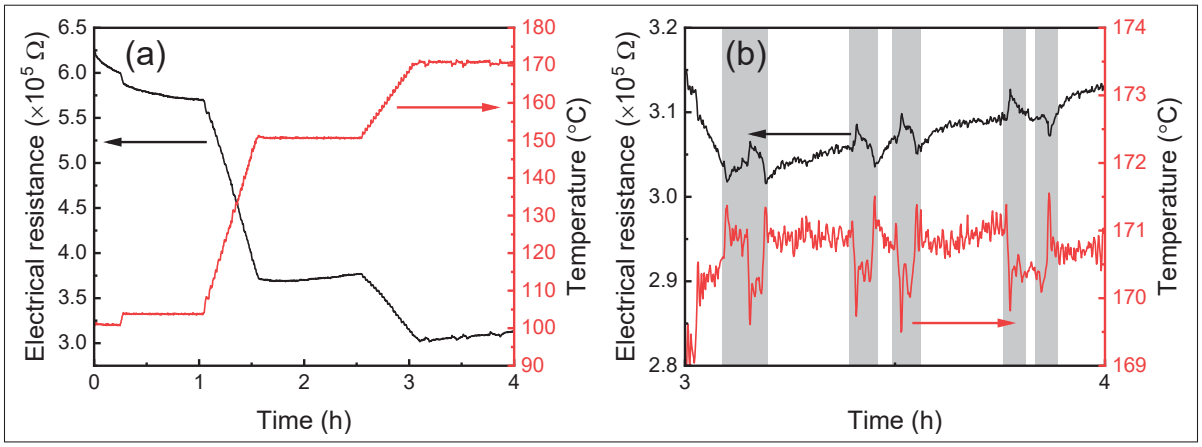

Figure-A V-3 (Stability test of the printed thermistor (a) for 1h at 100 °*C*, 150 °*C*, and 170 °*C*. (b) demonstrates that variation of temperature of 1 °*C* are detected by the thermistor

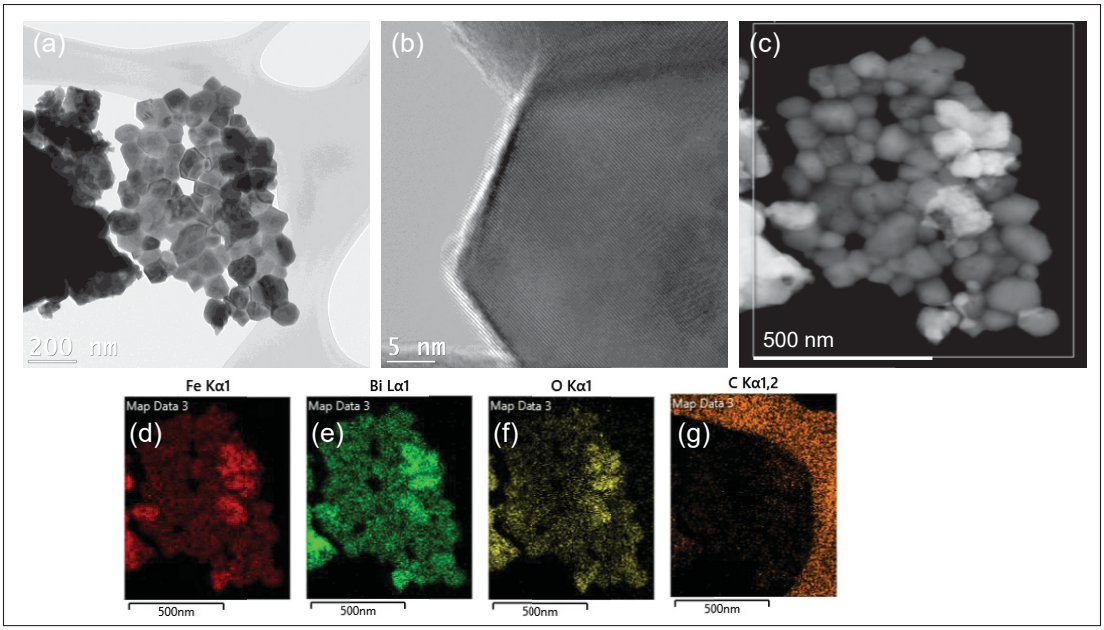

Figure-A V-4 (a-c) TEM micrographs of the BFO powder. (d-g) EDS elemental mapping of the BFO powder

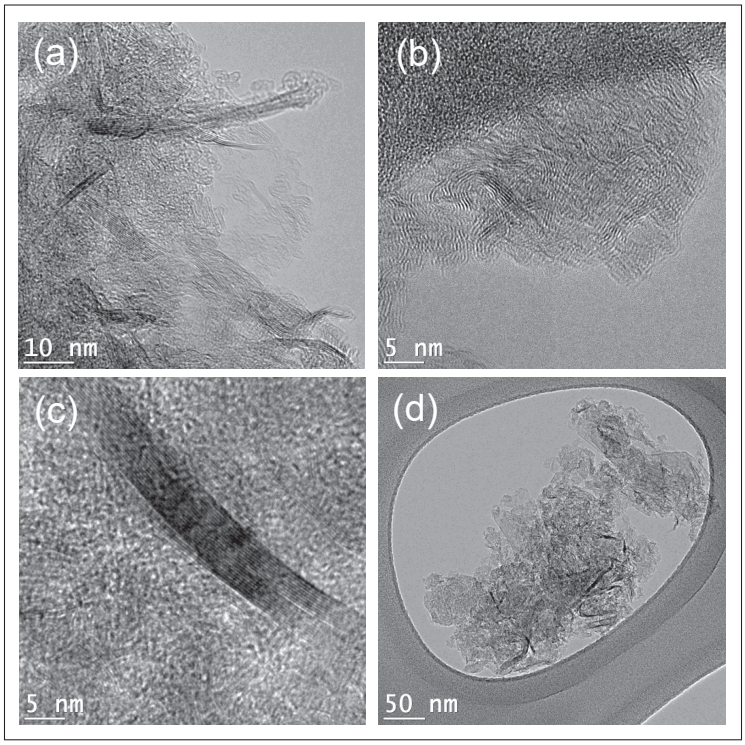

Figure-A V-5 (a-d) TEM micrographs of the commercial graphene mixed with BFO powder to print the thermistors

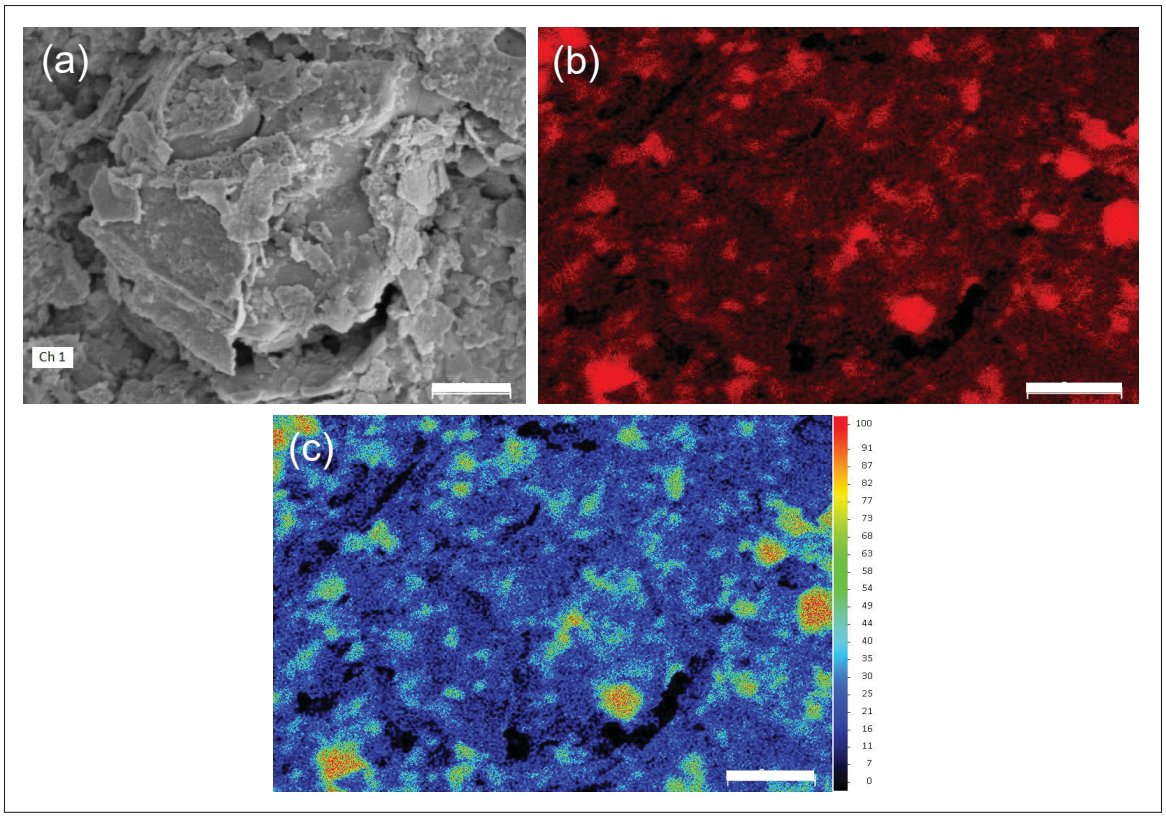

Figure-A V-6 EDS elemental mapping of the printed ink with a 5 wt.% loading of graphene. (a) SEM micrograph. (b) Carbon distribution mapping. (c) Intensity mapping of Carbon. The scale bar for all the images is 2 μm

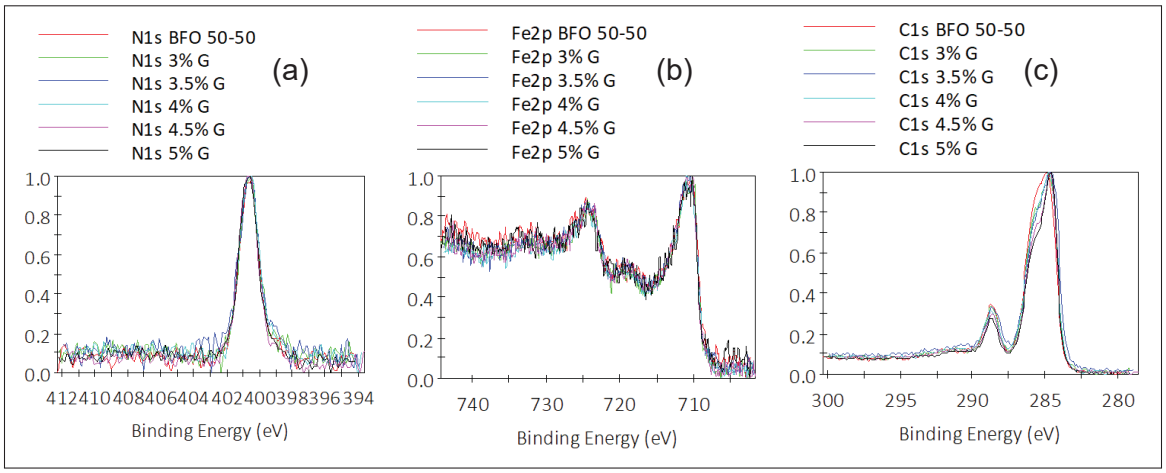

Figure-A V-7 XPS spectra of all the printed inks for (a) N 1s, (b) Fe 2p, (c) C 1s

BIBLIOGRAPHY

Abdel Aziz, A., Elsayed, M., Abu Bakr, H., El-Rifai, J., Van der Donck, T., Celis, J.-P., Leonov, V., Fiorini, P. & Sedky, S. (2010). Pulsed laser deposition of bismuth telluride thin films for microelectromechanical systems thermoelectric energy harvesters. *Journal of electronic materials*, 39(9), 1920–1925.

Achenbach, G., James, W. & Gerson, R. (1967). Preparation of single-phase polycrystalline BiFeO3. *Journal of the American Ceramic Society*, 50(8), 437–437.

Afroze, S., Karim, A., Cheok, Q., Eriksson, S. & Azad, A. K. (2019). Latest development of double perovskite electrode materials for solid oxide fuel cells: a review. *Frontiers in Energy*, 13(4), 770–797.

Ahmad, H., Kamarudin, S., Minggu, L. & Kassim, M. (2015). Hydrogen from photo-catalytic water splitting process: A review. *Renewable and Sustainable Energy Reviews*, 43, 599–610.

Al-Mumen, H., Rao, F., Dong, L. & Li, W. (2013). Design, fabrication, and characterization of graphene thermistor. *The 8th Annual IEEE International Conference on Nano/Micro Engineered and Molecular Systems*, pp. 1135–1138.

Aleksic, O. & Nikolić, P. M. (2017). Recent advances in NTC thick film thermistor properties and applications. *Facta Universitatis, Series: Electronics and Energetics*, 30(3), 267–284.

Anton, S. R. & Sodano, H. A. (2007). A review of power harvesting using piezoelectric materials (2003–2006). *Smart materials and Structures*, 16(3), R1.

Arnold, D. C. (2015). Composition-driven structural phase transitions in rare-earth-doped BiFeO3 ceramics: A review. *IEEE Transactions on Ultrasonics, Ferroelectrics, and Frequency Control*, 62(1), 62–82.

Arunachalam, P. & Al Mayouf, A. M. (2019). Photoelectrochemical water splitting. In *Noble Metal-Metal Oxide Hybrid Nanoparticles* (pp. 585–606). Elsevier.

Arya, G., Kotnala, R. K. & Negi, N. S. (2014). A novel approach to improve properties of BiFeO3 nanomultiferroics. *Journal of the American Ceramic Society*, 97(5), 1475–1480.

Asuo, I. M., Fourmont, P., Ka, I., Gedamu, D., Bouzidi, S., Pignolet, A., Nechache, R. & Cloutier, S. G. (2019). Highly efficient and ultrasensitive large-area flexible photodetector based on perovskite nanowires. *Small*, 15(1), 1804150.

Aviño-Salvado, O., Sabbah, W., Buttay, C., Morel, H. & Bevilacqua, P. (2017). Evaluation of Printed-Circuit Board Materials for High-Temperature Operation. *Journal of Microelectronics*

and Electronic Packaging, 14(4), 166–171.

Badding, J. V., Meng, J. & Polvani, D. (1998). Pressure tuning in the search for new and improved solid state materials. *Chemistry of Materials*, 10(10), 2889–2894.

Badran, A., Marshall, D., Legault, Z., Makovetsky, R., Provencher, B., Piché, N. & Marsh, M. (2020). Automated segmentation of computed tomography images of fiber-reinforced composites by deep learning. *Journal of Materials Science*, 55(34), 16273–16289.

Bai, X., Wei, J., Tian, B., Liu, Y., Reiss, T., Guiblin, N., Gemeiner, P., Dkhil, B. & C. Infante, I. (2016). Size effect on optical and photocatalytic properties in BiFeO3 nanoparticles. *The Journal of Physical Chemistry C*, 120(7), 3595–3601.

Bailini, A., Donati, F., Zamboni, M., Russo, V., Passoni, M., Casari, C. S., Bassi, A. L. & Bottani, C. E. (2007). Pulsed laser deposition of Bi2Te3 thermoelectric films. *Applied Surface Science*, 254(4), 1249–1254.

Baily, S. & Emin, D. (2006). Transport properties of amorphous antimony telluride. *Physical Review B*, 73(16), 165211.

Batool, M., Nazar, M. F., Awan, A., Tahir, M. B., Rahdar, A., Shalan, A. E., Lanceros-Méndez, S. & Zafar, M. N. (2021). Bismuth-based heterojunction nanocomposites for photocatalysis and heavy metal detection applications. *Nano-Structures & Nano-Objects*, 27, 100762.

Bell, L. E. (2008). Cooling, heating, generating power, and recovering waste heat with thermoelectric systems. *Science*, 321(5895), 1457–1461.

Bendi, R., Bhavanasi, V., Parida, K., Nguyen, V. C., Sumboja, A., Tsukagoshi, K. & Lee, P. S. (2016). Self-powered graphene thermistor. *Nano Energy*, 26, 586–594.

Bernardo, M. S., Jardiel, T., Peiteado, M., Caballero, A. & Villegas, M. (2011). Reaction pathways in the solid state synthesis of multiferroic BiFeO3. *Journal of the European Ceramic Society*, 31(16), 3047–3053.

Bhadala, F., Suthar, L. & Roy, M. (2019). Structural, dielectric and thermal properties of 0.25 BFO-0.75 CTO composite. *AIP Conference Proceedings*, 2100(1), 020144.

Bhalla, A., Guo, R. & Roy, R. (2000). The perovskite structure—a review of its role in ceramic science and technology. *Materials research innovations*, 4(1), 3–26.

Bharathkumar, S., Sakar, M., Balakumar, S. et al. (2015). Versatility of electrospinning in the fabrication of fibrous mat and mesh nanostructures of bismuth ferrite (BiFeO3) and their magnetic and photocatalytic activities. *Physical Chemistry Chemical Physics*, 17(27),

17745–17754.

Bhattacherjee, A., Sneha, M., Lewis-Borrell, L., Tau, O., Clark, I. P. & Orr-Ewing, A. J. (2019). Picosecond to millisecond tracking of a photocatalytic decarboxylation reaction provides direct mechanistic insights. *Nature communications*, 10(1), 1–7.

Bi, W., Li, X., Zhang, L., Jin, T., Zhang, L., Zhang, Q., Luo, Y., Wu, C. & Xie, Y. (2015). Molecular co-catalyst accelerating hole transfer for enhanced photocatalytic H2 evolution. *Nature communications*, 6(1), 1–7.

Bilisik, K. & Akter, M. (2021). Graphene nanocomposites: A review on processes, properties, and applications. *Journal of Industrial Textiles*, 15280837211024252.

Biswas, A., Das, R., Dey, C., Banerjee, R. & Poddar, P. (2014). Ligand-free one-step synthesis of {001} faceted semiconducting BiOCl single crystals and their photocatalytic activity. *Crystal growth & design*, 14(1), 236–239.

Blasdel, N. J., Wujcik, E. K., Carletta, J. E., Lee, K.-S. & Monty, C. N. (2014). Fabric nanocomposite resistance temperature detector. *IEEE Sensors Journal*, 15(1), 300–306.

Bouzouraa, M.-B., Battie, Y., Dalmasso, S., Zaibi, M.-A., Oueslati, M. & Naciri, A. E. (2017). Comparative study of ZnO optical dispersion laws. *Superlattices and Microstructures*, 104, 24–36.

Bowen, C. R., Taylor, J., LeBoulbar, E., Zabek, D., Chauhan, A. & Vaish, R. (2014). Pyroelectric materials and devices for energy harvesting applications. *Energy & Environmental Science*, 7(12), 3836–3856.

Buga, S. G., Serebryanaya, N. R., Dubitskiy, G. A., Semenova, E. E., Aksenenkov, V. V. & Blank, V. D. (2011). Structure and electrical properties of Sb2Te3 and Bi0.4Sb1. 6Te3 metastable phases obtained by HPHT treatment. *High Pressure Research*, 31(1), 86–90.

Bux, S. K., Fleurial, J.-P. & Kaner, R. B. (2010). Nanostructured materials for thermoelectric applications. *Chemical Communications*, 46(44), 8311–8324.

Cadenbach, T., Lascano, L., Vera, C. C., Vizuete, K. & Debut, A. (2019). Size-tunable fabrication of BiFeO3 nanoparticles with enhanced visible-light photocatalytic activity using a facile co-precipitation method. *Materials Research Express*, 6(10), 105034.

Cao, D., Wang, Z., Wen, L., Mi, Y. & Lei, Y. (2014). Switchable charge-transfer in the photoelectrochemical energy-conversion process of ferroelectric BiFeO3 photoelectrodes. *Angewandte Chemie*, 126(41), 11207–11211.

Catalan, G. & Scott, J. F. (2009). Physics and applications of bismuth ferrite. *Advanced materials*, 21(24), 2463–2485.

Chakrabartty, J., Barba, D., Jin, L., Benetti, D., Rosei, F. & Nechache, R. (2017). Photoelectrochemical properties of BiMnO3 thin films and nanostructures. *Journal of Power Sources*, 365, 162–168.

Chakrabartty, J., Harnagea, C., Celikin, M., Rosei, F. & Nechache, R. (2018). Improved photovoltaic performance from inorganic perovskite oxide thin films with mixed crystal phases. *Nature Photonics*, 12(5), 271–276.

Chauhan, S., Kumar, M., Chhoker, S. & Katyal, S. (2016). A comparative study on structural, vibrational, dielectric and magnetic properties of microcrystalline BiFeO3, nanocrystalline BiFeO3 and core–shell structured BiFeO3@ SiO2 nanoparticles. *Journal of Alloys and Compounds*, 666, 454–467.

Chen, A., Madan, D., Wright, P. & Evans, J. (2011). Dispenser-printed planar thick-film thermoelectric energy generators. *Journal of Micromechanics and Microengineering*, 21(10), 104006.

Chen, G., Dresselhaus, M., Dresselhaus, G., Fleurial, J.-P. & Caillat, T. (2003). Recent developments in thermoelectric materials. *International materials reviews*, 48(1), 45–66.

Chen, G., Chen, J., Pei, W., Lu, Y., Zhang, Q., Zhang, Q. & He, Y. (2019). Bismuth ferrite materials for solar cells: current status and prospects. *Materials Research Bulletin*, 110, 39–49.

Chen, J.-C. & Wu, J.-M. (2007). Dielectric properties and ac conductivities of dense single-phased Bi Fe O 3 ceramics. *Applied Physics Letters*, 91(18), 182903.

Chen, Q., Feng, N.-b., Huang, X.-h., Yao, Y., Jin, Y.-r., Pan, W. & Liu, D. (2020a). Humidity-sensing properties of a BiOCl-coated quartz crystal microbalance. *ACS omega*, 5(30), 18818–18825.

Chen, S., Huang, D., Xu, P., Xue, W., Lei, L., Cheng, M., Wang, R., Liu, X. & Deng, R. (2020b). Semiconductor-based photocatalysts for photocatalytic and photoelectrochemical water splitting: will we stop with photocorrosion? *Journal of Materials Chemistry A*, 8(5), 2286–2322.

Chen, Z., Jaramillo, T. F., Deutsch, T. G., Kleiman-Shwarsctein, A., Forman, A. J., Gaillard, N., Garland, R., Takanabe, K., Heske, C., Sunkara, M. et al. (2010). Accelerating materials development for photoelectrochemical hydrogen production: Standards for methods, definitions, and reporting protocols. *Journal of Materials Research*, 25(1), 3–16.

Chen, Z.-G., Han, G., Yang, L., Cheng, L. & Zou, J. (2012). Nanostructured thermoelectric materials: Current research and future challenge. *Progress in Natural Science: Materials International*, 22(6), 535–549.

Cheng, J., Wang, C., Zou, X. & Liao, L. (2019). Recent advances in optoelectronic devices based on 2D materials and their heterostructures. *Advanced Optical Materials*, 7(1), 1800441.

Cho, I. S., Chen, Z., Forman, A. J., Kim, D. R., Rao, P. M., Jaramillo, T. F. & Zheng, X. (2011). Branched TiO2 nanorods for photoelectrochemical hydrogen production. *Nano letters*, 11(11), 4978–4984.

Choi, T., Lee, S., Choi, Y., Kiryukhin, V. & Cheong, S.-W. (2009). Switchable ferroelectric diode and photovoltaic effect in BiFeO3. *Science*, 324(5923), 63–66.

Choi, W., Lahiri, I., Seelaboyina, R. & Kang, Y. S. (2010). Synthesis of graphene and its applications: a review. *Critical Reviews in Solid State and Materials Sciences*, 35(1), 52–71.

Chu, Y.-H., Martin, L. W., Holcomb, M. B., Gajek, M., Han, S.-J., He, Q., Balke, N., Yang, C.-H., Lee, D., Hu, W. et al. (2008). Electric-field control of local ferromagnetism using a magnetoelectric multiferroic. *Nature materials*, 7(6), 478–482.

Cox, N., Pantazis, D. A., Neese, F. & Lubitz, W. (2015). Artificial photosynthesis: understanding water splitting in nature. *Interface Focus*, 5(3), 20150009.

Czubacka, E. & Czerczak, S. (2019). Are platinum nanoparticles safe to human health? *Medycyna Pracy*, 70.

Dadarlat, D., Gibkes, J., Bicanic, D. & Pasca, A. (1996). Photopyroelectric (PPE) measurement of thermal parameters in food products. *Journal of food engineering*, 30(1-2), 155–162.

D'Aleo, F. P., Stalder, R. & Prasser, H.-M. (2015). Design and development of resistive temperature detector arrays on aluminium substrates. Measurements in mixing experiments. *Flow Measurement and Instrumentation*, 45, 176–187.

Damodara Das, V., Soundararajan, N. & Pattabi, M. (1987). Electrical conductivity and thermoelectric power of amorphous Sb2Te3 thin films and amorphous-crystalline transition. *Journal of materials science*, 22(10), 3522–3528.

Dandapat, A., Gnayem, H. & Sasson, Y. (2016). The fabrication of BiOCl x Br 1- x/alumina composite films with highly exposed {001} facets and their superior photocatalytic activities. *Chemical Communications*, 52(10), 2161–2164.

Dankoco, M., Tesfay, G., Bènevent, E. & Bendahan, M. (2016). Temperature sensor realized by inkjet printing process on flexible substrate. *Materials Science and Engineering: B*, 205, 1–5.

Das, R., Khan, G. G., Varma, S., Mukherjee, G. D. & Mandal, K. (2013). Effect of quantum confinement on optical and magnetic properties of Pr–Cr-codoped bismuth ferrite nanowires. *The Journal of Physical Chemistry C*, 117(39), 20209–20216.

Das, S., Ghara, S., Mahadevan, P., Sundaresan, A., Gopalakrishnan, J. & Sarma, D. (2018). Designing a lower band gap bulk ferroelectric material with a sizable polarization at room temperature. *ACS Energy Letters*, 3(5), 1176–1182.

Das, S., Fourmont, P., Benetti, D., Cloutier, S. G., Nechache, R., Wang, Z. M. & Rosei, F. (2020). High performance BiFeO3 ferroelectric nanostructured photocathodes. *The Journal of Chemical Physics*, 153(8), 084705.

Dauscher, A., Thomy, A. & Scherrer, H. (1996). Pulsed laser deposition of Bi2Te3 thin films. *Thin Solid Films*, 280(1-2), 61–66.

Davaji, B., Cho, H. D., Malakoutian, M., Lee, J.-K., Panin, G., Kang, T. W. & Lee, C. H. (2017). A patterned single layer graphene resistance temperature sensor. *Scientific reports*, 7(1), 1–10.

De Picciotto, R., Pfeiffer, L., Baldwin, K. & West, K. (2004). Nonlinear response of a clean one-dimensional wire. *Physical review letters*, 92(3), 036805.

Di, L., Yang, H., Xian, T. & Chen, X. (2017). Enhanced photocatalytic activity of NaBH4 reduced BiFeO3 nanoparticles for rhodamine B decolorization. *Materials*, 10(10), 1118.

Di, L., Yang, H., Hu, G., Xian, T., Ma, J., Jiang, J., Li, R. & Wei, Z. (2014). Enhanced photocatalytic activity of BiFeO3 particles by surface decoration with Ag nanoparticles. *Journal of Materials Science: Materials in Electronics*, 25(6), 2463–2469.

DiSalvo, F. J. (1999). Thermoelectric cooling and power generation. *Science*, 285(5428), 703–706.

Dong, F., Xiong, T., Sun, Y., Zhang, Y. & Zhou, Y. (2015). Controlling interfacial contact and exposed facets for enhancing photocatalysis via 2D–2D heterostructures. *Chemical Communications*, 51(39), 8249–8252.

Douani, R., Lamrani, N., Saidi, M., Guhel, Y., Chaouchi, A., Boudart, B. et al. (2020). Improvement of humidity sensing performance of BiFeO3 nanoparticles-based sensor by the addition of carbon fibers. *Sensors and Actuators A: Physical*, 307, 111981.

Dresselhaus, M. S., Chen, G., Tang, M. Y., Yang, R., Lee, H., Wang, D., Ren, Z., Fleurial, J.-P. & Gogna, P. (2007). New directions for low-dimensional thermoelectric materials. *Advanced materials*, 19(8), 1043–1053.

Duan, F., Ma, Y., Lv, P., Sheng, J., Lu, S., Zhu, H., Du, M., Chen, X. & Chen, M. (2021). Oxygen vacancy-enriched Bi2O3/BiFeO3 pn heterojunction nanofibers with highly efficient photocatalytic activity under visible light irradiation. *Applied Surface Science*, 562, 150171.

Eason, R. (2007). *Pulsed laser deposition of thin films: applications-led growth of functional materials* [1]. John Wiley & Sons. doi: 10.1002/0470052120.

Eerenstein, W., Mathur, N. & Scott, J. F. (2006). Multiferroic and magnetoelectric materials. *nature*, 442(7104), 759–765.

Eibner, A. (1911). Action of light on pigments I. *Chem-Ztg*, 35, 753–755.

Eliaz, N. (2019). Corrosion of metallic biomaterials: a review. *Materials*, 12(3), 407.

Esposito, S. (2019). "Traditional" sol-gel chemistry as a powerful tool for the preparation of supported metal and metal oxide catalysts. *Materials*, 12(4), 668.

Falkowski, P. G., Fenchel, T. & Delong, E. F. (2008). The microbial engines that drive Earth's biogeochemical cycles. *science*, 320(5879), 1034–1039.

Fan, P., Zheng, Z.-H., Liang, G.-X., Zhang, D.-P. & Cai, X.-M. (2010). Thermoelectric characterization of ion beam sputtered Sb2Te3 thin films. *Journal of Alloys and Compounds*, 505(1), 278–280.

Fang, B., Zeng, Z., Yan, X. & Hu, Z. (2013). Effects of annealing on thermoelectric properties of Sb2Te3 thin films prepared by radio frequency magnetron sputtering. *Journal of Materials Science: Materials in Electronics*, 24(4), 1105–1111.

Fei, L., Hu, Y., Li, X., Song, R., Sun, L., Huang, H., Gu, H., Chan, H. L. & Wang, Y. (2015). Electrospun bismuth ferrite nanofibers for potential applications in ferroelectric photovoltaic devices. *ACS applied materials & interfaces*, 7(6), 3665–3670.

Feinaeugle, M., Sones, C., Koukharenko, E. & Eason, R. (2013). Fabrication of a thermoelectric generator on a polymer-coated substrate via laser-induced forward transfer of chalcogenide thin films. *Smart materials and structures*, 22(11), 115023.

Fernández-Ibáñez, P. ., Blanco, J., Malato, S. & De Las Nieves, F. (2003). Application of the colloidal stability of TiO2 particles for recovery and reuse in solar photocatalysis. *Water Research*, 37(13), 3180–3188.

Feteira, A. (2009). Negative temperature coefficient resistance (NTCR) ceramic thermistors: an industrial perspective. *Journal of the American Ceramic Society*, 92(5), 967–983.

Feteira, A. & Reichmann, K. (2010). NTC ceramics: past, present and future. *Advances in Science and Technology*, 67, 124–133.

Fourmont, P. & Cloutier, S. G. (2022). Screen-printed p–n BiOCl/BiFeO 3 heterojunctions for efficient photocatalytic degradation of Rhodamine B. *RSC advances*, 12(38), 24868–24875.

Fourmont, P., Gerlein, L. F., Fortier, F.-X., Cloutier, S. G. & Nechache, R. (2018). Highly efficient thermoelectric microgenerators using nearly room temperature pulsed laser deposition. *ACS applied materials & interfaces*, 10(12), 10194–10201.

Fourmont, P., Nechache, R. & Cloutier, S. G. (2021). Reusable BiFeO3 Nanofiber-Based Membranes for Photo-activated Organic Pollutant Removal with Negligible Colloidal Release. *ACS Applied Nano Materials*, 4(11), 12261–12269.

Franco, M., Alves, R., Perinka, N., Tubio, C., Costa, P. & Lanceros-Mendez, S. (2020). Water-based graphene inks for all-printed temperature and deformation sensors. *ACS Applied Electronic Materials*, 2(9), 2857–2867.

Fresno, F., Portela, R., Suárez, S. & Coronado, J. M. (2014). Photocatalytic materials: recent achievements and near future trends. *Journal of Materials Chemistry A*, 2(9), 2863–2884.

Fujishima, A. & Honda, K. (1972). Electrochemical photolysis of water at a semiconductor electrode. *nature*, 238(5358), 37–38.

Gao, F., Chen, X., Yin, K., Dong, S., Ren, Z., Yuan, F., Yu, T., Zou, Z. & Liu, J.-M. (2007). Visible-light photocatalytic properties of weak magnetic BiFeO3 nanoparticles. *Advanced materials*, 19(19), 2889–2892.

Gao, T., Chen, Z., Zhu, Y., Niu, F., Huang, Q., Qin, L., Sun, X. & Huang, Y. (2014). Synthesis of BiFeO3 nanoparticles for the visible-light induced photocatalytic property. *Materials Research Bulletin*, 59, 6–12.

Gao, T., Chen, Z., Huang, Q., Niu, F., Huang, X., Qin, L. & Huang, Y. (2015). A review: preparation of bismuth ferrite nanoparticles and its applications in visible-light induced photocatalyses. *Rev. adv. mater. sci*, 40(2), 97–109.

Gebhardt, J. & Rappe, A. M. (2018). Doping of BiFeO3: A comprehensive study on substitutional doping. *Physical Review B*, 98(12), 125202.

Gerischer, H. (1966). Electrochemical behavior of semiconductors under illumination. *Journal of the electrochemical society*, 113(11), 1174.

Ghosh, S., Dasgupta, S., Sen, A. & Maiti, H. S. (2005). Low temperature synthesis of bismuth ferrite nanoparticles by a ferrioxalate precursor method. *Materials research bulletin*, 40(12), 2073–2079.

Giocondi, J. L. & Rohrer, G. S. (2001). Spatial separation of photochemical oxidation and reduction reactions on the surface of ferroelectric BaTiO3. *The Journal of Physical Chemistry B*, 105(35), 8275–8277.

Giraldo, D., Almodóvar, P., López, M., Rodríguez-Aguado, E., Rodríguez-Castellón, E., Galdámez, A. & Álvarez-Serrano, I. (2021). Exploring multiferroicity in BiFeO3-NaNbO3 thermistor electroceramics. *Journal of the European Ceramic Society*, 41(14), 7069–7076.

Goldschmidt, V. (1927). Geochemische verteilungsgesetze der elemente. *Oslo: Norske Videnskap*.

Gómez, J. M., Canaria, C., Burgos, R. O., Ortiz, C., Supelano, G. & Vargas, C. P. (2016). Structural study of yttrium substituted BiFeO3. *Journal of Physics: Conference Series*, 687(1), 012091.

Goncalves, L., Alpuim, P., Min, G., Rowe, D. M., Couto, C. & Correia, J. (2008). Optimization of Bi2Te3 and Sb2Te3 thin films deposited by co-evaporation on polyimide for thermoelectric applications. *Vacuum*, 82(12), 1499–1502.

Grätzel, M. (2001). Photoelectrochemical cells. *Nature*, 414(6861), 338–344.

Grinberg, I., West, D. V., Torres, M., Gou, G., Stein, D. M., Wu, L., Chen, G., Gallo, E. M., Akbashev, A. R., Davies, P. K. et al. (2013). Perovskite oxides for visible-light-absorbing ferroelectric and photovoltaic materials. *Nature*, 503(7477), 509–512.

Gu, S., Zhou, X., Zheng, F., Fang, L., Dong, W. & Shen, M. (2017a). Improved photocathodic performance in Pt catalyzed ferroelectric BiFeO3 films sandwiched by a porous carbon layer. *Chemical Communications*, 53(52), 7052–7055.

Gu, Y.-y., Zhao, L., Yang, M.-y., Xiong, Y.-q., Wu, Z., Zhou, M.-j. & Yan, J. (2017b). Preparation and characterization of highly photocatalytic active hierarchical BiOX (X= Cl, Br, I) microflowers for rhodamine B degradation with kinetic modelling studies. *Journal of Central South University*, 24(4), 754–765.

Hao, C., Xiang, J., Hou, H., Lv, W., Lv, Y., Hu, W., Liu, Z. et al. (2014). Photocatalytic performances of BiFeO3 particles with the average size in nanometer, submicrometer, and

micrometer. *Materials Research Bulletin*, 50, 369–373.

Haras, M. & Skotnicki, T. (2018). Thermoelectricity for IoT–A review. *Nano Energy*, 54, 461–476.

Haruna, A., Abdulkadir, I. & Idris, S. (2020). Photocatalytic activity and doping effects of BiFeO3 nanoparticles in model organic dyes. *Heliyon*, 6(1), e03237.

He, J., Guo, R., Fang, L., Dong, W., Zheng, F. & Shen, M. (2013). Characterization and visible light photocatalytic mechanism of size-controlled BiFeO3 nanoparticles. *Materials Research Bulletin*, 48(9), 3017–3024.

He, Z., Shi, Y., Gao, C., Wen, L., Chen, J. & Song, S. (2014). BiOCl/BiVO4 p–n heterojunction with enhanced photocatalytic activity under visible-light irradiation. *The Journal of Physical Chemistry C*, 118(1), 389–398.

Heinig, A. & Papaioannou, D. (2017). Comparison between thermal simulations and experimental measurements on an advanced microelectronics test-system. *2017 16th IEEE Intersociety Conference on Thermal and Thermomechanical Phenomena in Electronic Systems (ITherm)*, pp. 428–435.

Hernández, S., Hidalgo, D., Sacco, A., Chiodoni, A., Lamberti, A., Cauda, V., Tresso, E. & Saracco, G. (2015). Comparison of photocatalytic and transport properties of TiO2 and ZnO nanostructures for solar-driven water splitting. *Physical Chemistry Chemical Physics*, 17(12), 7775–7786.

Heron, J., Schlom, D. & Ramesh, R. (2014). Electric field control of magnetism using BiFeO3-based heterostructures. *Applied Physics Reviews*, 1(2), 021303.

Herrmann, J.-M. (2000). Photocatalysis. *Kirk-Othmer Encyclopedia of Chemical Technology*, 1–44.

Hirose, K., Sinmyo, R. & Hernlund, J. (2017). Perovskite in Earth's deep interior. *Science*, 358(6364), 734–738.

Hochbaum, A. I. & Yang, P. (2010). Semiconductor nanowires for energy conversion. *Chemical reviews*, 110(1), 527–546.

Hu, Y., Li, D., Wang, H., Zeng, G., Li, X. & Shao, Y. (2015). Role of active oxygen species in the liquid-phase photocatalytic degradation of RhB using BiVO4/TiO2 heterostructure under visible light irradiation. *Journal of Molecular Catalysis A: Chemical*, 408, 172–178.

Huang, B., Lawrence, C., Gross, A., Hwang, G.-S., Ghafouri, N., Lee, S.-W., Kim, H., Li, C.-P., Uher, C., Najafi, K. et al. (2008). Low-temperature characterization and micropatterning of coevaporated Bi2Te3 and Sb2Te3 films. *Journal of Applied Physics*, 104(11), 113710.

Huang, C., Hu, J., Cong, S., Zhao, Z. & Qiu, X. (2015). Hierarchical BiOCl microflowers with improved visible-light-driven photocatalytic activity by Fe (III) modification. *Applied Catalysis B: Environmental*, 174, 105–112.

Huang, C.-C., Kao, Z.-K. & Liao, Y.-C. (2013). Flexible miniaturized nickel oxide thermistor arrays via inkjet printing technology. *ACS applied materials & interfaces*, 5(24), 12954–12959.

Huang, W., Harnagea, C., Benetti, D., Chaker, M., Rosei, F. & Nechache, R. (2017). Multiferroic Bi2FeCrO6 based p–i–n heterojunction photovoltaic devices. *Journal of Materials Chemistry A*, 5(21), 10355–10364.

Huang, W., Harnagea, C., Tong, X., Benetti, D., Sun, S., Chaker, M., Rosei, F. & Nechache, R. (2019). Epitaxial Bi2FeCrO6 multiferroic thin-film photoanodes with ultrathin p-type NiO layers for improved solar water oxidation. *ACS applied materials & interfaces*, 11(14), 13185–13193.

Huang, Y.-L., Chang, W. S., Van, C. N., Liu, H.-J., Tsai, K.-A., Chen, J.-W., Kuo, H.-H., Tzeng, W.-Y., Chen, Y.-C., Wu, C.-L. et al. (2016). Tunable photoelectrochemical performance of Au/BiFeO3 heterostructure. *Nanoscale*, 8(34), 15795–15801.

Humayun, M., Zada, A., Li, Z., Xie, M., Zhang, X., Qu, Y., Raziq, F. & Jing, L. (2016). Enhanced visible-light activities of porous BiFeO3 by coupling with nanocrystalline TiO2 and mechanism. *Applied Catalysis B: Environmental*, 180, 219–226.

Huo, Y., Jin, Y. & Zhang, Y. (2010). Citric acid assisted solvothermal synthesis of BiFeO3 microspheres with high visible-light photocatalytic activity. *Journal of Molecular Catalysis A: Chemical*, 331(1-2), 15–20.

Hussain, A., Xu, X., Yuan, G., Wang, Y., Yang, Y., Yin, J., Liu, J. & Liu, Z. (2014). The development of BiFeO3-based ceramics. *Chinese science bulletin*, 59(36), 5161–5169.

Ijaz, H., Zia, R., Taj, A., Jameel, F., Butt, F. K., Asim, T., Jameel, N., Abbas, W., Iqbal, M., Bajwa, S. Z. et al. (2020). Synthesis of BiOCl nanoplatelets as the dual interfaces for the detection of glutathione linked disease biomarkers and biocompatibility assessment in vitro against HCT cell lines model. *Applied Nanoscience*, 10(9), 3569–3576.

Ikegami, A., Arima, H., Tosaki, H., Matsuoka, Y., Ai, M., Minorikawa, H. & Asahino, Y. (1980). Thick-film thermistor and its applications. *IEEE Transactions on Components, Hybrids, and Manufacturing Technology*, 3(4), 541–550.

Ipek, B. & Uner, D. (2019). On the limits of photocatalytic water splitting. In *Water Chemistry* (pp. 177). IntechOpen.

Irshad, M., tul Ain, Q., Zaman, M., Aslam, M. Z., Kousar, N., Asim, M., Rafique, M., Siraj, K., Tabish, A. N., Usman, M. et al. (2022). Photocatalysis and perovskite oxide-based materials: a remedy for a clean and sustainable future. *RSC advances*, 12(12), 7009–7039.

Ishiwara, H. (2012). Impurity substitution effects in BiFeO3 thin films—From a viewpoint of FeRAM applications. *Current Applied Physics*, 12(3), 603–611.

Ivanov, K., Aleksandrov, A. & Belovski, I. (2019). Synthesis and Study on Waste Heat Thermoelectric Generator. *2019 II International Conference on High Technology for Sustainable Development (HiTech)*, pp. 1–4.

Jaffari, Z. H., Lam, S. M., Sin, J. C. & Mohamed, A. R. (2019a). Constructing magnetic Pt-loaded BiFeO3 nanocomposite for boosted visible light photocatalytic and antibacterial activities. *Environmental Science and Pollution Research*, 26(10), 10204–10218.

Jaffari, Z. H., Lam, S.-M., Sin, J.-C. & Zeng, H. (2019b). Boosting visible light photocatalytic and antibacterial performance by decoration of silver on magnetic spindle-like bismuth ferrite. *Materials Science in Semiconductor Processing*, 101, 103–115.

Jagtap, S., Rane, S., Mulik, U. & Amalnerkar, D. (2007). Thick film NTC thermistor for wide range of temperature sensing. *Microelectronics international*.

Jamkhande, P. G., Ghule, N. W., Bamer, A. H. & Kalaskar, M. G. (2019). Metal nanoparticles synthesis: An overview on methods of preparation, advantages and disadvantages, and applications. *Journal of drug delivery science and technology*, 53, 101174.

Jang, Y. J. & Lee, J. S. (2019). Photoelectrochemical water splitting with p-type metal oxide semiconductor photocathodes. *ChemSusChem*, 12(9), 1835–1845.

Jangid, S., Barbar, S. & Roy, M. (2014). Structural, Electrical and Magnetic Properties of Pure and Substituted BiFeO3. *Biosensors Nanotechnology*, 433–506.

Jenkins, J., Rayne, J. & Ure Jr, R. (1972). Elastic moduli and phonon properties of Bi2Te3. *Physical Review B*, 5(8), 3171.

Jeong, S. Y., Song, J. & Lee, S. (2018). Photoelectrochemical device designs toward practical solar water splitting: A review on the recent progress of bivo4 and bifeo3 photoanodes. *Applied Sciences*, 8(8), 1388.

Ji, W., Yao, K., Lim, Y.-F., Liang, Y. C. & Suwardi, A. (2013). Epitaxial ferroelectric BiFeO3 thin films for unassisted photocatalytic water splitting. *Applied Physics Letters*, 103(6), 062901.

Jiang, C.-M., Reyes-Lillo, S. E., Liang, Y., Liu, Y.-S., Liu, G., Toma, F. M., Prendergast, D., Sharp, I. D. & Cooper, J. K. (2019). Electronic structure and performance bottlenecks of CuFeO2 photocathodes. *Chemistry of Materials*, 31(7), 2524–2534.

Johar, M. A., Afzal, R. A., Alazba, A. A. & Manzoor, U. (2015). Photocatalysis and bandgap engineering using ZnO nanocomposites. *Advances in Materials Science and Engineering*, 2015.

Joy, J., Mathew, J. & George, S. C. (2018). Nanomaterials for photoelectrochemical water splitting–review. *International Journal of hydrogen energy*, 43(10), 4804–4817.

Ka, I., Asuo, I. M., Basu, S., Fourmont, P., Gedamu, D. M., Pignolet, A., Cloutier, S. G. & Nechache, R. (2018). Hysteresis-Free 1D Network Mixed Halide-Perovskite Semitransparent Solar Cells. *Small*, 14(38), 1802319.

Kabra, K., Chaudhary, R. & Sawhney, R. L. (2004). Treatment of hazardous organic and inorganic compounds through aqueous-phase photocatalysis: a review. *Industrial & engineering chemistry research*, 43(24), 7683–7696.

Kang, D., Hill, J. C., Park, Y. & Choi, K.-S. (2016). Photoelectrochemical properties and photostabilities of high surface area CuBi2O4 and Ag-doped CuBi2O4 photocathodes. *Chemistry of Materials*, 28(12), 4331–4340.

Katerinopoulou, D., Zalar, P., Sweelssen, J., Kiriakidis, G., Rentrop, C., Groen, P., Gelinck, G. H., van den Brand, J. & Smits, E. C. (2019). Large-area all-printed temperature sensing surfaces using novel composite thermistor materials. *Advanced Electronic Materials*, 5(2), 1800605.

Katsounaros, I., Schneider, W. B., Meier, J. C., Benedikt, U., Biedermann, P. U., Auer, A. A. & Mayrhofer, K. J. (2012). Hydrogen peroxide electrochemistry on platinum: towards understanding the oxygen reduction reaction mechanism. *Physical Chemistry Chemical Physics*, 14(20), 7384–7391.

Ke, Q., Lou, X., Wang, Y. & Wang, J. (2010). Oxygen-vacancy-related relaxation and scaling behaviors of Bi 0.9 La 0.1 Fe 0.98 Mg 0.02 O 3 ferroelectric thin films. *Physical Review B*, 82(2), 024102.

Keramidas, K., Voutsas, G. & Rentzeperis, P. (1993). The crystal structure of BiOCl. *Zeitschrift für Kristallographie-Crystalline Materials*, 205(1), 35–40.

Khan, M. R., Chuan, T. W., Yousuf, A., Chowdhury, M. & Cheng, C. K. (2015). Schottky barrier and surface plasmonic resonance phenomena towards the photocatalytic reaction: study of their mechanisms to enhance photocatalytic activity. *Catalysis Science & Technology*, 5(5), 2522–2531.

Khan, Y., Ostfeld, A. E., Lochner, C. M., Pierre, A. & Arias, A. C. (2016). Monitoring of vital signs with flexible and wearable medical devices. *Advanced materials*, 28(22), 4373–4395.

Kim, H.-B., Hayashi, M., Nakatani, K., Kitamura, N., Sasaki, K., Hotta, J.-i. & Masuhara, H. (1996). In situ measurements of ion-exchange processes in single polymer particles: laser trapping microspectroscopy and confocal fluorescence microspectroscopy. *Analytical chemistry*, 68(3), 409–414.

Kim, H. G., Hwang, D. W. & Lee, J. S. (2004). An undoped, single-phase oxide photocatalyst working under visible light. *Journal of the American Chemical Society*, 126(29), 8912–8913.

Kim, J.-H., Choi, J.-Y., Bae, J.-M., Kim, M.-Y. & Oh, T.-S. (2013). Thermoelectric characteristics of n-type Bi2Te3 and p-type Sb2Te3 thin films prepared by co-evaporation and annealing for thermopile sensor applications. *Materials Transactions*, 54(4), 618–625.

Kim, J. K., Kim, S. S. & Kim, W.-J. (2005). Sol–gel synthesis and properties of multiferroic BiFeO3. *Materials Letters*, 59(29-30), 4006–4009.

Kong, D., Le, L. T., Li, Y., Zunino, J. L. & Lee, W. (2012). Temperature-dependent electrical properties of graphene inkjet-printed on flexible materials. *Langmuir*, 28(37), 13467–13472.

Kozhukh, M. (2008). High temperature thermistors. Google Patents. US Patent 7,405,457.

Kullmann, W., Geurts, J., Richter, W., Lehner, N., Rauh, H., Steigenberger, U., Eichhorn, G. & Geick, R. (1984). Effect of hydrostatic and uniaxial pressure on structural properties and Raman active lattice vibrations in Bi2Te3. *physica status solidi (b)*, 125(1), 131–138.

Kumar, A., Scott, J., Martinez, R., Srinivasan, G. & Katiyar, R. (2012). In-plane dielectric and magnetoelectric studies of BiFeO3. *physica status solidi (a)*, 209(7), 1207–1212.

Kumar, S., Bhatt, K., Kumar, P., Sharma, S., Kumar, A. & Tripathi, C. (2019). Laser patterned, high-power graphene paper resistor with dual temperature coefficient of resistance. *RSC advances*, 9(15), 8262–8270.

Kuzubasoglu, B. A. & Bahadir, S. K. (2020). Flexible temperature sensors: A review. *Sensors and Actuators A: Physical*, 315, 112282.

Laboratory, L. L. N. (2013). Estimated U.S. Energy Used in 2013. Retrieved on 2022-05-01 from: https://flowcharts.llnl.gov/content/energy/energy_archive/energy_flow_2013/2013USEnergy.png.

Lahokallio, S., Hoikkanen, M., Vuorinen, J. & Frisk, L. (2015). High-temperature storage testing of acf attached sensor structures. *Materials*, 8(12), 8641–8660.

Lam, S.-M., Sin, J.-C. & Mohamed, A. R. (2017). A newly emerging visible light-responsive BiFeO3 perovskite for photocatalytic applications: a mini review. *Materials Research Bulletin*, 90, 15–30.

Lan, Y., Yang, S., Chen, G. & Yang, S. (2020). Characteristics of a Type of NTC Thermistors for Cryogenic Applications. *Advances in Materials Physics and Chemistry*, 10(08), 167.

LeBlanc, S., Yee, S. K., Scullin, M. L., Dames, C. & Goodson, K. E. (2014). Material and manufacturing cost considerations for thermoelectrics. *Renewable and Sustainable Energy Reviews*, 32, 313–327.

Lee, H., Joo, H.-y., Yoon, C., Lee, J., Lee, H., Choi, J., Park, B. & Choi, T. (2017). Ferroelectric BiFeO3/TiO2 nanotube heterostructures for enhanced photoelectrochemical performance. *Current Applied Physics*, 17(5), 679–683.

Lee, J. H., Fina, I., Marti, X., Kim, Y. H., Hesse, D. & Alexe, M. (2014). Spintronic functionality of BiFeO3 domain walls. *Advanced Materials*, 26(41), 7078–7082.

Lee, S.-W., Bae, S., Kim, D. & Lee, H.-S. (2020). Historical Analysis of High-Efficiency, Large-Area Solar Cells: Toward Upscaling of Perovskite Solar Cells. *Advanced Materials*, 32(51), 2002202.

Lee, S., Fernandez-Diaz, M., Kimura, H., Noda, Y., Adroja, D., Lee, S., Park, J., Kiryukhin, V., Cheong, S.-W., Mostovoy, M. et al. (2013). Negative magnetostrictive magnetoelectric coupling of BiFeO3. *Physical Review B*, 88(6), 060103.

Li, H., Li, F., Shen, Z., Han, S.-T., Chen, J., Dong, C., Chen, C., Zhou, Y. & Wang, M. (2021). Photoferroelectric perovskite solar cells: Principles, advances and insights. *Nano Today*, 37, 101062.

Li, J., Zhang, G., Han, S., Cao, J., Duan, L. & Zeng, T. (2018). Enhanced solar absorption and visible-light photocatalytic and photoelectrochemical properties of aluminium-reduced BaTiO3 nanoparticles. *Chemical Communications*, 54(7), 723–726.

Li, S., Lin, Y.-H., Zhang, B.-P., Nan, C.-W. & Wang, Y. (2009). Photocatalytic and magnetic behaviors observed in nanostructured BiFeO3 particles. American Institute of Physics.

Li, S., Zhang, J., Kibria, M. G., Mi, Z., Chaker, M., Ma, D., Nechache, R. & Rosei, F. (2013). Remarkably enhanced photocatalytic activity of laser ablated Au nanoparticle decorated BiFeO3 nanowires under visible-light. *Chemical Communications*, 49(52), 5856–5858.

Li, S., AlOtaibi, B., Huang, W., Mi, Z., Serpone, N., Nechache, R. & Rosei, F. (2015). Epitaxial Bi2FeCrO6 multiferroic thin film as a new visible light absorbing photocathode material. *Small*, 11(32), 4018–4026.

Li, S., Zhang, J., Zhang, B.-P., Huang, W., Harnagea, C., Nechache, R., Zhu, L., Zhang, S., Lin, Y.-H., Ni, L. et al. (2017). Manipulation of charge transfer in vertically aligned epitaxial ferroelectric KNbO3 nanowire array photoelectrodes. *Nano Energy*, 35, 92–100.

Li, Y., Wang, X.-T., Zhang, X.-Q., Li, X., Wang, J. & Wang, C.-W. (2020). New hydrothermal synthesis strategy of nano-sized BiFeO3 for high-efficient photocatalytic applications. *Physica E: Low-dimensional Systems and Nanostructures*, 118, 113865.

Li, Y., Li, J., Chen, L., Sun, H., Zhang, H., Guo, H. & Feng, L. (2019). In situ synthesis of Au-induced hierarchical nanofibers/nanoflakes structured BiFeO3 homojunction photocatalyst with enhanced photocatalytic activity. *Frontiers in Chemistry*, 649.

Liang, S.-J., Cheng, B., Cui, X. & Miao, F. (2020). Van der Waals heterostructures for high-performance device applications: challenges and opportunities. *Advanced Materials*, 32(27), 1903800.

Lin, N., Gong, Y., Wang, R., Wang, Y. & Zhang, X. (2022). Critical review of perovskite-based materials in advanced oxidation system for wastewater treatment: Design, applications and mechanisms. *Journal of Hazardous Materials*, 424, 127637.

Liu, M., Zhang, H., Gedamu, D., Fourmont, P., Rekola, H., Hiltunen, A., Cloutier, S. G., Nechache, R., Priimagi, A. & Vivo, P. (2019). Halide Perovskite Nanocrystals for Next-Generation Optoelectronics. *Small*, 15(28), 1900801.

Liu, Q., Zhou, Y., You, L., Wang, J., Shen, M. & Fang, L. (2016). Enhanced ferroelectric photoelectrochemical properties of polycrystalline BiFeO3 film by decorating with Ag nanoparticles. *Applied Physics Letters*, 108(2), 022902.

Liu, W., Jie, Q., Kim, H. S. & Ren, Z. (2015). Current progress and future challenges in thermoelectric power generation: From materials to devices. *Acta Materialia*, 87, 357–376.

Liu, Z. & Yan, F. (2011). Photovoltaic effect of BiFeO3/poly(3-hexylthiophene) heterojunction. *physica status solidi (RRL)–Rapid Research Letters*, 5(10-11), 367–369.

Liu, Z. & Yan, F. (2012). The application of bismuth-based oxides in organic-inorganic hybrid photovoltaic devices. *Journal of the American Ceramic Society*, 95(6), 1944–1948.

Long, M., Cai, W., Cai, J., Zhou, B., Chai, X. & Wu, Y. (2006). Efficient photocatalytic degradation of phenol over Co3O4/BiVO4 composite under visible light irradiation. *The Journal of Physical Chemistry B*, 110(41), 20211–20216.

Lu, J., Günther, A., Schrettle, F., Mayr, F., Krohns, S., Lunkenheimer, P., Pimenov, A., Travkin, V., Mukhin, A. & Loidl, A. (2010). On the room temperature multiferroic BiFeO3: magnetic, dielectric and thermal properties. *The European Physical Journal B*, 75(4), 451–460.

Luo, W., Zhu, L., Wang, N., Tang, H., Cao, M. & She, Y. (2010). Efficient removal of organic pollutants with magnetic nanoscaled BiFeO3 as a reusable heterogeneous Fenton-like catalyst. *Environmental science & technology*, 44(5), 1786–1791.

Ma, C.-J., Li, N. & Song, W.-L. (2020). Tailoring the electrochemical behaviors of bismuth ferrite using Ca ion doping. *Frontiers in Materials*, 15.

Macher, A., Reichmann, K., Fruhwirth, O., Gatterer, K. & Herzog, G. (1996). Perovskite versus spinel type NTC materials for application at elevated temperatures. *INFORMACIJE MIDEM-LJUBLJANA-*, 26, 79–85.

Macklen, E. (1986). Electrical conductivity and cation distribution in nickel manganite. *Journal of Physics and Chemistry of Solids*, 47(11), 1073–1079.

Madan, D., Chen, A., Wright, P. K. & Evans, J. W. (2012). Printed Se-doped MA n-type Bi2Te3 thick-film thermoelectric generators. *Journal of electronic materials*, 41(6), 1481–1486.

Makhdoom, A., Akhtar, M., Khan, R., Rafiq, M., Hasan, M., Sher, F. & Fitch, A. (2013). Association of microstructure and electric heterogeneity in BiFeO3. *Materials Chemistry and Physics*, 143(1), 256–262.

Mamur, H., Bhuiyan, M., Korkmaz, F. & Nil, M. (2018). A review on bismuth telluride (Bi2Te3) nanostructure for thermoelectric applications. *Renewable and Sustainable Energy Reviews*, 82, 4159–4169.

Mandelis, A. & Zver, M. M. (1985). Theory of photopyroelectric spectroscopy of solids. *Journal of applied physics*, 57(9), 4421–4430.

Marshall, M. S., Malashevich, A., Disa, A. S., Han, M.-G., Chen, H., Zhu, Y., Ismail-Beigi, S., Walker, F. J. & Ahn, C. H. (2014). Conduction at a ferroelectric interface. *Physical Review Applied*, 2(5), 051001.

Maso, N. & West, A. R. (2012). Electrical properties of Ca-doped BiFeO3 ceramics: from p-type semiconduction to oxide-ion conduction. *Chemistry of Materials*, 24(11), 2127–2132.

Mazumder, R., Ghosh, S., Mondal, P., Bhattacharya, D., Dasgupta, S., Das, N., Sen, A., Tyagi, A., Sivakumar, M., Takami, T. et al. (2006). Particle size dependence of magnetization and phase transition near TN in multiferroic Bi Fe O 3. *Journal of Applied Physics*, 100(3), 033908.

Melo, G. H., Santos, J. P., Gualdi, A. J., Tsai, C.-M., Sigmund, W. M. & Bretas, R. E. (2017). Correlation between electrospinning parameters and magnetic properties of BiFeO3 nanofibers. *Electrospinning*, 1(1), 73–86.

Michel, C., Moreau, J.-M., Achenbach, G. D., Gerson, R. & James, W. J. (1969). The atomic structure of BiFeO3. *Solid State Communications*, 7(9), 701–704.

Michel, M., Biswas, C., Tiwary, C. S., Saenz, G. A., Hossain, R. F., Ajayan, P. & Kaul, A. B. (2017). A thermally-invariant, additively manufactured, high-power graphene resistor for flexible electronics. *2D Materials*, 4(2), 025076.

Miller, N. C. & Bernechea, M. (2018). Research Update: Bismuth based materials for photovoltaics. *APL Materials*, 6(8), 084503.

Min, H., Lee, D. Y., Kim, J., Kim, G., Lee, K. S., Kim, J., Paik, M. J., Kim, Y. K., Kim, K. S., Kim, M. G. et al. (2021). Perovskite solar cells with atomically coherent interlayers on SnO2 electrodes. *Nature*, 598(7881), 444–450.

Mocherla, P. S., Karthik, C., Ubic, R., Ramachandra Rao, M. & Sudakar, C. (2013). Tunable bandgap in BiFeO3 nanoparticles: the role of microstrain and oxygen defects. *Applied Physics Letters*, 103(2), 022910.

Mohan, S., Subramanian, B. & Sarveswaran, G. (2014). A prototypical development of plasmonic multiferroic bismuth ferrite particulate and fiber nanostructures and their remarkable photocatalytic activity under sunlight. *Journal of Materials Chemistry C*, 2(33), 6835–6842.

Moitra, D., Anand, C., Ghosh, B. K., Chandel, M. & Ghosh, N. N. (2018). One-dimensional BiFeO3 nanowire-reduced graphene oxide nanocomposite as excellent supercapacitor electrode material. *ACS Applied Energy Materials*, 1(2), 464–474.

Moniz, S. J., Quesada-Cabrera, R., Blackman, C. S., Tang, J., Southern, P., Weaver, P. M. & Carmalt, C. J. (2014). A simple, low-cost CVD route to thin films of BiFeO3 for efficient water photo-oxidation. *Journal of Materials Chemistry A*, 2(9), 2922–2927.

Moon, C. W., Choi, M.-J., Hyun, J. K. & Jang, H. W. (2021). Enhancing photoelectrochemical water splitting with plasmonic Au nanoparticles. *Nanoscale Advances*, 3(21), 5981–6006.

Morris, M. R., Pendlebury, S. R., Hong, J., Dunn, S. & Durrant, J. R. (2016). Effect of internal electric fields on charge carrier dynamics in a ferroelectric material for solar energy conversion. *Advanced materials*, 28(33), 7123–7128.

Müller, M., Budde, W., Gottfried-Gottfried, R., Hübel, A., Jähne, R. & Kück, H. (1996). A thermoelectric infrared radiation sensor with monolithically integrated amplifier stage and temperature sensor. *Sensors and Actuators A: Physical*, 54(1-3), 601–605.

Muralidharan, M., Sunny, E., Dayas, K., Seema, A. & Resmi, K. (2011). Optimization of process parameters for the production of Ni–Mn–Co–Fe based NTC chip thermistors through tape casting route. *Journal of alloys and compounds*, 509(38), 9363–9371.

Nasby, R. & Quinn, R. K. (1976). Photoassisted electrolysis of water using a BaTiO3 electrode. *Materials Research Bulletin*, 11(8), 985–992.

Nassar, N. T., Graedel, T. E. & Harper, E. (2015). By-product metals are technologically essential but have problematic supply. *Science advances*, 1(3), e1400180.

Nechache, R., Harnagea, C., Licoccia, S., Traversa, E., Ruediger, A., Pignolet, A. & Rosei, F. (2011). Photovoltaic properties of Bi 2 FeCrO 6 epitaxial thin films. *Applied Physics Letters*, 98(20), 202902.

Nechache, R., Huang, W., Li, S. & Rosei, F. (2016). Photovoltaic properties of Bi2FeCrO6 films epitaxially grown on (100)-oriented silicon substrates. *Nanoscale*, 8(6), 3237–3243.

Nechache, R., Harnagea, C., Carignan, L.-P., Gautreau, O., Pintilie, L., Singh, M. P., Ménard, D., Fournier, P., Alexe, M. & Pignolet, A. (2009). Epitaxial thin films of the multiferroic double perovskite Bi2FeCrO 6 grown on (100)-oriented SrTiO3 substrates: growth, characterization, and optimization. *Journal of Applied Physics*, 105(6), 061621.

Nechache, R., Harnagea, C., Li, S., Cardenas, L., Huang, W., Chakrabartty, J. & Rosei, F. (2015). Bandgap tuning of multiferroic oxide solar cells. *Nature Photonics*, 9(1), 61–67.

Nelson, J. A. (2003). *The physics of solar cells*. World Scientific Publishing Company.

Nieto, A., Bisht, A., Lahiri, D., Zhang, C. & Agarwal, A. (2017). Graphene reinforced metal and ceramic matrix composites: a review. *International Materials Reviews*, 62(5), 241–302.

Niu, F., Chen, D., Qin, L., Gao, T., Zhang, N., Wang, S., Chen, Z., Wang, J., Sun, X. & Huang, Y. (2015). Synthesis of Pt/BiFeO3 heterostructured photocatalysts for highly efficient visible-light

photocatalytic performances. *Solar Energy Materials and Solar Cells*, 143, 386–396.

Novoselov, K. S., Geim, A. K., Morozov, S. V., Jiang, D., Zhang, Y., Dubonos, S. V., Grigorieva, I. V. & Firsov, A. A. (2004). Electric Field Effect in Atomically Thin Carbon Films. *Science*, 306(5696), 666–669. doi: 10.1126/science.1102896.

Nozariasbmarz, A., Poudel, B., Li, W., Kang, H. B., Zhu, H. & Priya, S. (2020). Bismuth telluride thermoelectrics with 8% module efficiency for waste heat recovery application. *Iscience*, 23(7), 101340.

Numata, S., Kinjo, N. & Makino, D. (1988). Chemical structures and properties of low thermal expansion coefficient polyimides. *Polymer Engineering & Science*, 28(14), 906–911.

Ohly, C., Hoffmann-Eifert, S., Guo, X., Schubert, J. & Waser, R. (2006). Electrical conductivity of epitaxial SrTiO3 thin films as a function of oxygen partial pressure and temperature. *Journal of the American Ceramic Society*, 89(9), 2845–2852.

Ortiz-Quiñonez, J. L., Díaz, D., Zumeta-Dubé, I., Arriola-Santamaría, H., Betancourt, I., Santiago-Jacinto, P. & Nava-Etzana, N. (2013). Easy synthesis of high-purity BiFeO3 nanoparticles: new insights derived from the structural, optical, and magnetic characterization. *Inorganic chemistry*, 52(18), 10306–10317.

Osterloh, F. E. (2017). Photocatalysis versus photosynthesis: A sensitivity analysis of devices for solar energy conversion and chemical transformations. *ACS Energy Letters*, 2(2), 445–453.

Ovsyannikov, S. V., Shchennikov, V. V., Vorontsov, G. V., Manakov, A. Y., Likhacheva, A. Y. & Kulbachinskii, V. A. (2008). Giant improvement of thermoelectric power factor of Bi2Te3 under pressure. *Journal of Applied Physics*, 104(5), 053713.

Ozek, E. A., Tanyeli, S. & Yapici, M. K. (2021). Flexible graphene textile temperature sensing RFID coils based on spray printing. *IEEE Sensors Journal*, 21(23), 26382–26388.

Park, M. S., Song, J.-H., Medvedeva, J. E., Kim, M., Kim, I. G. & Freeman, A. J. (2010). Electronic structure and volume effect on thermoelectric transport in p-type Bi and Sb tellurides. *Physical Review B*, 81(15), 155211.

Passemard, S., Staedler, D., Sonego, G., Magouroux, T., Schneiter, G. S., Juillerat-Jeanneret, L., Bonacina, L. & Gerber-Lemaire, S. (2015). Functionalized bismuth ferrite harmonic nanoparticles for cancer cells labeling and imaging. *Journal of Nanoparticle Research*, 17(10), 1–13.

Patel, S., Park, H., Bonato, P., Chan, L. & Rodgers, M. (2012). A review of wearable sensors and systems with application in rehabilitation. *Journal of neuroengineering and rehabilitation*,

9(1), 1–17.

Pattnaik, S. P., Behera, A., Martha, S., Acharya, R. & Parida, K. (2018). Synthesis, photoelectrochemical properties and solar light-induced photocatalytic activity of bismuth ferrite nanoparticles. *Journal of Nanoparticle Research*, 20(1), 1–15.

Pei, Y., LaLonde, A. D., Heinz, N. A., Shi, X., Iwanaga, S., Wang, H., Chen, L. & Snyder, G. J. (2011). Stabilizing the optimal carrier concentration for high thermoelectric efficiency. *Advanced materials*, 23(47), 5674–5678.

Peres, N. & Ribeiro, R. M. (2009). Focus on graphene. *New Journal of Physics*, 11(9), 095002.

Persson, L., Carney Almroth, B. M., Collins, C. D., Cornell, S., de Wit, C. A., Diamond, M. L., Fantke, P., Hassellov, M., MacLeod, M., Ryberg, M. W. et al. (2022). Outside the Safe Operating Space of the Planetary Boundary for Novel Entities. *Environmental science & technology*, 1510-1521.

Pica, M., Calzuola, S., Donnadio, A., Gentili, P. L., Nocchetti, M. & Casciola, M. (2018). Deethylation and cleavage of rhodamine B by a zirconium phosphate/silver bromide composite photocatalyst. *Catalysts*, 9(1), 3.

Polanskỳ, R., Prosr, P. & Čermák, M. (2014). Determination of the thermal endurance of PCB FR4 epoxy laminates via thermal analyses. *Polymer degradation and stability*, 105, 107–115.

Poncharal, P., Berger, C., Yi, Y., Wang, Z. & de Heer, W. A. (2002). Room temperature ballistic conduction in carbon nanotubes. ACS Publications.

Ponraj, C., Vinitha, G. & Daniel, J. (2020). Visible light photocatalytic activity of Mn-doped BiFeO3 nanoparticles. *International Journal of Green Energy*, 17(1), 71–83.

Ponzoni, C., Rosa, R., Cannio, M., Buscaglia, V., Finocchio, E., Nanni, P. & Leonelli, C. (2013). Optimization of BFO microwave-hydrothermal synthesis: Influence of process parameters. *Journal of alloys and compounds*, 558, 150–159.

Porwal, H., Grasso, S. & Reece, M. (2013). Review of graphene–ceramic matrix composites. *Advances in Applied Ceramics*, 112(8), 443–454.

Prudenziati, M. (1994). *Thick film sensors*. Elsevier Science.

Qi, H., Wolfe, J., Fichou, D. & Chen, Z. (2016). Cu2O photocathode for low bias photoelectrochemical water splitting enabled by NiFe-layered double hydroxide co-catalyst. *Scientific reports*, 6(1), 1–8.

Qi, X., Dho, J., Blamire, M., Jia, Q., Lee, J.-S., Foltyn, S. & MacManus-Driscoll, J. L. (2004). Epitaxial growth of BiFeO3 thin films by LPE and sol–gel methods. *Journal of magnetism and magnetic materials*, 283(2-3), 415–421.

Qian, K., Sweeny, B. C., Johnston-Peck, A. C., Niu, W., Graham, J. O., DuChene, J. S., Qiu, J., Wang, Y.-C., Engelhard, M. H., Su, D. et al. (2014). Surface plasmon-driven water reduction: gold nanoparticle size matters. *Journal of the American Chemical Society*, 136(28), 9842–9845.

Qu, Y. & Duan, X. (2013). Progress, challenge and perspective of heterogeneous photocatalysts. *Chemical Society Reviews*, 42(7), 2568–2580.

Queraltó, A. & Mathur, S. (2018). Photoelectrochemical response of Fe2O3 films reinforced with BiFeO3 nanofibers. *MRS Communications*, 8(3), 1211–1215.

Radmilovic, A., Smart, T. J., Ping, Y. & Choi, K.-S. (2020). Combined experimental and Theoretical investigations of n-type BiFeO3 for use as a photoanode in a photoelectrochemical Cell. *Chemistry of Materials*, 32(7), 3262–3270.

Rajaee, A., Wang, S., Zhao, L. & Liu, Y. (2019). Gel dosimetry measurement of dose enhancement bismuth-based nanoparticles in radiation therapy. *Journal of Physics: Conference Series*, 1305(1), 012046.

Rajan, G., Morgan, J. J., Murphy, C., Torres Alonso, E., Wade, J., Ott, A. K., Russo, S., Alves, H., Craciun, M. F. & Neves, A. I. (2020). Low operating voltage carbon-graphene hybrid E-textile for temperature sensing. *ACS Applied Materials & Interfaces*, 12(26), 29861–29867.

Ramaraj, S., Mani, S., Chen, S.-M., Kokulnathan, T., Lou, B.-S., Ali, M. A., Hatamleh, A. & Al-Hemaid, F. M. (2018). Synthesis and application of bismuth ferrite nanosheets supported functionalized carbon nanofiber for enhanced electrochemical detection of toxic organic compound in water samples. *Journal of colloid and interface science*, 514, 59–69.

Reimann, T., Töpfer, J., Barth, S., Bartsch, H. & Müller, J. (2013). Low-Temperature Sintered NTC Thermistor Ceramics for Thick-Film Temperature Sensors. *International Journal of Applied Ceramic Technology*, 10(3), 428–434.

Rioult, M., Datta, S., Stanescu, D., Stanescu, S., Belkhou, R., Maccherozzi, F., Magnan, H. & Barbier, A. (2015). Tailoring the photocurrent in BaTiO3/Nb: SrTiO3 photoanodes by controlled ferroelectric polarization. *Applied Physics Letters*, 107(10), 103901.

Rockström, J., Steffen, W., Noone, K., Persson, A., Chapin, F. S., Lambin, E. F., Lenton, T. M., Scheffer, M., Folke, C., Schellnhuber, H. J., Nykvist, B., de Wit, C. A., Hughes, T., van der Leeuw, S., Rodhe, H., Sörlin, S., Snyder, P. K., Costanza, R., Svedin, U., Falkenmark, M.,

Karlberg, L., Corell, R. W., Fabry, V. J., Hansen, J., Walker, B., Liverman, D., Richardson, K., Crutzen, P. & Foley, J. A. (2009). A safe operating space for humanity. *Nature*, 461(7263), 472-475. doi: 10.1038/461472a.

Rojac, T., Bencan, A., Malic, B., Tutuncu, G., Jones, J. L., Daniels, J. E. & Damjanovic, D. (2014a). BiFeO3 ceramics: processing, electrical, and electromechanical properties. *Journal of the American Ceramic Society*, 97(7), 1993–2011.

Rojac, T., Bencan, A., Malic, B., Tutuncu, G., Jones, J. L., Daniels, J. E. & Damjanovic, D. (2014b). BiFeO3 ceramics: processing, electrical, and electromechanical properties. *Journal of the American Ceramic Society*, 97(7), 1993–2011.

Rosales, B. A. (2019). *Synthesis and advanced spectroscopy of new and emerging energy materials*. (Ph.D. thesis, Iowa State University).

Ruby, S., Rosaline, D. R., Inbanathan, S., Anand, K., Kavitha, G., Srinivasan, R., Umar, A., Hegazy, H. & Algarni, H. (2020). Sunlight-driven photocatalytic degradation of methyl orange based on bismuth ferrite (BiFeO3) heterostructures composed of interconnected nanosheets. *Journal of Nanoscience and Nanotechnology*, 20(3), 1851–1858.

Rueda-Marquez, J. J., Levchuk, I., Ibanez, P. F. & Sillanpää, M. (2020). A critical review on application of photocatalysis for toxicity reduction of real wastewaters. *Journal of Cleaner Production*, 258, 120694.

Saeidi-Javash, M., Du, Y., Zeng, M., Wyatt, B. C., Zhang, B., Kempf, N., Anasori, B. & Zhang, Y. (2021). All-printed MXene–graphene nanosheet-based bimodal sensors for simultaneous strain and temperature sensing. *ACS Applied Electronic Materials*, 3(5), 2341–2348.

Safi, R. & Shokrollahi, H. (2012). Physics, chemistry and synthesis methods of nanostructured bismuth ferrite (BiFeO3) as a ferroelectro-magnetic material. *Progress in Solid State Chemistry*, 40(1-2), 6–15.

Saha-Dasgupta, T. (2020). Double perovskites with 3d and 4d/5d transition metals: compounds with promises. *Materials Research Express*, 7(1), 014003.

Sahraoui, A. H., Longuemart, S., Dadarlat, D., Delenclos, S., Kolinsky, C. & Buisine, J. (2002). The application of the photopyroelectric method for measuring the thermal parameters of pyroelectric materials. *Review of scientific instruments*, 73(7), 2766–2772.

Samran, B., Tonnonchiang, S., Chaiwichian, S. et al. (2019). BiFeO3/BiVO4 nanocomposite photocatalysts with highly enhanced photocatalytic activity for rhodamine B degradation under visible light irradiation. *Physica B: Condensed Matter*, 561, 23–28.

Sando, D., Yang, Y., Bousquet, E., Carrétéro, C., Garcia, V., Fusil, S., Dolfi, D., Barthélémy, A., Ghosez, P., Bellaiche, L. et al. (2016). Large elasto-optic effect and reversible electrochromism in multiferroic BiFeO3. *Nature communications*, 7(1), 1–7.

Saravana Kumar, K., Aswini, P. & Venkateswaran, C. (2014). Effect of Tb–Mn substitution on the magnetic and electrical properties of BiFeO3 ceramics. *Journal of Magnetism and Magnetic Materials*, 364.

Sarrión, M. L. M. & Morales, M. (1995). Preparation and characterization of NTC thermistors: nickel manganites doped with lithium. *Journal of the American Ceramic Society*, 78(4), 915–921.

Sassi, S., Candolfi, C., Vaney, J.-B., Ohorodniichuk, V., Masschelein, P., Dauscher, A. & Lenoir, B. (2014). Assessment of the thermoelectric performance of polycrystalline p-type SnSe. *Applied Physics Letters*, 104(21), 212105.

Sathre, R., Greenblatt, J. B., Walczak, K., Sharp, I. D., Stevens, J. C., Ager, J. W. & Houle, F. A. (2016). Opportunities to improve the net energy performance of photoelectrochemical water-splitting technology. *Energy & Environmental Science*, 9(3), 803–819.

Sato, T., Takagi, S., Deledda, S., Hauback, B. C. & Orimo, S.-i. (2016). Extending the applicability of the Goldschmidt tolerance factor to arbitrary ionic compounds. *Scientific reports*, 6(1), 1–10.

Satterthwaite, C. & Ure Jr, R. (1957). Electrical and thermal properties of Bi2Te3. *Physical review*, 108(5), 1164.

Schubert, M., Münch, C., Schuurman, S., Poulain, V., Kita, J. & Moos, R. (2018). Characterization of nickel manganite NTC thermistor films prepared by aerosol deposition at room temperature. *Journal of the European Ceramic Society*, 38(2), 613–619.

Sebastian, M. T. (2010). *Dielectric materials for wireless communication*. Elsevier.

Sehrawat, P., Islam, S. & Mishra, P. (2018). Reduced graphene oxide based temperature sensor: Extraordinary performance governed by lattice dynamics assisted carrier transport. *Sensors and Actuators B: Chemical*, 258, 424–435.

Selbach, S. M., Tybell, T., Einarsrud, M.-A. & Grande, T. (2008). The ferroic phase transitions of BiFeO3. *Advanced materials*, 20(19), 3692–3696.

Seliem, M. K., Komarneni, S. & Khadra, M. R. A. (2016). Phosphate removal from solution by composite of MCM-41 silica with rice husk: kinetic and equilibrium studies. *Microporous and Mesoporous Materials*, 224, 51–57.

Shahid, M. Z., Mehmood, R., Athar, M., Hussain, J., Wei, Y. & Khaliq, A. (2020). BiOCl nanoplates doped with Fe3+ ions for the visible-light degradation of aqueous pollutants. *ACS Applied Nano Materials*, 4(1), 746–758.

Shahil, K., Hossain, M., Teweldebrhan, D. & Balandin, A. (2010). Crystal symmetry breaking in few-quintuple Bi2Te3 films: Applications in nanometrology of topological insulators. *Applied physics letters*, 96(15), 153103.

Shang, J., Chen, H., Chen, T., Wang, X., Feng, G., Zhu, M., Yang, Y. & Jia, X. (2019). Photocatalytic degradation of rhodamine B and phenol over BiFeO3/BiOCl nanocomposite. *Applied Physics A*, 125(2), 1–7.

Shen, Z., Li, F., Lu, J., Wang, Z., Li, R., Zhang, X., Zhang, C., Wang, Y., Wang, Y., Lv, Z. et al. (2021). Enhanced N2 photofixation activity of flower-like BiOCl by in situ Fe (III) doped as an activation center. *Journal of Colloid and Interface Science*, 584, 174–181.

Shi, L., Benetti, D., Li, F., Wei, Q. & Rosei, F. (2020). Phase-junction design of MOF-derived TiO2 photoanodes sensitized with quantum dots for efficient hydrogen generation. *Applied Catalysis B: Environmental*, 263, 118317.

Silva, J., Reyes, A., Esparza, H., Camacho, H. & Fuentes, L. (2011). BiFeO3: a review on synthesis, doping and crystal structure. *Integrated Ferroelectrics*, 126(1), 47–59.

Singerling, S. A. & Callaghan, R. M. (2018). volume III, Area Reports–International–Europe and Central Eurasia. *US Geological Survey*.

Singh, S. & Khare, N. (2017). Electrically tuned photoelectrochemical properties of ferroelectric nanostructure NaNbO3 films. *Applied Physics Letters*, 110(15), 152902.

Skákalová, V., Kaiser, A. B., Yoo, J. S., Obergfell, D. & Roth, S. (2009). Correlation between resistance fluctuations and temperature dependence of conductivity in graphene. *Physical Review B*, 80(15), 153404.

Skubi, K. L. & Yoon, T. P. (2014). Shape control in reactions with light. *Nature*, 515(7525), 45–46.

Smalley, R. E. (2005). Future global energy prosperity: the terawatt challenge. *Mrs Bulletin*, 30(6), 412–417.

Snyder, G. J. & Toberer, E. S. (2011). Complex thermoelectric materials. In *Materials for sustainable energy: a collection of peer-reviewed research and review articles from Nature Publishing Group* (pp. 101–110). World Scientific.

Song, J., Kim, T. L., Lee, J., Cho, S. Y., Cha, J., Jeong, S. Y., An, H., Kim, W. S., Jung, Y.-S., Park, J. et al. (2018). Domain-engineered BiFeO3 thin-film photoanodes for highly enhanced ferroelectric solar water splitting. *Nano Research*, 11(2), 642–655.

Sosso, G., Caravati, S. & Bernasconi, M. (2009). Vibrational properties of crystalline Sb2Te3 from first principles. *Journal of Physics: Condensed Matter*, 21(9), 095410.

Souza, S., Trichês, D., De Lima, J., Grandi, T. & De Biasi, R. (2010). Structural, optical and photoacoustic study of Sb2Te3 prepared by mechanical alloying. *Physica B: Condensed Matter*, 405(13), 2807–2814.

Spaldin, N. A. (2010). *Magnetic materials: fundamentals and applications*. Cambridge university press.

Spaldin, N. A., Cheong, S.-W. & Ramesh, R. (2010). Multiferroics: Past, present, and future. *Phys. Today*, 63(10), 38–43.

Stankovich, S., Dikin, D. A., Dommett, G. H., Kohlhaas, K. M., Zimney, E. J., Stach, E. A., Piner, R. D., Nguyen, S. T. & Ruoff, R. S. (2006). Graphene-based composite materials. *nature*, 442(7100), 282–286.

Sun, J., Cai, Y., Xu, H., Zou, Z., Hu, M., Jin, X., Sun, L., Li, D. & Xia, D. (2018). Synthesis of porous BiOCl nanocubes with enhanced visible light photocatalytic performance. *Chemical Physics Letters*, 711, 207–212.

Sun, Y. & Rogers, J. A. (2007). Inorganic semiconductors for flexible electronics. *Advanced materials*, 19(15), 1897–1916.

Sze, S. M., Li, Y. & Ng, K. K. (2006). *Physics of semiconductor devices*. John wiley & sons.

Szuromi, P. & Grocholski, B. (2017). Natural and engineered perovskites. American Association for the Advancement of Science.

Takahashi, K., Kida, N. & Tonouchi, M. (2006). Terahertz radiation by an ultrafast spontaneous polarization modulation of multiferroic BiFeO3 thin films. *Physical review letters*, 96(11), 117402.

Talbayev, D., Lee, S., Cheong, S.-W. & Taylor, A. (2008). Terahertz wave generation via optical rectification from multiferroic BiFeO3. *Applied Physics Letters*, 93(21), 212906.

Tan, D. K., Nokhodchi, A. & Münzenrieder, N. (2021). Fabrication of Flexible and Transferable RTDs via Fused Deposition Modelling 3D Printing. *2021 IEEE International Conference on Flexible and Printable Sensors and Systems (FLEPS)*, pp. 1–4.

Tian, F., Li, G., Zhao, H., Chen, F., Li, M., Liu, Y. & Chen, R. (2019). Residual Fe enhances the activity of BiOCl hierarchical nanostructure for hydrogen peroxide activation. *Journal of Catalysis*, 370, 265–273.

Tiwari, D., Fermin, D. J., Chaudhuri, T. & Ray, A. (2015). Solution processed bismuth ferrite thin films for all-oxide solar photovoltaics. *The Journal of Physical Chemistry C*, 119(11), 5872–5877.

Toberer, E. S., Baranowski, L. L. & Dames, C. (2012). Advances in thermal conductivity. *Annual Review of Materials Research*, 42, 179–209.

Tompkins, H. G., Tasic, S., Baker, J. & Convey, D. (2000). Spectroscopic ellipsometry measurements of thin metal films. *Surface and Interface Analysis: An International Journal devoted to the development and application of techniques for the analysis of surfaces, interfaces and thin films*, 29(3), 179–187.

Torok, J. J. (1955). Thermistor. Google Patents. US Patent 2,700,720.

Tremel, K. & Ludwigs, S. (2014). Morphology of P3HT in thin films in relation to optical and electrical properties. *P3HT revisited–from molecular scale to solar cell devices*, 39–82.

Trung, T. Q. & Lee, N.-E. (2016). Flexible and stretchable physical sensor integrated platforms for wearable human-activity monitoringand personal healthcare. *Advanced materials*, 28(22), 4338–4372.

Turkani, V. S., Maddipatla, D., Narakathu, B. B., Bazuin, B. J. & Atashbar, M. Z. (2018). A carbon nanotube based NTC thermistor using additive print manufacturing processes. *Sensors and Actuators A: Physical*, 279, 1–9.

Turkani, V. S., Maddipatla, D., Narakathu, B. B., Altay, B. N., Fleming, D., Bazuin, B. J. & Atashbar, M. Z. (2020). A screen-printed nickel based resistance temperature detector (RTD) on thin ceramic substrate. *2020 IEEE International Conference on Electro Information Technology (EIT)*, pp. 577–580.

Uchino, K. (2018). *Ferroelectric devices*. CRC press.

Verraes, C., Van Boxstael, S., Van Meervenne, E., Van Coillie, E., Butaye, P., Catry, B., De Schaetzen, M.-A., Van Huffel, X., Imberechts, H., Dierick, K. et al. (2013). Antimicrobial resistance in the food chain: a review. *International journal of environmental research and public health*, 10(7), 2643–2669.

Vesborg, P. C. (2017). Photocatalysis: HI-time for perovskites. *Nature Energy*, 2(1), 1–2.

Vesborg, P. C. & Jaramillo, T. F. (2012). Addressing the terawatt challenge: scalability in the supply of chemical elements for renewable energy. *Rsc Advances*, 2(21), 7933–7947.

Viezbicke, B. D., Patel, S., Davis, B. E. & Birnie III, D. P. (2015). Evaluation of the Tauc method for optical absorption edge determination: ZnO thin films as a model system. *physica status solidi (b)*, 252(8), 1700–1710.

Vilarinho, P. M., Rosenwaks, Y. & Kingon, A. (2006). *Scanning Probe Microscopy: Characterization, Nanofabrication and Device Application of Functional Materials: Proceedings of the NATO Advanced Study Institute on Scanning Probe Microscopy: Characterization, Nanofabrication and Device Application of Functional Materials, Algarve, Portugal, 1-13 October 2002*. Springer Science & Business Media.

Vilarinho, P. (2005). Functional materials: properties, processing and applications. In *Scanning Probe Microscopy: Characterization, Nanofabrication and Device Application of Functional Materials* (pp. 3–33). Springer.

Völklein, F., Baier, V., Dillner, U. & Kessler, E. (1990). Transport properties of flash-evaporated (Bi1- xSbx)2Te3 films I: Optimization of film properties. *Thin solid films*, 187(2), 253–262.

Vollset, S. E., Goren, E., Yuan, C.-W., Cao, J., Smith, A. E., Hsiao, T., Bisignano, C., Azhar, G. S., Castro, E., Chalek, J. et al. (2020). Fertility, mortality, migration, and population scenarios for 195 countries and territories from 2017 to 2100: a forecasting analysis for the Global Burden of Disease Study. *The Lancet*, 396(10258), 1285–1306.

Vonrüti, N. & Aschauer, U. (2020). Catalysis on oxidized ferroelectric surfaces—Epitaxially strained LaTiO2N and BaTiO3 for photocatalytic water splitting. *The Journal of Chemical Physics*, 152(2), 024701.

Wang, G., Ouyang, M., Huang, Y., Huang, Y., Yang, Z., Guo, B., Wu, J., Zhang, M. & Wen, W. (2021a). Synergistic Superiority of a Silver-Carbon Black-Filled Conductive Polymer Composite for Temperature–Pressure Sensing. *Advanced Engineering Materials*, 23(4), 2001392.

Wang, G., Lu, Z., Li, Y., Li, L., Ji, H., Feteira, A., Zhou, D., Wang, D., Zhang, S. & Reaney, I. M. (2021b). Electroceramics for high-energy density capacitors: current status and future perspectives. *Chemical Reviews*, 121(10), 6124–6172.

Wang, G., Cheng, D., He, T., Hu, Y., Deng, Q., Mao, Y. & Wang, S. (2019a). Enhanced visible-light responsive photocatalytic activity of Bi25FeO40/Bi2Fe4O9 composites and mechanism investigation. *Journal of Materials Science: Materials in Electronics*, 30(11), 10923–10933.

Wang, H., Liu, W., He, X., Zhang, P., Zhang, X. & Xie, Y. (2020a). An excitonic perspective on low-dimensional semiconductors for photocatalysis. *Journal of the American Chemical Society*, 142(33), 14007–14022.

Wang, J., Neaton, J., Zheng, H., Nagarajan, V., Ogale, S., Liu, B., Viehland, D., Vaithyanathan, V., Schlom, D., Waghmare, U. et al. (2003). Epitaxial BiFeO3 multiferroic thin film heterostructures. *Science*, 299(5613), 1719–1722.

Wang, J., Luo, L., Han, C., Yun, R., Tang, X., Zhu, Y., Nie, Z., Zhao, W. & Feng, Z. (2019b). The Microstructure, electric, optical and photovoltaic properties of BiFeO3 thin films prepared by low temperature sol–gel method. *Materials*, 12(9), 1444.

Wang, N., Luo, X., Han, L., Zhang, Z., Zhang, R., Olin, H. & Yang, Y. (2020b). Structure, performance, and application of BiFeO3 nanomaterials. *Nano-Micro Letters*, 12(1), 1–23.

Wang, R., Shi, M., Xu, F., Qiu, Y., Zhang, P., Shen, K., Zhao, Q., Yu, J. & Zhang, Y. (2020c). Graphdiyne-modified TiO2 nanofibers with osteoinductive and enhanced photocatalytic antibacterial activities to prevent implant infection. *Nature communications*, 11(1), 1–12.

Wang, S., Chen, D., Niu, F., Zhang, N., Qin, L. & Huang, Y. (2016a). Hydrogenation-induced surface oxygen vacancies in BiFeO3 nanoparticles for enhanced visible light photocatalytic performance. *Journal of Alloys and Compounds*, 688, 399–406.

Wang, S., Chen, D., Niu, F., Zhang, N., Qin, L. & Huang, Y. (2016b). Pd cocatalyst on Sm-doped BiFeO3 nanoparticles: synergetic effect of a Pd cocatalyst and samarium doping on photocatalysis. *RSC advances*, 6(41), 34574–34587.

Wang, T., Bai, Y., Si, W., Mao, W., Gao, Y. & Liu, S. (2021c). Heterogeneous photo-Fenton system of novel ternary Bi2WO6/BiFeO3/g-C3N4 heterojunctions for highly efficient degrading persistent organic pollutants in wastewater. *Journal of Photochemistry and Photobiology A: Chemistry*, 404, 112856.

Wang, W., Li, N., Chi, Y., Li, Y., Yan, W., Li, X. & Shao, C. (2013). Electrospinning of magnetical bismuth ferrite nanofibers with photocatalytic activity. *Ceramics International*, 39(4), 3511–3518.

Wang, Y., Zhang, C., Li, J., Ding, G. & Duan, L. (2017). Fabrication and characterization of ITO thin film resistance temperature detector. *Vacuum*, 140, 121–125.

Wang, Z., Gao, W., Zhang, Q., Zheng, K., Xu, J., Xu, W., Shang, E., Jiang, J., Zhang, J. & Liu, Y. (2018). 3D-printed graphene/polydimethylsiloxane composites for stretchable and strain-insensitive temperature sensors. *ACS Applied Materials & Interfaces*, 11(1), 1344–1352.

Wang, Z., Cao, D., Wen, L., Xu, R., Obergfell, M., Mi, Y., Zhan, Z., Nasori, N., Demsar, J. & Lei, Y. (2016c). Manipulation of charge transfer and transport in plasmonic-ferroelectric hybrids for photoelectrochemical applications. *Nature communications*, 7(1), 1–8.

Wang, Z., Chen, A., Winslow, R., Madan, D., Juang, R., Nill, M., Evans, J. & Wright, P. (2012). Integration of dispenser-printed ultra-low-voltage thermoelectric and energy storage devices. *Journal of Micromechanics and Microengineering*, 22(9), 094001.

Wang-Erlandsson, L., Tobian, A., van der Ent, R. J., Fetzer, I., te Wierik, S., Porkka, M., Staal, A., Jaramillo, F., Dahlmann, H., Singh, C. et al. (2022). A planetary boundary for green water. *Nature Reviews Earth & Environment*, 1–13.

Watanabe, T., Takizawa, T. & Honda, K. (1977). Photocatalysis through excitation of adsorbates. 1. Highly efficient N-deethylation of rhodamine B adsorbed to cadmium sulfide. *The Journal of Physical Chemistry*, 81(19), 1845–1851.

Way, A., Luke, J., Evans, A. D., Li, Z., Kim, J.-S., Durrant, J. R., Hin Lee, H. K. & Tsoi, W. C. (2019). Fluorine doped tin oxide as an alternative of indium tin oxide for bottom electrode of semi-transparent organic photovoltaic devices. *AIP Advances*, 9(8), 085220.

Wei, J., Yang, L., Ma, Z., Song, P., Zhang, M., Ma, J., Yang, F. & Wang, X. (2020). Review of current high-ZT thermoelectric materials. *Journal of Materials Science*, 55(27), 12642–12704.

Wei, X., Akbar, M. U., Raza, A. & Li, G. (2021). A review on bismuth oxyhalide based materials for photocatalysis. *Nanoscale Advances*, 3(12), 3353–3372.

Weidong, H., Wei, Q., Xiaohong, W., Xianbo, D., Long, C. & Zhaohua, J. (2007). The photocatalytic properties of bismuth oxide films prepared through the sol–gel method. *Thin Solid Films*, 515(13), 5362–5365.

Wheeler, G. P. & Choi, K.-S. (2018). Investigation of p-type Ca2Fe2O5 as a Photocathode for Use in a Water Splitting Photoelectrochemical Cell. *ACS Applied Energy Materials*, 1(9), 4917–4923.

Wilson, D., Stenzenberger, H. D. & Hergenrother, P. M. (1990). *Polyimides*. Springer.

Wong, K. V. & Hernandez, A. (2012). A review of additive manufacturing. *International scholarly research notices*, 2012.

Woo, T.-G., Park, I.-S., Jung, K.-H., Jeon, W.-Y. & Seol, K.-W. (2011). Effect of N2 plasma treatment on the adhesion of Cu/Ni thin film to polyimide. *Metals and Materials International*, 17(5), 789–795.

Wu, H., Zhou, J., Liang, L., Li, L. & Zhu, X. (2014). Fabrication, characterization, properties, and applications of low-dimensional BiFeO3 nanostructures. *Journal of Nanomaterials*, 2014.

Wu, J., Wang, J., Xiao, D. & Zhu, J. (2011). Migration kinetics of oxygen vacancies in Mn-modified BiFeO3 thin films. *ACS Applied Materials & Interfaces*, 3(7), 2504–2511.

Wu, T., Liu, G., Zhao, J., Hidaka, H. & Serpone, N. (1998). Photoassisted degradation of dye pollutants. V. Self-photosensitized oxidative transformation of rhodamine B under visible light irradiation in aqueous TiO2 dispersions. *The Journal of Physical Chemistry B*, 102(30), 5845–5851.

Wu, X., Li, H., Wang, X., Jiang, L., Xi, J., Du, G. & Ji, Z. (2019). Ferroelectric enhanced photoelectrochemical water splitting in BiFeO3/TiO2 composite photoanode. *Journal of Alloys and Compounds*, 783, 643–651.

Wu, Y., Yuan, B., Li, M., Zhang, W.-H., Liu, Y. & Li, C. (2015). Well-defined BiOCl colloidal ultrathin nanosheets: synthesis, characterization, and application in photocatalytic aerobic oxidation of secondary amines. *Chemical science*, 6(3), 1873–1878.

Xia, J., Xu, L., Zhang, J., Yin, S., Li, H., Xu, H. & Di, J. (2013). Improved visible light photocatalytic properties of Fe/BiOCl microspheres synthesized via self-doped reactable ionic liquids. *CrystEngComm*, 15(46), 10132–10141.

Xian, T., Yang, H., Dai, J., Wei, Z., Ma, J. & Feng, W. (2011). Photocatalytic properties of BiFeO3 nanoparticles with different sizes. *Materials Letters*, 65(11), 1573–1575.

Xie, Z.-H., Zhou, H.-Y., He, C.-S., Pan, Z.-C., Yao, G. & Lai, B. (2021). Synthesis, application and catalytic performance of layered double hydroxide based catalysts in advanced oxidation processes for wastewater decontamination: A review. *Chemical Engineering Journal*, 414, 128713.

Xing, J., Guo, E.-J., Dong, J., Hao, H., Zheng, Z. & Zhao, C. (2015). High-sensitive switchable photodetector based on BiFeO3 film with in-plane polarization. *Applied Physics Letters*, 106(3), 033504.

Xiong, J., Cheng, G., Li, G., Qin, F. & Chen, R. (2011). Well-crystallized square-like 2D BiOCl nanoplates: mannitol-assisted hydrothermal synthesis and improved visible-light-driven photocatalytic performance. *RSC advances*, 1(8), 1542–1553.

Xu, Y., Xu, S., Wang, S., Zhang, Y. & Li, G. (2014). Citric acid modulated electrochemical synthesis and photocatalytic behavior of BiOCl nanoplates with exposed {001} facets. *Dalton transactions*, 43(2), 479–485.

Xue, J., Wu, T., Dai, Y. & Xia, Y. (2019). Electrospinning and electrospun nanofibers: Methods, materials, and applications. *Chemical reviews*, 119(8), 5298–5415.

Yadav, B., Srivastava, R., Singh, S., Kumar, A. & Yadav, A. (2012). Temperature sensors based on semiconducting oxides: an overview. *arXiv e-prints*.

Yakout, S. M. (2021). Spintronics and Innovative Memory Devices: a Review on Advances in Magnetoelectric BiFeO3. *Journal of Superconductivity and Novel Magnetism*, 34(2), 317–338.

Yan, C., Wang, J. & Lee, P. S. (2015). Stretchable graphene thermistor with tunable thermal index. *ACS nano*, 9(2), 2130–2137.

Yan, Y., Yang, H., Yi, Z. & Xian, T. (2019). NaBH4-reduction induced evolution of Bi nanoparticles from BiOCl nanoplates and construction of promising Bi@ BiOCl hybrid photocatalysts. *Catalysts*, 9(10), 795.

Yang, C., Song, G. & Lim, W. (2020a). A review of the toxicity in fish exposed to antibiotics. *Comparative Biochemistry and Physiology Part C: Toxicology & Pharmacology*, 237, 108840.

Yang, F., Chu, X., Sun, J., Zhang, Y., Li, Z., Liu, H., Bai, L., Qu, Y. & Jing, L. (2020b). Efficient singlet oxygen generation by excitonic energy transfer on ultrathin g-C3N4 for selective photocatalytic oxidation of methyl-phenyl-sulfide with O2. *Chinese Chemical Letters*, 31(10), 2784–2788.

Yang, H. (2021). A short review on heterojunction photocatalysts: Carrier transfer behavior and photocatalytic mechanisms. *Materials Research Bulletin*, 142, 111406.

Yang, J.-C., He, Q., Yu, P. & Chu, Y.-H. (2015). BiFeO3 thin films: a playground for exploring electric-field control of multifunctionalities. *Annual Review of Materials Research*, 45, 249–275.

Yang, X., Zhou, Z., Nan, T., Gao, Y., Yang, G., Liu, M. & Sun, N. (2016). Recent advances in multiferroic oxide heterostructures and devices. *Journal of Materials Chemistry C*, 4(2), 234–243.

Yang, X., Sun, S., Cui, J., Yang, M., Luo, Y. & Liang, S. (2021). Synthesis, functional modifications, and diversified applications of hybrid BiOCl-based heterogeneous photocatalysts: a review. *Crystal Growth & Design*, 21(11), 6576–6618.

Yang, Y., Sun, J., Zhu, K., Liu, Y. & Wan, L. (2008). Structure properties of BiFeO3 films studied by micro-Raman scattering. *Journal of Applied Physics*, 103(9), 093532.

Yang, Y., Liu, Y., Wei, J., Pan, C., Xiong, R. & Shi, J. (2014). Electrospun nanofibers of p-type BiFeO3/n-type TiO2 hetero-junctions with enhanced visible-light photocatalytic activity. *RSC Advances*, 4(60), 31941–31947.

Yao, W. F., Xu, X. H., Wang, H., Zhou, J. T., Yang, X. N., Zhang, Y., Shang, S. X. & Huang, B. B. (2004). Photocatalytic property of perovskite bismuth titanate. *Applied Catalysis B: Environmental*, 52(2), 109–116.

Yi, H., Choi, T., Choi, S., Oh, Y. S. & Cheong, S.-W. (2011). Mechanism of the switchable photovoltaic effect in ferroelectric BiFeO3. *Advanced Materials*, 23(30), 3403–3407.

Yin, L. & Mi, W. (2020). Progress in BiFeO3-based heterostructures: materials, properties and applications. *Nanoscale*, 12(2), 477–523.

Yin, W.-J., Weng, B., Ge, J., Sun, Q., Li, Z. & Yan, Y. (2019). Oxide perovskites, double perovskites and derivatives for electrocatalysis, photocatalysis, and photovoltaics. *Energy & Environmental Science*, 12(2), 442–462.

You, L., Zheng, F., Fang, L., Zhou, Y., Tan, L. Z., Zhang, Z., Ma, G., Schmidt, D., Rusydi, A., Wang, L. et al. (2018). Enhancing ferroelectric photovoltaic effect by polar order engineering. *Science advances*, 4(7), eaat3438.

Young, R. J., Kinloch, I. A., Gong, L. & Novoselov, K. S. (2012). The mechanics of graphene nanocomposites: a review. *Composites Science and Technology*, 72(12), 1459–1476.

Yu, C., Zhou, W., Jimmy, C. Y., Liu, H. & Wei, L. (2014). Design and fabrication of heterojunction photocatalysts for energy conversion and pollutant degradation. *Chinese Journal of Catalysis*, 35(10), 1609–1618.

Yu, D., Liu, Z., Zhang, J., Li, S., Zhao, Z., Zhu, L., Liu, W., Lin, Y., Liu, H. & Zhang, Z. (2019). Enhanced catalytic performance by multi-field coupling in KNbO3 nanostructures: Piezo-photocatalytic and ferro-photoelectrochemical effects. *Nano Energy*, 58, 695–705.

Yu, X.-L., Wang, Y., Hu, Y.-M., Cao, C.-B. & Chan, H. L.-W. (2009). Gas-Sensing Properties of Perovskite BiFeO3 Nanoparticles. *Journal of the American ceramic society*, 92(12), 3105–3107.

Yu, Y. & Wang, X. (2018). Piezotronics in Photo-Electrochemistry. *Advanced Materials*, 30(43), 1800154.

Yu, Y., Huang, Q., Rhodes, S., Fang, J. & An, L. (2017). Si CNO–GO composites with the negative temperature coefficient of resistance for high-temperature sensor applications. *Journal of the American Ceramic Society*, 100(2), 592–601.

Zaki, N., Gu, G., Tsvelik, A., Wu, C. & Johnson, P. D. (2021). Time-reversal symmetry breaking in the Fe-chalcogenide superconductors. *Proceedings of the National Academy of Sciences*, 118(3).

Zeches, R., Rossell, M., Zhang, J., Hatt, A., He, Q., Yang, C.-H., Kumar, A., Wang, C., Melville, A., Adamo, C. et al. (2009). A strain-driven morphotropic phase boundary in BiFeO3. *science*, 326(5955), 977–980.

Zeng, Y., Lu, G., Wang, H., Du, J., Ying, Z. & Liu, C. (2014). Positive temperature coefficient thermistors based on carbon nanotube/polymer composites. *Scientific reports*, 4(1), 1–7.

Zeng, Z., Yang, P. & Hu, Z. (2013). Temperature and size effects on electrical properties and thermoelectric power of Bismuth Telluride thin films deposited by co-sputtering. *Applied Surface Science*, 268, 472–476.

Zevalkink, A., Smiadak, D. M., Blackburn, J. L., Ferguson, A. J., Chabinyc, M. L., Delaire, O., Wang, J., Kovnir, K., Martin, J., Schelhas, L. T. et al. (2018). A practical field guide to thermoelectrics: Fundamentals, synthesis, and characterization. *Applied Physics Reviews*, 5(2), 021303.

Zhang, B., Zhao, Q., Chang, A., Ye, H., Chen, S. & Wu, Y. (2014). New negative temperature coefficient thermistor ceramics in Mn-doped CaCu3-xMnxTi4O12 (0<x<1) system. *Ceramics International*, 40(7), 11221–11227.

Zhang, C., Li, Y., Chu, M., Rong, N., Xiao, P. & Zhang, Y. (2016a). Hydrogen-treated BiFeO3 nanoparticles with enhanced photoelectrochemical performance. *RSC advances*, 6(29), 24760–24767.

Zhang, D., Wu, H., Bowen, C. R. & Yang, Y. (2021). Recent advances in pyroelectric materials and applications. *Small*, 17(51), 2103960.

Zhang, H., Liu, G., Shi, L. & Ye, J. (2018). Single-atom catalysts: emerging multifunctional materials in heterogeneous catalysis. *Advanced Energy Materials*, 8(1), 1701343.

Zhang, J., Huang, Y., Jin, L., Rosei, F., Vetrone, F. & Claverie, J. P. (2017a). Efficient upconverting multiferroic core@ shell photocatalysts: visible-to-near-infrared photon harvesting. *ACS Applied Materials & Interfaces*, 9(9), 8142–8150.

Zhang, N., Chen, D., Niu, F., Wang, S., Qin, L. & Huang, Y. (2016b). Enhanced visible light photocatalytic activity of Gd-doped BiFeO3 nanoparticles and mechanism insight. *Scientific reports*, 6(1), 1–11.

Zhang, Q., Sando, D. & Nagarajan, V. (2016c). Chemical route derived bismuth ferrite thin films and nanomaterials. *Journal of Materials Chemistry C*, 4(19), 4092–4124.

Zhang, Q., Gong, W., Wang, J., Ning, X., Wang, Z., Zhao, X., Ren, W. & Zhang, Z. (2011). Size-dependent magnetic, photoabsorbing, and photocatalytic properties of single-crystalline Bi2Fe4O9 semiconductor nanocrystals. *The Journal of Physical Chemistry C*, 115(51), 25241–25246.

Zhang, T., Shen, Y., Qiu, Y., Liu, Y., Xiong, R., Shi, J. & Wei, J. (2017b). Facial synthesis and photoreaction mechanism of BiFeO3/Bi2Fe4O9 heterojunction nanofibers. *ACS Sustainable Chemistry & Engineering*, 5(6), 4630–4636.

Zhang, X., Wang, B., Wang, X., Xiao, X., Dai, Z., Wu, W., Zheng, J., Ren, F. & Jiang, C. (2015a). Preparation of M@BiFeO3 nanocomposites (M= Ag, Au) bowl arrays with enhanced visible light photocatalytic activity. *Journal of the American Ceramic Society*, 98(7), 2255–2263.

Zhang, Y., Cai, Z. & Ma, X. (2015b). Photocatalysis enhancement of Au/BFO nanoparticles using plasmon resonance of Au NPs. *Physica B: Condensed Matter*, 479, 101–106.

Zhang, Y., Xu, X., Xing, Y., Wang, H., Fu, H., Lin, X. & Wang, J. (2015c). Growth and electronic transport property of layered BiOCl microplates. *Advanced Materials Interfaces*, 2(12), 1500194.

Zhao, L.-D., Lo, S.-H., Zhang, Y., Sun, H., Tan, G., Uher, C., Wolverton, C., Dravid, V. P. & Kanatzidis, M. G. (2014). Ultralow thermal conductivity and high thermoelectric figure of merit in SnSe crystals. *Nature*, 508(7496), 373–377.

Zhao, Y., Hughes, R. W., Su, Z., Zhou, W. & Gregory, D. H. (2011). One-Step Synthesis of Bismuth Telluride Nanosheets of a Few Quintuple Layers in Thickness. *Angewandte Chemie International Edition*, 50(44), 10397–10401.

Zheng, X., Liu, C., Yan, Y. & Wang, Q. (2014). A review of thermoelectrics research-Recent developments and potentials for sustainable and renewable energy applications. *Renewable and Sustainable Energy Reviews*, 32, 486–503.

Zhou, L., Xu, Y.-F., Chen, B.-X., Kuang, D.-B. & Su, C.-Y. (2018a). Synthesis and photocatalytic application of stable lead-free Cs2AgBiBr6 perovskite nanocrystals. *Small*, 14(11), 1703762.

Zhou, W., Umezawa, N., Ma, R., Sakai, N., Ebina, Y., Sano, K., Liu, M., Ishida, Y., Aida, T. & Sasaki, T. (2018b). Spontaneous direct band gap, high hole mobility, and huge exciton energy in atomic-thin TiO2 nanosheet. *Chemistry of Materials*, 30(18), 6449–6457.

Zhou, Z., Zhang, H., Liu, J. & Huang, W. (2021). Flexible electronics from intrinsically soft materials. *Giant*, 6, 100051.

Zhu, A., Zhao, Q., Li, X. & Shi, Y. (2014). BiFeO3/TiO2 nanotube arrays composite electrode: construction, characterization, and enhanced photoelectrochemical properties. *ACS applied materials & interfaces*, 6(1), 671–679.

Zhu, H., Yang, Q., Liu, D., Liu, D., Zhang, W., Chu, Z., Wang, X., Yan, S., Li, Z. & Zou, Z. (2020). Polaron states as a massive electron-transfer pathway at heterojunction interface. *The Journal of Physical Chemistry Letters*, 11(21), 9184–9194.

Zimmermann, S., Wolff, C. & Sures, B. (2017). Toxicity of platinum, palladium and rhodium to Daphnia magna in single and binary metal exposure experiments. *Environmental Pollution*, 224, 368–376.

Zou, H., Rowe, D. M. & Min, G. (2001). Growth of p-and n-type bismuth telluride thin films by co-evaporation. *Journal of crystal growth*, 222(1-2), 82–87.